2009

DEVELOPMENT OF A NEW GENERATION OF BONE CEMENTS USING NANOTECHNOLOGY

S.M. Zahangir Khaled

Recommended Citation

Khaled, S.M. Zahangir, "DEVELOPMENT OF A NEW GENERATION OF BONE CEMENTS USING NANOTECHNOLOGY" (2009). *Digitized Theses*. 3937.
https://ir.lib.uwo.ca/digitizedtheses/3937

DEVELOPMENT OF A NEW GENERATION OF BONE CEMENTS USING NANOTECHNOLOGY

(Spine title: Nanocomposite Bone Cements)

(Thesis format: Monograph)

by

S.M. Zahangir Khaled

Graduate Program
in
Engineering Science
Department of Chemical and Biochemical Engineering

A thesis submitted in partial fulfillment
of the requirements for the degree of
Doctor of Philosophy

School of Graduate and Postdoctoral Studies
The University of Western Ontario
London, Ontario, Canada

Abstract and Key Words

Fundamental and applied research on the reinforcement of polymeric materials using nanotechnology is of tremendous potential importance to many industrial and scientific areas, such as the biomedical, automobile and aeronautical industries. In the biomedical industry, there is a sustained interest to develop novel bone cements with enhanced mechanical properties. Bone cement is a self-polymerizing composite material of poly(methyl methacrylate) (PMMA) which has been used in joint replacement surgeries since the 1950s. Bone cement fills the space between the prosthesis and bone to stabilize the implant and transmit functional loading. Joint replacement failure is due to a number of factors, one of which is known to be bone cement mantle failure resulting from the cement's poor mechanical properties. The aim of this research was to test the efficacy of using nanotechnology to improve the mechanical properties of PMMA based bone cement.

This was accomplished through a range of different investigations. Focusing on nanostructured titania (n-TiO_2) initially, titania nanofibers (n-TiO_2 fiber) and nanotubes (n-TiO_2 tube) were introduced into a commercial PMMA matrix with the achievement of increased fracture toughness (K_{IC}), flexural strength (FS) and flexural modulus (FM) of the resulting nanocomposites. The n-TiO_2 fiber/tubes were surface treated to improve dispersion and ensure compatibility with the PMMA matrix using the bifunctional monomeric coupling agent, methacrylic acid (MA). MA has two distinct centers of reactivity, one links with the inorganic nanofiller through a molecular bridge, while the other establishes a covalent bond with the polymer chain. On the basis of the determined mechanical properties, an optimum composition was found at 2 wt% loading of n-TiO_2

which provided a significant increase in K_{IC} (10-20%), FS (20-40%) and FM (96-122%) when compared with the unfilled PMMA matrix ($P<0.05$, one way ANOVA). These improvements were attributed to a high level of interaction and strong chemical adhesion between the n-TiO_2 and PMMA matrix. However, both the n-TiO_2 fibers and tubes did not provide sufficient radiopacity to the PMMA matrix at their optimum level of loading in the composites, which restricts the application of the resulting composites as bone cements.

Secondly, the n-TiO_2 tubes were modified through an in-situ integration process incorporating strontium into tube at the time of the tube synthesis. The modified n-TiO_2 tubes were shown to provide reasonably higher radiopacity to the PMMA matrix than the unmodified tubes at the same level of loading, attributed to the presence of the highly radiopaque strontium atom. While keeping the K_{IC} values of the nanocomposites the same as those reinforced by n-TiO_2 tubes, the strontium modified tubes were shown to enhance the *in vitro* biocompatibility of the PMMA matrix with rat calvariar osteoblast cells.

Finally, the functionalized n-TiO_2 fibers and tubes were introduced into a clinically used commercial radiopaque bone cement CMW$^{®}$1, with the n-TiO_2 acting as a reinforcing phase. Mechanical and other important physical characteristics of the reinforced cements were analyzed according to the universal bone cement standard ISO 5833. Based on the determined mechanical properties of the reinforced cements, the optimum composition was found at 1 wt% loading of the n-TiO_2 fibers and tubes separately. The observed optimum loading provided a significant increase in K_{IC} (63-73%), FS (20-42%) and FM (22-56%) of the reinforced cements when compared to the as received CMW$^{®}$1 cement

($P<0.05$, one way ANOVA). In addition, the setting and rheological characteristics of the curing cement as well as its *in vitro* biocompatibility were shown to remain unaltered at the optimized small loading (1%).

This study demonstrated a novel pathway to augment the mechanical properties of PMMA based bone cement by providing an enhanced interfacial interaction and strong adhesion between functionalized n-TiO_2 and PMMA matrix. This approach enhanced the effective load transfer within the cement while providing excellent biocompatibility. From the studied experimental outcomes, it is considered that nanotechnology using modified n-TiO_2 provides a new vehicle to improve the mechanical properties of acrylic bone cement.

Key Words: Titania nanofibers, Titania nanotubes, Functionalization, Polymer nanocomposites, Acrylic bone cement, Fracture toughness, Flexural strength, Flexural modulus, Rheology, Setting characteristics, Radiopacity, In vitro biocompatibility, Alkaline hydrothermal, Supercritical carbon dioxide.

Dedication

To my dearest wife and son:

Mahera and Ayaan.

Acknowledgements

First and foremost, I would like to express my heartfelt gratitude to my beloved mother Shahinara Hoque, and my father Mahfuzul Hoque for their cares and sacrifices for me throughout their whole life. I would like to thank my wife Mahera, and son Ayaan. Throughout all my endeavors, their love, support, guidance and endless patience have been truly inspirational.

I would like to convey my grateful appreciation to my supervisors, Professors Amin Rizkalla and Paul Charpentier, for their supervision, advice and guidance throughout my Ph.D. research at Western. Above all and the most needed, they provided me unflinching encouragement and support in various ways, without which this work would not have been completed.

I gratefully acknowledge Professors Kibret Meqaunint and Sohrab Rohani, for their kind help and constructive advices during my research.

I would like to express my sincere gratitude to Dr. Douglas Hamilton and Mr. Richard Miron of the Oral Biology department, UWO for their expert work on the cellular study of my materials. Many thanks go to Mr. Ron Smith and Dr. Richard Gardiner of the Biology department, UWO, for TEM, to Dr. Todd Simpson of Nanofabrication laboratory, UWO for SEM and to Dr. Richard Bohay of Dentistry department, UWO for X-ray Radiography.

I have been indebted to Dr. Ruohong Sui, my former colleague of the research group, for sharing his scientific and technical knowledge and experiences on initiating my research.

I would like to express my passion to all the colleagues in my group: to Mr. Jeff Gribbon for sharing his knowledge of DSC-TGA, to Ms. Behnez Hojjati for her cooperation on

GPC, to Bedilu Allo for his scientific discussion and helping me on the final formatting of my thesis, and to William Xu, Muhammad Chowdhury, Selma Sadaldin, Nasrin, Farhangi, Sahar Samimih, Sepideh Rezvani, Daniel Costa and Christina Chan for their friendship and help.

I would like to thank OGSST scholarship and the financial funding from the Canadian Natural Science and Engineering Research Council (NSERC) and the Materials and Manufacturing Ontario EMK program.

Table of Contents

List of Tables

List of Figures

List of Appendices

List of Abbreviations, Symbols, Nomenclature

Abbreviations:

n-TiO_2 fibers: titania nanofibers

n-TiO_2 tubes: titania nanotubes

SrO-n-TiO_2 tubes: strontium oxide incorporated titania nanotubes

MMA: methyl methacrylate

PMMA: poly(methyl methacrylate)

MA: methacrylic acid

PVA: poly(vinyl alcohol)

BPO: benzoyl peroxide

PBS: phosphate buffered saline

FBS: fetal bovine serum

α-MEM : alpha-modified eagle medium

PFA: paraformaldehyde

XRD: X-ray diffraction

FTIR: Fourier transform infrared spectroscopy

SEM: scanning electron microscopy

TEM: transmission electron microscopy

STEM: scanning transmission electron microscopy

EDS: energy dispersive X-ray spectroscopy

EELS: electron energy loss spectroscopy

DSC: differential scanning calorimetry

TGA: thermogravimetric analysis

DTG: differential thermogravimetry

IEP: isoelectric point

RCO: rat calvarial osteoblast

NTP: nothless triangular prism

CNSR: Chevron notched short rod

K_{IC}: fracture toughness

FS: flexural strength

FM: flexural modulus

t_{dough}: dough time

t_{set}: setting time

t_{ons}: onset time of viscosity increase

t_{cure}: curing time

T_{max}: maximum polymerization temperature

Symbols:

σ: shear stress

$\dot{\gamma}$: shear rate

ε_0: amplitude of oscillatory strain

ω: frequency of oscillation

G': storage modulus

G'': loss modulus

G^*: complex modulus

η': dynamic viscosity

η^* : complex viscosity

I : intensity of transmitted radiation

I_0 : intensity of incident radiation

μ : mass attenuation coefficient

M: bending moment

δ : bending deflection

K : stress intensity factor

K_c : critical stress intensisty factor

$\gamma^*_{\min}$: dimensionless stress intensity factor coefficient minimum

C_L: velocity of longitudinal wave

C_S: velocity of transverse wave

ρ : density of solid

ν : Poisson's ratio

G_{pullout} : energy need to pull out fibers

τ : interfacial shear strength

Chapter 1: Introduction

1.1.Overview

This thesis focuses on developing poly(methyl methacrylate) (PMMA) based bone cements reinforced with titanium dioxide having novel nanostructure, i.e. nanofibers and nanotubes. A novel functionalization route of the nanostructured titania has been introduced in this work to compatibilize the nanomaterials with the organic PMMA matrix. Using this route, methacrylic acid (MA) was used for its bifunctional characteristics of a carboxyl group for coordination and electrostatic interaction with the titania and a vinyl group for subsequent polymerization with methyl methacrylate (MMA) monomer. Fundamental studies on the resulting functionalized nanomaterials and reinforced bone cements were carried out using various physico-chemical, mechanical and biocompatibility testing including FTIR, TGA, DSC, electron microscopy, universal mechanical tester, rheometer, medical X-ray and osteoblast cellular response.

In this chapter, the motivation of the research and the potential application of the synthesized bone cements are addressed.

1.2.Motivation of the research

A new generation of acrylic bone cements with mechanical properties significantly higher than those commercially available are strongly desired in order to ensure the long term clinical performance of the cemented arthroplasty. In all acrylic bone cement formulations clinically used today, micron-sized particles of either $BaSO_4$ or ZrO_2 are introduced to provide radiopacity, but which also lead to a deterioration in mechanical properties.[1] In an effort to develop mechanically strong cements, various studies have been performed in synthesizing reinforced cements with various inorganic oxides and other materials.[2-5]

The purpose of this research was to develop a new generation of acrylic bone cements reinforced with nanostructured titania having fibrous and tubular morphology which would exhibit enhanced static and dynamic mechanical properties with sufficient radiopacity and biocompatibility.

1.3.What is a bone cement?

PMMA-based bone cements are the predominant synthetic biomaterials used in orthopaedic surgery for cemented arthroplasty as a means of fixation of the prosthesis in the bone. It functions by filling the gap between the prosthesis and the contiguous bone and transmitting load from the prosthesis to the bone (Fig 1.1).[1,2]

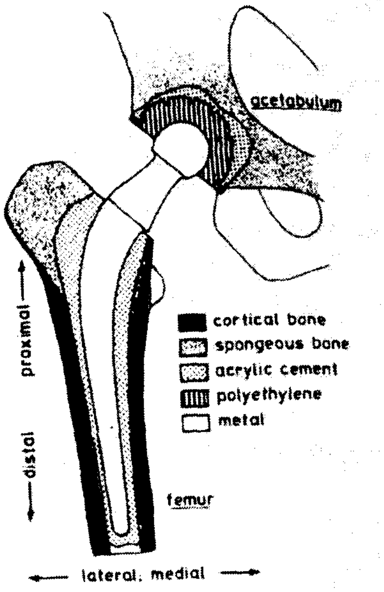

Figure 1.1. Schematic diagram of prostheses and PMMA bone cement in an acetabular socket and femur. (Ref.[6])

The history of bone cements dates back more than 100 years. In 1890, Dr. Gluck described the use of ivory ball-and-socket joints which were especially useful in the treatment of diseases of the hip joint. These joints were stabilized in the bone with a cement composed of colophony, pumice powder, and plaster.[7] In 1951, Dr. Haboush used a self-curing acrylic dental cement to secure a total hip replacement.[8] Also at this time, PMMA cements were used primarily in dentistry to fabricate partial dentures, orthodontic retainers, artificial teeth, denture repair resins, and an all-acrylic dental restorative. However, the major breakthrough in the use of PMMA in total hip replacement (THR) was the work of Charnley in 1964 who used it to secure fixation of the acetabular and femoral components and to transfer loads to bone.[9,10] Today several million joint replacements are conducted annually world-wide with more than half of them using bone cements, with this trend increasing.[11] Bone cement is considered a reliable anchorage material being easy to use for clinical practice and providing an excellent primary fixation between the bone and implant, while allowing faster recovery of the patient.

1.4.Chemical composition and chemistry of bone cements

Bone cements are self curing systems generally dispensed as powder and liquid phases, which are packaged separately and are mixed *in situ* in the operating theatre, prior to use. Cements are mixed prior to insertion and introduced in the intramedullary canal in a dough state which subsequently undergoes *in situ* polymerization to yield the hardened cement mass.[1,12]

1.4.1. Solid phase

The solid phase of bone cement is mainly composed of spherical particles (beads) of poly(methylmethacrylate) (PMMA) or acrylic copolymers containing ethyl acrylate, methyl acrylate, or even methylmethacrylate (MMA)-styrene copolymers in various trademark cements.[1] The prepolymer is present at a concentration of approximately 80 wt% with the bead size ranging from 30 to 150 μm. Average molecular weights of the beads are reported to be in the range from 44,000 to 1,980,000.[13] The solid phase also contains the initiator, benzoyl peroxide (BPO), in a concentration ranging from 0.75 to 2.5 wt%, which is physically mixed with the beads. Another component of this phase is the radiopaque agent, either barium sulphate or zirconium dioxide, that are normally incorporated as an X-ray contrast agent to allow X-ray follow-up analysis of the prosthesis. The concentration of the radiopaque agent is generally around 10 wt% on the basis of the solid component, however, some formulations contain up to 15 wt%, and the average diameter of the radiopaque particles is around 5 μm.[1]

1.4.2. Liquid phase

The liquid phase of the cement formulation consists of MMA monomer at a concentration of 95 wt%, although a few formulations contain small fractions of butylmethacrylate (BMA).[1] In order to initiate the polymerization at room temperature, *N,N*-dimethyl-4-toluidine (DMT) is added in the liquid phase as the activator in a concentration range of 0.89-2.7 wt%, however, a recent commercial formulation has an alternative tertiary aromatic amine, namely, 2-(4-dimethlyamino)phenyl ethanol. Finally, an inhibitor is added to the liquid phase to avoid any premature polymerization that may occur in the presence of heat or light during storage. The inhibitor belongs to the family of quinones, of which the most frequently used is hydroquinone. This acts as a radical scavenger forming radicals that are stabilised resonance.

An important parameter of acrylic bone cement formulations is the solid: liquid ratio, which is normally 2.18:1 in the majority of cements,[1] although may vary in the range from 2:1 to 2.7:1. In the acrylic bone cement formulation, the solid: liquid ratio needs to be optimized, because it is very sensitive for the cement's setting parameters. Care must be taken as manipulation of this ratio may have an adverse effect on excessive polymerization shrinkage or under-polymerization.[13]

As well, it has also been shown that the initiator/activator ratio has a significant effect on setting time, polymerization temperature and mechanical strength. The polymerization rate of MMA normally occurs in monomer solutions containing about 1.5 moles of peroxide per mole of amine,[13] although, this ratio can range from 0.5 to 2.5 in some commercial formulations.

The preparation of the cement starts when both the solid and liquid phases are mixed in a bowl, usually at room temperature. On mixing the two phases, the monomer begins to solvate the surface of the prepolymerized beads producing a paste-like consistency. The viscosity increases with time, so that in a few minute the mix becomes a viscous mass and then attains a rigid state. This setting process has been classified into four phases called the: 1) mixing phase, 2) waiting phase, 3) working phase and 4) hardening phase.[1,13] The physical processes involved throughout the setting of the cement are wetting of the prepolymerized particles by the monomer, the subsequent swelling and partial dissolution of the PMMA particles into the monomer, diffusion of the liquid into the organic powder and monomer evaporation. From a chemical point of view, when both components are mixed, the reaction between the initiator and the activator starts giving rise to primary free radicals, which initiate the free radical polymerization of the monomer. During the mixing step, the wetting process predominates while during the waiting phase, the radical polymerization commences causing the viscosity to increase. During the working phase the polymerization progresses resulting in a reduction in the mobility of the growing macromolecular species and a sudden increase in the viscosity and heat generation. Finally, in the setting step the cement hardens with the subsequent cessation of the polymerization due to vitrification of the material.[13]

During the polymerization process, the MMA monomer with a density of 0.937 g/ml, converts to a polymer of higher density (1.18 g/ml). This phenomenon leads to a volume shrinkage which is of great concern in orthopaedic and dental applications. PMMA derived from pure MMA exhibits a volume shrinkage of approximately 21%, however, the presence of prepolymerized powder in acrylic bone cement formulations significantly reduces this value.[1,13] Also, the real shrinkage is lower due to porosity generated by the air bubble inclusion during the dough stage, release of absorbed air during polymerization, vaporisation of monomer and air absorbed during insertion of the metal stem.

1.5.Properties of bone cements

As described above, bone cement is an implant biomaterial that is prepared right before the operation. Once inserted into the bone joint, the transfer of the forces from bone-to-implant and implant-to-bone is the primary function of the bone cement. Moreover it is supposed to be radiopaque in order to allow follow up on its post operative condition by X-ray examination. Above all, the bone cement should exhibit biocompatibility. Hence, the bone cement must possess a number of mechanical, handling and physical properties as described below.

1.5.1. Mechanical properties

The cement layer has the main task of resisting and transferring the loads between the natural and synthetic coupled materials, while functioning as a mechanical buffer, reducing the stress concentrations and absorbing mechanical shock.[6] Since the forces transmitted through the hip are as high as three times body weight when walking and eight times body weight when falling, bone cement is subjected to high stresses. Also the cement has to perform in the aggressive environment of the body,[14,15] with the ability to do this reliably for a long period of time being critical to the long-term survival of the implant. If the external stress factors are greater than the inherent strength of the cement, a break will result. For this reason, it is extremely important that the bone cement is mechanically stable possessing a substantial degree of strength and toughness.

1.5.1.1. Stiffness

Stiffness is the resistance of an elastic body to deflection or deformation by an applied force which is the state of being rigid.[16] Therefore, it is the measure of the ability of the bone cement to act as an elastic buffer between the prosthesis and the bone.[1] Both static and dynamic mechanical testing can be applied to measure a cement's stiffness. The most prominent static method includes tensile and flexural moduli while the dynamic methods include dynamic elastic and storage moduli.

1.5.1.1.1. Flexural properties

Flexural or bending properties of a material are resistance of the material against flexural load, which is a combination of tensile, compression and shear forces. These properties of cements are germane to the life of the arthroplasty because *in vivo* loading invariably involves a combination of shear, tension and compression forces.[13,16] Flexural properties reflect the rigidity of bone cements against bending through two of its key components, flexural strength (FS) and flexural modulus (FM). FM represents the ratio of stress to corresponding strain of the material within the elastic region. Stiff materials demonstrate a high modulus while compliant materials exhibit a low modulus. Within the elastic region the stress and strain are directly proportional following Hooke's Law, and, if the load is released, the material regains its original dimensions (Figure 1.2). The elastic region is limited by a stress limit.

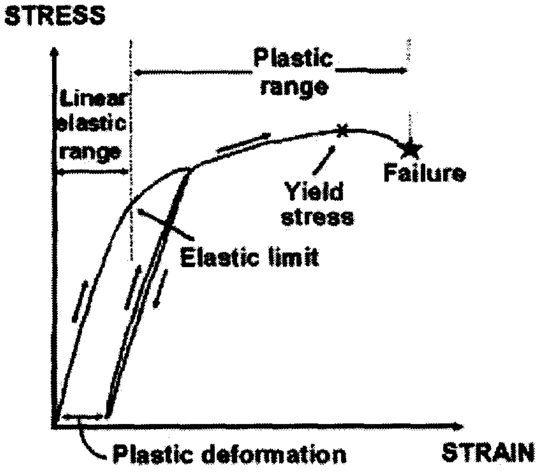

Figure 1.2. Typical stress-strain curve of materials. (Ref.[17])

Beyond this limit is where the mechanical properties of the material actually change, and the material might not recover its initial shape after releasing the load. FS is a measure of the maximum bending stress the material can withstand before rupture.[13,18,19]

1.5.1.1.2. Dynamic elastic modulus

The dynamic elastic modulus of bone cement is a measure of its rigidity under dynamic loading. This is a vital material property of bone cements as normal daily activities would subject the cemented arthroplasty to dynamic loading.[18] Moreover, having acrylic polymer as the cement matrix, bone cement is a viscoelastic material. Traditional static elastic modulus focuses on the elastic component of the material while dynamic elastic modulus indicates both the elastic and viscous response of the material.[20,21] Moreover, dynamic testing is very sensitive to structural property changes of the material, and is a measure of the composite's isotropy.[21,22]

1.5.1.1.3. Dynamic storage modulus

The dynamic storage modulus of the bone cement is another dynamic mechanical property which reflects its ability to return or store energy under cyclical loading.[23] As the cement is orders of magnitude weaker than either the bone or implant, cyclic mechanical stresses *in vivo* can lead to failure at the bone-cement or cement-prosthesis interface. Dynamic mechanical properties are considered as long-term properties of bone cement indicative of the transfer of load into the bone over the normal working life of a total joint replacement. Dynamic mechanical analysis measures the response of bone cement to a sinusoidal stress over a wide range of frequencies and temperatures and is especially sensitive to the chemical and physical nature of polymeric cement matrix and the inclusions within the bone cement. The dynamic storage modulus represents the elastic phase of the system, and is equivalent to the energy stored through deformation.[13]

1.5.1.2. Toughness

Toughness of a material is a measure of its ability to absorb energy prior to fracture and is an indication of the amount of energy necessary to cause fracture.[18] Toughness represents the strain energy per unit volume (strain-energy density) in the material at fracture. The strain-energy density is equal to the area under the stress-strain diagram to fracture (Figure 1.2).[24] The higher the toughness is, the greater is the ability of a material to absorb energy without fracturing. This toughness is generally termed as fracture toughness (K_{IC}) when characterizing bone cement.

K_{IC} of bone cement is a measure of its ability to absorb energy prior to crack propagation. In normal daily activities, the implant is subjected to cyclical loading which may result in cement failure by fracturing through the discontinuities in its weak link zones with the implant. The K_{IC} of the cement then is clearly an important parameter as far as the prosthesis performance is concerned.

1.5.2. Rheological properties

The rheological properties of bone cements during their curing phase are related to their mixing/handling characteristics and viscoelastic properties. Furthermore, these properties have a significant influence on material porosity, ability of the cement to penetrate into bone, and the ultimate strength of the cement/prosthesis interface.[25] For instance, the viscosity of the bone cement in its early life represents the capacity of the system to flow into interstices within cancellous bone and thus enable effective mechanical interlock at the bone cement-bone interface. Typically, at early time periods the cement represents its lowest viscosity and as the reaction proceeds, viscosity increases, thereby decreasing the cement's flowability. Bone cement is usually applied in two ways. The first method consists of mixing the cement into a dough stage with sufficient viscosity, then the cement is inserted into the bone. The other method involves the use of a syringe or cement gun to inject the paste, which has the advantage of reducing the porosity and providing higher penetration into the bone cavity.[13] For each method, bone cements with different flow characteristics are required. Two of these rheological or handling characteristics are working time and setting time of the cements. These can be directly evaluated from the trend of viscosity of the cement with time during curing.[26] According to this property, commercially available acrylic bone cements can be found as low, medium, and high-viscosity formulations having different characteristic setting parameters.

1.5.3. Radiopacity

Radiopacity refers to the relative inability of electromagnetic radiation, particularly X-rays, to pass through a particular material. Radiopaque substances are those that do not allow X-rays or similar radiation to pass through, and exhibit a white appearance in radiographic imaging when using X-rays.[27,28] PMMA is not a radiopaque material, therefore it is impossible to directly determine the boundaries of bone cement having pure PMMA matrix during the surgery by ordinary X-ray imaging techniques. Until 1972, PMMA cement did not contain any radiopaque materials and was, therefore, radiolucent.[6] Radiopacity is a desirable property in acrylic bone cements, to allow post-operative assessment of the implant using X-radiography. Hence, it is important that the orthopaedic surgeon can easily monitor and evaluate the healing and loosening processes to differentiate between bone, bone cement and osteolysis after a joint replacement.[29] For this reason, radiopaque media are added to PMMA bone cements. Barium sulphate ($BaSO_4$) or Zirconium dioxide (ZrO_2) are used as radiopacifiers in all commercially available bone cements.[1,16,30] These radiopacifiers are added externally to the cement and are dispersed uniformly through the polymer powder and in the resulting hardened bone cement.[6] All current PMMA bone cements contain 8-15% X-ray contrast agent within the polymer powder.[1]

1.5.4. Biological properties of acrylic bone cements

All biomaterials must be biocompatible. PMMA bone cements are considered biocompatible despite the toxic potential of the bone cement residual monomer and the heat generated during the exothermic polymerization.

Initially, the major problems of acrylic bone cement are related to the temperature increase during the polymerization and the release of residual monomer after polymerization. The human osteoblast cell which is responsible for bone formation interacts with the cement while it is in the body.[31] Cell necrosis, which is a phenomena of osteoblast cellular reaction with the toxic components of the cement may occur because of the following: (1) monomer toxicity, (2) the high temperature of cement polymerization, and (3) osteolysis caused by wear debris generation.[32] PMMA is generally considered non-toxic, but the residual monomer (MMA) can cause an irreversible deterioration of osteoblast cells. After fifteen minutes of polymerization, there is a residual monomer of approximately 3-5% and 2.7% after 24 hours.[33] According to Schoenfeld *et al.*[34] the toxicity of the monomer disappears after 4 hours. MMA is vey volatile and is rapidly cleared from the body through the lungs resulting in a local concentration that remains vey low.[35] MMA monomer molecules escaping from the implanted polymerizing cement could cause a drop in the partial pressure of arterial oxygen leading to an increased heart rate.[36] However, residual MMA monomer is normally considered to be converted by the body to methacrylic acid. The methacrylic acid, as a coenzyme A ester, is a normal intermediate in the catabolism of valine, and the existence of an enzymic system would permit methacrylic acid to enter a normal pathway leading to carbon dioxide formation. It has been shown that over 80% of an administered dose of MMA is expired as carbon dioxide within 5-6 hours.[37]

The production of heat occurs at the bone-cement interface during cement polymerization, which in vitro has been measured to be between 60 and 90 °C and in vivo between 40 and 50 °C, both depending on the thickness of the cement.[32] The effect of this heat generation on bone was studied by Lundskog *et al.*[38], who concluded that the exothermic polymerization did not add to the surgical trauma and had no influence on bone generation. Lee *et al.*[39] found that the leakage of monomer was very low after the curing phase. Likewise Rhinelander *et al.*[40] reported a maximal temperature of 55 °C with the placement of thermometers at the bone-cement interface, and concluded that thermal necrosis from cement polymerization was not a significant factor.

In most cases, revision of the cemented orthopaedic prosthesis becomes necessary when pain occurs due to either movement of the prosthesis, bone fracture, bone cement fracture, or prosthesis fracture. More specifically, these complications may result from the prosthesis-cement, or cement-bone interfacial loosening or micromotion due to cement fracture or cement creep. Loosening of the prosthesis and fracture of the cement may lead to increased wear and bone cement particle formation. Those particles less than approximately 5 μm in size are phagocytosed by macrophages, which become activated and directly or indirectly cause bone remodelling and osteolysis. The final result is cell death leading to tissue necrosis and chronic inflammation. For the femoral stem, lower-viscosity bone cement had a revision rate 2.5 times greater when compared to the use of higher-viscosity cements. Additionally, a lower-modulus cement had a revision rate that was 8.7 times greater than the higher-viscosity cements.[32]

1.6.Commercial aspects and potential limitations of bone cements

As a result of our longer life expectancy, musculoskeletal disorders are affecting millions of people around the world, with an increasing frequency of joint diseases, which account for more than half of all chronic conditions in persons aged 60 years and over. As well, back pain is the second leading cause of sick leave.[41] According to the American Agency for Healthcare Research and Quality, in 2005 musculoskeletal procedures were performed with over 3.4 million hospital stays, causing aggregate costs of $31.5 billion.[42] Knee arthroplasty, hip replacement, and spinal fusion have been the most common musculoskeletal procedures, accounting for about 1.2 million hospital stays. From 1997 to 2005, the volume of knee and hip replacements in the US rose by about 69% and 32% respectively.[42] The demand for these procedures is projected to double in the next two decades. As a result, societies and healthcare systems face huge financial burdens which need to be addressed. The level of reimbursement has changed in most societies, and healthcare providers are challenged to deliver high-quality patient care with limited financial resources.

In this challenging economic environment, bone cement plays a vital role. Still, to date, about 90% of all knee arthroplasties and about 60% of all hip arthroplasties worldwide are fixated by a bone cement.[11] Cementless arthroplasty is another way of joint replacement surgery which entails special surface finish, less stiff and more biologically inert metal alloys as the implant. However, the clinical outcomes of cementless total hip and knee arthroplasties have proved to be below expectation with a new set of problems being spawned by their use.[43] For instance, cementless hip arthroplasty has been beset by perioprosthetic osteolysis, high thigh pain and failure of the bone-implant interface.[44] In addition, cementless implants may be more expensive than their cemented counterparts and in price-sensitive markets, the choice of implants may be a very commercial, non-clinical decision.[11]

In spite of the significant successful performance in total joint replacement surgery, cemented arthroplasty is beset with a number of drawbacks mainly resulting from the physical and mechanical failure of the cement.

The heavy metal salts of barium or zirconium used as an X-ray contrast medium in most acrylic cements clinically used today, significantly affects its physical and mechanical properties.[6] First of all, these inorganic compounds are highly polar and ionic and are not compatible with the non-polar polymeric matrix of the acrylic cement.[2,6,28] Without having any chemical adhesion to the polymer chains, these inorganic radiopacifying agents can only interact with the acrylic matrix by either mechanical or physical interactions.[6,28] These limited interactions provide poor adhesion of the filler to the matrix with a resultant detrimental effect on the mechanical properties of the cement. The elastic properties of any composite largely depend upon the transfer of the external load from the filler to the matrix.[20] Poor adhesion of the radiopacifying particles and the acrylic matrix is also detrimental to the effective load transfer from the filler to the matrix, resulting in the cement being mechanically weak to external load. As previously mentioned, cemented arthroplasty is subjected to dynamic loading in daily life activities which provides frequent tensile and compressive stresses.[2] Without being strong enough to transfer these loads, the filler particles tend to debond at the interface from the matrix, which results in the formation of pores within the matrix.[6] These pores provide sites for stress concentration and subsequently facilitate mechanical failure by allowing any crack or discontinuity to propagate through the cement.[2,6,30,45] The microstructure of the radiopacifying particles plays a vital role here. Spherical shaped $BaSO_4$ particles are less likely to withstand these tensile loads while the ZrO_2 particles having cauliflower-like shape, can secure mechanically to the polymer matrix to a certain degree.[6] Moreover, being smaller in size than the ZrO_2 particles, the $BaSO_4$ particles tend to agglomerate facilitating the growth of pores within the cement matrix.[45] It has been shown that $BaSO_4$ reduces the tensile strength and K_{IC} considerably and this reduction seems to be lower than that of ZrO_2 filled cements.[46,47] Reductions in the FS with the addition of these radiopacifying agents has also been reported.[48]

Moreover, without having any strong bond to the polymer matrix, the radiopacifying particles are more likely to separate from the cement matrix resulting from the frequent wearing or friction of the cement mantle with the implant.[49] This phenomenon would facilitate the exposure of the inorganic radiopacifying particles to the surrounding biological tissue. There is evidence that these compounds evoke a significant pathological response in the surrounding tissue.[50] Moreover, barium is known to have the capacity for toxicity.[49] Intradermal injection of $BaSO_4$ into experimental animals is known to cause a foreign-body inflammatory reaction.[51] The inflammation caused by the release of toxic barium ions results in bone resorption with a subsequent loosening of the implant.[13] Animal experiments with different cell cultures have shown greater differences in bone resorption around the bone cement application area when using $BaSO_4$ in comparison to ZrO_2.[12,52] Barium has also been shown to intensify the release of inflammatory mediators in response to PMMA particles.[53]

In addition, the liberation of hard zirconium particles at the interface between the cement and metal implant is regarded to cause prosthesis loosening due to mechanical abrasion.[52] Moreover, being harder than the metallic femoral head, both $BaSO_4$ and ZrO_2 particles may cause damage to the articulating surface with a marked increase in the production of polyethylene wear debris.[54] For all these reasons, bone cements with X-ray contrast agents cause considerably more bone resorption than the cements without any radiopacifier.[49,55]

1.7.Literature review on reinforcing bone cements

Acrylic bone cement occupies a distinctive place in the hierarchy of synthetic biomaterials, as it is the only material currently used for anchoring a prosthesis to the contiguous bone in a cemented arthroplasty. However, the cement is not without its drawbacks. The main drawback is the postulated role in aseptic loosening and hence, the limited clinical life of the arthroplasty. In turn, this role is directly related to the mechanical properties of the cement, especially the resistance to fracture of the cement in the mantle at the cement-prosthesis interface or the cement-bone interface. Taking this into account, significant efforts have been made in recent years to enhance the mechanical properties of bone cements. These experimental investigations to reinforce bone cements can be divided into two broad categories: 1) design of experimental bone cements by developing novel radiopaque agents that are more compatible with the organic cement matrix and the surrounding biological tissue, and 2) reinforcement of the commercial bone cements by incorporating different fillers as reinforcing agents.

F. Kjellson *et al.*[56] attempted to produce radiopaque bone cements by incorporating the water soluble non-ionic iodine- based radiopacifiers, iohexol (IHX) and iodixanol (IDX).

They reported the mechanical properties of bone cements containing different loadings of IHX and IDX with different particle sizes. For a size range of 15-16 μm of IHX and IDX, they were able to obtain significantly higher ultimate tensile strength and strain to failure at 8wt% loading of the radiopacifiers compared to the Palacos® commercial cement (containing 8 wt% of ZrO_2). However, the Young's modulus of both cements were significantly lower than that of Palacos®, likely due to the incompatibility of the radiopacifiers with the cement matrix as well as the larger size of the radiopacifiers. Being water soluble, the radiopacifying particles would dissolve in the body fluid when escaping from the cement during wearing, which was hypothesized to minimize harm to the surrounding tissue.

S. Deb *et al.*[28] reported the incorporation of organo-bismuth compounds, namely, triphenyl bismuth (TPB), as a radiopacifying agent for acrylic bone cement. Triphenyl bismuth is an organometallic compound containing the heavy metal atom, bismuth. TPB is soluble in MMA monomer, therefore, allowing homogenous distribution in the polymer forming optically lucent radiopaque cements. These cements were found to exhibit superior mechanical properties such as ultimate tensile strain and modulus in comparison to the control commercial cement containing $BaSO_4$ as radiopacifier. An optimum concentration of TPB was achieved at 10wt%, above which the measured mechanical properties started to decrease. However, the fracture toughness and flexural modulus as well as cellular response were not performed in this study. Similarly, L. Hernandez *et al.*[57] reported the use of another organo-bismuth compound namely, bismuth salicylate (BS) as the radiopacifier in an acrylic cement matrix. BS is soluble in MMA monomer which leads to the homogeneous distribution of the radiopacifiers in the acrylic matrix. An optimum condition was achieved at 10wt% loading of BS which allowed the cement to exhibit significantly lower exotherms and higher setting times than the control cement containing 10wt% $BaSO_4$. However, this wt.% loading did not allow the cement to possess significantly enhanced compressive and tensile strength compared to the control cement. Moreover, BS is hydrolyzed by the body fluid and is readily prone to be released from the cement.

In order to develop radiopacifying agents that are more compatible with the organic matrix, another significant approach is to develop radiopaque monomers or copolymer bearing covalently bound halogen atoms, i.e. bromine or iodine, which can be copolymerized with acrylic monomers producing homogeneous radiopaque cements. K. Davy *et al.*[58] prepared polymer beads based on copolymers of methacrylic monomers containing the group triiodobenzoate, and used them as the solid phase to formulate cold-curing systems with good mechanical properties. Other cements prepared from radiopaque polymer beads are based on an equimolar copolymer of MMA and 2-[4-iodobenzoyl]-oxo-ethyl-methacrylate (4-IEMA).[59] These cements have intrinsic mechanical properties in compression tests superior to those of $BaSO_4$-containing cements. Results of in vitro biological evaluation of this novel radiopaque cement did not differ from those of translucent PMMA or $BaSO_4$-containing cement, and the in vivo experiments showed no inflammation or foreign body reaction near the iodine-containing bone cement.[60] Further studies on the mechanical, thermal and physical properties of the 4-IEMA-containing cement led to the conclusion that this formulation was a viable alternative to current formulation for use in cemented arthroplasties.[30] J. Roman *et al.*[61] reported the incorporation of an iodine-containing methacrylate in the liquid phase of the acrylic bone cement. Thus, cements prepared with 5.0-7.5 wt% of 2,5-diiodo-8-quinolyl methacrylate (IHQM) with respect to the liquid phase were shown to present sufficient radiopacity, have a lowered exotherm and provide a statistically significant increase in the tensile strength, K_{IC} and ductility in comparison to the $BaSO_4$-containing cement.[62] However, the fatigue crack propagation resistance of these cements remained similar to that of the radiolucent one,[63] providing poor K_{IC}. The biocompatibility of the iodine-containing cements is good, showing neither chronic inflammatory response nor macrophages in the area of the implanted rods in rats.[61,64] Following this approach, Artola *et al.*[65] have formulated radiopaque acrylic cements with different amounts (5-20 % v/v) of 4-iodophenyl methacrylate (IPMA) in the liquid phase and the addition of 15% v/v IPMA is enough to attain a radiopacity similar to that of a 10wt% $BaSO_4$-containing cement. These iodine-containing cements showed enhanced compressive and tensile strengths, elastic modulus and strain to failure with respect to conventional radiopaque bone cements. Other iodine-containing monomers that have been employed in the preparation of radiopaque acrylic bone cements are 2-[2', 3', 5'-triiodobenzoyl] ethyl methacrylate (TIBMA) and 3,5-diiodosalicylic methacrylate (DISMA).[66] The mechanical evaluation of the resulting cements showed an increase in the compressive strength and elastic modulus in comparison to $BaSO_4$-containing cements. The cement prepared with 5 wt% DISMA showed the highest value for compressive strength in dry specimens, although for wet samples the opposite behaviour was observed, probably due to the higher water uptake of this cement bearing carboxylic groups.

As stated above, one of the reasons for the detrimental effect of the radiopacifying agent on mechanical and biological properties is the lack of adhesion between the particles and the polymer matrix. One solution for improving the interfacial adhesion consists of establishing covalent chemical bonding between both materials by using a silane coupling agent. This agent needs to be able to react with the oxide surface of the inorganic particles and to copolymerize with organic monomers. This approach has been reported by J. Behiri *et al.*[67] in the reinforcement of poly(ethylmethacrylate)-based cements with 3-(trimethoxysilyl)propyl methacrylate (γ-MPS)-treated HA particles, giving cements with enhanced tensile modulus and yield strength compared with untreated fillers. However, the radiopacity of this bone cement was not reported in their work and HA is a poorly radiopaque material. M. Abboud *et al.*[68] proposed the use of alumina (Al_2O_3) particles treated with γ-MPS to prepare radiopaque acrylic bone cements as shown in scheme 1.

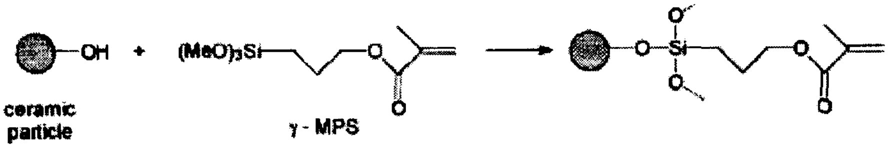

Scheme 1

The grafted γ-MPS on the Al_2O_3 particles acts as a coupling agent by covalently binding with the polymer matrix making the silanized Al_2O_3 act as a radiopacifying and reinforcing agent. The effectiveness of the surface modification of ceramic oxide particles such as Al_2O_3, TiO_2 and ZrO_2 through grafting of γ-MPS was previously reported.[69] The mechanical characterization of the so-prepared cements reveals an improvement in compression with values of modulus of the order of 3.40 GPa; however, the formulations require high processability because of poor wetting of the filler surface with liquid monomer which results in very large void formation inside the cement.[5] M. Abboud *et al.*[70] also reported the formulation of a new acrylic bone cement where the γ-

MPS- modified alumina particles are embedded in poly(methyl methacrylate-co-ethyl acrylate) beads by copolymerization with the corresponding acrylic monomer through suspension polymerization, prior to mixing with the liquid part of the cement. The cement is prepared by mixing these hybrid beads with liquid monomer resulting in a cement with uniform distribution of the radiopacifying fillers. The compressive strength of the cement cured with the hybrid beads decreased with alumina content whereas the compressive modulus remained roughly constant. The covalent bonding established between the acrylic matrix and the alumina fillers was hypothesized to reduce the production of abrasive ceramic debris in the tissue around the joint with a subsequent improvement of the biological properties.[64]

On the other hand, there is a sustained interest to improve the mechanical properties of commercial bone cements by incorporating filler materials or additives acting as reinforcing agents for the cement. One of the methods for improving the performance of the bone cement involves dispersing ultra high molecular weight polyethylene (UHMWPE) fibers in the bone cement matrix. UHMWPE is highly inert, has an excellent chemical resistance, low moisture uptake, with high toughness and good abrasion resistance.[12] B. Pourdehyimi *et al.*[71] investigated the feasibility of using UHMWPE fibers as reinforcing fillers in PMMA bone cements. Fibers mixed with PMMA powder at 1, 4 and 7% by weight were reacted with monomer to yield the bone cement composite. Linear elastic and non linear elastic fracture mechanics indicated a significant reinforcing effect at low levels of fiber content (1%), above which a plateau was reached. The K_{IC} remained unaffected with increasing fiber content. However, the FS and FM did not improve, which was attributed to poor mixing, the presence of voids, or poor interfacial adhesion. J. Yang *et al.*[72] also incorporated UHMWPE fibers and tested the mechanical properties of the resulting cement. Poor compatibility between polyethylene fibers and PMMA resulted in inadequate mixing and the inherent weakness of the interfacial bonds led to the formation of more voids in the matrix. In order to enhance the interfacial interaction of the UHMWPE within the polymer matrix, D. Hild *et al.*[73] modified the surface of UHMWPE by plasma treatment with gases such as carbon dioxide, nitrogen and argon, that improved the wettability of the fibers by the addition of polar groups. However, the surface topography remained unaltered, thus such composites were also limited by inadequate adhesion to the matrix. MMA graft UHMWPE fibers were obtained by using surface treated UHMWPE fibers with argon plasma, stored in a chamber containing methacrylate solution and subsequently irradiated with UV light.[74] Cements were formed with varying grafted UHMWPE fiber content, ranging from 0 to 6% by weight. The tensile strength of the cement containing MMA grafted fibers was found to increase with 4% by weight of the fibers, while the tensile modulus was not affected significantly with incorporation of the fibers.[75]

S. Saha *et al.*[76,77] investigated the effect of carbon fibers in bone cement matrices. Addition of carbon fibers in low volume fraction (1-2%) showed an improvement in the compressive, shear and tensile strengths with a higher Young's modulus. The ultimate tensile strength improved from 24 to 38 MPa and the modulus increased from 2.8 to 5.5 GPa with 2% by volume of carbon fibers. The addition of carbon fibers was also reported to lower the maximum polymerization temperatures of the cements during curing.. Moreover, PMMA reinforced with carbon fibers was demonstrated to give superior crack propagation resistance compared to conventional cements at the same stress intensity factor. However, the handling characteristics remained poor and it was suggested that better cements could be obtained with superior fiber mixing methods.[12,78]

B. Pourdehyimi *et al.*[79,80] and T. Wright *et al.*[81] have reported the incorporation of Kevlar 29, an aramid fiber, as a reinforcing filler for acrylic cements. An increase in the ultimate tensile strength was reported from 31 to 40 MPa with 7% by weight of aramid fibers with a large increase in stiffness. Aramid fibers were found to impart better properties than carbon fibers, in terms of fracture energy dissipation. The strength of these composites were however much lower than composites containing a similar content of carbon fibers.

Incorporation of metal fibers is another approach to reinforce acrylic bone cements. J. Taitsman *et al.*[82] reported the incorporation of two metal alloys, stainless steel and vitallium in the form of wires in PMMA bone cements and both were found to increase the tensile strengths. The mean tensile strength was found to improve from 27.5 to 50.5 MPa for the vitallium reinforced cement. S. Kotha *et al.*[3] introduced short titanium fiber heat treated at 800 °C in the acrylic bone cement containing $BaSO_4$. Because of the heat treatment, rutile titania particles were formed on the surface of the titanium fiber. They obtained an augmentation in K_{IC} using 14% fibered Ti and 14% $BaSO_4$ which is about 30% higher than the control cement containing pure $BaSO_4$. However, their effect on rheology and setting time were not reported. In another work done by S. Kotha *et al.*[83], the incorporation of short 316L stainless steel fibers in the acrylic cement matrix was reported. Having high K_{IC} of about 30-50 $MPam^{1/2}$ stainless steel exhibits a large energy absorption capacity. Therefore, cements reinforced with stainless steel fibers gave K_{IC} improvements of about 2.6 times compared to the control commercial bone cements having 10% $BaSO_4$ as radiopacifier. Increasing the volume fraction of the steel fibers resulted in a significant increase in the K_{IC}. However, the higher volume fractions of steel fiber additives adversely affected the cements rheology. In an attempt to enhance the interfacial adhesion between the steel fibers and acrylic cement matrix, S. Kotha *et al.*[84] incorporated silane coupling agents on the surface of steel fibers in another work. It was shown that the organosilane coating significantly increased the shear strength of the 316L SS-acrylic interface, which resulted in a significant improvement in the tensile mechanical properties of the bone cement. The K_{IC} of the 316L SS fiber reinforced specimen was improved to a small extent because of the silane coating. However, the bonds between the silicon atoms of the silane and the oxygen atoms of the oxidized metal surfaces are susceptible to weakening by water intrusion as observed by a reduction in the mechanical properties caused by the aging protocol. Another recent contribution of S. Kotha *et al.*[85] reported the incorporation of zirconia (ZrO_2) fibers in the bone cement matrix. In order to lessen the risk of wear debris coming out of cement resulting from the abrasion, each individual fiber was encapsulated in PMMA beads. With the incorporation of 5 volume% of coated or uncoated ZrO_2 fibers having 30 μm diameter, the K_{IC} of the resulting cements was improved by 41% compared to the control cement containing 6 wt% of $BaSO_4$.

Although a fair amount of research has concentrated on fiber reinforced cements, none of these experimental cements are yet in clinical use. Most fiber reinforced cements in general are adversely affected by the poor interfacial adhesion between the matrix and fiber which may cause voids due to improper mixing. Another problem with fiber incorporation is the detrimental effects on flow characteristics with intrusion properties being severely compromised. Although fiber reinforced cements tend to show enhanced mechanical properties, they also show an increase in the elastic modulus. The stiffness of the fiber reinforced cement resulting from very high elastic modulus causes an undesirable distribution of load from the prosthesis to the bone.

In order to achieve enhanced adhesion and thus better mechanical properties, self reinforced composites based on the inclusion of fibers of the same materials as the matrix has been developed. J. Gilbert *et al.*[86] have reported a self reinforced PMMA composite using oriented fibers of PMMA as a potential candidate for bone cement application. Thermomechanical processing of PMMA led to an increase its strength to about 220 MPa, strains to failure to about 25% and modulus values as high as 8 GPa, depending on the orientation imparted.[87] With the incorporation of PMMA fiber having a diameter of 120 microns, the tensile strength and modulus improved by 87 and 93% respectively compared to the conventional bone cements. The improvement become 132 % and 112% when the diameter of the PMMA fiber become 40 microns.[86]Therefore, the interfacial adhesion between the PMMA matrix and PMMA fibers is no doubt superior compared to dissimilar materials used in reinforcing the matrix.

There have been some attempts to incorporate particulate fillers in the cement matrix to reinforce the cement. Composites with particulate fillers are expected to have a lower strengthening efficiency and allow higher amounts of filler to be incorporated in comparison to fibers. J. Williams *et al.*[88] reported the use of natural cancellous bone particles from bovine tibiae to reinforce acrylic bone cements. The stiffness was found to increase with increasing content of bone particles to about 40% by volume. *In vivo* evaluation of experimental bone cement with inorganic bone particles as the fillers, in a canine hip prostheses showed a bony ingrowth in the resorbed bone particle spaces.[89]

This study demonstrated a viable cement/bone interface which could result in improved implant fixation, not only providing the immediate immobilisation of the prosthesis but also provide long term stability. A number of works have been reported on the incorporation of hydroxyapatite (HA) particles in bone cement. HA is a calcium phosphate ceramic which is similar to the mineral phase of bone. HA is an attractive filler for bone cements due to its similarity of the mineral phase of bone, and bioactive nature, which may allow formation of new bone to grow to the surface of the cement-bone interface, provided HA is present on the surface of the cement. A number of studies with HA as a reinforcing material in PMMA cements reported enhanced mechanical, physical and biological properties. The Young's modulus of HA-PMMA cements increased from 2.6 to 3.5 GPa with increasing content of HA volume fraction from 2 to 25%.[90] J. Perek and R. Pilliar[91] conducted K_{IC} measurements of the HA reinforced cements and demonstrated that 40% by weight of HA increased toughness from 1.0 $MNm^{-3/2}$ to 1.55 $MNm^{-3/2}$. Bone cements with such heavily loaded HA contents might give some hindrance in flow and result in poor intrusion characteristics. A. Murukami *et al.*[92] used HA in the form of fibers to reinforce PMMA cements. At about 6% by weight of the HA fibers, the K_{IC} improved from 1.6 to 2.20 $MNm^{-3/2}$.

Although a significant number of research studies have been performed in an attempt to develop a bone cement possessing sufficient mechanical properties, radiopacity, improved biocompatibility and reasonable handling properties, none of these efforts have successfully yielded an acrylic bone cement combining all these properties. Therefore, there is a sustained interest and need for the development of a new generation of bone cements exhibiting the above mentioned properties in order to overcome the prevailing limitations of current commercial bone cements. Nanotechnology is a tremendously fast growing field and breakthroughs in the bone cement properties can be envisioned by using nanotechnology. A very limited number of studies have been performed to improve the mechanical and physical properties of bone cements using nanotechnology.

1.8.Nanotechnology and bone cement

Nanotechnology is defined as the design, characterization, production and application of structures, devices and systems by controlling the shape and size at the nanometer scale.[93] The nanoscale generally is defined to be from 100 nm down to the size of atoms (approximately 0.2 nm). The unique properties and improved performance of nanomaterials are determined by their sizes, surface structures, and interparticle interactions. Nanoscale materials have a large surface area for a given volume.[94] Since many important physical and chemical interactions are governed by surfaces and surface properties, a nanostructured material can have substantially different properties from a large-dimensional material of the same composition.[95] In the case of particles and fibers, the surface area per unit volume is inversely proportional to the material's diameter, thus, the smaller the diameter, the greater the surface area per unit volume. Common particle geometries and their respective surface area-to-volume ratios are shown in Figure 2. For the fiber and layered material, the surface area/volume is dominated, especially for nanomaterials, by the first term in the ratios. The second term (2/l and 4/l) has a very small influence, and is often omitted compared to the first term. Therefore, a change in particle diameter, layer thickness, or fibrous material diameter from the micrometer to nanometer range can affect the surface area-to-volume ratio by up to three orders of magnitude.[96]

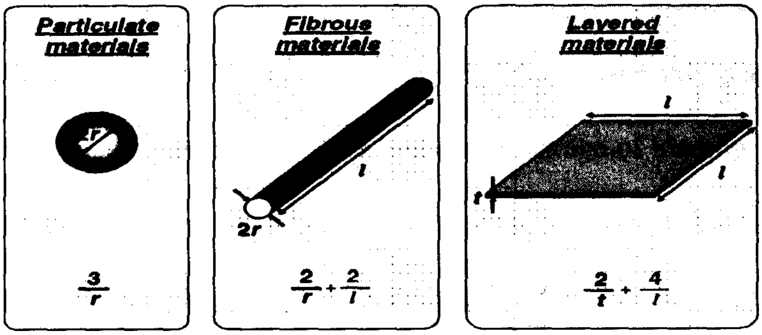

Figure 1.3. Common particle geometries and their respective surface area to volume ratios. (Ref.[93])

The extra-ordinarily high surface-to-volume ratios make nanoparticles ideal for use in polymeric materials as reinforcing agents. In the case of polymer nanocomposites, where the length scale of the reinforcement is in the nanometer range, the distance between the polymer and filler components is extremely short. Polymer coils are approximately 40 nm in diameter, and the nanoparticles are on the same order of magnitude as the polymer. As a result, molecular interactions between the polymer and the nanoparticles will give the polymer nanocomposites multifunctional, high performance characteristics beyond what traditional filled polymeric materials possess.[93] Therefore, nanotechnology offers new promise for improving the mechanical and physical properties of bone cement, and thereby succeeding where other material augmentation efforts have failed.

Only very few works have been reported to date for the incorporation of nanostructured particles in a bone cement matrix to improve its mechanical and physical properties. K. Goto *et al.*[97] developed bioactive PMMA based bone cements by incorporating nanosized titania particles (average diameter 200 nm) having anatase crystalline phase into the cement matrix and evaluated its mechanical properties. Incorporation of 60wt% silanized titania nanoparticles significantly increased the FM of the bone cement compared to the control commercial cement, while the FS of the reinforced cements were significantly low or similar compared to the commercial cement. This is probably due to the presence of agglomerates of nano titania particles at higher percentage of loading which can act as stress concentrators. Moreover, at this high loading the resulting bone cements exhibited very short setting times exhibiting a detrimental effect on its handling properties. However anatase titania is reported to have the apatite forming ability in vitro and osteoconductivity in vivo.[98] Therefore, the resulting cement containing 60wt% titania particles exhibited higher osteoconductivity compared to the control commercial cement. Due to the faster setting time and higher stiffness compared to commercial acrylic cement, the bioactive cement containing nano-sized titania particles has potential for use in vertebroplasty, where bone cement is injected into a fractured vertebra in order to stabilize it. B. Marrs *et al.*[99] reported the augmentation of acrylic bone cement by incorporating multi-walled carbon nanotubes (MWCNT) into a cement matrix. 2 wt% loading of the MWCNT enhanced the flexural strength by 12.8% and yield stress by 13.1% compared to the control cement. However, larger concentrations of MWCNT did not produce the enhancements observed with the 2wt% loading, probably due to the inadequate dispersion of the MWCNTs at higher loading. Moreover, there is a sustained debate on the biocompatibility of carbon nanotubes and the bone cement reinforced with MWCNT might have some adverse effects on the living cells around the prosthesis.[99,100] J-H. Wang *et al.*[101] investigated the reinforcement of acrylic bone cement by incorporating organically modified montmorillonite (MMT) nanoclay into the cement matrix. MMT/PMMA nanocomposites were prepared by melt blending at 200 °C with different blending times by intercalating the PMMA chains into the inter-lamellar space of the modified MMT. Then the MMT/PMMA nanocomposites were reported to carry out the role of PMMA beads in the powder part of the bone cement. Nanocomposites containing 5 and 9 wt% MMT exhibited an impact strength improved of 47 and 54% respectively compared to the composites without MMT. Nanocomposites prepared with longer blending times exhibited higher impact strength which was associated with the uniformity and exfoliation features of the composites. Moreover, MTT cell analysis exhibited an improved MG63 cell growth on the cement specimens containing MMT/PMMA nanocomposites, which reflected its biocompatibility. However, intercalation of PMMA chains into the inter-lameller space of MMT might pose an adverse effect on the rheological properties of the resulting cements which was not studied. J. Hill *et al.*[102] investigated the inclusion of calcium carbonate ($CaCO_3$) nanoparticles into a bone cement matrix (Colacryl B866) in an attempt to increase its mechanical properties. In order to enhance the dispersion of the nanoparticles, its surface was treated with sodium citrate. With the incorporation of 0.25% $CaCO_3$ nanoparticles, the FS and FM were improved by 6.5 and 7.4 % respectively, while the compressive strength was decreased by 7.7 % compared to control cement. However, with the incorporation of 0.75% $CaCO_3$ nanoparticles, the bending strength and compressive strength were decreased by 3 and 12.6% respectively. The energy to maximum load was also reported to decrease significantly compared to the control cement when the percentage loading of nanoparticles was increased from 0.25 to 0.75%. The main reason for the deterioration of the mechanical properties was reported to be caused by agglomeration of the $CaCO_3$ nanoparticles. Although there would not be any detrimental effect on the radiopacity and rheology of the reinforced cement with such a small loading of nanoparticles, this technique was not recommended for clinical use by the authors because of the low improvement in the bending properties of the resulting cements. A. H. Gomoll *et al.*[103] reported the enhancement of mechanical strength of a commercial bone cement by incorporating nano-sized (100 nm) $BaSO_4$ particles. A 41% increase in tensile strain-to-failure and 70% increase in tensile work-of-fracture were reported for the cement containing 10 wt.% nanosized $BaSO_4$ particles compared with the commercial cement containing 1 to 3 micron sized $BaSO_4$ particles. However, there were no reports on the cytotoxicity of the cement surface reinforced with nanoparticles, as particles may be toxic on the nanoscale. Moreover, without having any chemical bonding between the inter-bead PMMA matrix and the nano-$BaSO_4$ particles, the ultrafine nanoparticles may separate from the PMMA matrix and reach the surrounding biological tissue resulting in inflammation and implant loosening.

A. Ricker *et al.*[104] investigated the effect of nano MgO and nano $BaSO_4$ on the PMMA matrix in an attempt to improve the cytocompatibility and radiopacity of the PMMA based bone cements. It was reported that the poor osteoblast function of PMMA[105-107] could be improved by incorporation of MgO or $BaSO_4$ nanoparticles. These showed higher osteoblast cell growth on the surface of PMMA reinforced with the nanoparticles compared with unfilled PMMA. However, the effect of the nano MgO or nano $BaSO_4$ on the mechanical properties of the PMMA cement was not reported in this work.

From the above discussion it is apparent that nanotechnology has the potential to make a radical change in the development of bone cements in terms of enhanced mechanical properties. As mentioned earlier, mechanical properties of a composite largely depend on the interactions of the filler materials with the matrix as well as the interfacial adhesion between the filler and the matrix.[108] Nanostructured fillers in the bone cement matrix promote filler-matrix interactions, enhancing mechanical properties as described above. However, limitation in the above approaches is due to the poor interfacial adhesion between the inorganic nanofillers and the matrix. Therefore, nanotechnology would provide the best results in terms of augmenting the mechanical and physical properties of bone cements if there were a chemical bond between the nanofillers and the acrylic matrix. Hence, an objective of this research was to develop a reactive nanofiller for the reinforcement of the acrylic bone cement. There is also a sustained debate on the biocompatibility of nanoscale materials focusing on escaping sharp needle-like nanofibers as wear debris into the surrounding bone tissue. The strong chemical bond between the fillers and matrix would reduce the production of nanofiller wear debris as these materials are bonded with the matrix. This thesis is based on examining the reinforcement of the acrylic bone cement using reactive titania nanofibers and nanotubes. The investigation has been limited to the effect of nano inclusions on the mechanical and handling properties, radiopacity and biocompatibility of the reinforced bone cements.

1.9.Titania in biomaterials and medicine

Titanium is a common clinically used biomaterial exhibiting a combination of corrosion resistance and biocompatibility with excellent mechanical performance.[109] A TiO_2 coating on the surface of titanium provides a passive surface layer to the implant increasing its corrosion resistance, which at the same time impedes the passage of metal ions (primarily Ti^{4+}) into the body.[110] Moreover, the ceramic TiO_2 coating exhibits high external hardness. Therefore, the titanium alloy implant coated with TiO_2 simultaneously displays both excellent biocompatibility and high mechanical strength, explaining why this material is overwhelmingly used as a replacement for teeth (dental implants) and bones (maxillofacial devices, components of hip and knee replacements).[109]

The high biocompatibility of titanium is useful not only in load-bearing implants, but also in implants which are intended to stimulate metabolic responses, such as implantable cell-carriers, and also in cell-culture substrate for *in vitro* culture and tissue engineering.[111] The carrier material should be of the highest biocompatiblity to enable the ongrowth of vascularized healthy tissue which can establish a long-term vascular supply for transplanted cells.[112] Moreover, the materials should provide permeability for cell-culture media which is needed to support nutrition of cells adhering to the surface. The bifunctional element of titanium-based biomaterials is a surface layer consisting of titanium dioxide which offers numerous opportunities to create the porosities needed to achieve permeability for nutrients as well as a biologically viable environment.[111]

Titania is a widely used white pigment because of its brightness and very high refractive index (n=2.7) being an effective opacifier.[113] Moreover, normal-sized (>100 nm) titanium dioxide is classified as being biologically inert in both humans and animals.[114,115] It has been widely used as a pigment[116] to provide whiteness and opacity to products such as foods and medicines[117] and has also been used in cosmetic creams and sunscreens.[118]

With the development of nanotechnology, size effects of particles have gradually been considered to be important. Nanoparticles may be more toxic than larger particles of the same substance[119] because of their larger surface area, enhanced chemical reactivity, and easier penetration into cells. As an example, the high photocatalytic efficiency of nanophase titania results in potential phototoxic effects on bacteria, cancer cells and tumors.[112] This phototoxic effect occurs due to the reaction between the oxidizing agents produced from the redox reaction of the photogenerated holes and electrons, and the biomolecules which leads to damage of the biomolecular structure through a series of peroxidative chain reactions.[120,121] Nanostructured titania promotes the generation of photogenerated holes and electrons owing to its high surface-to-volume ratio and a large interfacial surface area.[122] The cytotoxic effect of photoexcited titania nanometer particles on cancer cells suggests that the phototoxic effect might be exploited as a possible anti-cancer modality. This approach is particularly suitable for treatment of superficial tumors for example, on the skin, oral cavity or trachea which are freely accessible to light of wavelength 300-400 nm.[111] Recently, titania has been used as a photosensitizer for photodynamic therapy for endobronchial and esophageal cancers.[113]

Nevertheless, without UV irradiation, nano-sized titania has no inflammatory effect or genotoxicity in the rat,[123] and induced no DNA damage in human cells.[124] Moreover, several studies have shown that the cytotoxicity of nanosized titania was very low or negligible as compared to other nanoparticles,[125-127] and the size was not the effective factor for cytotoxicity.[126]

Therefore, due to the low cytotoxicity and fair biocompatibility of titania nanoparticles and widespread use of titania in biomaterials, we have introduced titania nanofibers and nanotubes in acrylic bone cement matrix in order to examine the physical, mechanical and biological properties of the resulting novel bone cements.

Chapter 2: Materials and Methods

2.1. Outline

In this chapter, the experimental setup used for the synthesis of titania nanomaterials, functionalization of titania nanomaterials, preparation of bone cements and the methods used for characterizing bone cements throughout this thesis are described.

The synthesis of the titania nanomaterials was carried out either in a high-pressure view cell reactor or an autoclave bomb.

Functionalization of the synthesised nanomaterials was carried out in a three neck round bottom glass flask fitted with a reflux condenser and thermometer.

The bone cements were prepared according to standard clinical procedure in a polycarbonate container by mixing the powder and liquid components which undergo bulk polymerization.

A variety of characterization methods were employed for examining the synthesised nanomaterials, functionalized nanomaterials and prepared bone cements including: scanning electron microscopy (SEM), transmission electron microscopy (TEM), X-ray diffraction (XRD), Fourier transform infrared spectroscopy (FTIR), thermogravimetric analysis (TGA), differential scanning calorimetry (DSC), scanning transmission electron microscopy (STEM), energy dispersive X-ray spectroscopy (EDX), electron energy loss spectroscopy (EELS), ultrasonic pulse analysis, universal mechanical testing analysis, X-ray radiography, rheometry and biological cellular interaction analysis.

2.2. Synthesis setup

For synthesizing the titania nanofibers, the experiments were carried out in 10 mL high pressure view cell made of stainless steel. For synthesizing the titania nanotubes, the experiments were carried out in a teflon-lined stainless steel autoclave.

2.2.1. Setup for titania nanofibers synthesis

2.2.1.1. View cell, pump, valves and connections

View cell. The view cell is a high pressure reactor made of stainless steel (Figure 2.1) used for synthesizing titania nanofibers using the direct sol-gel method in supercritical carbon dioxide.

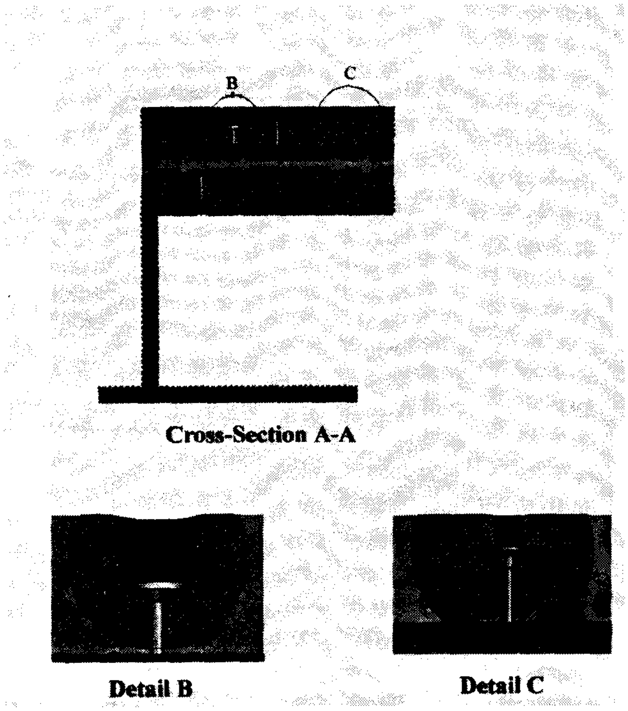

Figure 2.1: The view cell

There are four holes with thread on the wall. The big hole is for a pressure transducer, and the three small holes are for a thermocouple, inlet and outlet connections respectively.

Pump. Syringe pumps (ISCO 100 or 260D) were used for pumping CO_2 into the reactor and for maintaining a constant CO_2 pressure throughout the reaction. The operation of the syringe pump was performed using the electronic controller provided by ISCO.

2.2.1.2. View cell instrumentation

The 10 mL view cell was connected with the syringe pump (ISCO 100 DM) for pumping CO_2 from a dip tube. The check valve next to the pumps was used to prevent possible back flow from the view cell. The temperature in the view cell was measured and controlled by means of a T-type thermocouple, a heating tape (Omega SRT051-040, 0.5x4 FT) and a temperature controller (Fuji PXZ-4). The pressure was measured and

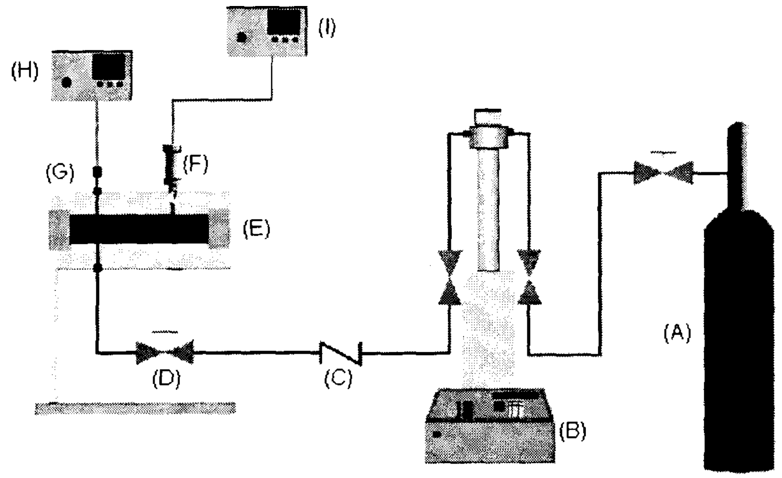

Figure 2.2: Schematic of experimental setup: (A) CO_2 cylinder, (B) Syringe pump, (C) Check valve, (D) Needle valve, (E) stainless steel view cell equipped with sapphire windows, (F) pressure transducer, (G) Thermocouple, (H) Temperature controller, (I) Pressure monitor

controlled by means of a pressure transducer (Omega PX302-10KGV) and a control valve (Badger-78S) (Figure 2.2)

2.2.2. Setup for titania nanotube synthesis.

Stainless steel autoclave. The autoclave is a 125mL acid digestion bomb (Parr 4748) supplied by the Parr instrument company, Illinois, USA. This PTFE-lined digestion bomb provides a convenient and safe means for dissolving or dispersing sample rapidly in strong acid or alkali. As shown in Figure 2.3, the bomb consists of several parts such as bottom plate (301 AC) , stainless steel bomb body (302AC), PTFE cup having a capacity of 50mL with cover (A305AC), pressure plate (306AC), compression ring (307AC), screw cap with cap screws (A308AC), cap screws with dimension of 3/8-24 x 3/4 (308ACF), wave spring (336AC), Stainless corrosion disc with thickness of 0.002" (310AC), Inconel rupture disc with thickness of 0.003" (311AC).

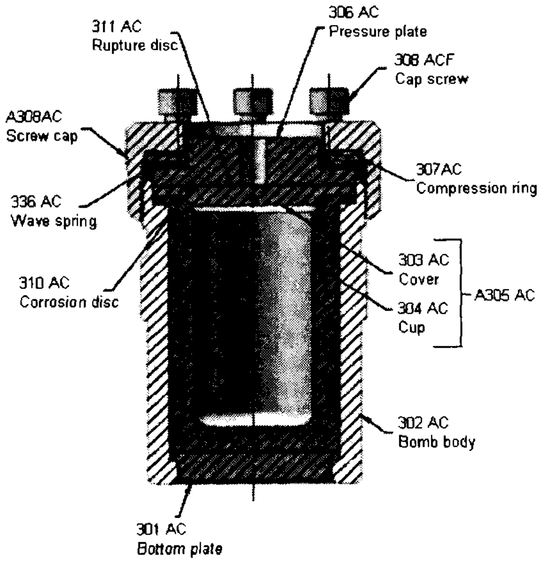

Figure 2.3: PTFE-lined stainless steel autoclave

Autoclave instrumentation. The Parr 4748 bomb autoclave is designed for handling highly corrosive environments at elevated temperature. PTFE offers such unique inertness and high temperature resistance that it is an obvious choice as the material of construction for lining.

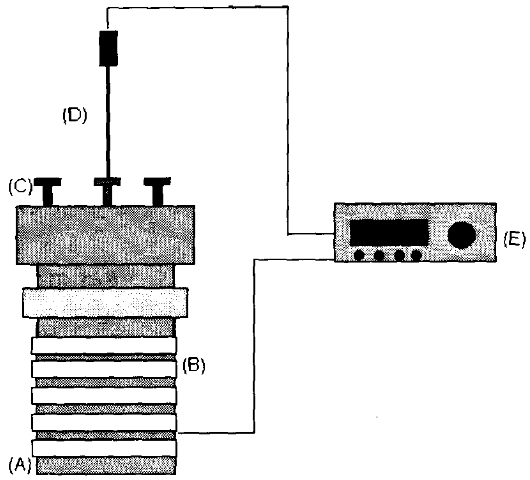

Figure 2.4: Schematic of experimental setup: (A) Stainless steel autoclave, (B) Heating tape, (C) Screw caps, (D) Thermocouple, (E) Temperature controller

In the experimental setup, the temperature in the bomb was measured and controlled by means of a T-type thermocouple, a heating tape (Omega FGH051-060L, 0.5x6 FT) and a temperature controller (Omega HRC5A) (Figure 2.4)

2.3. Synthesis Procedures

2.3.1. Synthesis of titania nanofibers.

TiO_2 nanofibers were synthesised in this work using the direct sol-gel technique in supercritical carbon dioxide according to a previously described procedure.[128] Briefly, the experimental procedures for synthesizing TiO_2 aerogels included the addition of a carboxylic acid and an alkoxide into the view cell, followed by addition of CO_2 to the desired temperature (60 °C) and pressure (6000 psi). TiO_2 monolithic aerogels formed after one day and typically 2-3 days were allowed to age after the gel was formed. After CO_2 extraction and venting, the resulting aerogels were subject to further drying and calcination in air.

2.3.2. Synthesis of titania nanotubes.

TiO_2 nanotubes were synthesised in this work using the hydrothermal method in highly basic alkali solution according to a previously described procedure.[129] Briefly the experimental procedure includes the dispersion of commercial titania nanopowder in 10M NaOH solution in the Teflon-lined stainless steel autoclave, followed by raising the temperature to 110 °C and maintaining it for 20 hours. The reaction products were then subjected to washing by distilled water until the pH of the product become 10. Finally the synthesised materials were washed by 0.1N HCl solution to attain a pH 7.0 at room temperature.

2.4. Functionalization setup

Functionalization is the chemical reaction designed to modify the surface of the synthesised titania nanomaterials in an attempt to compatibilize the nanomaterials with the organic polymer matrix. The functionalization reactions have been carried out in a 250 mL three-neck round bottom flask fitted with reflux condenser and thermometer. The reactor was heated by a heating mantle (Glas-Col 1662868) controlled by a voltage regulator (Powerstat 3PN116C) (Figure 2.5).

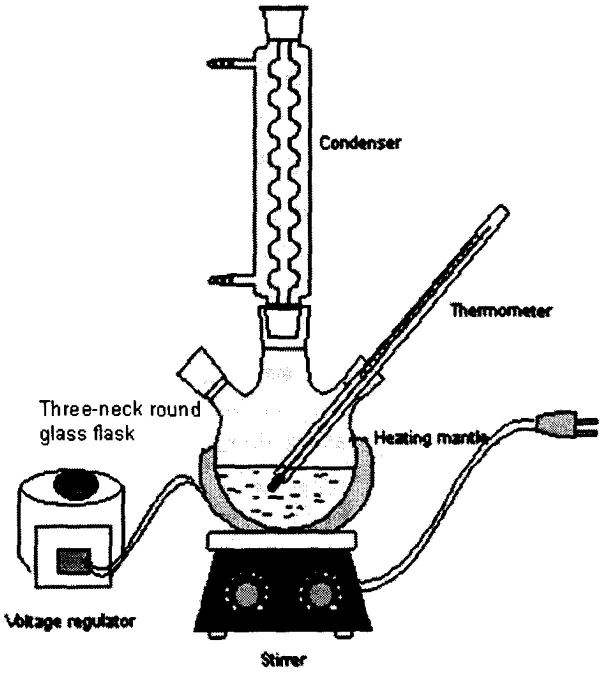

Figure: 2.5: Schematic of experimental setup for functionalization of titania nanomaterials

2.5. Functionalization procedure

The experimental procedure for functionalizing the titania nanofibers and nanotubes included dispersion of the nanomaterials in a solution of methacrylic acid (MA) and isopropyl alcohol with the aid of ultrasonic agitation for 5 minutes, followed by heating the reaction content to 85 °C for 24 hours with constant stirring. The reaction product was separated by vacuum filtration and then dried under vacuum at 100 °C for 8-12 hours. More details of the functionalization procedure for titania nanofibers and nanotubes are described in chapter 3.

2.6. Preparation of bone cement

Bone cement specimens were prepared by mixing the powder and liquid components based on a commercial formulation. The powder component contains prepolymerized PMMA beads, benzoyl peroxide initiator and radiopaque agent, while the liquid component includes MMA monomer, aromatic amine activator, hydroquinone inhibitor and/or dimethacrylate cross-linking agents. Two approaches were adopted to incorporate the functionalized titania nanofillers as a radiopacifying agent into the bone cement matrix. In the first approach, the functionalized nanofillers were attached to the PMMA beads by *in-situ* suspension polymerization of MMA monomer in the presence of functionalized nanomaterials, followed by mixing the synthesised PMMA beads mixed with titania nanofillers in the liquid portion. In the second approach, the functionalized titania nanomaterials were mixed with the liquid part of the cement prior to the mixing of the powder and liquid.

2.6.1. Preparation setup

The suspension polymerization setup includes a 1L four-neck flask attached with thermometer, reflux condenser and mechanical stirrer (VWR 14215-252 high viscosity mixer) (Figure 2.6). The flask was heated with a heating mantle whose electrical resistance was controlled by a voltage regulator.

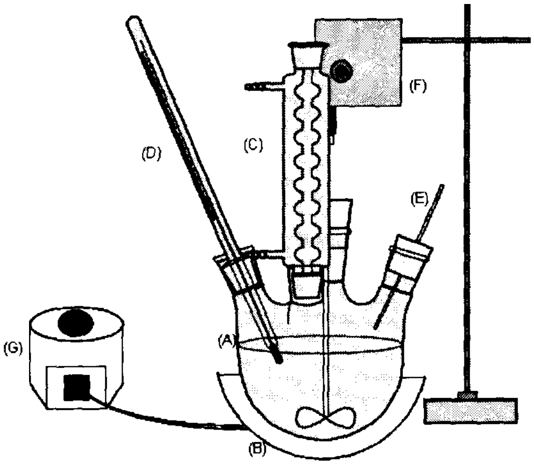

Figure 2.6: Schematic of experimental setup for suspension polymerization: (A) Four-neck round bottom flask, (B) Heating mantle, (C) Reflux condenser, (D) Thermometer, (E) Nitrogen inlet, (F) Mechanical stirrer, (G) Voltage regulator

The powder part or the prepolymerized PMMA beads with titania nanofillers and liquid part are mixed in a polycarbonate container and a polycarbonate spatula was used to mix them.

2.6.2. Preparation procedure

The bone cement specimens were prepared in this work by incorporating the functionalized titania nanofibers and nanotubes into the acrylic polymer matrix. The suspension polymerization technique was used to bind titania with PMMA beads, where free radical addition polymerization of MMA monomer was carried out using water as the suspension medium containing the functionalized titania nanofillers, benzoyl peroxide initiator and poly(vinyl alcohol) stabilizer at 80 °C while stirring constantly. The synthesised PMMA beads mixed with titania nanofillers were then mixed with the liquid portion to produce the bone cement specimens. In the other approach, the functionalized titania nanomaterials were mixed with the liquid part of the cement with the aid of ultrasonic agitation for 15 minutes prior to the mixing of the powder and liquid.

The powder portion was then added to liquid monomer containing the dispersed nanomaterials at a ratio of 2.18 and hand mixed into a dough state and loaded into Teflon molds. The molds were kept for 24 h at room temperature for complete curing.

2.7. Characterization

2.7.1. Rheological properties of bone cement

Bone cement is applied to the bone prior to setting, when the viscosity of the cement dough is high enough such that it can be manually manipulated.[13] The other method of insertion involves the use of a syringe or cement gun to inject the paste into the bone cavity which has the advantage of providing better penetration.[13] For either method it is very important to know the flow characteristics of the cements before they set. The viscosity or flow characteristics of bone cement during curing or setting is mostly evaluated by using a rheometer.

A rheometer is a laboratory device used to measure the way in which a liquid, suspension or slurry flows in response to applied forces or with respect to time at constant applied forces.[130] It is used for those materials which cannot be defined by a single value of viscosity and therefore requires more parameters to be set and measured than is the case for a viscometer. The most common type of materials which require a rheometer to characterize their flow properties are called viscoelastic materials. A viscoelastic material exhibits both viscous and elastic properties. Bone cement, during its curing stage, is clearly a viscoelastic material, where the cement changes from having predominantly liquid-like properties immediately after mixing, to having predominantly solid-like properties once sets.

For a viscous material, considering a simple shear flow, Newton's law of viscosity relates the shear stress, σ, to the velocity gradient or shear rate, $\dot{\gamma}$, through the equation:

$$\sigma = \eta \dot{\gamma} \tag{2.1}$$

Where η is the coefficient of viscosity, or simply the viscosity. For Newtonian fluids, the viscosity, η, is a constant, independent of shear rate.[26,131]

On the other hand for a viscoelastic material, the viscosity increase over time and the material transfers from the viscous to the elastic state. Therefore, the flow characteristic of a viscoelastic material is conveniently done by an oscillatory shear.[26] In the case of oscillatory shear, the material is subjected to a sinusoidal shearing strain, which can be represented by a sine function.[131,132] Consider an oscillatory strain, with amplitude ε_0 and frequency of oscillation, ω, is applied to a material such that:

$$\varepsilon(t) = \varepsilon_0 \sin(\omega t) \quad (2.2)$$

If the strain amplitude is sufficiently small so that the material behaves linearly, it can be shown that the resulting steady-state stress will also oscillate sinusoidally at the same frequency but will be shifted by a phase angle δ with respect to the strain wave, that is,

$$\sigma = \sigma_0 \sin(\omega t + \delta) \quad (2.3)$$

The stress leads the strain by phase angle δ. For purely elastic materials, $\delta = 0°$ (stress is in phase with strain). For purely viscous materials, $\delta = 90°$ (stress leads the strain by 90° although the stress is in phase with the strain rate). For viscoelastic materials, $0 < \delta < 90°$.

Now from Equation 2.2:

$$\sigma = \sigma_0[(\cos\delta)\sin\omega t + (\sin\delta)\cos\omega t] \quad (2.4)$$

The storage modulus (G') is defined as:

$$G' = \frac{\text{In-phase stress component}}{\text{2 x strain}} = \frac{\sigma_0 \cos\delta}{2\varepsilon_0} \quad (2.5)$$

And the loss modulus (G'') is defined as follows:

$$\frac{G''}{\omega} = \frac{\text{Out-of-phase stress component}}{\text{2 x strain rate}} = \frac{\sigma_0 \sin\delta}{2\omega\varepsilon_0} \quad (2.6)$$

That is,

$$G'' = \frac{\sigma_0 \sin\delta}{2\varepsilon_0} \quad (2.7)$$

Now, the sinusoidal shearing strain can also be termed in complex notation as,

$$\varepsilon^* = \varepsilon_0 e^{i\omega t} = \varepsilon_0(\cos \omega t + i \sin \omega t) \tag{2.8}$$

Where, $i = \sqrt{-1}$. In this expression, the real and imaginary parts each represent two oscillatory strains of frequency ω. The resulting stress is also complex and is related to strain as:

$$\sigma^* = 2G^* \varepsilon^* \tag{2.9}$$

Where G^* is the complex modulus, which can be written in terms of storage and loss moduli as:

$$G^* = G' + iG'' \tag{2.10}$$

The oscillatory shear behaviour of a material can also be characterized in terms of complex viscosity rather than complex modulus. The complex viscosity η^* of a viscoelastic material is related to the complex shear modulus G^* as follows:

$$\eta^* = G^* / i\omega = \eta' - i\eta'' = \frac{\sigma_0}{\varepsilon_0 \omega}(\sin \delta - i \cos \delta) \tag{2.11}$$

where $\eta' (= G''/\omega)$ is the dynamic viscosity and η'' $(= G'/\omega)$ is the imaginary part of the complex viscosity.

It is conventional to show the results of oscillatory measurements of viscoelasticity in terms of η^* or G'.[26,133]

The oscillatory technique can be used with a number of different geometries. The most suitable for characterizing bone cements is either the cone and plate or the parallel plate. As bone cement is a suspension with PMMA particles, the shear gap in the rheometer must be significantly greater than the size of the particles.[26] As the PMMA particles in bone cements are typically of the order of 100 μm, the shear gap must hence be at least 500 μm. Even though the plate and cone rheometer provides near constant shear rate throughout the sample, it is unable to provide such a large shear gap. However, parallel plate geometry conveniently provides this much shear gap which makes it ideal for evaluating the rheology of bone cements.[26,134]

In parallel plate geometry, the test fluid is held between two parallel plates, the bottom of which is fixed. A torque is applied to the top plate, forcing it to oscillate, and the response of the material is measured by the rotation of the same upper plate (Figure 2.7).

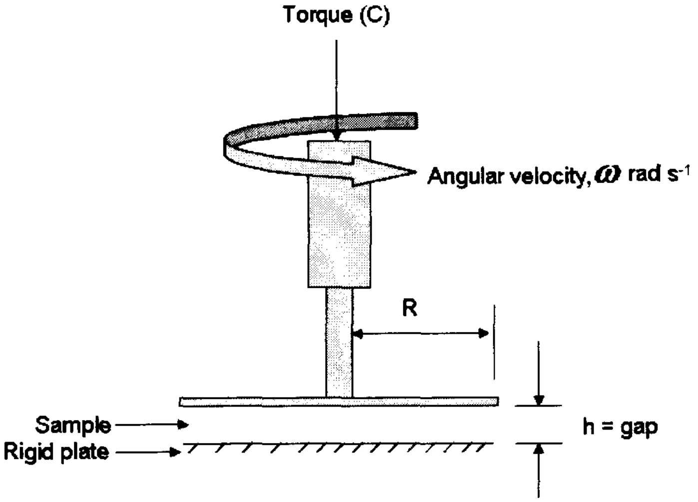

Figure 2.7: Schematic of a parallel plate

The rheological properties in the controlled stress parallel-plate rheometer is based on the shear rate at the rim of the plate. The strain rate and stress at the rim are given by the following equation[26,131]:

$$\dot{\varepsilon}_{rim} = \frac{R\omega}{h} \tag{2.11}$$

where R is the radius, ω the frequency and h the distance between plates.

$$\text{and } \sigma_{rim} = \frac{2C}{\pi R^3} \text{ (for a Newtonian fluid)} \qquad (2.12)$$

$$\sigma_{rim} = \frac{2C}{\pi R^3}\left[3 + \frac{d(\log C)}{d(\log \dot{\varepsilon}_{rim})}\right] \text{(for a non-Newtonian fluid)} \quad (2.13)$$

where C is the total torque.

Furthermore, it is possible to show that the dynamic viscosity (η') and the storage modulus (G') are given by:

$$\eta' = \frac{2hC_0 \sin c}{\pi R^4 \omega \phi_0} \qquad (2.14)$$

$$\text{and, } G' = \frac{2h(C_0 \cos c + I\omega^2\phi_{0)}}{\pi R^4 \phi_0} + \frac{h^2\omega^2\rho}{3} \qquad (2.15)$$

where C_0 is the amplitude of applied torque, ϕ_0 the amplitude of measured displacement, c the phase lag of the motion of the top plate behind the input torque, I the moment of inertia of top plate and ρ the density of the test fluid.

The rheometer thus applies an oscillatory torque of known amplitude and frequency and measures the corresponding angular displacement wave form. The amplitude ratio and phase lag between the input and output displacement waveforms is obtained, and η', G' and η^* were calculated using the expressions given above by the instrument software.[26]

In this work the rheology of curing bone cements was investigated using a rheometer (AR 2000ex, TA instrument Ltd., Delaware, USA) by monitoring the change in complex viscosity (η^*) of the cement mass with time. The tests were performed in the dynamic oscillation mode, at a frequency and strain amplitude of 5 Hz and 5 x 10^{-4} rad. respectively, which was low enough to maintain the material's linearity. Parallel plate configuration was used with the diameter of the upper and lower plates 25 mm each and the gap between the plates 1800 μm. All measurements were made at both room temperature (25 ± 1 °C) and body temperature (37 ± 1 °C). In a typical experiment, 2 g of cement dough was prepared by mixing the liquid and solid components in a PTFE container with the time initiated at the initial contact of solid and liquid. The dough was mixed by hand with a plastic spatula for approximately 30 sec and the cement was then loaded into the rheometer. The plates were brought together and, after the excess cement was removed, the rheometer was started and the time was noted. The time between the start of mixing and the beginning of measurements being made by the rheometer was ≅ 60-70 sec. The test was continued until the top parallel plate was no longer able to oscillate and a plateau of complex viscosity was reached due to complete hardening of the cement. The onset time of viscosity increase (t_{ons}) and the curing time (t_{cure}) of the setting cement were determined from the complex viscosity-versus-time curves as shown in Figure 2.8.

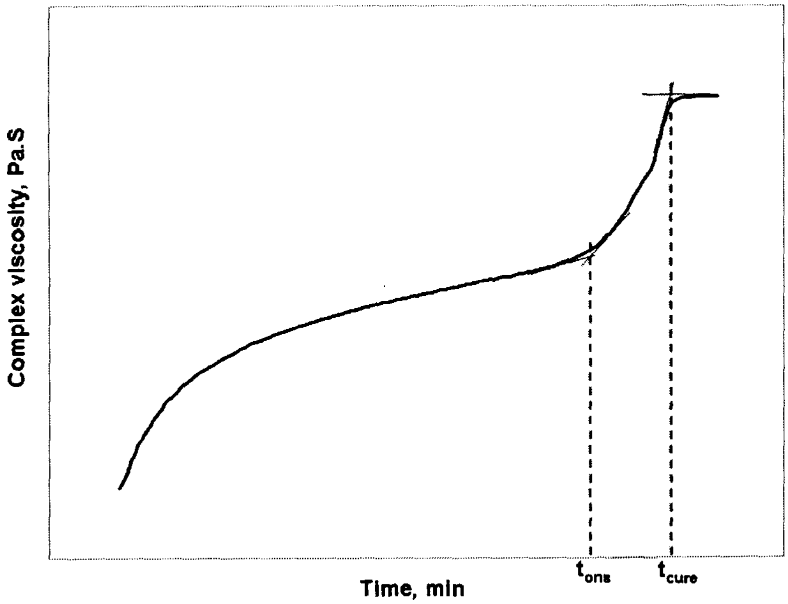

Figure 2.8. Typical complex viscosity versus time trace of curing cement

2.7.2. Setting characteristics of bone cement

During curing of the bone cement, it undergoes a transition from the dough stage to the purely solid stage when the cement becomes completely hardened. Moreover, it is cured through the polymerization reaction of MMA which is an exothermic reaction resulting in a temperature increase. Therefore, the curing parameters that characterise the polymerization reaction or curing of bone cements are: doughing time, maximum temperature and setting time.[13]

The maximum temperature, frequently called the peak temperature (T_{max}), is obtained from the maximum of the exotherm, and corresponds to the maximum temperature attained by the bulk cement during polymerization. The setting time (t_{set}) is defined as the time taken to reach a temperature midway between ambient and maximum, and doughing time is the time elapsed between the beginning of mixing until the mixture is able to separate cleanly from a gloved finger. Another important parameter that describes the handling characteristics of the cement is the working time which has been defined as the difference between both the setting and doughing times.[1]

All these curing parameters except the working time have been clearly defined in the ASTM F451-99a[135] and ISO 5833[136] standards used for characterizing acrylic bone cements. According to the standards employed to measure dough time of bone cement, a complete package (maintained at 23 ± 1 °C and 50 ± 10% humidity) of cement is mixed and a stopwatch is started just at the time of addition of liquid to the powder. The surface of the cement dough is probed gently with a gloved finger (powder-free latex glove). The time when there is no fiber formed between the dough and the glove as the finger leaves the surface is recorded as the dough time of the cement.

Similarly, according to the standards, in order to measure the maximum polymerization temperature (T_{max}) and setting time (t_{set}), 25 g of cement is mixed and filled in a high density poly(ethylene) (HDPE) mould with specific dimensions. A plunger made of HDPE is pressed on the cement dough in the mould and the superfluous cement expelled from the mould is trimmed off. A T type thermocouple having a wire diameter of approximately 0.5 mm is positioned with its junction (3 ± 0.5) mm above the internal surface of the mould base. The temperature measurement is to be continued until the temperature of the cement dough during curing starts to fall after reaching its highest value. The maximum polymerization temperature was recorded at the peak of the plot of temperature against time as shown in Figure 2.9.

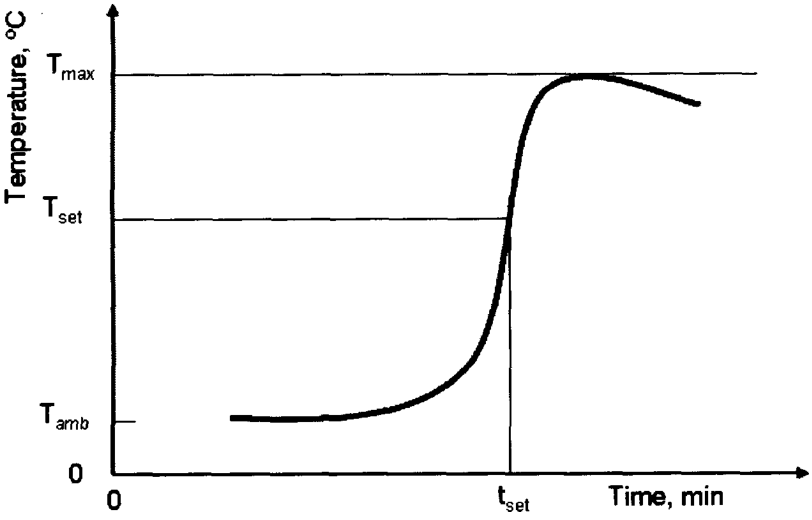

Figure 2.9: Typical curve for determination of maximum temperature and setting time

Similarly, the setting time (t_{set}) is measured from the corresponding setting temperature (T_{set}) in the plot which is defined according to the standards as:

$$T_{set} = \frac{T_{\max} + T_{amb}}{2} \tag{2.16}$$

where T_{amb} is the recorded ambient temperature and T_{max} is the highest temperature attained.

In this work, the curing parameters of the bone cements were evaluated according to ISO 5833 standards with a slight modification to make the procedure viable for laboratory–scale as described by B. Pascual *et al.*[137] According to the modified method, 2 g of cement mass were inserted in a cylindrical Teflon mold with 10 mm in diameter and 15 mm in height. The mold was kept in a water bath at 37 °C while a T type thermocouple was introduced into the center of the mass located 5 mm from the bottom of the cylinder. Figure 2.10 shows schematically the experimental setup used in this work to measure the curing parameters of the cements.

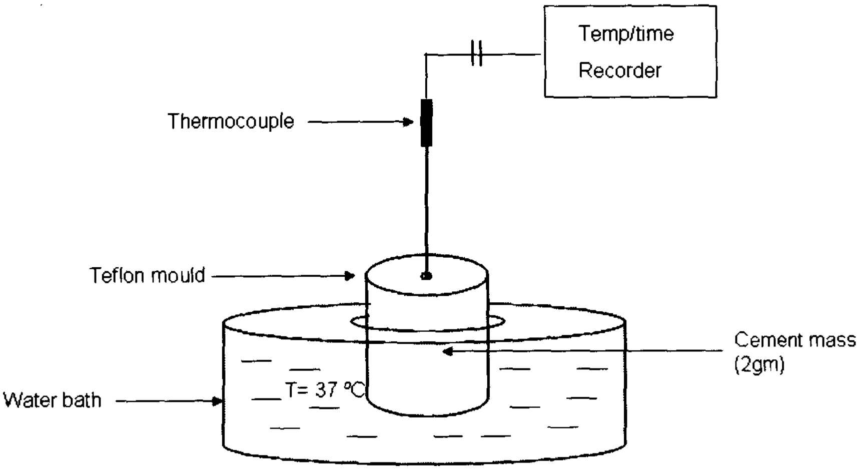

Figure 2.10: Schematic diagram of the experimental setup for measuring the setting parameters of bone cements.

2.7.3. Radiopacity of bone cement

Radiopacity is a material property which makes the material inaccessible to X-rays resulting in a white appearance of the material during X-ray radiography. In the case of bone cement, this white appearance on the X-ray film allows the physician to assess the condition of the cement and implant after the joint replacement surgery.

Radiopacity depends on the capacity of an atom to attenuate X-ray photons by the photoelectric effect. The degree of X-ray attenuation is defined by the following equation[27,138]:

$$I = I_0 e^{-\mu x} \tag{2.17}$$

where, I is the intensity of the transmitted radiation through the material, I_0 is the intensity of the incident radiation, x is thickness of the material and μ is the mass attenuation coefficient of the material, which is a function of K-edge energy of the material.

Radiopacity is a quantitative measurement of the opacity of the bone cement against the standard medical X-ray which is measured from the X-ray image generated on the X-ray film. Different techniques are followed for the quantitative evaluation of the radiopacity from the X-ray image. The most commonly followed technique involves the measurement of optical density of the X-ray image using a densitometer.[27,139,140] Optical density is a logarithmic measure of the ratio (transmitted light I/incident light I_0) through the film image which can be formulated as:

$$\text{Optical density, } OD = -\log_{10}(I/I_0) \tag{2.18}$$

Optical density thus depends on the X-ray absorption of the radiopacifying agents and therefore, the higher the optical density the lower the radiopacity of the material. In this method, aluminium is used as a comparative standard as it has the absorption coefficient which is approximately equivalent to that of human dentine of the same thickness.[27] Therefore, in this technique, a calibration curve was constructed with the optical density of an aluminum step-wedge having varying thickness and radiopacity of the material as reported in terms of equivalent aluminum thickness.

In order to measure radiopacity in this work, disc specimens (n=3), 4.6 mm in diameter and 1 mm in thickness were placed on medical X-ray film along with a high-purity Al step-wedge of varying thickness from 0.5 to 5.0 mm with increments of 0.5 mm. The X-ray film was positioned on a sheet of lead to minimize back-scatter. A standard dental X-ray source was positioned perpendicularly to the radiographic film. The unit was operated with an accelerating voltage of 60 kVp, intensity of 10 mA, with a focus to film distance of 52.5 cm and exposure time of 0.05 s. Following standard techniques, the films were developed in an automatic X-ray processor and digitized. A Digital color meter® (Apple computer) was used in this work to measure the % RGB scale of the radiographic images of the various groups as well as the Al step-wedge on the same film using an aperture size of 1 x 1 pixel. A correction factor for background radiation was taken into account in the calculation of the percentage RGB for all groups. From the Al step-wedge radiograph, a calibration curve relating the logarithm of %RGB vs. the logarithm of Al thickness was constructed. The radiopacity of the specimens was calculated from the regression equation in term of mm Al thickness. To obtain the radiopacity in terms of Al equivalent of 1mm specimen thickness, each radiopacity value was divided by its specimen thickness.

2.7.4. Mechanical properties of bone cement

The primary target of this thesis was to investigate the mechanical properties of nanocomposite bone cements. In order to evaluate the long term surgical efficacy of cemented arthroplasties, two major mechanical properties of the bone cements are important, i.e. stiffness and toughness. As mentioned in Chapter 1, tensile testing is one of the most widely used techniques for evaluating a material's stiffness. However, simple tensile loading does not play a major role in vivo; complex combinations of different modes of loading are more appropriate. From a physical point of view, flexural or bending combines tensile and compressive loading; therefore, the flexural test is the most pragmatic test.[6]

In this work stiffness of the nanocomposite bone cement was evaluated by measuring the flexural properties (flexural strength, FS and modulus, FM) while the toughness was evaluated from the measurement of its fracture toughness (K_{IC}). Moreover, dynamic elastic properties were evaluated to measure the micro-structural rigidity as well as the extent of inter-phase adhesion wihin the composite materials.

2.7.4.1. Flexural properties

Flexural properties of a material are generally characterized by bend testing or flexure testing. The FS is defined as the maximum stress at failure of the material and is often referred to as the modulus of rupture. The test specimen can have a circular, square, or rectangular cross section and is uniform along the complete length. For a rectangular test specimen the FS can be calculated from the following formula[141]:

$$\sigma = \frac{My}{I} \tag{2.19}$$

Where, σ is the FS, M is the bending moment, y is the distance from the neutral axis (plane of the sample, which is stress free) to the outer surface of sample, and I is the second moment of inertia, which indicates the distribution of forces relative to the sample geometry.

For rectangular test specimen having width b and thickness d, the second moment of inertia is defined as[142]:

$$I = \frac{bd^3}{12} \tag{2.20}$$

And also the distance from the neutral axis to the outer surface of sample, y = d/2

Therefore, the FS for a rectangular specimen is given by the equation,

$$\sigma = \frac{6M}{bd^2} \tag{2.21}$$

The recommended flexural test for evaluating FS and FM of a bone cement is the technique set out by ASTM D790[143] or ISO 5833[136] standards. The ASTM standard involves 3 point loading while the ISO standard involves four point loading fixture during the test.

2.7.4.1.1. Three point bending test

The three point bending test involves the application of compression load in the middle of a rectangular test specimen, which is supported at each end (Figure 2.11).

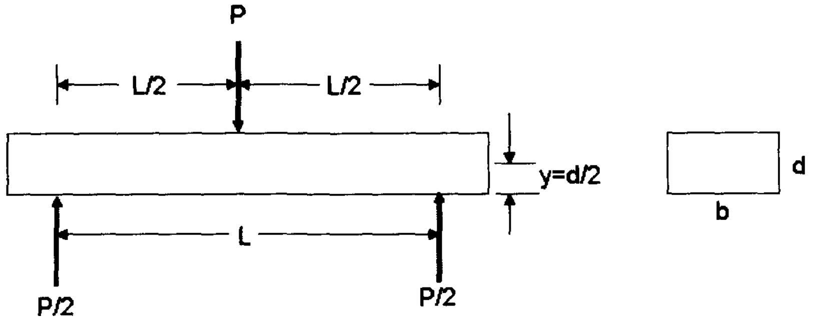

(a) (b)

Figure 2.11: Three point bending test specimen, a) side view; b) end view.

For a load P, applied in the center of a rectangular test specimen having length L, the bending moment is defined as[141,144],

$$M = (\frac{L}{2})(\frac{P}{2}) = \frac{PL}{4} \tag{2.22}$$

From Equation 2.21 and 2.22, the FS in three point bending is:

$$\sigma = \frac{3PL}{2bd^2} \tag{2.23}$$

where, P is the maximum load, L is the specimen length in between two supports, b is the specimen width and d is the specimen thickness.

The FM in three point bending is determined from the deflection at the straight line portion of the force-deflection curve.

Now, the differential equation of the deflection curve for linear elastic plane bending[145]:

$$\frac{d^2\delta}{dx^2} = -\frac{M}{EI} \tag{2.24}$$

where E is the FM and EI is the flexural stiffness.

Solving this differential equation, the deflection formula obtains the following form[17]:

$$\delta(x) = \frac{1}{EI}\left(\frac{P}{16}L^2 x - \frac{P}{12}x^3\right) \tag{2.25}$$

where, x is the point of location on the specimen where the deflection is measured.

The maximum deflection, δ occurs at the middle of the specimen at point, x=L/2

$$\delta = \frac{PL^3}{48EI} = \frac{PL^3}{4Ebd^3} \tag{2.26}$$

Therefore, the FM in three point bending is,

$$E = \frac{PL^3}{4\delta bd^3} \tag{2.27}$$

where, δ is the longitudinal deflection of the specimen at L/2 determined from the straight line portion of the load-deflection curve where it follow's the Hooke's law and P is the corresponding load of δ from the load-deflection curve.

In a typical experiment, rectangular bar specimens (n=12) (32 mm x 3.15 mm x 2mm) were produced by putting 1 g of cement dough in a PTFE mold. Following the curing for 24 hours at room temperature, the specimens were kept in demineralised water at 37 °C for seven days prior to testing. In a typical test, each specimen was removed from water and loaded in the three point loading fixture of a computer controlled Universal mechanical tester (Instron 3345, Instron, Norwood, MA, USA). The test was performed in flexural mode at a cross head speed of 1 mm/min and continued until failure occurred. The software associated with the interface computer calculated the FS value from the value of maximum load at failure using the formula stated in Equation 2.23. The FM value was calculated according to Equation 2.27 from the linear portion of the force-deflection curve (typically shown in Figure 2.12) generated by the computer.

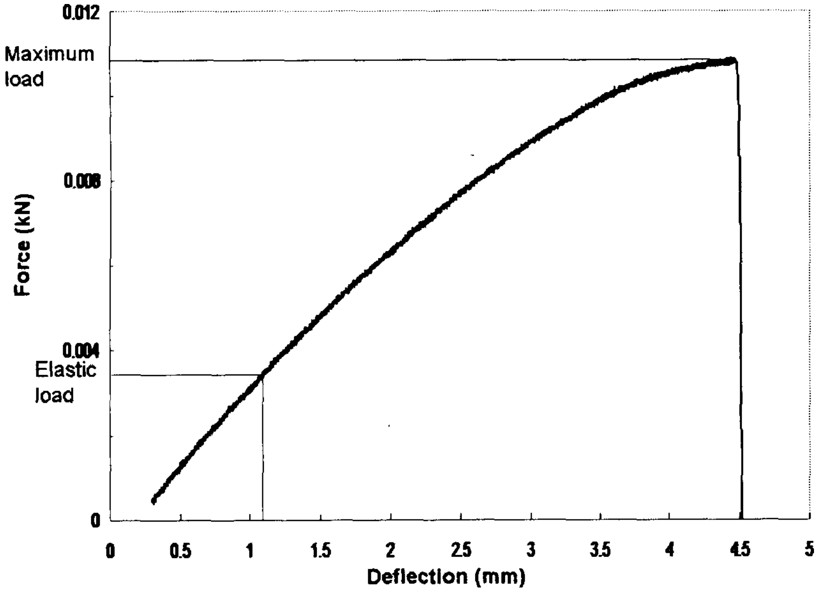

Figure 2.12. Typical force-deflection curve generated during three point bending test

2.7.4.1.2. Four point bending test

The four point bending test involves the application of compression load at two positions of a rectangular test specimen, which is supported at each end (Figure 2.13).

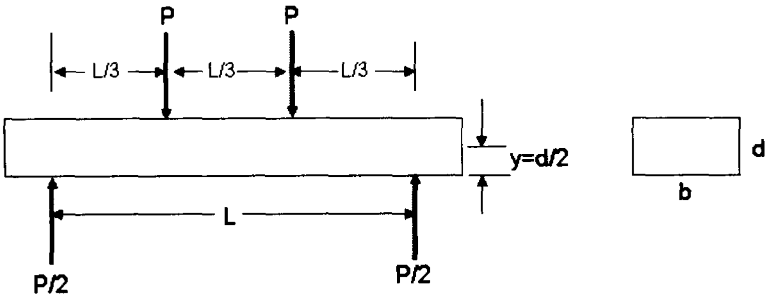

Figure 2.13: Four point bending test specimen, a) side view; b) end view.

For two loads having equal magnitude of P, applied in two positions of the specimen having rectangular cross section as shown in Figure 2.12, the bending moment is defined as[144],

$$M = (\frac{P}{2})(\frac{L}{3}) = (\frac{P}{2})a \tag{2.28}$$

where, a = L/3

From Equation 2.21 and 2.28, the FS in four point bending is:

$$\sigma = \frac{3Pa}{bd^2} \tag{2.29}$$

Similarly the FM is determined from the straight line portion of the force-deflection curve.

For four point bending, the maximum deflection occurs a the center, at x = L/2 with the deflection equation[17]:

$$\delta = \frac{Pa}{48EI}(3L^2 - 4a^2) = \frac{Pa}{4Ebd^3}(3L^2 - 4a^2) \quad (2.30)$$

Therefore, the FM in four point bending is,

$$E = \frac{Pa}{4\delta bd^3}(3L^2 - 4a^2) \quad (2.31)$$

where, δ is the longitudinal deflection of the specimen at L/2 determined from the initial linear section of the load-deflection curve where it follows the Hooke's law and P is the corresponding load of δ from the load-deflection curve.

Four point bending test is the recommended technique for characterizing the flexural properties of bone cement according to ISO 5833 standard. In a typical experiment, rectangular bar specimens (n=12) (32mm x 3.15mm x 2 mm) were produced as per the method followed in preparing specimens for the three point bending test. Testing was conducted using the computer controlled Instron 3345 at a crosshead speed of 5 mm/min. Four point FS was calculated from the maxium stress at fracture while the four point FM was calculated from the straight portion of the force-deflection curve according to Equation 2.31.

The specimens under three or four point loading experience normal stress which is compression (above the neutral axis) and tensile (below the neutral axis) during the bending test with negative bending moment. Besides normal stress, additional shear stress develops in the specimen that can influence the result of the bend test. In order to minimize this effect, the ratio of support length, L to specimen thickness, d must be considered as L = (16±1)d.[17] Therefore, the effect of shear stress was negligible in this work as we maintained the L/d ratio of the test specimens at 16 ± 1.

2.7.4.2. Fracture toughness

Fracture toughness of a material is defined as the energy absorbed by the material before a crack propagates through it. This is a measure of the amount of energy required for fracture.

The fracture toughness of a material is characterized by the energy release rate and the stress intensity factor. The energy release rate is a function of the energy involved in crack propagation, whereas the stress intensity factor describes the stress state or stress intensity at the tip of a crack.[18] The stress intensity factor changes with crack length and stress according to[19] :

$$K = Y\sigma^{1/2} \tag{2.32}$$

where K is the stress intensity factor and Y is a function that is dependent on crack size and geometry. A material fractures when the stress intensity reaches a critical value K_C, This value of the stress intensity at fracture is called the fracture toughness, which gives a relative value of a material's ability to resist crack propagation. The critical stress intensity factor or fracture toughness is generally denoted as K_{IC}, where the subscripts I refers to the direction of load application which is perpendicular to the crack as in the case of tensile test.[146] The units of K_{IC} are units of stress (force/length^2) x units of length$^{1/2}$ and are typically reported as Mpa-m$^{1/2}$.

The fracture toughness test is a standard procedure to characterize the fracture behaviour of bone and dental cements. A commonly used method to measure the K_{IC} of bone cement is based on the chevron notched short rod (CNSR) configuration introduced by Barker[147] which is set by the ASTM B771-87[148] standard. In this work, we characterized the K_{IC} of nanocomposite bone cements using the notchless triangular prism (NTP) method as developed by Ruse et al,[149] which is a simplified modification of the CNSR configuration to accommodate small samples and to avoid the cumbersome notching procedure.

The NTP method uses a 6 x 6 x 6 x 12 mm notchless triangular prism specimen (Figure 2.14 a). The assembly of the NTP specimen and the specimen holder achieves a final configuration (Figure 2.14 b) similar to one present in a CNSR test (Figure 2.14 c). The prism, when fitted into the holder, reproduces the chevron shape of the area to be fractured during the test.

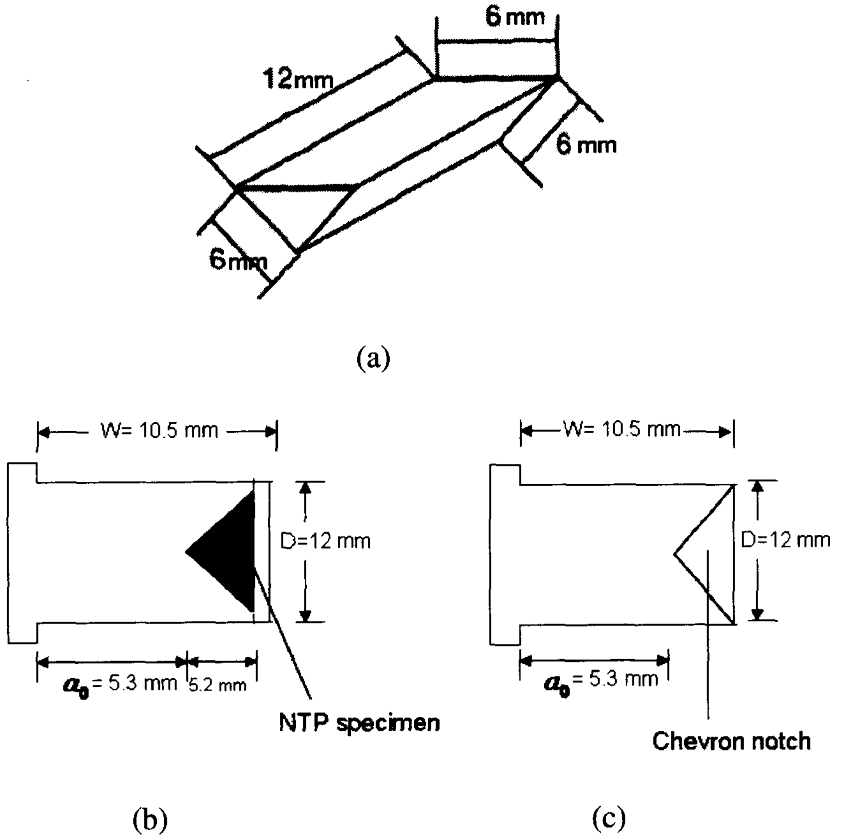

(a)

(b)

(c)

Figure 2.14: (a) Notchless triangular prism (NTP) used as a test specimen; (b) diagram showing the configuration of an NTP specimen in holder; (c) diagram showing the configuration of a CNSR specimen.

The holder has four components (Figure 2.15). Two symmetrical half cylinders (ϕ = 12 mm, h = 9 mm) with a loading collar (ϕ = 18mm, h = 3 mm) at one end and a triangular prismatic groove (6 x 6 x 6 x 6 mm) at the other form the base into which the NTP is placed. Two symmetrical half-disks (ϕ = 12 mm, h = 1.5 mm), fastened with screws across the triangular prismatic grooves of the corresponding half-cylinders of the base, restrain the NTP test specimen.

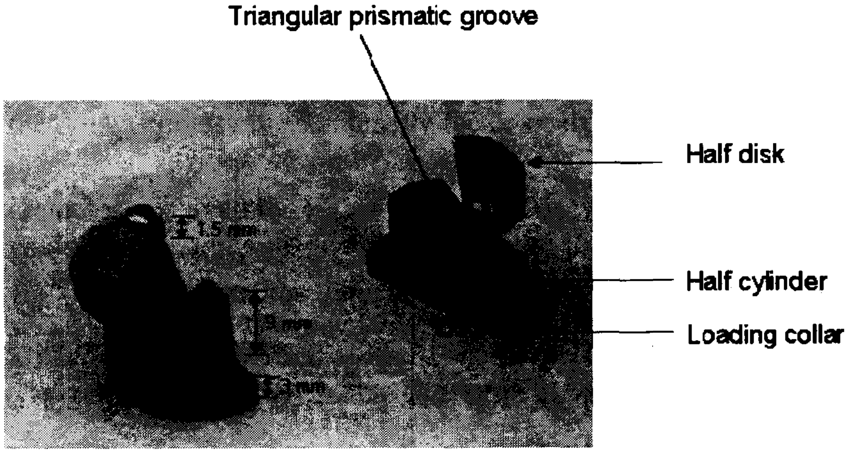

Figure 2.15: Holder for the NTP specimen. (Ref.[149])

During the testing, NTP specimens (n=12) were produced with dimensions as mentioned above by placing 0.4 gm cement dough in PTFE mold. After curing the specimens at room temperature for 24 hours, they were submerged in demineralised water at 37 °C for seven days. Prior to mounting the specimens for each test, each specimen was removed from water and a ~0.1 mm deep crack was created using a sharp blade midway along one of the edges of the NTP specimen. The specimen was placed into the groove with the crack initiation point aligned with the split line of the holder and secured in place by the two screw-tightened lids. The test assembly was secured in the custom designed grips attached to the computer controlled Universal testing machine (Instron 3345) and loaded in tension at a crosshead speed of 0.1 mm/min, and the load and the displacement were constantly monitored and recorded.

The K_{IC} value was obtained using the standard formula used in CNSR method[150]:

$$K_{IC} = \frac{P_{\max}}{DW^{1/2}} \gamma^*_{\min} \tag{2.33}$$

where, P_{max} = maximum load recorded during testing, D = specimen diameter (12 m) (in case of NTP, it is the diameter of the half cylinder), W = specimen length (10.5 mm) (in case of NTP, it is the total height of the half cylinder and the half disk that restrains the specimen) and $\gamma^*_{\min}$ = the dimensionless stress intensity factor coefficient minimum which is a function of two parameters as given by $\gamma^*_{\min} = f(\alpha_0, W/D)$, where α_0 is the ratio of initial crack length, a_0 (distance from the line of load application to the tip of the chevron), to specimen length, W , i.e. $\alpha_0 = \frac{a_0}{W}$, and W/D is the specimen length to diameter ratio.

Bubsey et al.[150] reported values for $\gamma^*_{\min}$ for specimens with W/D ranging from 1.5 to 2.0 and α_0 ranging from 0.2 to 0.5 and established a linear regression analysis between the experimentally determined $\gamma^*_{\min}$ and W/D at α_0= 0.5 (Figure 2.16).

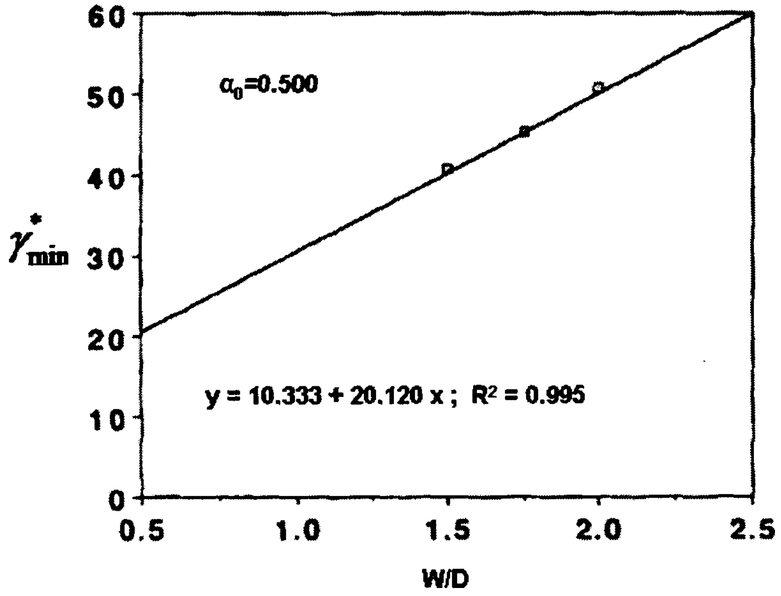

Figure 2.16: Plot of $\gamma^*_{\min}$ versus W/D, redrawn from article published by Bubsey et al.[150], used to determine the dimensionless stress intensity factor coefficient minimum, $\gamma^*_{\min}$ for the NTP test.

In the case of a NTP specimen, $\alpha_0 = \frac{a_0}{W} = \frac{5.3}{10.5} = 0.5$

and W/D = 0.88

Because the W/D ratio is outside the range reported by Bubsey et al.[149,150], a $\gamma^*_{\min}$ value for the NTP configuration was extrapolated and a $\gamma^*_{\min} = 28$ was obtained for the NTP configuration.

A very good correlation between the NTP and CNSR fracture toughness indicated that the NTP fracture toughness test can be used to determine the fracture behaviour of acrylic bone cement and other composite materials.[149]

2.7.4.3. Dynamic elastic properties

Dynamic elastic properties of a material is a measure of its rigidity and were evaluated by non-destructive testing with ultrasonic waves using a pulse method.

Ultrasonic waves or elastic waves propagate in elastic bodies like solids, liquids and gases by vibrating or oscillating the particles of the bodies. This oscillatory motion of particles can occur along the direction of wave propagation (longitudinal wave) or perpendicular to it (transversal wave). Only in solid bodies transversal waves arise in addition to longitudinal waves, since oscillating return to a state of rest presumes the existence of restoring elastic forces.[151] The velocity of the longitudinal wave can be expressed in terms of the materials elastic properties as[151],

$$C_L = \sqrt{\frac{E}{\rho}} \tag{2.34}$$

Similarly, the propagating velocity of transverse wave in solids can be expressed as,

$$C_S = \sqrt{\frac{\mu}{\rho}} \tag{2.35}$$

where, μ is the shear modulus of the material.

Therefore, the lighter the material and/or the greater its rigidity, the greater is the magnitude of the sound velocity in it.

Now for a infinitely extended solid medium or material, when its cross-sectional dimensions are large in comparison with the length of the wave propagated in it, and where the reflection of waves from the boundary of the medium can be neglected, the velocity of longitudinal wave will be[21,152]:

$$C_L = \sqrt{\frac{E(1-\nu)}{\rho(1+\nu)(1-2\nu)}} \tag{2.36}$$

where, ν is the poisson's ratio of the material.

Similarly, the propagation velocity of transverse waves is related to the elastic properties of the solid medium as:

Ultrasonic waves or elastic waves propagate in elastic bodies like solids, liquids and gases by vibrating or oscillating the particles of the bodies. This oscillatory motion of particles can occur along the direction of wave propagation (longitudinal wave) or perpendicular to it (transversal wave). Only in solid bodies transversal waves arise in addition to longitudinal waves, since oscillating return to a state of rest presumes the existence of restoring elastic forces.[151] The velocity of the longitudinal wave can be expressed in terms of the materials elastic properties as[151],

$$C_L = \sqrt{\frac{E}{\rho}} \tag{2.34}$$

Similarly, the propagating velocity of transverse wave in solids can be expressed as,

$$C_S = \sqrt{\frac{\mu}{\rho}} \tag{2.35}$$

where, μ is the shear modulus of the material.

Therefore, the lighter the material and/or the greater its rigidity, the greater is the magnitude of the sound velocity in it.

Now for a infinitely extended solid medium or material, when its cross-sectional dimensions are large in comparison with the length of the wave propagated in it, and where the reflection of waves from the boundary of the medium can be neglected, the velocity of longitudinal wave will be[21,152]:

$$C_L = \sqrt{\frac{E(1-\nu)}{\rho(1+\nu)(1-2\nu)}} \tag{2.36}$$

where, ν is the poisson's ratio of the material.

Similarly, the propagation velocity of transverse waves is related to the elastic properties of the solid medium as:

$$C_S = \sqrt{\frac{E}{2\rho(1+\nu)}} \tag{2.37}$$

From equations 2.37 and 2.38 the dynamic elastic properties of the solid are provided below:

Dynamic Young's modulus, $E = \frac{(1+\nu)(1-2\nu)}{(1-\nu)}(\rho C_L^2)$ (2.38)

Dynamic shear modulus, $\mu = \rho C_S^2$ (2.39)

And Poisson's ratio, $\nu = \frac{\frac{1}{2}(C_L / C_S)^2 - 1}{(C_L / C_S)^2 - 1}$ (2.40)

The ultrasonic pulse method is the most convenient technique to evaluate the elastic properties of a material. Along with the measurement of a materials rigidity, this method also qualitatively reflects the interfacial adhesion between the filler and matrix of a reinforced composite.[21] The stronger the adhesion, the faster the propagation of an ultrasonic wave through the filler-matrix interface. The values dynamic elastic moduli determined by this technique exhibit very low coefficient of variation and this is why, it has been found to be quite sensitive to composition and structural changes within the material and also the material's isotropy.[22] Therefore, this method is quite valuable when developing new materials and was followed in this research to characterize the dynamic elastic properties and interfacial adhesion between the nanofillers and acrylic matrix of nanocomposite bone cement. This technique is based on the analyses of the propagation time of ultrasonic wave. The principal operating units in the pulse apparatus are a synchronizing pulse generator, transmitting and receiving piezoelectric elements, amplifier, and oscilloscope.

In a typical testing procedure, an ultrasonic mechanical vibration with resonant frequency of 20 MHz was emitted by piezoelectric transducers (Lithium niobate crystal) when a high-frequency pulse was applied using a pulse/function generator (811A, 20 MHz, Hewlett-Packard). As the piezoelectric effect is reversible, an ultrasonic wave reaching a piezoelectric element generates a pulse of the same frequency at its electrodes and is delivered to the time-sweep of an oscilloscope (60 MHz, V-665, Hitachi). Therefore, two lithium niobate crystals were attached to the two opposite surfaces of the specimen. One crystal emits an ultrasonic wave through the material while the other crystal receives the wave and converts it into an electrical signal. Both the transmitting and receiving signals were generated in a storage oscilloscope and the traversal time of wave in the investigated specimen was determined from the receiving signal presented in the oscilloscope as shown in Figure 2.17.

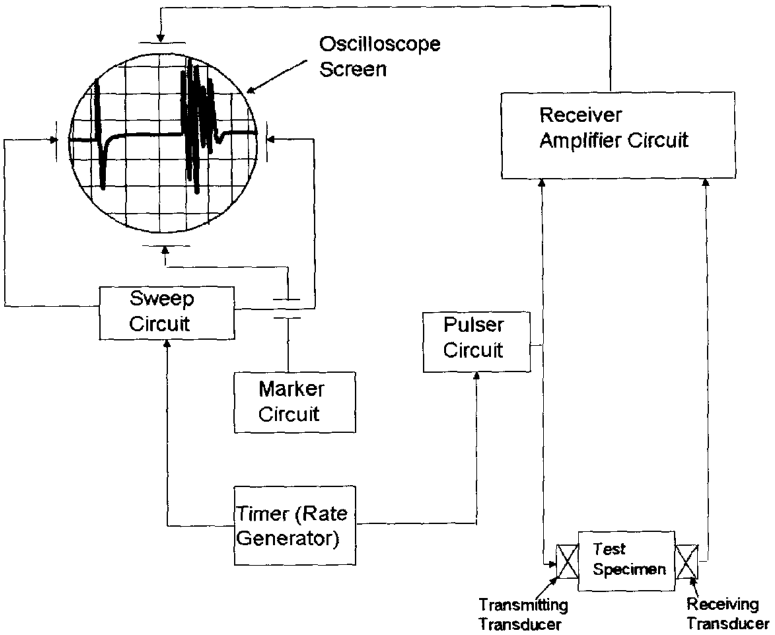

Figure 2.17. Block diagram of the ultrasonic-pulse setup.

Knowing the specimen thickness, which was confined between the two transmitting and receiving crystals, the velocity of ultrasonic wave was determined using the following relationship:

$$C=\frac{\text{Specimen thickness}}{t} \tag{2.41}$$

Where C is velocity of sound (m/μs); t = T- Δt; T is total travelling time (μs) of the ultrasonic wave across the sample and the receiving crystal; and Δt is the travelling time (μs) of the ultrasonic wave through the receiving crystal.

X- and Y-cut crystals were used for excitation of longitudinal and transverse oscillation in the test specimen. For the excitation of longitudinal wave, the piezoelectric crystal was cut at 36° with the X-axis while for transverse wave was cut at 41° with Y-axis.

2.7.5. In vitro biocompatibility of bone cement

Being a biomaterial, bone cements must be biocompatible. In this thesis biocompatibility of the bone cements were determined *in-vitro* by using the osteoblast cellular response method. This method is evaluated by the extent of cell adhesion, cell proliferation and live/dead analysis after applying the osteoblast cells on the surface of the composite specimens.

The *in-vitro* study on the cellular response of bone cement specimens was carried out by a graduate student in Prof. Douglas Hamilton's Lab using osteoblast cells of neonatal rat calvariae.

In order to determine the *in vitro* biocompatibility of the cements, the following components were purchased from Invitrogen: phosphate buffered saline (PBS), heat-inactivated fetal bovine serum (FBS), alpha-modified eagle medium (α-MEM) (Gibco, Grand Island, NY, USA), live/dead kit and antibiotic solution (10,000 units/ml penicillin, 10,000 μg/ml streptomycin, and 25μg/ml amphotericin). Paraformaldehyde (PFA) and collagenase type II were purchased from Sigma-Aldrich.

Rat calvarial osteoblasts were isolated from 1-d-old rats using sequential collagenase digestion, as described by Bellows et al.[153] Prior to the experiment, stock collagenase mixture was made and aliquoted into 50ml tubes. For 300ml solution, 2 g NaCl, 120 mg KCl, 160 mg K_2HPO_4, 40 mg $CaCl_2$, 1.8 g HEPES buffer and 298 ml water were placed into a sterile beaker with tissue culture stir bar. Solution was dissolved and pH was adjusted to 7.3 using 1M NaOH. Following pH adjustment, 1.6 g Mannitol, 0.6 g Glucose, 0.6 g BSA, 350 U/mL of Collagenase (Sigma Aldrich) and 3 mL antibiotics were added into the same beaker.

Following addition and dissolution of the ingredients, collagenase mixture was filtered through a 0.22um filter (Millipore).

2.7.5.1. Dissection of mouse calvarial osteoblasts.

Each digestion procedure was for a maximum of 8-12 pieces of calvariae. One day old pups were decapitated and placed into chilled PBS and brought into a sterile flow hood. The skin above the skull was cut from the base of the skull towards the forehead. The calvariae was dissected from parietal bones along suture lines and placed in a petri dish with PBS. Following dissections, leftover connective tissue was removed from calvariae using a surgical blade (No.10). Once removed, calvariae was transferred to a new petri dish and minced in PBS. Freshly cut calvariae was then transferred into a 15 ml Eppendorf tube filled with 6ml of collagenase mixture and agitated in a 37 C shaker at 70rounds/min for 10 minutes. Following agitation, the collagenase mixture was removed and discarded with the remaining minced calvariae left in the ependorf tube. 6 ml of fresh collagenase mixture was added to eppendorf tube with calvariae and inserted in the shaker at 70 round/min at 37 °C for 10 minutes. Following agitation, 6ml of collagenase is collected and placed in a new eppendorf tube. Repeat 3 more times with 6ml of fresh collagenase and agitate for 10, 20, and 20 minutes. In total, 4 samples were collected and pooled together. Samples were centrifuged at 1000g for 8 minutes and cells were plated in T-25 flask using alpha-MEM supplemented with 10% FBS and 1% antibiotics. For in vitro bone formation assay, cells were subcultured and plated at a density of 3 x 10^5 cells/cm^2. The medium was changed the following day and every 2 days until confluency was reached.

2.7.5.2. Surface treatment of the specimen by plasma cleaning

In order to increase the surface energy and promote cell attachment, all nanocomposite specimens were plasma cleaned using argon gas. The samples were loaded on a 24 well cover and placed inside the plasma cleaner vacuum for a period of 5 minutes. The samples were then flushed with argon gas twice for 30 seconds followed by 3 minutes of rest to create a proper vacuum. Following 2 argon flushes, the plasma RF value was turned to medium and the argon tank was opened halfway for 4 minutes to allow plasma cleaning to take place. The vacuum was then removed and samples were removed into sterile 24 well culture dishes.

2.7.5.3. Immunofluorescence staining

Primary rat calvarial osteoblasts were plated at a density of 10 000 cells per 15 mm structure in a 24 well culture dishes. At desired time points, osteoblasts were fixed with 4% PFA for 5 minutes followed by washing with PBS 3 times. Cells were then permeablized with 0.1% triton x-100 in PBS for 2 minutes followed by 3 washes of PBS. Cells were blocked with PBS/0.5% BSA for 75 minutes. Primary antibody was diluted based on data sheet standards (usually 1:100) in PBS/0.5% BSA for 1h at room temperature followed by 5 washes with PBS. Secondary antibody was applied at a dilution of 1:200 in PBS/0.5% BSA for 1 hour at room temperature in the dark. For experiments involving actin staining, phalloidin was added after secondary antibody for 1 hour at room temperature in the dark.

For cell adhesion experiments, samples were tested for differences for p-Tyr (PY99, Santa Cruz Biotechnology) and phalloidin-FITC (Sigma-Aldrich) antibodies, followed by an appropriate secondary antibody (Chemicon International). Cells were nuclear stained with Vectashield (Vector Laboratories, Inc.) and mounted using cover slips. Images were photographed with an Axiphot microscope (Zeiss), a Fast1394 digital camera (QICAM) and Northern Eclipse software (EMPIX).

2.7.5.4. Live/dead analysis

Live/dead analysis is a method which is designed to determine the viability/cytotoxicity of cells by differentiating between live and dead cells. Live/dead analysis kit (in this work, obtained from Invitrogen) allows the differentiation between live and dead cells with a two colour fluorescence. Calcein AM measures intracellular esterase activity and ethidium homodimer measures plasma membrane integrity. Live cells are viewed fluorescently in cells in the presence of ubiquitous intracellular esterase activity, which is determined by the enzymatic conversion of calcein AM to the fluorescently labeled calcein (green). Ethidium homodimer enters the cells through damaged cell membranes and undergoes fluorescence enhancement upon binding of EthD-1 to nucleic acids (red).

For live/dead analysis, primary rat calvarial osteoblasts were seeded onto bone cement specimen surfaces for a period of 1d, 2d and 3d. Following live/dead staining, 12 images of each structure were taken and analyzed microscopically.

2.8. Statistical analysis

All the statistical analysis performed on the experimental data for different tests in this work, were conducted using a one-way analysis of variance (ANOVA) and a Tukey B multiple comparative rank order test, with significance denoted at $P<0.05$ or as otherwise noted.

Chapter 3: Functionalization and characterization of titania nanomaterials

In this chapter, the functionalization of titania nanomaterials (nano fibers and nanospheres) and the effect of these nanomaterials on a poly(methyl methacrylate) (PMMA) matrix are described. Part of this chapter is reproduced from the published article by the author: Synthesis of TiO_2-PMMA Nanocomposites: Using Methacrylic Acid as a Coupling Agent,[20] with permission from Langmuir 23 (7), 3988-3995, Copyright [2007] American Chemical Society.

This chapter describes a new method for functionalizing TiO_2 nanomaterials (n-TiO_2) to provide compatibility with the organic polymer matrix for the synthesis of TiO_2-PMMA nanocomposite bone cements. Methacrylic acid (MA), a bifunctional agent that can chemically link to both n-TiO_2 and the polymer matrix, was used to modify the surface of n-TiO_2 using a Ti-carboxylic coordination bond. Then, the double bond in MA was copolymerized with methyl methacrylate (MMA) to form a n-TiO_2-PMMA composite. The resulting nanocomposites were characterized by using electron microscopy and elemental analysis. The interfacial adhesion between the functionalized n-TiO_2 and polymer matrix was characterized by thermal analysis and non-destructive dynamic testing. The electron microscopy results showed a good distribution of the n-TiO_2 in the polymer matrix. It was found that the interfacial adhesion between the functionalized n-TiO_2 and PMMA matrix is stronger than that with non-functionalized n-TiO_2 as evidenced by a higher value of the glass transition and thermal degradation temperatures and a higher magnitude of dynamic Young's and shear moduli. Moreover, titania nanofibers (n-TiO_2fiber) exhibited a better reinforcing effect on the nanocomposites than that delivered by titania nanospheres (n-TiO_2 sphere).

3.1.Introduction

In recent decades, the synthesis of polymer nanocomposite materials has been intensely studied due to their extraordinary properties and wide-spread potential applications. In this regards, nanocomposite bone cements have drawn attention to overcome their prevailing shortcomings in clinical applications. As an example, commercial acrylic bone-cements mostly use $BaSO_4$ or ZrO_2 as radiopaque fillers.[28,154] The addition of these fillers causes phase separation and agglomeration in the composites due to the incompatibility of highly polar, ionic radiopaque substances with low-polarity resins, which in turn leads to the degradation of physical and mechanical properties.[28] A diversity of crystalline nano-materials, i.e., three-dimensional nano metal oxides, two-dimensional layered silicates, and one-dimensional carbon nanotubes, have been used for reinforcement of the polymer matrices of bone cement.[155] In addition to nanoclay and carbon nanotubes, oxide nanoparticles are emerging fillers for bone cement applications. For instance, TiO_2 was used as a radiopacifier in dental composites and bone cements.[154,156] The one-dimensional oxides, such as fibered or tubular SiO_2, TiO_2, and ZrO_2 are promising for reinforcement due to their unique properties and low cost compared with carbon nanotubes, however, only a few research studies have been reported in this area.[157,158]

One of the challenges for preparing nanocomposite materials is the agglomeration of the nano-fillers in the polymer matrix that leads to poor performance of the composite. To solve this problem, ultrasonic irradiation was used for dispersion of SiO_2, TiO_2 and Al_2O_3

nanoparticles during the synthesis of inorganic-polymer nanocomposite materials.[159] However, without any chemical bonding, enhanced interaction between the matrix and filler was not achieved.[160] Goto et al. used silane coupling agents, i.e., organofunctional silanes to functionalize nanosized titania fillers in order to make them compatible with the PMMA matrix when producing bioactive PMMA based bone cement.[97] But the silanized nanofiller did not favorably affect the mechanical properties of the cement due to the agglomeration of the titania particles.[97,161] Yoshida *et al.* treated SiO_2/Al_2O_3 -coated TiO_2 filler with silane coupling agent in order to produce opaque resin composites but failed to get improved mechanical properties due to the smaller surface area of the micron sized fillers.[154] Matsumura and Nakabayashi encapsulated micron sized titania particles with PMMA by in situ polymerization when producing opaque resin adhesives for veneering on cast metal,[162] but did not get enhanced interaction between the matrix and fillers, likely due to the larger particle size and absence of chemical bonding.

In this chapter, we present a new method of functionalizing titania nanostructures and synthesizing a nanocomposite with the functionalized n-TiO_2 in the polymer matrix by using MA, which has both a carboxyl group for coordination to the nano-titania,[163,164] and a vinyl group for subsequent polymerization. Gratzel *et al.* described three possible structures of carboxylate coordinated to a titania surface (Scheme 3.1).[165]

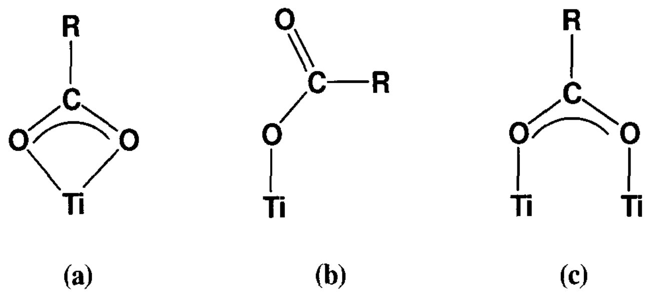

Scheme 3.1. Binding modes of RCOO- with titania surface (R= H or CH_3). (a) chelating bidentate. (b) monodentate and (c) bridging bidentate.

In the first structure, carboxylate is bound to one Ti^{IV} center in a chelating bidentate mode (a). The carboxylate could also be bound to one Ti^{IV} in a monodentate (ester-like linkage) mode (b) and finally, the carboxyl group could bind with each of its oxygen atoms to a Ti^{IV} center of the surface yielding the bridging bidentate mode (c). The carboxylic ions adsorb in a dissociative process with the two oxygen atoms bonding to the surface titanium ions, with the proton (H^+) bonding to the bridging oxygen ions.[166] After functionalization of the n-TiO_2 with the bifunctional molecule, MA, the PMMA-TiO_2 nanocomposite was synthesized through free radical copolymerization between the MA bridged to the n-TiO_2 and methyl methacrylate (MMA) monomer either by suspension polymerization in water or by bulk polymerization (Figure 3.1).

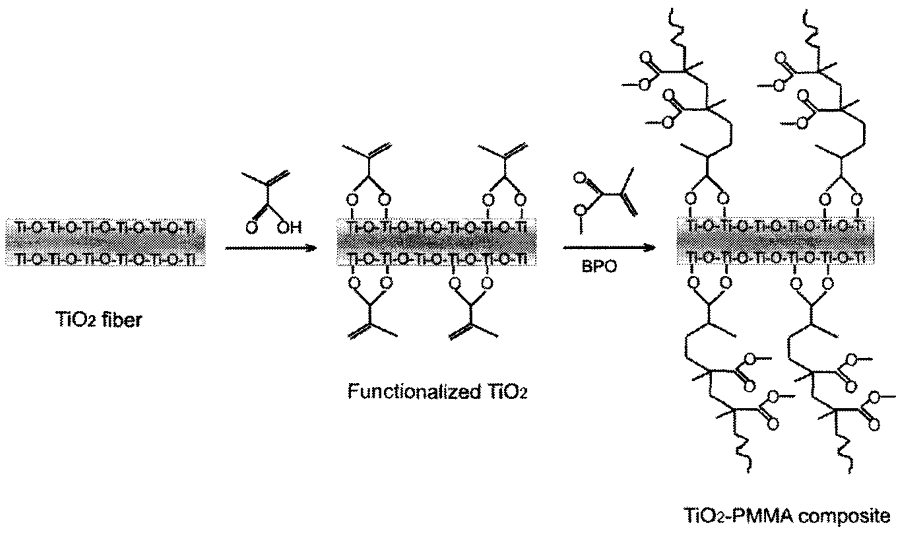

Figure 3.1: Schematic: functionalization of n-TiO_2 and formation of TiO_2-PMMA nanocomposite.

The copolymerization between MA and MMA will occur according to the *Q-e scheme* as first proposed by Alfrey and Price.[167] Having Q and e values almost similar to one another, monomer MMA ($Q = 0.78$, $e = 0.40$) and MA ($Q = 0.98$, $e = 0.62$) will have tendency to copolymerize in a random fashion as extensively studied by others.[168-170]

The resulting copolymerization products (nanocomposites) were characterized by electron microscopy, thermal and mechanical analysis.

3.2. Experimental details

3.2.1. Materials.

n-TiO_2 fiber with an average diameter of 12 nm were prepared by a direct sol-gel process in supercritical carbon dioxide (scCO_2) as described in Chapter 2.[128] Commercial titania nanospherical particles (99.5%, Sigma-Aldrich), 2-propanol and MA (99.99%, Sigma-Aldrich), poly (vinyl alcohol) (PVA) (99+% hydrolyzed, Sigma-Aldrich) and benzoyl peroxide (BPO) (97%, Sigma-Aldrich), MMA monomer (95.9wt%, Ivoclar Vivadent) containing a crosslinker butanediol dimethacrylate (4 wt %) and an activator (0.1 %) were used as received. PMMA beads (99.2 wt %, Ivoclar Vivadent) having an average particle diameter of 57.7 microns (as measured by laser diffraction using a Malvern Mastersizer 2000), an average molecular weight of 207kDa (as measured by gel permeation chromatography, see appendix 2) with a free-radical initiator BPO (0.8 wt %) were used without further treatment. MMA monomer (99%, Sigma-Aldrich, inhibited with 10-100ppm monomethyl ether hydroquinone) was passed through an inhibitor removal column (capacity 3L at 100 ppm hydroquinone, Sigma-Aldrich) before use.

3.2.2. Experimental setup

The experimental setup for synthesis and functionalization of n-TiO_2, and preparation of the n-TiO_2-PMMA composites both by suspension and bulk polymerization techniques were described in detail in Chapter 2.

3.2.3. Functionalization of n-TiO_2

The as-prepared n-TiO_2 fibers synthesized by the sol-gel method in $scCO_2$ were calcined at 600 °C to impart crystallinity and thermodynamic stability.[171] The diameter and length of the n-TiO_2 fibers were determined from the electron micrographs of the nanofibers by using Image J software on the basis of 100 numbers of nanofibers.

In order to functionalize the surface of the nanofibers, 0.1 g of calcined TiO_2 powder was dispersed in 35 mL of 2-propanol with the aid of ultrasonic agitation, followed by reacting with 3 mL of MA at 80-85 °C for 24 hours with constant stirring. The pH of the reaction medium was measured using a pH meter (VWR SB301), with the initial pH value being 3.85. The reaction product was then filtered and washed by ultra pure distilled water, and dried at 80 °C for 5 hours under vacuum. For comparison purposes, the commercial n-TiO_2 spheres were functionalized using the same technique.

3.2.4. Preparation of n-TiO_2 – PMMA composites

TiO_2–PMMA nanocomposites were synthesized by both suspension and bulk polymerization free-radical techniques.

In the suspension polymerization, a 1 L flask was equipped with a turbine stirrer, reflux condenser, thermometer and a nitrogen inlet. 0.1 gm PVA was dissolved in 250 ml warm deionized water in a reactor under N_2 atmosphere and constant stirring for 30 minutes. The mixture of 0.5 g of functionalized n-titania, 0.25 gm of BPO and 5 ml of MMA (after ultrasonication) was then introduced into the reactor and the polymerization was performed at 80-85 °C under N_2 atmosphere with a stirring speed of 800 rpm for 8 hours.

In the case of bulk polymerization, the nanocomposite was synthesized at room temperature using a known amount of PMMA powder and MMA liquid (weight of powder/weight of liquid = 2.18). The powder portion contained 99.2wt% PMMA beads (57.7 micron) and 0.8wt% benzoyl peroxide (BPO). The liquid portion contained MMA (95.9 wt %), a dimethacrylate crosslinker (4 wt %), and an activator (0.1 wt %) for room temperature initiator decomposition.[172] The viscosity increase, polymerization shrinkage, and heat of reaction during bulk polymerization was controlled by the partial dissolution of PMMA beads in the liquid MMA monomer due to the solubility of the PMMA beads in liquid MMA.[1,172]

The functionalized n-TiO_2 were dispersed in the liquid monomer portion by ultrasonic agitation for one hour. The resulting materials were hand-mixed with the powder portion (according to the standard technique for preparing acrylic bone cement)[172] into a dough state and then injected into different molds for different types of characterization. On each end of the mold, glass slides were firmly held. After complete curing at room temperature, specimens were taken out of the mold and aged for 24 h at room temperature, as described previously.[172] Then the specimens were subjected to different testing in the dry condition.

3.2.5. Characterization

X-ray diffraction (XRD) was conducted utilizing Rigaku-Geigerflex CN2029 employing CuKα1 + Kα2 radiation with a power of 40kVx35mA. The FTIR spectra were collected using KBr pellet form with a Bruker IFS 55 FTIR instrument with an attached MCT detector. Scanning electron microscopy (SEM) images were recorded using a LEO 1530 instrument without gold coating. Transmission electron microscopy (TEM), scanning transmission electron microscopy (STEM), energy dispersive X-ray spectroscopy (EDS) and electron energy loss spectroscopy (EELS, with a dispersion of 0.2 eV/pixel, a probe size of 1 nm and a camera length of 0.2 gif A) images of the composite were studied using a JEOL 2010f operated at 200 KV. Differential scanning calorimetric (DSC) analysis was performed using a Mettler Toledo DSC822^e (second heat, midpoint method) with a temperature ramp from 25 to 150 °C at a heating rate of 10 °C/min under nitrogen atmosphere. Thermo gravimetric analysis (TGA) was performed using a Mettler-Toledo TGA/SDTA851^e from 25 to 600 °C at a heating rate of 10 °C/min under nitrogen atmosphere.

The dynamic elastic modulus (Young's and shear modulus) of the nanocomposite specimens were evaluated by an ultrasonic pulse method as described in Chapter 2. During the preparation of specimens for this test, the functionalized n-TiO_2 (2 to 15 wt%) was dispersed in the liquid monomer portion by ultrasonic agitation for one hour following mixing the powder and liquid into a dough state and injection of the dough into a polysiloxane mold having diameter and height of 16 and 2 mm respectively. The dynamic Young's and shear moduli, and Poisson's ratio were calculated from the velocities of the longitudinal and transverse waves as described in chapter 2.

3.3.Results and Discussion

3.3.1. XRD

The powder X-ray diffraction patterns, as described in previous work, [128,171] showed that the n-TiO_2fibers calcined at 600 °C exhibited both anatase and rutile nanocrystallites and the ratio of anatase to rutile was 0.79:1, according to Zhang and Banfield's correlation. Powder X-ray diffraction patterns of the commercial n-TiO_2 showed the ratio of anatase to rutile as 1.25:1 (see Appendix 3). The results showed that the crystallinity of the fibers and spheres were similar, so that the effect of the crystallinity on the nanocomposite could be eliminated when comparing the properties of the polymer nanocomposites, as described in the subsequent paragraphs.

3.3.2. FTIR

The FTIR spectra of both the calcined and the functionalized titania nanofibers are shown in Figure 3.2. In Figure 3.2(a) the absence of any peak from 1300-1800 cm^{-1} indicates the absence of any organic groups on the titania surface. In Figure 3.2(b) the very strong bands at 1546, 1444 and 1414 cm^{-1} are due to the bidentate coordination between titanium atoms and the carboxylic groups of MA.

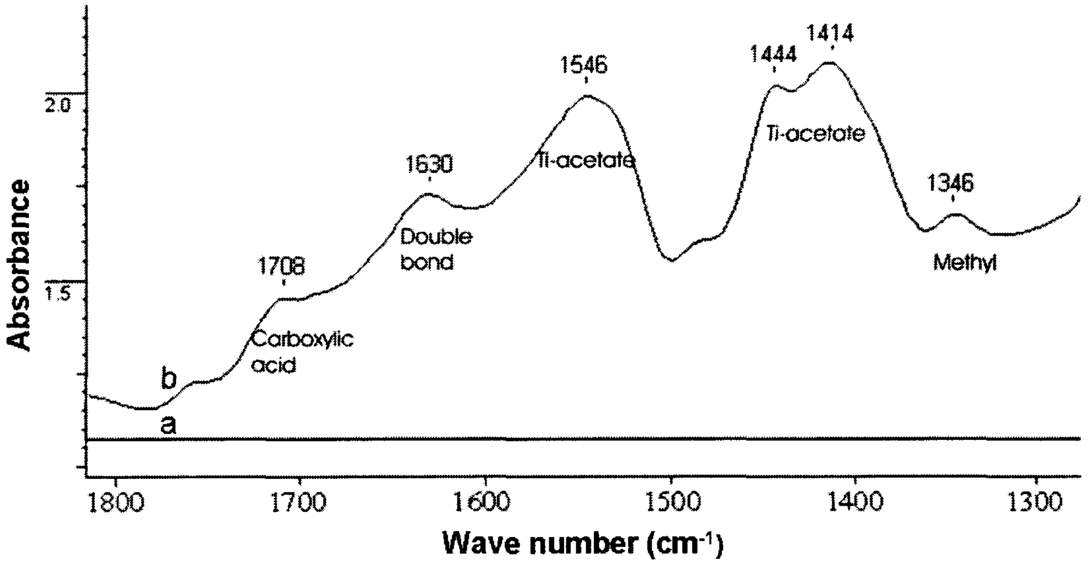

Figure 3.2: FT-IR Spectra: the non-functionalized (a) and functionalized (b) n-TiO_2 fibers.

The band at 1630 cm^{-1} shows the existence of the vinyl bond of MA, and the small band at 1346 cm^{-1} corresponds to a CH_3 group and the weak band at 1708 cm^{-1} corresponds to the C=O bonds of very small amounts of carboxylic acid residue.[173,174] The IR spectrum shown in Figure 3.2(b) confirms that the carboxyl group of MA has been coordinated to the titania surface through the bridging bidentate mode, as shown in scheme 3.1(c). As a result of this, titania was functionalized with a vinyl group for subsequent polymerization with unsaturated monomer during the synthesis of polymer-titania nanocomposites. Before functionalization, n-TiO_2 is hydrophilic. After the coordination of methacrylic acid to the surface of the n-TiO_2, however, it becomes both organophilic and hydrophilic. The organo- and hydrophilicity were contributed by the CH_2=CH- of the methacrylate group and H^+ on the bridging oxygen atom of the surface of titania, respectively.[166,175] Figure 3.3 a and b show the dispersion of the n-TiO_2 in layers of MMA and water at room temperature. The nonfunctionalized n-TiO_2 is well dispersed in the water phase, while the functionalized n-TiO_2 exhibited good dispersion in the monomer organic phase with a tendency towards the interface. This indicates the hydrophilicity change into amphiphilicity. After heating at 80 °C, the functionalized n-TiO_2 is completely suspended at the interface of the monomer and water layers (Figure 3.3 c). Interestingly, without water, the functionalized n-TiO_2 dispersed well in the monomer at both room temperature (Figure 3.3 d) and 80 °C.

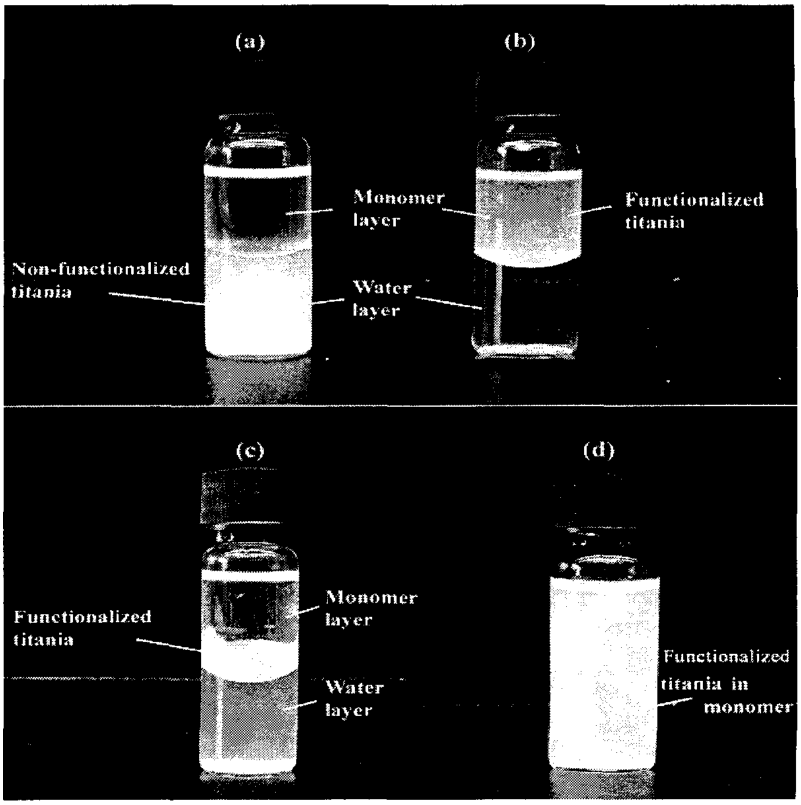

Figure 3.3: Photograph of n-TiO_2 powder dispersed in the mixture of MMA and water: (a) non-functionalized n-TiO_2 at room temperature; (b) functionalized n-TiO_2 at room temperature; (c) functionalized n-TiO_2 at 80 °C; (d) functionalized n-TiO_2 powder dispersed in monomer at room temperature.

3.3.3. Electron microscopy

In order to evaluate the microstructure and size distribution of the n-TiO_2 fibers as well as to examine the distribution of the n-TiO_2 fibers within the nanocomposites, SEM and TEM analysis were conducted. Figure 3.4 a shows the SEM micrograph of the functionalized n-TiO_2 fibers which confirmed that the morphology of the n-TiO_2 fibers after functionalization were in the fiber form. Based on this micrograph, the particle size distribution revealed normal behaviour with a mean value for diameter and length of 12 nm and 2 µm respectively (Figure 3.4 c and d). Figure 3.4b shows the SEM image of the PMMA composite with functionalized n-TiO_2 fibers synthesized by suspension polymerization at 80 °C. Many fibers can be observed in the area surrounding the PMMA

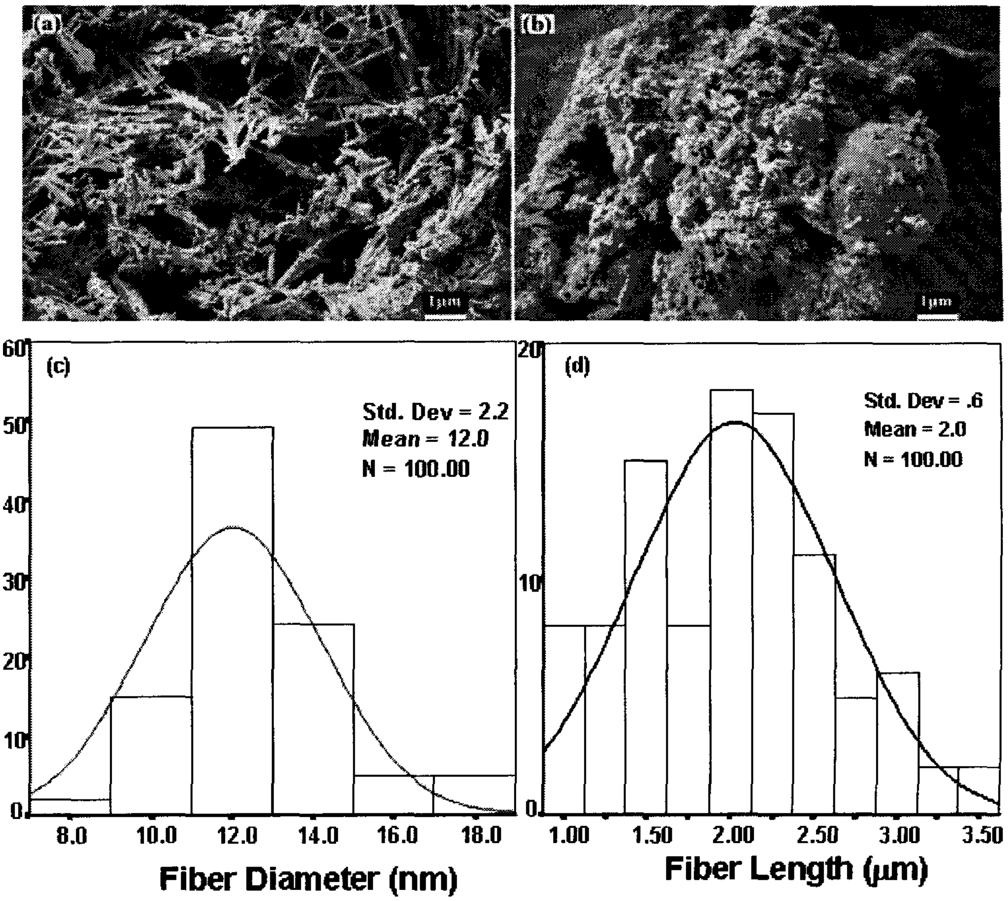

Figure 3.4: (a) SEM of the functionalized n-TiO_2 fiber bundles; (b) SEM of the 3 wt % functionalized n-TiO_2 fibers-PMMA composite produced by the suspension polymerization; (c) distribution of diameters of n-TiO_2 fibers; (d) distribution of length of n-TiO_2 fibers.

beads, indicating a poor distribution of nanofiller in the polymer due to the amphiphilic nature of the functionalized n-TiO_2 in the presence of water as described earlier.

The dispersion of the filler was improved significantly when the polymerization reaction was conducted at room temperature using bulk polymerization. Figure 3.5 compares the fracture surface of the composite with functionalized n-TiO_2 fibers and unfilled PMMA matrix prepared by bulk polymerization at room temperature. From this figure it is obvious that the n-TiO_2 fibers are well dispersed in the composite without any phase separation from the polymer matrix. Figure 3.6 a shows the fracture surface of 3 wt % functionalized n-TiO_2 fiber-PMMA composite produced by bulk polymerization. In this

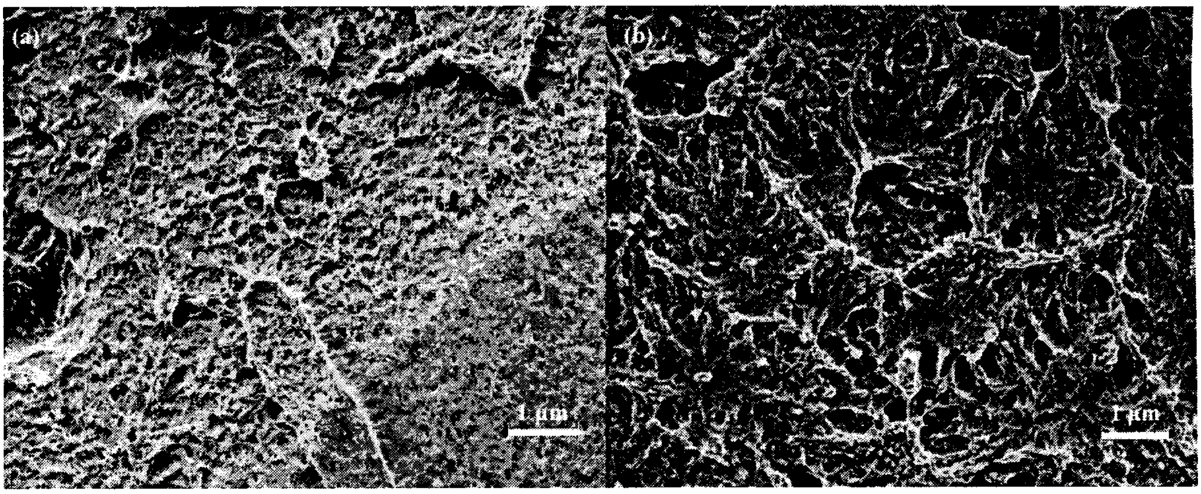

Figure 3.5. SEM: (a) Fracture surface of 3 wt % functionalized n-TiO_2 fiber-PMMA composite; (b) fracture surface of unfilled PMMA matrix produced by the bulk polymerization.

Figure we can see that the 58 micron diameter prepolymerized PMMA beads are firmly embedded in the matrix. The excellent adhesion and strong interfacial bonding between the polymer matrix /functionalized n-TiO_2 filler establishes a strong network throughout the matrix which confines the PMMA beads. This shows that the hand-mixing procedure of the bulk-polymerization works very well and the n-TiO_2 fibers functionalized with methacrylic acid provides an excellent matrix.

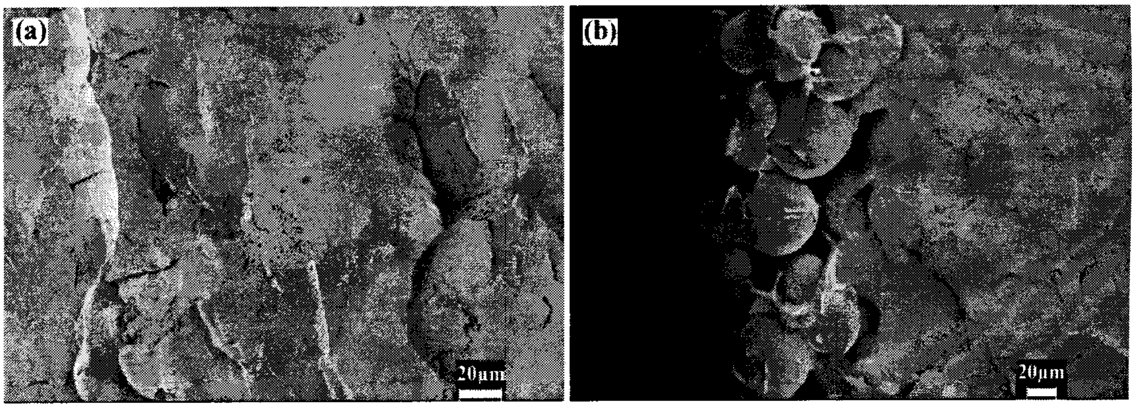

Figure 3.6 SEM: (a) Fracture sufrce 3 wt % functionalized n-TiO_2 fiber-PMMA composite; (b) and fracture surface of 3 wt % non-functionalized n-TiO_2fiber-PMMA composite produced by the bulk polymerization.

In comparison, Figure 3.6 b shows the fracture surface of a 3 wt% non-functionalized n-TiO_2 fiber-PMMA composite produced by the same procedure. Here we can see delaminating of the polymer beads from the matrix, further illustrating the importance of the nanomaterials having organophilic behavior in order for both good dispersion in the monomer phase, and good bonding to the relatively non-polar PMMA beads.

TEM has proven to be a powerful tool for studying the dispersion and microstructure of nanofillers embedded within a polymer matrix.[176-178] Figure 3.7 shows TEM images of functionalized n-TiO_2 fibers (Figure 3.7 a) as well as TEM images of PMMA composites with n-TiO_2 fibers (Figure 3.7 b, c) and composites with commercial TiO_2 nanospheres (Figure 3.7 d) prepared by bulk polymerization. From Figure 3.7 b and 3.7 c it is observed that while there are several individual particles distributed throughout the polymer matrix, most are clumped together in bundles.

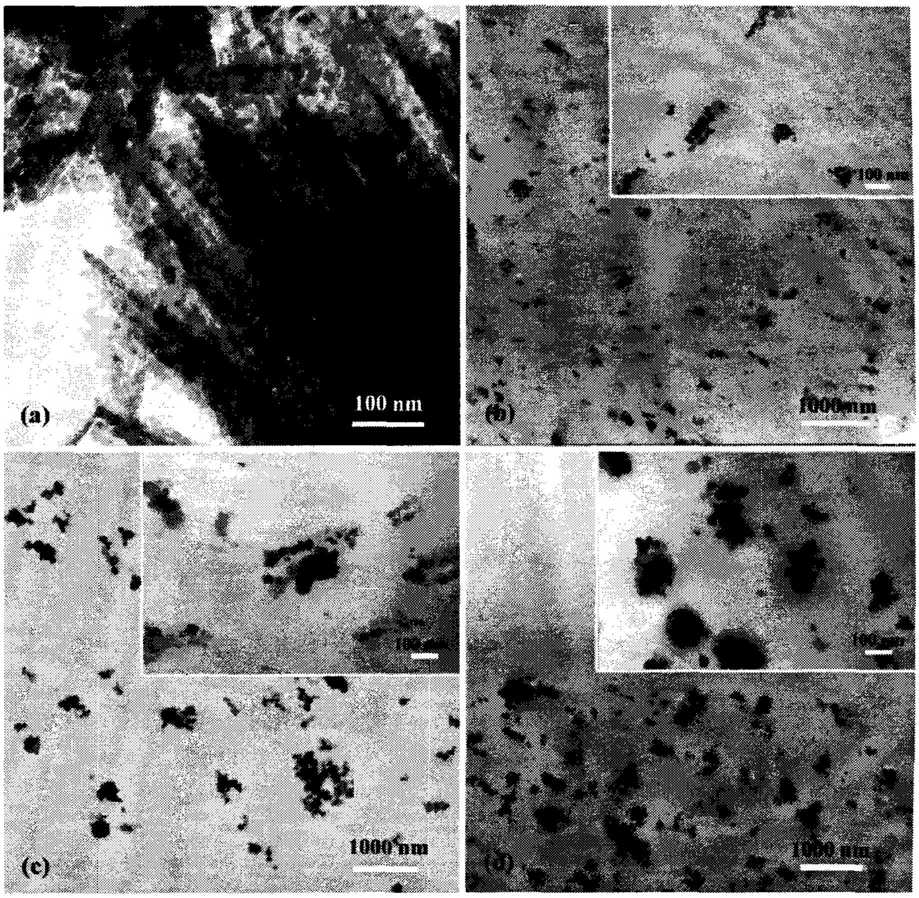

Figure 3.7. TEM: (a) functionalized n-TiO_2 fibers; (b) 3wt% functionalized n-TiO_2 fiber-PMMA composites at low magnification; (c) 3wt% non-functionalized n- TiO_2 fiber-PMMA composites; (d) 3wt% functionalized commercial n-TiO_2 sphere-PMMA composites. The insets are the ones with higher magnifications.

The bundles are in the nanosize range, and are uniformly dispersed throughout the polymer matrix, particularly when comparing with the functionalized fibers before polymerization as shown in Figure 3.4 a. Partial breaking of the fibers may be due to the high heat evolved during the exothermic bulk polymerization, which could break some of the oxo bonds between individual crystal structures or from the ultrasonic agitation treatment. Figure 3.7 d shows the functionalized commercial TiO_2 nanospheres in the PMMA matrix, in which the spheres exhibited a size range from 25-100 nm, and are uniformly dispersed throughout the polymer matrix.

The nanostructure of the composites was further studied by using STEM equipped with elemental analysis. Figure 3.8 a shows the STEM high angle annular dark field image of 10 wt % n-TiO_2 fiber in the PMMA matrix synthesized by the suspension polymerization technique. The bright white area is attributed to the polycrystalline TiO_2 and grey area is due to the amorphous PMMA matrix, and this was clarified by means of EDS mapping and EELS analysis. Using EDS elemental mapping, the distribution and intensity of the titanium and oxygen elements can be visualized (Figure 3.8 b and c). Also, using a certain signal energy windows of the EELS spectra, the elemental intensity along a line can be envisioned. Figure 3.8(d) shows the STEM image with EELS landscape, showing the intensity profile of titanium along the horizontal line.

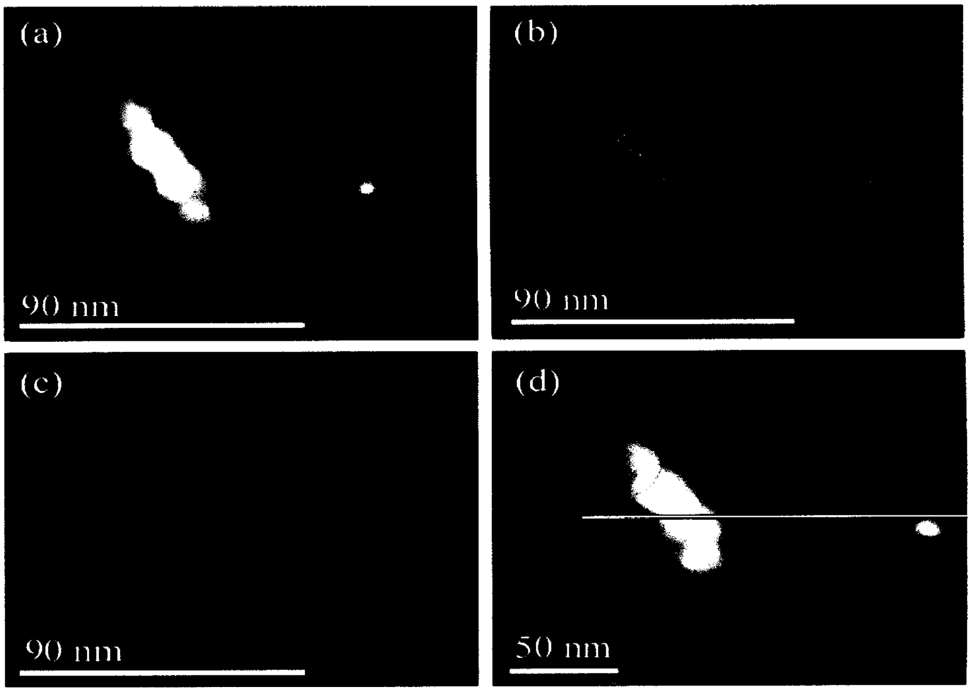

Figure 3.8: (a) STEM: n-TiO_2 fiber PMMA composite made from suspension polymerization; (b) EDS: titanium mapping; (c) EDS: oxygen mapping; (d) STEM and EELS landscape.

3.3.4. DSC and TGA

An enhanced thermal stability of the nanocomposite with functionalized titania nanofibers was observed compared to the nanocomposites with non-functionalized nanofibers using both DSC and TGA. As shown in Table 3.1, the unfilled PMMA exhibited a glass transition temperature (T_g) at 106 °C, while the PMMA-functionalized titania nanocomposites prepared by bulk polymerization exhibited elevated T_g of 118 °C at 3.0 wt% of the functionalized n-TiO_2 fiber. Strong interfacial bonding between the functionalized nanofibers and polymer matrix leads to an increase of the T_g by impeding the chain flexibility.[179,180]

Table 3.1. Thermal properties of n-TiO_2 fiber-PMMA composites.

Wt.% n-TiO_2 fiber	T_g (°C)		40% wt. loss (°C)	
	Func.	Non-func.	Func.	Non-func.
0	106	106	355	355
3.0	118	90	362	358

Nanocomposites prepared with non-functionalized n-TiO_2 exhibited lower T_g values than that of nanocomposites with functionalized n-TiO_2, due to the poor interfacial interaction between non-functionalized n-TiO_2 and PMMA matrix. Furthermore, the nanocomposite with 3.0 wt% non-functionalized nanofibers exhibits a lower T_g than the unfilled PMMA. This is probably due to the organophobic behavior of the non-functionalized titania, which leads to the presence of free mobile regions at the interface, which enhances the mobility of the bulk polymer chain.[181]

3.3.5. Dynamic elastic properties

The elastic properties of polymer nanocomposites are greatly influenced by the adhesion between the nanomaterial ceramic filler and the polymer matrix. Hence by measuring the elastic properties, we can gain insight into the effect of both: a) the adhesion between the n-TiO_2 and the PMMA matrix using methacrylic acid, and b) the morphological effect of nanofiber compared to nanosphere structure. Ultrasonic techniques were used for this testing which are well established methods to determine the dynamic properties of viscoelastic and composite materials.[18] This technique has proven to be more effective than the traditional static test in assessing and comparing materials that show viscoelastic behavior under load.[182] Static testing focuses only on the elastic component of the material. Dynamic testing on the other hand, can determine both the elastic and viscous response of the samples, and is very sensitive to structural differences within ceramic-polymer composites.[21,182] The TiO_2-PMMA nanocomposite samples with various amounts of functionalized and non-functionalized nanofillers from 0 to 15wt% prepared by bulk polymerization were evaluated for their dynamic elastic moduli. Figure 3.9(a) shows that the dynamic Young's moduli ranged from 5.1 to 7.8 GPa for the functionalized nanofibers, and 5.1 to 6.7 GPa for the non-functionalized nanofibers. The functionalized commercial nanospheres gave dynamic Young's moduli ranging from 5.1 to 6.9 GPa, which are not significantly different from those of the non-functionalized nanofibers at $P<0.001$. The non-functionalized nanospheres had the poorest Young's moduli, ranging from 5.1 to 6.3 GPa. As shown in Figure 3.9(b), essentially identical behavior was observed for the dynamic Shear modulus for the effect of n-TiO_2 in the PMMA nanocomposites.

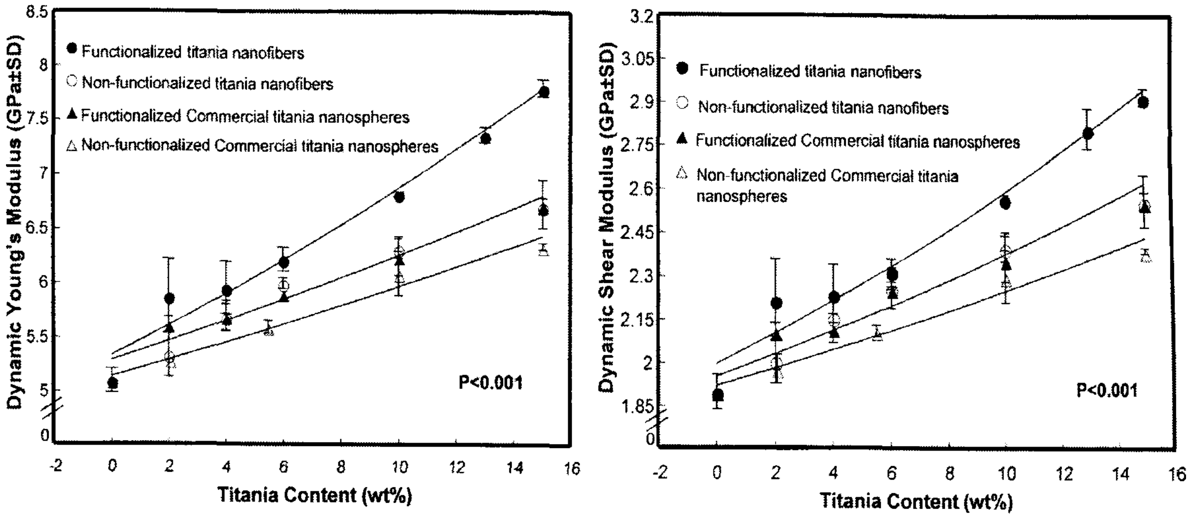

Figure 3.9: Mechanical properties: (a) dynamic Young's modulus versus weight percentage of the n-TiO_2 ; (b) dynamic Shear modulus versus weight percentage of the n-TiO_2 .

The mechanical properties of nanocomposites largely depend on the external load transfer between the reinforcing nanofiller phase and the matrix.[183,184] Hence, these results show that the chemical bonding between the functionalized titania nanofibers and the PMMA matrix produced significantly higher values ($P<0.001$) of dynamic elastic moduli compared to the composites with non-functionalized titania nanofibers. This further illustrates the strong adhesion between the functionalized nanofibers and surrounding polymer matrix in allowing an external load to be effectively transferred to the nanofibers from the polymer matrix.[184] As well, by comparing the morphological effect of the nanofiller on the mechanical performance of the nanocomposites, it is observed that the TiO_2 nanofibers are better reinforcers than nanospheres. Even though the nanofibers were found to partially break during polymerization, they provide higher aspect ratios, which are known to provide superior properties.[184]

As titania is an established radiopaque material[97], the resulting nanocomposites containing functionalized n-TiO_2 would exhibit unique combination of radiopacity and mechanical stability when applied as a bone cement. Our resulting nanocomposites exhibited some superior mechanical properties to the other PMMA-based composite cements containing titania particles,[97,154,162] although our data could not be directly compared with the others, as the method of measurement reported by them was different. It was reported that an increasing trend in mechanical properties was observed as the filler size in PMMA-based composite cements decreased and as the filler morphology became fibered.[3,185] Therefore, this study demonstrated a novel technique to reinforce PMMA based composites with functionalized n-TiO_2 justifying its potential application to develop nanocomposite bone cement.

3.4.Conclusion

TiO_2-PMMA nanocomposites with chemical bonding between the n-TiO_2 and polymer matrix, were synthesized for the first time using the coupling agent MA. The coordination of methacrylic acid to the n-TiO_2 was confirmed by IR spectra and partitioning experiments in monomer-water bilayers. An excellent distribution of the n-TiO_2 in the polymer matrix was observed from room temperature bulk polymerization, and the distribution of the filler in the polymer was poor for heated suspension polymerization. Electron microscopy results showed breaking down of the n-TiO_2 fiber bundles into smaller sizes during synthesis of the composite while thermal analysis showed enhanced thermal stability and increased T_g of the nanocomposites with functionalized n-TiO_2 fibers. Using an ultrasonic technique for measuring dynamic elastic properties, the composites with functionalized n-TiO_2 fibers exhibited significantly higher elastic moduli than those with non-functionalized fibers at $P<0.001$. The nanofiber structure provided higher elastic properties in the PMMA matrix than those prepared using a commercial spherical structure. This study inspired us to evaluate the effect of the functionalized titania nanofibers and nanotubes in PMMA matrix focusing its application as bone cements which are described in the following two chapters.

Chapter 4: Preparation and characterization of PMMA based composites reinforced with titania nanofibers

This chapter describes the effect of functionalized titania nanofibers on the physical and mechanical properties of TiO_2-PMMA nanocomposites for its potential application as a bone cement. Part of this chapter is reproduced from an article submitted to Composite Science and Technology with the title: "Thermal and Mechanical Properties of PMMA Composites Reinforced with Functionalized Titania Nanofibers "

Novel nanostructured n-TiO_2 fibers were incorporated into a PMMA matrix as a reinforcing phase. The hydrophilic nature of the n-TiO_2 fibers was modified by varying the functionalization of the n-TiO_2 fibers using controlled amounts of the bi-functional monomer, MA. The effects of the varying extent of functionalization of the n-TiO_2 fibers in the PMMA matrix were reflected by enhanced thermal and mechanical properties of the TiO_2 nanocomposites. A control material was also synthesized consisting of unfilled PMMA matrix. Another control material was prepared by incorporating 6 wt% $BaSO_4$ particles in the same PMMA matrix to mimic commercial bone cement. From the studied nanocomposites, an optimum composition of the n-TiO_2 fibers was found at 2 wt% loading, which while functionalized at 10wt%, provided the nanocomposites with significantly higher FS, FM and K_{IC} values compared to the controls both in the dry and wet conditions at $P<0.05$. Moreover, the functionalized n-TiO_2 fibers were found to impose a minimal effect on the rheological behaviour of the curing polymer. However, using standard medical X-ray radiography analysis, the TiO_2 nanocomposites exhibited significantly lower levels of radiopacity ($P<0.05$) compared to the $BaSO_4$ composite.

4.1. Introduction

PMMA based bone cements commercially used today are beset with a number of limitations, the majority of which are imparted by its radiopacifying agents. As already described in Chapter 1, these radiopacifiers are heavy metal salts that lead frequently to degradation of the physical and mechanical properties of the cements because of their poor wetting and dispersion in the organic matrix.[1,161] Hence, there is an ongoing interest for developoing novel radiopacifying agents that are compatible with the polymer matrix, which can help to introduce radiopacity to the organic polymer without compromising its mechanical properties.[28,172]

In this work we have used n-TiO_2 fibers as the reinforcing agent in the PMMA matrix which are biocompatible as well as possess a certain level of radiopacity.[97,186,187] In order to make the nanofibers compatible with the polymer matrix, they were functionalized in accordance with the procedure described in chapter 3. In addition, the extent of carboxylic functionalization on the surface of n-TiO_2 fiber was varied in this work by controlling the surface charge of the n-TiO_2 fibers by controlling the pH of the reaction medium. This takes advantage of the amphoteric nature of the hydroxo-complexes of multivalent titanium (Ti^{IV}) cations which both show acidic and basic reactions in a aqueous environment depending on the pH (Scheme 4.1).[188]

$$\text{Ti-OH} + H_2O \Leftrightarrow [\text{Ti-O}]^- + H_3O^+ \qquad \text{(Basic reaction)}$$

$$\text{Ti-OH} + H_2O \Leftrightarrow [\text{Ti-OH}_2]^+ + OH^- \qquad \text{(Acidic reaction)}$$

Scheme 4.1: Acidic and basic reaction of hydrated TiO_2 in aqueous environment

There is a general agreement that titanium oxide surfaces show two kinds of hydroxide groups: a more acidic type and a more basic type.[188,189] Therefore, the overall charge that builds up at the surface depends on the pH of the aqueous solution. As a quantitative measure, the isoelectric point (IEP) is often specified in this context. For TiO_2, IEP values between 5 and 6.7 have been reported.[190,191] below which the surface hydroxyl ion is fairly positive to bind negative carboxylic ion of the MA (Figure 4.1).[192]

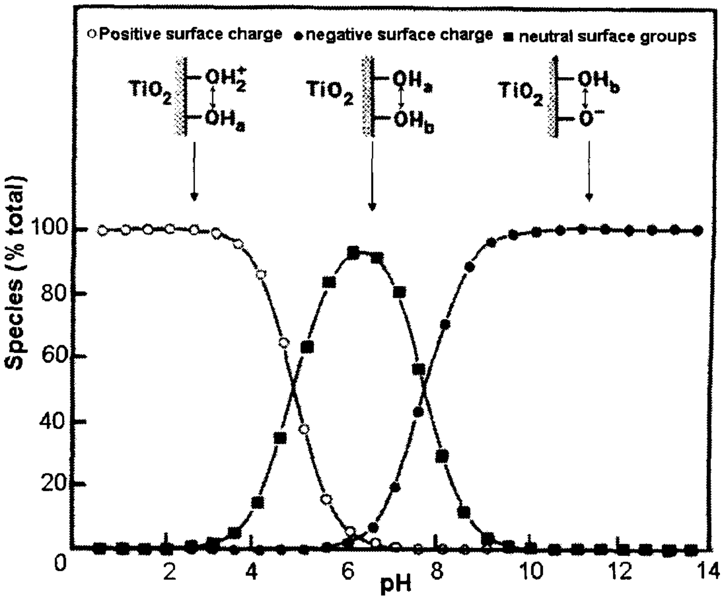

Figure 4.1: Concentration of charged and uncharged hydroxyl-related species at TiO_2 surface as a function of the pH of the aqueous solution. (Ref.[188])

Therefore, the functionalization reaction at different pH's yields different extents of functionalization.

The purpose of this study was to evaluate the physical and mechanical properties of PMMA based composites reinforced with n-TiO_2 fibers having varying extents of functionalization, and comparing them with composites reinforced with non-functionalized n-TiO_2 fibers and commercially available $BaSO_4$ particles.

4.2. Experimental details

4.2.1. Materials

TiO_2 nanofibers were synthesized using a direct sol-gel method in supercritical carbon dioxide in accordance with the procedure described in Chapter 2.[128] For comparison purposes, commercial radiopacifier $BaSO_4$ particles (99.5%, Sigma-Aldrich) were used as received. 2-propanol, MA (99.99%, Sigma-Aldrich) and MMA monomer (95.9 wt %) containing a butanediol dimethacrylate cross-linker (4 wt %) and activator (0.1 wt %) were used as received (Ivoclar Vivadent). PMMA beads (99.2 wt %, Ivoclar Vivadent) having an average particle diameter of 57.5 μm (as measured by laser diffraction using a Malvern Mastersizer 2000) with a free radical initiator BPO (0.8 wt %) were used as received.

4.2.2. Functionalization of n-TiO_2 fibers

The as-prepared n-TiO_2 fibers were calcined at 600°C for 2 hours in air to impart crystallinity and thermodynamic stability.[171] In order to functionalize the surface of the nanofibers, 0.1 g of calcined n-TiO_2 powder was dispersed in 35 mL of 2-propanol with the aid of ultrasonic agitation, followed by reacting with 3 mL of MA at 80-85 °C for 24 hours with constant stirring. The pH of the reaction medium was measured using a pH meter (VWR SB301), with the initial pH value being 3.85. In order to increase the extent of functionalization, the same reaction was carried out with the medium having pH 5.0, 5.5 and 6.0 adjusted by adding 0.3N potassium hydroxide solution dropwise to the reaction mixture prior to the reaction.

4.2.3. Preparation of n-TiO_2-PMMA composites

TiO_2-PMMA nanocomposites were prepared by a free-radical bulk polymerization technique as described in Section 2.6.2 of Chapter 2. Nanocomposite specimens with 2, 4 and 6 wt% loading of functionalized and non-functionalized n-TiO_2 fibers with two different extents of functionalization were prepared for evaluation of the mechanical properties. Moreover, unfilled PMMA matrix and control specimens analogous to commercial bone cement were prepared with 6wt% commercial $BaSO_4$ particles.

4.2.4. Characterization

Scanning electron microscopy (SEM) images were recorded using a LEO 1530 instrument without gold coating. Differential scanning calorimetry (DSC) analysis was performed using a Mettler Toledo DSC822^c (second heat, midpoint method) with a temperature range from 25 to 150 °C at a heating rate of 10 °C/min under nitrogen atmosphere. Thermogravimetric analysis (TGA) was performed using a Q500 TA instrument from 25 to 600 °C at a heating rate of 20 °C/min under air and nitrogen atmosphere for characterizing extent of functionalization of n-TiO_2 fibers and thermal stability of the nanocomposites respectively.

K_{IC} of the nanocomposite specimens (loaded with 2, 4 and 6% of functionalized n-TiO_2 fibers) was determined using the notchless triangular prism (NTP) method as described in section 2.7.4.2 of Chapter 2. During specimen preparation, the functionalized n-TiO_2 were dispersed in the liquid monomer portion by ultrasonic agitation for fifteen minutes, followed by preparation of triangular prism specimens. Testing was performed with the specimens both in the dry and wet conditions as described in Chapter 2.

FS and FM of the nanocomposites were determined by the three point bending test as described in section 2.7.4.1 of Chapter 2. The testing was conducted for specimens in the wet condition as described in Chapter 2.

The complex viscosity of the n-TiO_2 fiber-PMMA composites (loaded with 2, and 6 wt% functionalized and non-functionalized n-TiO_2 fibers separately) was measured with time during the curing phase as evaluated using a rheometer (AR 2000ex, TA instruments Ltd. Delaware, USA), and as described in section 2.7.1 of Chapter 2 The measurements were made at 25 ± 1 °C. The onset time of viscosity increase and curing of the setting cement were determined from the complex viscosity-versus-time curves.

The radiopacity of the nanocomposites based on both 2 and 6wt% loading of the functionalized n-TiO_2 fibers as well as the unfilled PMMA and composites reinforced with 6 wt% $BaSO_4$ were evaluated and expressed in terms of equivalent aluminum (Al) thickness according to the method described in section 2.7.3 of Chapter 2. For comparison purpose, and also to verify the evaluation method of radiopacity, specimens of bovine trabecular and cortical bones as well as human dentine and enamel were investigated with the experimental nanocomposites. From the Al step-wedge image, a calibration curve relating the logarithm of %RGB vs the logarithm of Al thickness was constructed (Figure 4.2).

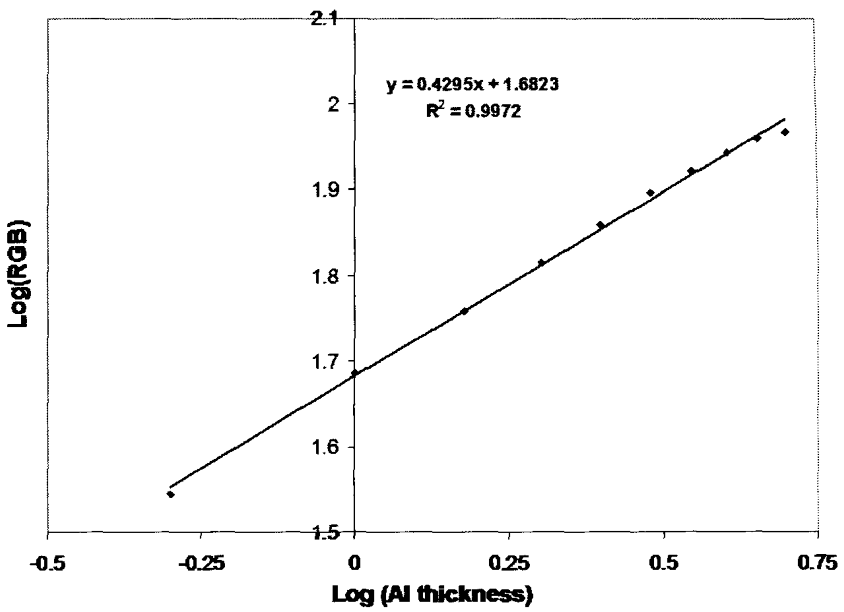

Figure 4.2. Calibration curve of % RGB versus Al thickness for measuring the radiopacity of n-TiO_2-PMMA composites.

The equivalent Al thickness (mm) for each group, which is a measure of the radiopacity was calculated from the linear regression equation (R^2=0.997) obtained from the calibration curve as presented below:

$$\log(\mathrm{Al}) = \frac{\log(\%\mathrm{RGB}) - 1.683}{0.430} \tag{4.1}$$

4.3. Results and Discussion

4.3.1. SEM

The physical morphology of the functionalized (two different extent) n-TiO_2 fibers and commercial $BaSO_4$ particles used in this work are shown in Figure 4.3 a, b, c. These micrographs show that the n-TiO_2 fibers, following different extents of functionalization, preserve their fibrous shape. (Figure 4.3 a, b), while commercial $BaSO_4$, as received, exhibits irregular shape morphology (Figure 4.3 c).

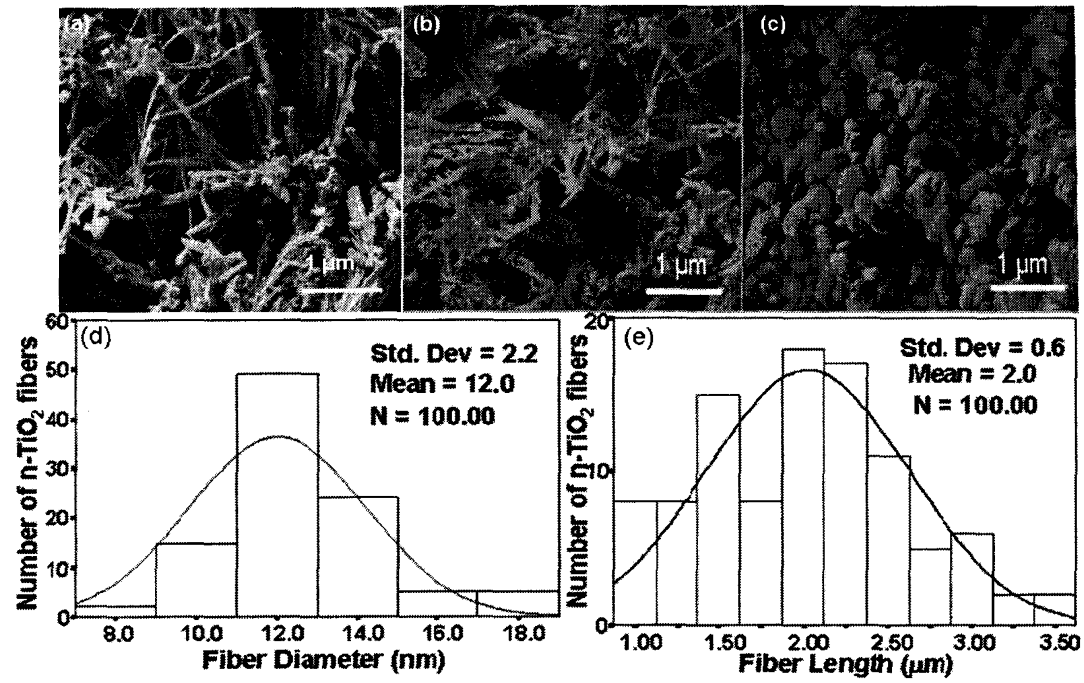

Figure 4.3. SEM: (a) 2.9% functionalized n-TiO$_2$ fibers; (b) 10% functionalized n-TiO$_2$ fibers and (c) Commercial BaSO$_4$ particles; Size distribution of the n-TiO$_2$ fibers : (d) diameter and (e) length.

The size and length of the n-TiO$_2$ fibers were analyzed from the SEM images and distributions of diameter and length were performed on the basis of 100+ n-TiO$_2$ fibers. The distributions are shown in Figure 4.3 d and e, which represent the normal distributions of both diameter and length with apparent average value of 12 nm and 2 μm respectively.

The SEM images of the fracture surfaces of the nanocomposites loaded with 2 and 6 wt% functionalized n-TiO$_2$ fibers with 10 wt% functionalization and control matrix with unfilled PMMA and 6 wt% BaSO$_4$ particles are shown in Figure 4.4. As shown in Figure 4.4 a, the unfilled PMMA matrix has smooth fracture surface without any filler in the matrix. On the other hand, the functionalized n-TiO$_2$ fibers when applied at 2 wt% loading exhibit strong adhesion with the polymer matrix, as reflected from their uniform delamination at the fracture surface (Figure 4.4 b). A significant number of fibers are also observed in the figure bridging the cracks providing additional reinforcement. However, the $BaSO_4$ particles are loosely embedded in the matrix and surrounded by a number of unbridged pores (Figure 4.4 d).

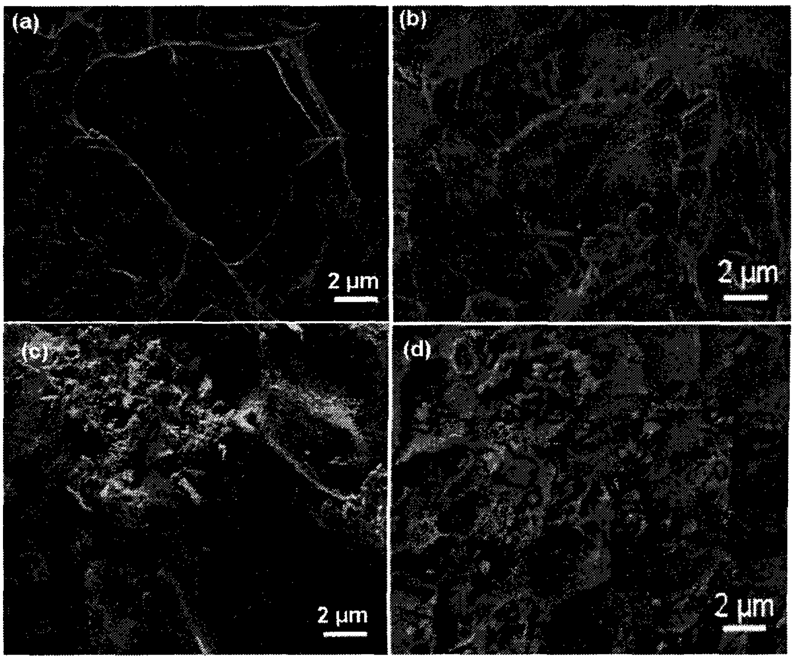

Figure 4.4. SEM of fracture surfaces: (a) Unfillled PMMA; (b) 2 wt% n-TiO_2 fibers-PMMA ; (c) 6 wt% n-TiO_2 fibers-PMMA and (d) 6 wt% $BaSO_4$-PMMA

Functionalization provides organophilicity to the n-TiO_2 fibers which resulted in strong adhesion of the nanofibers to the PMMA matrix while the $BaSO_4$ particles exhibited only a weak adhesion to the matrix. However, at 6 wt% loading, the functionalized n-TiO_2 fibers undergo agglomeration within the matrix (Figure 4.4 c).

4.3.2. TGA

The extent of functionalization of n-TiO_2 fibers was measured by TGA with Figure 4.5 showing the thermal weight loss of both nonfunctionalized and functionalized n-TiO_2

fibers. It can be seen that the nonfunctionalized n-TiO_2 fibers did not show any significant weight loss, while the functionalized n-TiO_2 fibers exhibited 2.9, 5.9, 8.5 and 10 % weight loss in the temperature range of 355 to 455 °C. This increasing weight loss corresponds to the increased amount of bonded carboxylic groups to the titania surface,[193,194] and these weight losses occurred with the pH of the reaction medium 3.85, 6.0, 5.0 and 5.5 respectively, hence determining their respective extents of functionalization. However, the total weight loss from the functionalized n-TiO_2 fibers as shown in the TGA analysis was higher than the extent of functionalization. This might be due to the loss of adsorbed water and unreacted methacrylic acid from the functionalized n-TiO_2 surface.

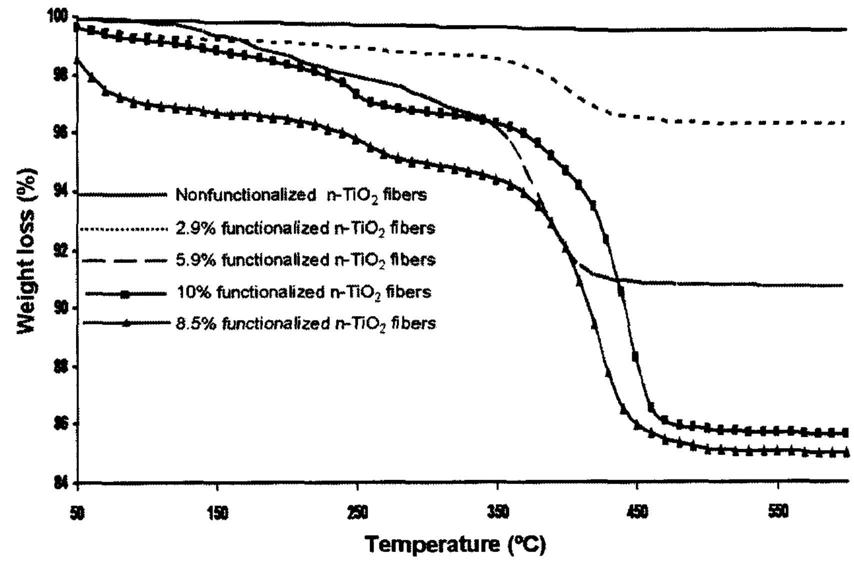

Figure 4.5. TGA curves of the non-functionalized and functionalized n-TiO_2 fibers

The carboxyl groups of the methacrylic acid attach to the surface of the n-TiO_2 fibers both by carboxylic coordination with the Ti ions and by electrostatic bonding with the surface OH^+ which predominates in acidic solution. Furthermore, dissociation of the carboxylic ions of the methacrylic acid increases with increasing pH of the media[195] from

3.85 to 5.5. Functionalization at pH 6.0 starts decreasing, which might partly be caused by the negative surface charge on the n-TiO_2 fibers over the IEP[188] and partly caused by the reaction of carboxylate ions with K^+ ions.[195] pH 5.5 was found to provide the maximum extent of functionalization among these four different pH values, which may be attributed to the optimum combination of surface charge on titania and the amount of dissociated carboxylate ions in solution.

Figure 4.6 displays the TGA and DTG curves for unfilled PMMA matrix and for nanocomposites reinforced with 2wt% n-TiO_2 fibers functionalized with 2.9 and 10 wt% carboxylic groups (as measured by TGA). The effect of the extent of functionalization of the nanofibers on the nanocomposites can be observed by the enhanced thermal stability of the nanocomposites reinforced with identical loading of nanofibers. The increased extent of functionalization on the n-TiO_2 fibers allows a higher number of polymer chains to be grown from the surface during polymerization, resulting in an increased thermal degradation temperature for the nanocomposite.[20]

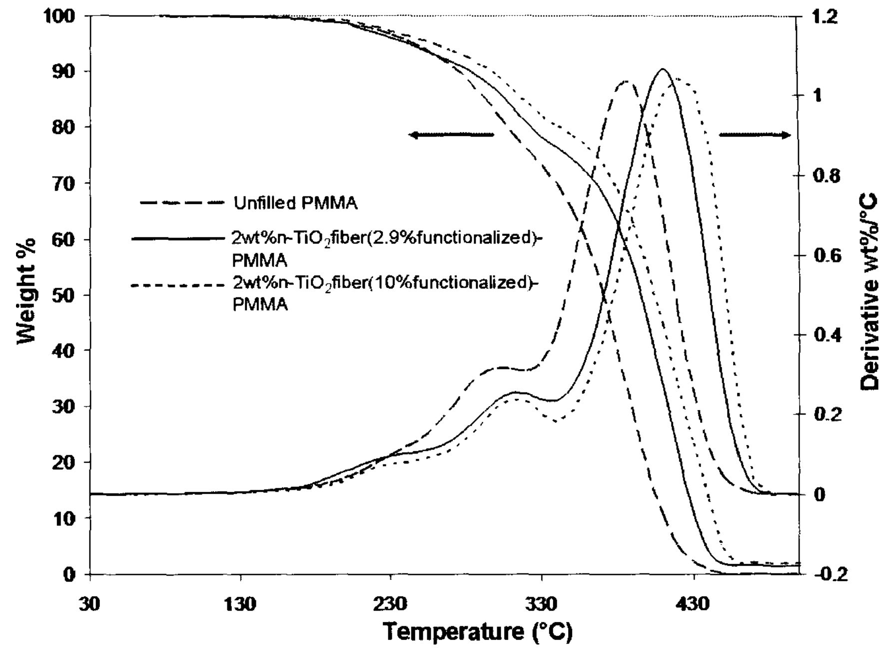

Figure 4.6. Thermogravimetric Analysis: study the degradation temperature of nanocomposites with 2wt% loading of nanofiber having different extent of functionalization.

As shown in Figure 4.6, the onset of thermal degradation increases with the extent of functionalization of the nanofibers incorporated in the PMMA matrix. The figure shows that the unfilled PMMA matrix and both the nanocomposites with different extents of functionalized nanofibers appear to have three degradation steps. The first two degradation steps have similar onset temperatures at 200 and 290 °C, which are generally attributed to the depolymerization initiated from the weak H-H linkages and the end-initiated depolymerization from the unsaturated vinyl ends, respectively.[194] The third peak as shown from the DTG curve in Figure 4.6 corresponds to the random internal scission of the polymer chains chemically attached to the titania surface.[193,194] For the nanocomposites reinforced with 2 wt% nanofibers, the onset of degradation of the polymer matrix and the temperature for 40% weight loss are increased by 7 and 5 °C respectively, while the extent of functionalization of the nanofibers increased from 2.9 to 10 wt%. The higher thermal dissociation temperature revealed from the TGA results of the nanocomposites reinforced with nanofibers having 10 wt% functionalization is attributed to the excellent interaction of the higher number of polymer chains to the titania surface.[20]

4.3.3. DSC

An enhanced thermal stability of the nanocomposites reinforced with nanofibers having 10 wt% functionalization compared to the nanocomposites with 2.9 wt% functionalization was also observed using DSC analysis. Table 4.1 shows that the nanocomposites reinforced with 2 wt% nanofibers functionalized with 2.9 wt% carboxylic groups exhibits a glass transition temperature (T_g) of 111 °C, while nanofibers with 10 wt% functionalization provide the nanocomposites with an enhanced T_g of 117 °C when loaded at 2wt%.

Table 4.1. Glass transition temperature of the composites reinforced with n-TiO_2 fibers with different extent of functionalizations.

Wt % n-TiO_2 fibers	Glass transition temperature T_g (°C)		
	Non-functionalized	2.9 wt% functionalized	10 wt% functionalized
0	106	106	106
2	90	111	117

As shown in Table 4.1, the thermal stability in terms of glass transition temperatures (T_g) of the nanocomposites also increases with the extent of functionalization of the nanofillers. Strong interfacial bonding between the nanofibers and polymer chains led to an increase of the T_g by impeding chain flexibility.[20] On the other hand, nanocomposites reinforced with 2 wt% non-functionalized n-TiO_2 fibers exhibits lower T_g than that of unfilled PMMA matrix, which is probably due to the presence of voids around the n-TiO_2

fiber/matrix interfacial area. These voids provide free mobile region for the polymer chains and results in the low T_g values of the composites.[181]

4.3.4. Dynamic Young's modulus

The enhanced interaction and strong adhesion between the functionalized n-TiO_2 fibers and PMMA matrix with a higher extent of functionalization was also confirmed by evaluating the values of dynamic young's moduli using the non-destructive ultrasonic pulse method. As shown in Table 4.2, the nanocomposite with n-TiO_2 fibers having 10wt% functionalization exhibits the highest modulus (7.22 GPa) which is significantly higher than that with non-functionalized (6.15 GPa) and 2.9 wt% functionalized n-TiO_2 fibers (6.62 GPa) at $P<0.05$.

Table 4.2. Dynamic Youngs moduli of the composites reinforced with n-TiO_2 fibers with different extent of functionalizations.

	Dynamic Young's Modulus (GPa)		
Wt % n-TiO_2 fibers	Non-functionalized	2.9 wt% functionalized	10 wt% functionalized
0	6.05 ± 0.17	6.05 ± 0.17	6.05 ± 0.17
2	6.15 ± 0.08^a	6.62 ± 0.10^b	7.22 ± 0.11^c

Mean ± 2SE, P<0.05

The ultrasonic pulse technique applies ultrasonic vibration through the test specimen with high frequency and measures the velocity of the vibration of the traveling longitudinal and transverse waves. The elastic modulus of the materials is inversely related with the velocity of the ultrasonic wave through the materials.[196] Nanocomposites with enhanced interaction and strong adhesion between the nanofillers and matrix are capable of allowing external strain through the fillers to the matrix more rapidly than those having weaker interactions.[20,21] Therefore, the higher magnitude of Young's moduli reflects the stronger adhesion between the n-TiO_2 fibers and PMMA matrix with a higher extent of functionalization.

4.3.5. Fracture toughness

Figure 4.7 a shows the K_{IC} values of the composites reinforced with 6wt% $BaSO_4$ and nanocomposites with 2, 4 and 6 wt% of n-TiO_2fibers having different extents of functionalization, as well as the unfilled PMMA matrix in dry condition.

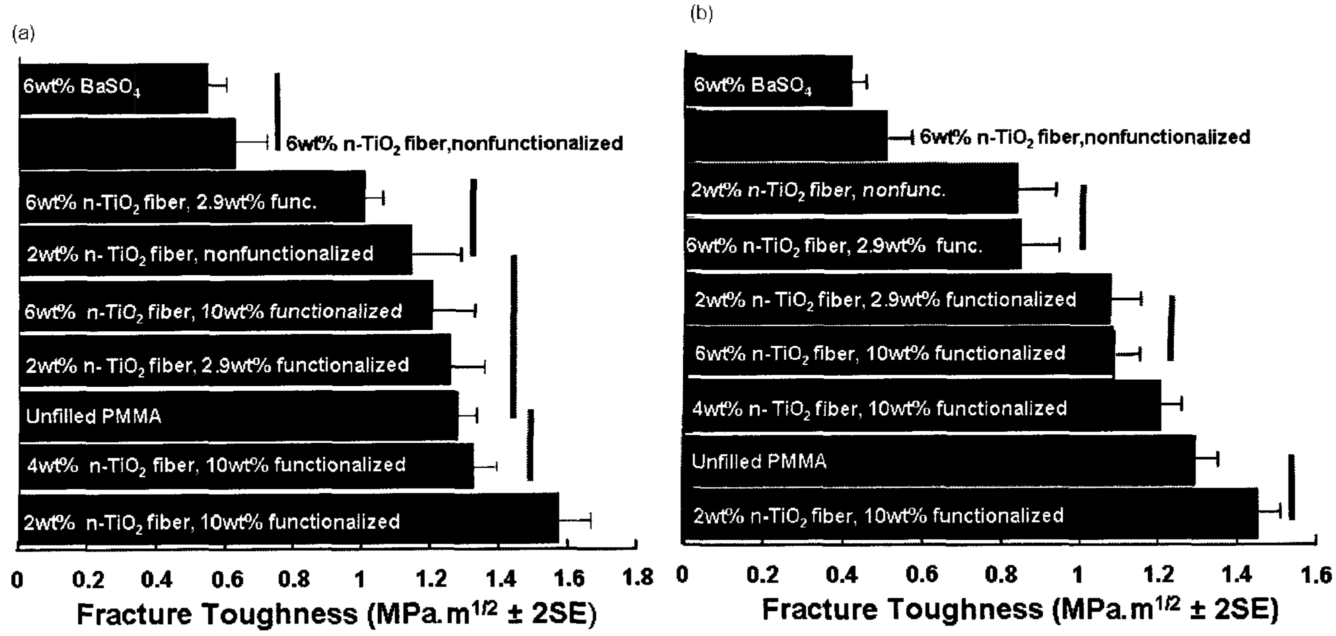

Figure 4.7. Fracture toughness of composites reinforced with n-TiO_2fibers and $BaSO_4$ (a) dry condition and (b) wet condition (a solid line connects those values which are not significantly different at $P=0.05$)

Nanocomposites reinforced with 2wt% n-TiO_2 fibers having 10wt% functionalization exhibit significantly higher values of fracture toughness amongst all other composites and the unfilled matrix at 95% level of confidence. Figure 4.7 b shows the K_{IC} of the composites reinforced with 6wt% $BaSO_4$ and nanocomposites with 2, 4 and 6 wt% of n-TiO_2 fibers having different extents of functionalizations as well as the unfilled PMMA matrix in the wet condition. Figure 4.8 shows the comparative study of the K_{IC} of the nanocomposites between dry and wet conditions at 2wt% filler loading. As shown in the figure, all the composites exhibit statistically significant difference in fracture toughness between the dry and wet conditions except the one with 2wt% n-TiO_2 fibers having 10wt% functionalization.

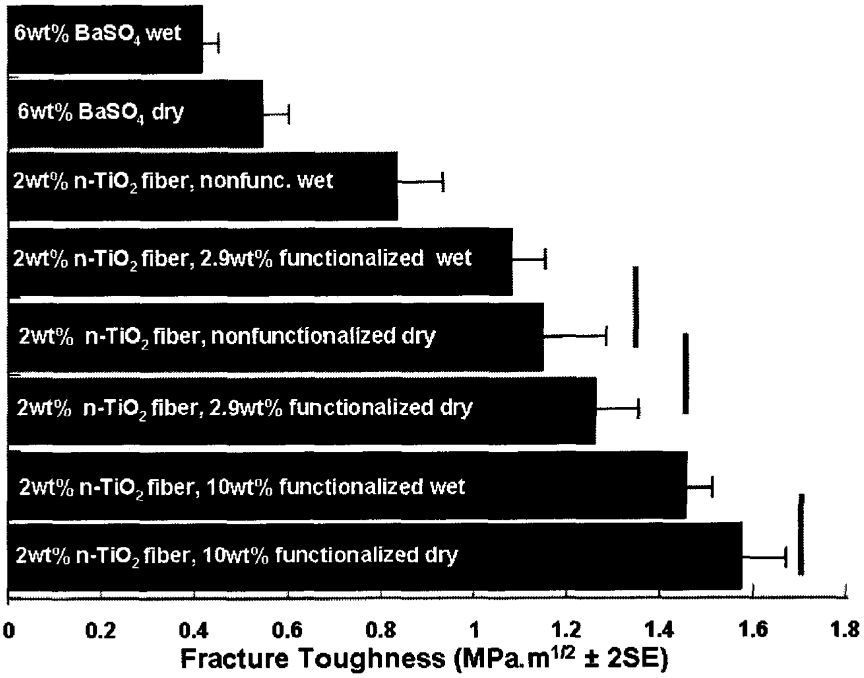

Figure 4.8. Fracture toughness of nanocomposites at 2wt% filler loading both in dry and wet conditions (P=0.05).

The K_{IC} of a material is defined by the ability of the material containing a crack to resist fracture, and in the case of bone cements this parameter reflects the reliability and defects tolerance capability of the cement.[2,197] Hence, K_{IC} is a very important property for experimental bone cements which is also affected by the morphology, dispersion and extent of functionalization of its radiopacifying fillers.[2,198] As shown in Figure 4.7 a, composite with 6wt% $BaSO_4$ exhibits significantly lower K_{IC} values compared to all other composites with functionalized nanofibers and also the unfilled PMMA matrix at

P<0.05. As reflecting from the highly magnified SEM of the fracture surface (Figure 4.9 b) there is a clear appearance of the smooth $BaSO_4$ particles protruding above the fracture surface without having any polymer matrix attached to them. This is a clear sign that the interfacial strength (adhesion) between the $BaSO_4$ particles and the matrix is poor, which accelerates debonding of the particles during tensile loading. This debonding with particle/matrix separation causes the generation of microvoids within the cement matrix.

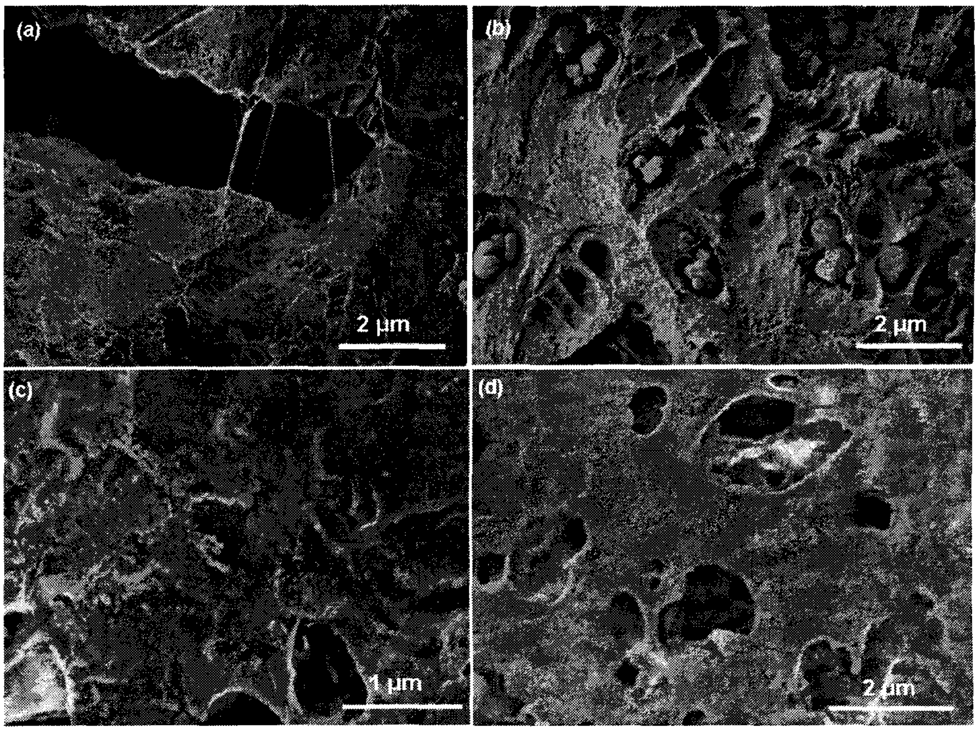

Figure 4.9. SEM with high magnification of the fracture surfaces of 2% n-TiO_2 fiber-PMMA in dry condition (a) and in wet condition (c); 6% $BaSO_4$-PMMA in dry condition (b) and in wet condition (d).

These microvoids act as stress concentrators and therefore, initiate local yielding processes during tensile loading on the cement which consequently results in the coalescence of the microvoids among themselves. Hence, the initial crack accelerates the crack propagation through the specimens.[2,198-200] This is why the composite with 6wt%

$BaSO_4$ exhibits statistically significant inferior K_{IC} values compared to the nanocomposites with functionalized nanofibers. Porosity reduction within the cement matrix minimizes the sites for crack propagation during tensile loading when measuring K_{IC}. Functionalized n-TiO_2 fibers develop improved adhesion with the PMMA matrix by chemical bonding which results in a lower number of pores generated within the matrix with an increase in K_{IC}. As shown in Figure 4.7 a, composites with 2wt% n-TiO_2 fibers having 10wt% functionalization exhibit higher values of fracture toughness, attributed to the enhanced interfacial bonding and strong adhesion between the nano-inclusion and polymer matrix. This strong interfacial interactions reduce the possibility of formation of voids in the interfacial area compared the composite with 6wt% $BaSO_4$, hence, take part in increasing the K_{IC} of the resulting composites by minimizing the sites for local stress concentrations during tensile loading.[199,200] In addition, the functionalized n-TiO_2 fibers are shown to bridge the cracks on the way of propagation of the crack and provide additional increase in K_{IC} values of the resulting composites by delaying or resisting the crack (Figure 4.9 a).[201,202] Moreover in Figure 4.9 a, n-TiO_2 fibers are shown to contain some polymer on its surface attributing to the strong interfacial bond of the polymer with the fibers.

From the wet test data as shown in Figure 4.7 b, the K_{IC} value of the unfilled PMMA matrix does not change in the wet condition because of the hydrophobicity of the net polymer matrix.[57] But in the case of the composites containing n-TiO_2 fibers and $BaSO_4$, the decrease in the K_{IC} values in the wet condition is due to the hydrophilic nature of the fillers which facilitates the absorption of water. As shown in Table 4.3, the composite with 6 wt% $BaSO_4$ exhibits the highest amount of water absorption.

Table 4.3. Percentage water uptake by the composites reinforced with n-TiO_2 fibers and $BaSO_4$ particles.

Composites	Water uptake (%)
Unfilled PMMA	1.4 ± 1.04^a
2% n-TiO_2 fiber (10% functionalized)-PMMA	1.49 ± 0.46^a
6% n-TiO_2 fiber (10% functionalized)-PMMA	2.05 ± 1.2^b
2% n-TiO_2 fiber (2.9% functionalized)-PMMA	2.04 ± 0.25^b
6% n-TiO_2 fiber (2.9% functionalized)-PMMA	3.46 ± 0.33^c
2% n-TiO_2 fiber (non- functionalized)-PMMA	3.42 ± 0.54^c
6% n-TiO_2 fiber (non- functionalized)-PMMA	3.78 ± 0.32^d
6% $BaSO_4$-PMMA	4.02 ± 0.19^e

Mean ± 2SE, P<0.05

This enhanced water absorption is due to the hydrophilic nature of $BaSO_4$ as well as the dense loading of these polar salts which allows access of the soaking medium into the inner layer of the sample. This leads to the creation of pores which act as stress concentrators during tensile loading.[57] Being organophilic in nature, functionalized n-TiO_2 fibers provide strong adhesion with the PMMA matrix which allows only a very small amount of water absorption. However, at higher loading of n-TiO_2 fibers there is an appreciable amount of water uptake due to the spatial proximity of the nanofibers, as well as agglomeration of the nanofibers within the matrix.

Absorbed water in the cement specimen should provide a plasticizing effect which increases the toughness of the materials. However, we have performed the test at room temperature keeping the wet test specimen in the dry state, which allows the entrapped water to dry, leaving channels within the specimen (Figure 4.9 c and d).

From the comparative study of the fracture toughness of composites both in the dry and wet condition (Figure 4.8), the nanocomposite with functionalized nanofibers retains its fracture toughness in the dry condition after submersion in water for one week. This is due to poor water uptake by the specimen resulting from the stronger and higher interfacial bonding between the 10wt% functionalized fibers and polymer matrix.

4.3.6. Flexural strength and modulus

Figure 4.10 compares the FS (a) and FM (b) of the composites reinforced with 6wt% $BaSO_4$ and nanocomposites with 2, and 6 wt% of n-TiO_2 fibers having different extents of functionalization in the wet condition. The nanocomposite reinforced with 2 wt% n-TiO_2 fibers having 10% functionalization exhibited the highest FS and FM which is about 25 and 96% higher respectively than both the unfilled PMMA matrix and composite with 6 wt% $BaSO_4$ particles. As mentioned in chapter 2, flexural force subjects the interface to a complex mixture of tension, compression and shear with the convex surface under tension, the concave surface under compression, and the central regions under shearing stresses.[16,203] FS and FM of the reinforced composites are mainly influenced by the transfer of applied load from the matrix to the filler.

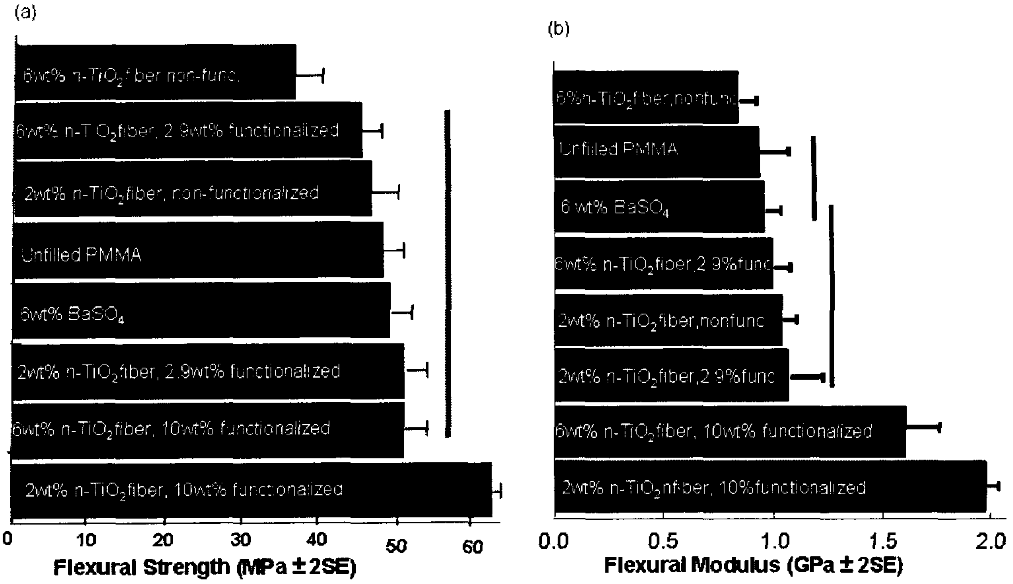

Figure 4.10: Flexural properties of composites reinforced with n-TiO_2 fibers and $BaSO_4$ particles in the wet condition: (a) Flexural strength and (b) Flexural modulus. (A solid line connects those values which are not significantly different at P=0.05)

The effectiveness of load transfer is controlled by a number of factors such as distribution and orientation of fillers within the matrix and most importantly the interfacial shear strength between the fillers and matrix. In a setting polymer system like acrylic bone cement, the interfacial shear strength is controlled to a great extent by chemical bonding between the fibers and the matrix.[204] In the case of one dimensional nano-fillers (such as nanofibers), the load is transferred from the matrix to the filler via the interfacial shear stresses between the two phases.[205] With a higher extent of functionalization, the n-TiO_2 fibers establish enhanced chemical bonds with the matrix which provides stronger interfacial shear strength between the fillers and matrix, allowing the flexural stress to be transferred effectively from matrix to fillers and vice versa.[206,207] Therefore, the flexural properties of composites increase with an increase in the functionalization of the n-TiO_2 fibers at 2wt% loading in PMMA matrix. This is shown by Figure 4.11, in which the representative force-deflection curves are provided for the composites loaded with 2wt% n-TiO_2 fibers having 0, 2.9 and 10wt% functionalization.

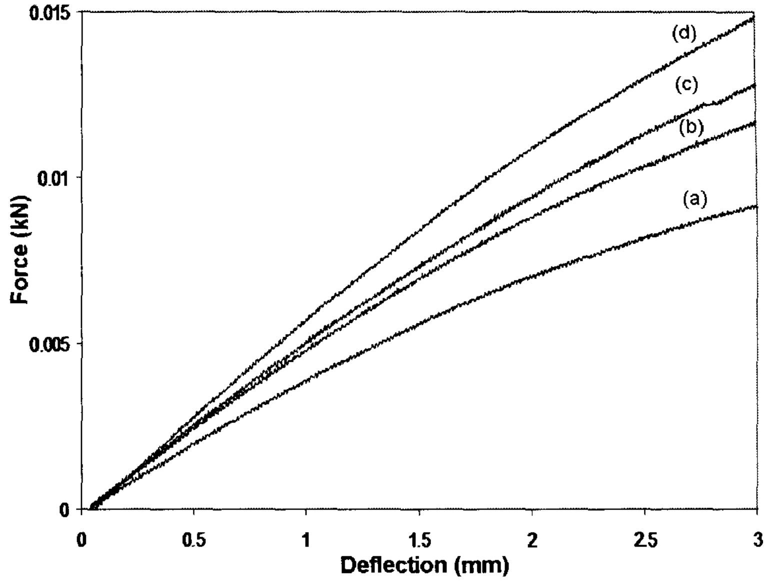

Figure 4.11: Representative force-deflection curves for the unfilled PMMA (a) and composites with 2wt% n-TiO_2 fibers with different extent of functionalization: nonfunctionalized (b), 2.9wt% functionalized (c) and 10wt% functionalized (d).

The FS and FM values of these composites were calculated as described in Chapter 2. The composites with 6wt% $BaSO_4$ exhibit a lower value of FS and FM which is due to the poor interaction and weak adhesion of the particulate fillers with the matrix, due to an absence of chemical bonding.[97] Moreover, water diffusion through the matrix accumulates at the interface causing deterioration of the flexural properties.[208] However, for composites with 6wt% functionalized n-TiO_2 fibers, the flexural properties are weak which is partly due to the agglomeration of n-TiO_2 fibers as shown in Figure 4.4 c. As well, any residual monomer from the higher monomer:polymer ratio may migrate toward the fiber surface and weaken the interfacial shear strength between the nanofibers and PMMA matrix.[208]

4.3.7. Rheology

Rheological properties of the PMMA based composite during its curing time are very important as they characterize the flow and viscoelastic behaviour of the composite throughout the period of polymerization. Rheological properties of curing cement are usually evaluated in terms of the change in complex viscosity as a function of time. Figure 4.12 shows the complex viscosity of unfilled PMMA as well as PMMA reinforced with 2 and 6 wt% n-TiO_2 fibers, each functionalized and nonfunctionalized as a function of time, one minute after the start of mixing at a temperature of 25 ± 1 °C. As shown in this figure, all the examined composites exhibit three distinct phases in the traces of complex viscosity versus time. There is an initial increase in viscosity which is followed by a plateau and then a final rapid increase in viscosity. The initial viscosity increase is due to the swelling and dissolution of the PMMA beads in liquid monomer, while the final rapid increase in viscosity is due to polymer formation through polymerization of the monomer. [26,134] At the final stage of plateau, the viscosity of the nanocomposites is the highest and the material is essentially fully cured.[25]

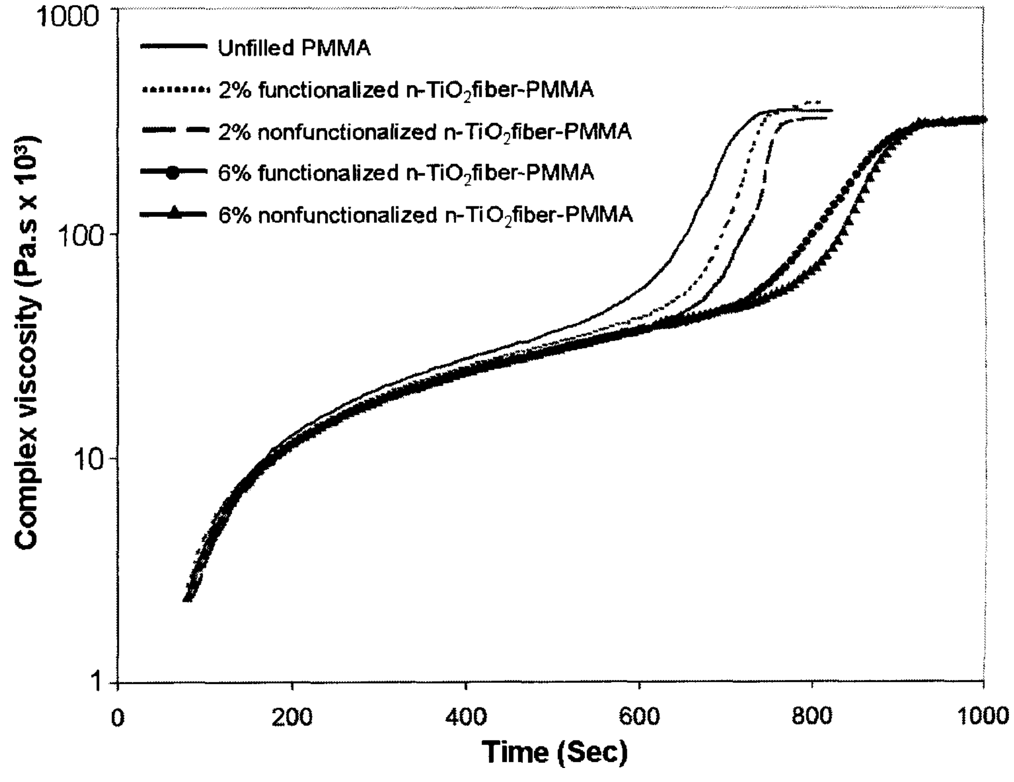

Figure 4.12: Viscosity during setting of PMMA composites.

There are two important rheological or flow characteristics that can be obtained from the complex viscosity-time curves: 1) the onset time t_{ons}, is the time for the PMMA beads to dissolve and swell in monomer controlling the viscosity increase, which can be calculated as the time at which the intersection between the linear fits of the initial and final stages of the complex viscosity is produced, and 2) the time when the cement mass reaches the plateau of the highest viscosity, called the curing time, t_{cure}.[133,134,209] As shown in Figure 4.12, the unfilled PMMA exhibits the highest initial viscosity and reaches the final plateau faster than for any of the composites, while the viscosity of the reinforced PMMA decreases with increasing incorporation of n-TiO_2 fibers. With the incorporation of n-TiO_2 fibers in the PMMA matrix, the polymer to liquid monomer ratio (P/M) of the composites decreases in order to maintain a fixed ratio of powder (prepolymerized beads + n-TiO_2 fibers) to liquid, which leads to a proportionate reduction of the amount BPO in the powder part. Therefore, incorporation of n-TiO_2 fibers contributes to the presence of residual monomer which leads to the initial lower viscosity and elongated t_{ons} and t_{cure} of the reinforced PMMA as listed in Table 4.4.[33,137]

Table 4.4. t_{ons} and t_{cure} of the unfilled PMMA and the n-TiO_2 fiber-PMMA composites.

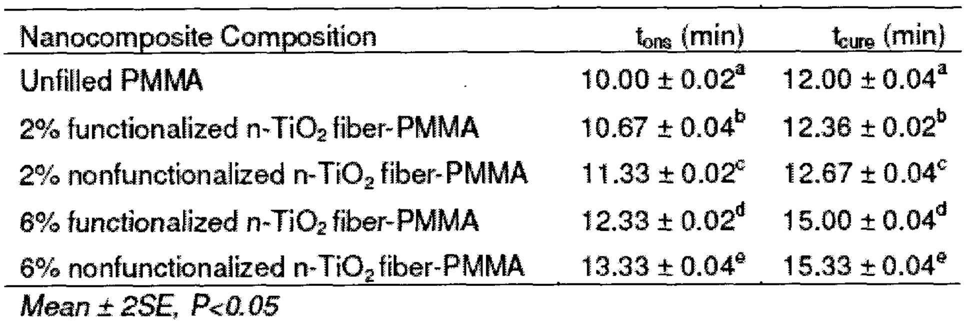

Nanocomposite Composition	t_{ons} (min)	t_{cure} (min)
Unfilled PMMA	10.00 ± 0.02^{a}	12.00 ± 0.04^{a}
2% functionalized n-TiO_2 fiber-PMMA	10.67 ± 0.04^{b}	12.36 ± 0.02^{b}
2% nonfunctionalized n-TiO_2 fiber-PMMA	11.33 ± 0.02^{c}	12.67 ± 0.04^{c}
6% functionalized n-TiO_2 fiber-PMMA	12.33 ± 0.02^{d}	15.00 ± 0.04^{d}
6% nonfunctionalized n-TiO_2 fiber-PMMA	13.33 ± 0.04^{e}	15.33 ± 0.04^{e}

Mean ± 2SE, $P<0.05$

With the same percentage loading, the non-functionalized n-TiO_2 fiber provides longer t_{ons} and t_{cure} to the PMMA matrix when compared to that provided by the functionalized

(10wt%) n-TiO_2 fibers as revealed from Table 4.4. Functionalization provides compatibility to the n-TiO_2 fiber surfaces with the liquid monomer. This enhanced compatibility reduces the amount of MMA required to achieve sufficient wetting of the fillers, so the mixing step is faster and thus the t_{ons} is significantly reduced with respect to the composites with non-functionalized n-TiO_2 fibers at $P<0.05$.[210] In addition, functionalized n-TiO_2 fibers may provide more reactive sites and establish strong adhesion with the growing polymer chains during polymerization which leads to the higher observed final viscosity and shorter t_{cure} of the curing composites.[211,212] Moreover, non-functionalized n-TiO_2 fibers when loaded at higher wt.%, facilitate pore formation within the matrix resulting from the poor interfacial adhesion with the matrix. Air or oxygen entrapped within these pores may inhibit the polymerization of monomer. This results in the presence of more unreacted monomer which contributes to the elongated t_{ons} and t_{cure} for these composites.[213,214] As studied by W. Bonfield *et al.*[215], the increase in residual monomer with percentage loading of functionalized and non-functionalized n-TiO_2 fibers can also be evidenced by the FTIR spectra of the surface of the curing composites at 10 and 12 minutes after mixing, which is shown in Figure 4.13. The residual monomer is shown by the absorption peak at 1637 cm^{-1}, confirming the presence of the C=C bond of the unreacted MMA.[215,216] As shown in this figure, the liquid MMA exhibits the highest peak at 1637 cm^{-1} showing the presence of the unsaturated C=C bond.

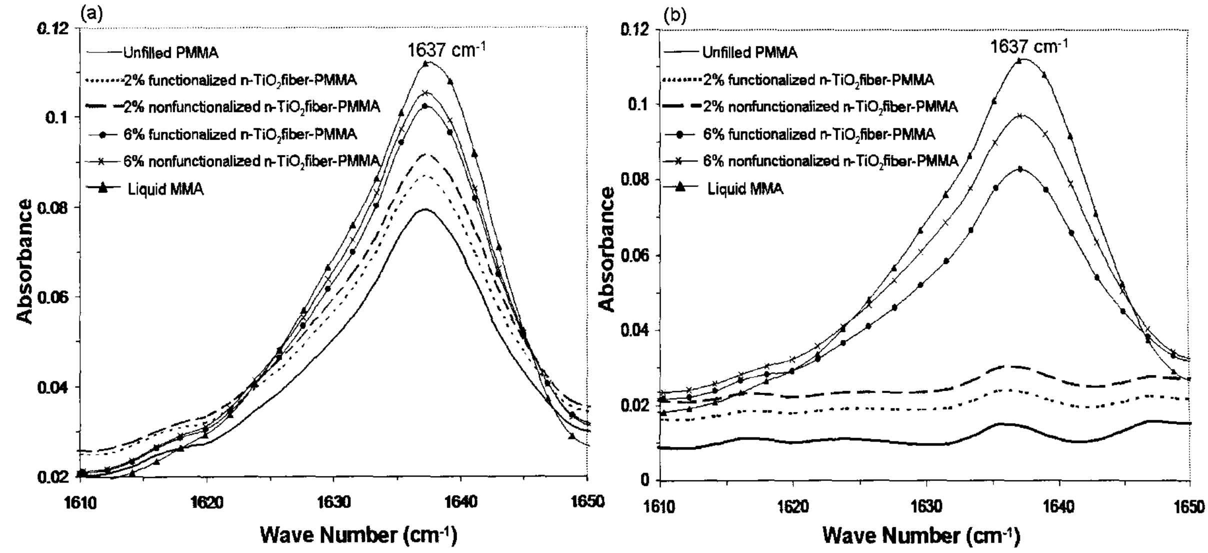

Figure 4.13. IR spectra of different composites to monitor the unreacted monomer with different time: (a) after 10 minutes and (b) after 12 minutes.

After 10 minutes of mixing time, the unfilled PMMA matrix reaches the onset stage for viscosity increase with the initiation of the polymerization reaction (Figure 4.13 and Table 4.4), while the other composites remain in the wetting phase resulting from the decreased P/M ratio. This is why the unfilled PMMA shows a comparatively lower absorption peak than the other composites at 1637 cm^{-1} (Figure 4.13 a). On the other hand, unfilled PMMA reaches its curing stage after 12 minutes, while composites with 2 % functionalized and non-functionalized n-TiO_2 fibers remain in the polymerization stage (Table 4.4). Hence, all of these composites exhibit a much lower amount of residual MMA compared to that measured after 10 minutes. However, the composites with 6wt% functionalized and non-functionalized n-TiO_2 fibers exhibit a substantial amount of unreacted C=C after 12 minutes, as they are still in the wetting phase at this time (Table 4.4). One of the limitations of this experimental technique is that it measures the amount of unreacted monomer from the surface of the sample only, and not in the bulk of the material. However, it provides a qualitative indication of the residual monomer in the composites.[215]

4.3.8. Radiopacity

In order to evaluate the efficacy of the n-TiO_2 fiber-PMMA composites as bone cement, the radiopacity of the composites was measured. The radiopacity values in Al equivalent of 1mm specimen thickness for all composites, as well as human dentine and enamel, and bovine cortical and trabecular bones are presented in Figure 4.14.

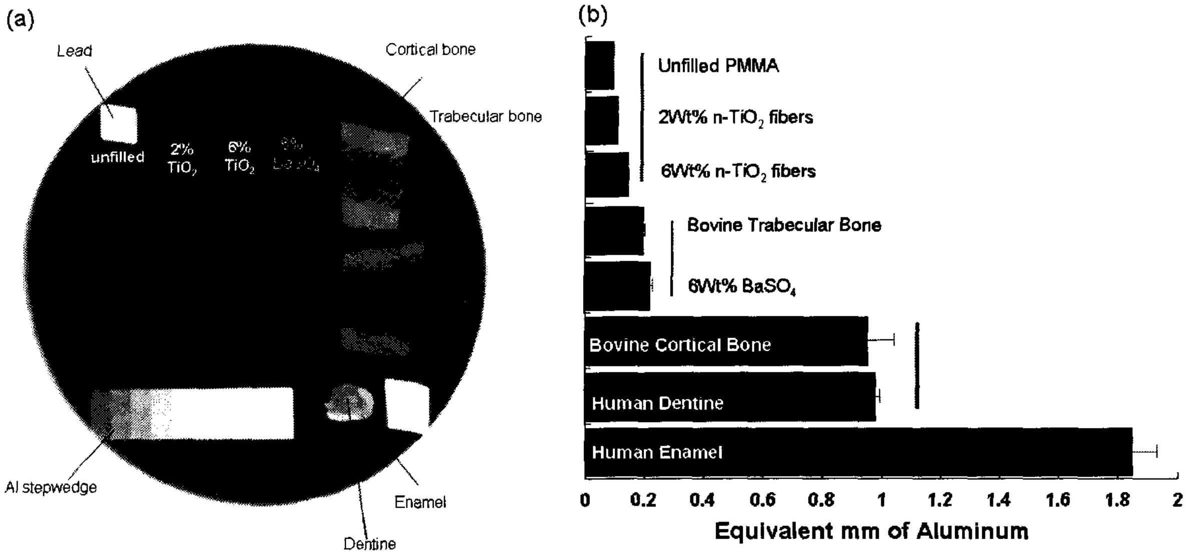

Figure 4.14: (a) X-ray image of different composites and (b) Radiopacity of different composites expressed in terms of equivalent Al thickness (P=0.05).

The statistical rank order test was able to separate the eight different materials into four significant groups at P=0.05. The radiopacity values for human enamel and dentine were around 2 and 1mm respectively, agreeing previously published values.[27,217] There was no significant difference between the radiopacity values for bovine cortical bone and human dentine at P>0.05. Similarly, there was no significant difference between bovine trabecular bone and composite containing 6wt% commercial $BaSO_4$ at $P>0.05$. It can also be seen that unfilled PMMA and nanocomposites reinforced with 2wt% and 6wt% TiO_2 were not significantly different ($P>0.05$) and exhibited the lowest level of radiopacity amongst the groups.

The radiopacity of an atom depends on its capacity of attenuating the array of X-ray photons via the photoelectric effect. As mentioned in equation (2.17), the degree of X-ray attenuation is influenced by the density of the atoms as well as the energy of the X-ray photons.[29,138] X-ray photons can be readily attenuated by an atom when its energy is close to the energy necessary to lift a K-electron from the atom.[29,138,218] The energy necessary to lift a K-electron is often called the K-edge energy and is specific for each atomic species,[138] i.e. 4.9 keV for Ti and 37.4 keV for Ba.[138,219] The energy distribution used in this work gives rise to a peak of photons with energies at about 30 keV, hence being closer to the K-edge energy of Ba than Ti. To obtain maximum attenuation or maximum radiopacity, *a tube voltage setting of below 30 kV would be necessary in the case of* TiO_2. This is much lower than the voltage normally used in medical radiology, and explains why barium sulfate is more radiopaque than TiO_2 at the voltages normally employed. Conversely, using the same X-ray source, the radiopacity of the nanocomposites can be noticeably increased by incorporating the n-TiO_2 fibers at high %loading, e.g. over 6wt%. However, this higher amount of loading would impose a negative effect on its mechanical and rheological properties.

4.4. Conclusion

n-TiO_2 fibers were successfully incorporated into the PMMA matrix as reinforcing agents to produce nanocomposites. Nanofibers with higher extents of functionalization established stronger interfacial adhesion with the polymer matrix, which was confirmed by the microscopic analysis of the fracture surfaces of the nanocomposites. The firm interfacial shear strength was also been confirmed by thermogravimetric, glass transition temperature and dynamic Young's modulus analyses of the produced nanocomposites. The effect of the strong and enhanced interfacial adhesion between the nanofibers and matrix on the bulk properties of the composites was studied in terms of the strength and toughness of the resulting composites. It was found that 2wt% n-TiO_2 fibers with an increased extent of functionalization (10wt %) provided the highest magnitude of K_{IC} and FS, both in the dry and wet conditions. The handling characteristics of the nanocomposites during its setting phase were also shown to be influenced by the nanofibers with an enhancement of its curing time. However, with the optimum incorporation (2wt %) of n-TiO_2 fibers, the nanocomposites did not exhibit sufficient radiopacity with the standard X-ray exposure available for medical treatment.

Chapter 5: Preparation and characterization of PMMA based composites reinforced with titania nanotubes

This chapter describes the effect of nanosized titania tubes on the physical and mechanical properties of poly(methyl methacrylate) (PMMA) for application as orthopaedic bone cements. Part of this chapter has been reproduced from an article submitted to Acta Biomateriallia with the title: "Synthesis and Characterization of PMMA Based Composites Reinforced with TiO_2-SrO Nanotubes."

Nanostructured titania tubes (n-TiO_2 tube) were compatibilized with a PMMA matrix by functionalization of the n-TiO_2 tubes using the bi-functional coupling agent, MA. Functionalization was confirmed by IR analysis. Uniform dispersion of the rigid n-TiO_2 tubes in the PMMA matrix was investigated by TEM analysis. Strong interfacial bonding between the functionalized n-TiO_2 tubes and PMMA matrix was evidenced by an increased thermal degradation temperature, glass transition temperature and dynamic Young's modulus of the resulting nanocomposites. Based on the determined mechanical properties of resulting nanocomposites reinforced with 2, 4 and 6 wt% n-TiO_2 tubes, an optimum condition was achieved at 2wt% loading, which provided a significant enhancement of the K_{IC} (12%) and FS (15%) compared to that exhibited by the optimum loading of n-TiO_2 fibers at $P<0.05$. Higher aspect ratios and the hollow tubular shape allows the n-TiO_2 tubes to transfer the interfacial shear stress more effectively than using n-TiO_2 fibers, making it an efficient reinforcing agent for the PMMA matrix. However, while characterizing the bone cement, the resulting nanocomposites did not exhibit sufficient radiopacity with the standard medical X-ray.

5.1. Introduction

The deleterious effects imparted by inorganic X-contrast agents to clinical PMMA based bone cements results from the poor wetting and weak interfacial bonding between these inorganic fillers and the non-polar polymer matrix.[16,220] These lower properties facilitate implant failure resulting from bone resorption, thus adversely affecting the clinical life of the cemented arthroplasty.[28,221] As mentioned in Chapter 1, many studies have tried to enhance the mechanical properties of bone cements by incorporating different additives. However, the large size of the fillers, poor filler-bone cement matrix bonding (and subsequent debonding), non-uniform filler material distribution, and function of the pores as stress concentration sites are among the reasons why these efforts have been less than ideally successful.[99,222] Nanotechnology provides a new avenue to develop composites with a combination of superior mechanical and physical properties. We have investigated the reinforcing effect of nanostructured titania fibers on the PMMA matrix in Chapter 4, achieving enhanced mechanical properties resulting from the strong interfacial adhesion of functionalized n-TiO_2 fibers with the polymer matrix. This investigation inspired us to incorporate nanostructured titania tubes having higher aspect ratios than the nanofibers into the PMMA matrix. Moreover, the hollow structure of the nanotube provides additional interlocking with the matrix through both the interior and exterior surfaces of the tubes. In order to establish chemical bonds between the n-TiO_2 tubes and PMMA matrix, we have functionalized the surface of the n-TiO_2 tube by following the techniques as described in Chapters 3 and 4.

5.2. Experimental details

5.2.1. Materials

The n-TiO_2 tubes were synthesised using the alkaline hydrothermal technique in accordance with the work studied by Kasuga *et. al.*[129,223] 2-propanol, MA (99.99%, Sigma-Aldrich) and MMA monomer (95.9 wt %) containing a butanediol dimethacrylate cross-linker (4 wt %) and activator (0.1 wt %) were used as received (Ivoclar Vivadent). PMMA beads (99.2 wt %, Ivoclar Vivadent) having an average particle diameter of 57.5 μm (as measured by laser diffraction using a Malvern Mastersizer 2000), an average molecular weight of 207 kDa (as measured by gel permeation chromatography, see appendix 2) with a free radical initiator BPO (0.8 wt %) were used as received.

5.2.2. Functionalization of n-TiO_2 tubes

The synthesised nanotubes as prepared by Kasuga *et. al.*[129], was layered hydrogen titanate having possible molecular structure of $H_2Ti_3O_7$ or $H_2Ti_2O_4(OH)_2$ as confirmed by other researchers.[224-226] The layered hydrogen titanate was converted to anatase TiO_2 with tubular morphology after calcination in air at 400 °C.[227,228]

In order to functionalize the surface of the n-TiO_2 tubes, 0.1 g of calcined powder was dispersed in 35 mL of 2-propanol with the aid of ultrasonic agitation, followed by reacting with 3 mL of MA at 80-85 °C for 24 hours with constant stirring. The reaction was carried out at different pH's of 5.0, 5.5 and 6.0 (as measured by pH meter UWR SB301) adjusted by adding a few drops (5-12 drops) of potassium hydroxide solution (0.3 N) to the reaction mixture prior to the reaction, which yielded different extents of functionalization.

5.2.3. Preparation of n-TiO_2 tube-PMMA composites.

The nanocomposites were prepared by mixing the powder and liquid parts according to the procedure described in Section 2.6.2 of Chapter 2. Nanocomposite specimens with 2, 4 and 6.0 wt% loading of functionalized nanotubes were prepared for determination of the mechanical properties. Moreover, control specimens were prepared using the unfilled PMMA.

5.2.4. Characterization of nanotubes and nanocomposites

The crystalline phase of the anatase n-TiO_2 tubes was examined by X-ray diffraction (XRD, Rigaku-Geigerflex CN2029, Rigaku corp. Tokyo, Japan) utilizing CuKα1 + Kα2 radiation with a power of 40kVx35mA.

The functionalization of the n-TiO_2 tubes was investigated by Fourier transform infrared spectroscopy (FTIR, Bruker IFS 55, Bruker Optic Inc. Ettlingen, Germany) using KBr pellet form with an attached MCT detector.

The morphology of the functionalized n-TiO_2 tubes and the micrographs of the fracture surfaces of the cements after fracture toughness testing were obtained using a scanning electron microscope (SEM, LEO 1540XB, Zeiss, Oberkochen, Germany) at an accelerating voltage of 1 kV. The microstructure of the functionalized n-TiO_2 tubes was also confirmed by transmission electron microscope (TEM, Philip CM10, AMT digital camera, Eindhoven, Netherlands) operated at an accelerating voltage of 100 kV. Moreover, the diameter and length of the n-TiO_2 tubes were measured from the electron micrographs using Image J software on the basis of a minimum of 100+ nanotubes.

The extent of functionalization of the n-TiO_2 tubes was investigated by using TGA, which was performed using a Q600 TA instrument (Delaware, USA) from 25 to 600 °C at a heating rate of 20 °C/min under air.

The interfacial adhesion between the functionalized n-TiO_2 tubes and the polymer matrix was also investigated by measuring the thermal degradation temperature of the resulting nanocomposites using TGA in the Q600 TA instrument from 25 to 600 °C under nitrogen atmosphere.

The interfacial bond strength was further tested by measuring the dynamic Young's modulus of the nanocomposite specimens by the ultrasonic pulse method as described in Chapter 2.

K_{IC} of the nanocomposite specimens (loaded with 2, 4 and 6% of functionalized n-TiO_2 tubes) was determined using the notchless triangular prism (NTP) method as described in Chapter 2.

FS and FM of the nanocomposites were determined by the three point bending test as described in Chapter 2.

The rheological behaviour of the n-TiO_2 tube-PMMA composites (loaded with 2 and 6 wt% functionalized and non-functionalized n-TiO_2 tubes) with time during the setting of the composites was evaluated by a rheometer (AR 2000ex, TA instruments Ltd. Delaware, USA), as described in Chapter 2.

The radiopacity of the nanocomposites based on 2 wt% loading of the functionalized n-TiO_2 tubes were evaluated and expressed in terms of equivalent aluminum (Al) thickness according to the method described in Chapter 2, with the calibration curve and regression equation described in Chapter 4.

5.3. Results and Discussion

5.3.1. XRD and FTIR

The X-ray diffraction of the calcined hydrogen titanate nanotube is shown in Figure 5.1 a, which represents the crystallinity of the product. The diffraction peaks correspond to the anatase crystalline phase of TiO_2.[226,229] Therefore, it is obvious that, hydrogen titanate converts to anatase TiO_2 after heat treatment at 400 °C. The FTIR spectra of the functionalized TiO_2 is shown in Figure 1b, which exhibits several absorption peaks at 1547, 1442 and 1413cm^{-1} which are due to the bidentate coordination between the titanium atom and the carboxylic group of MA.[20,165] There is also a peak at 1630 cm^{-1}, which corresponds to the vinyl (C=C) bond of the MA. Moreover, the peak at 1344 cm^{-1} is attribute to the alkyl group of the MA and the peak at 1709 cm^{-1} is attributed to the C=O bond of the unreacted MA.

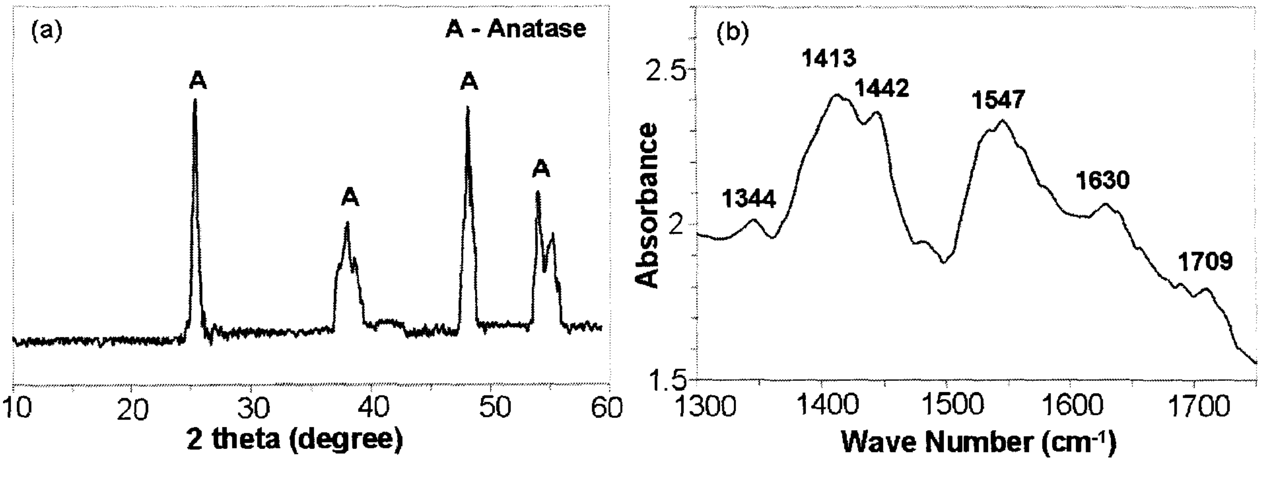

Figure 5.1. (a) X-ray diffraction of n-TiO_2 tubes and (b) FTIR spectra of functionalized n-TiO_2 tubes.

Therefore, n-TiO_2 tubes became functionalized with methacrylic acid with its carboxylic group co-ordinated to the titania surface, while its organofunctional group (C=C) establishes covalent bond with the polymer chains during polymerization.

5.3.2. SEM and TEM

The micrographs obtained by SEM and TEM exhibit the physical morphology of the functionalized n-TiO_2 which are shown in Figure 5.2 a and b, respectively. These micrographs show that the n-TiO_2 following functionalization preserve its hollow tubular shape. Moreover, the statistical distribution of the diameter and length of the n-TiO_2 tubes, as obtained by SEM, exhibit a normal behaviour with mean values of 8 nm and 1.67 µm, respectively (Figure 5.2 c and d).

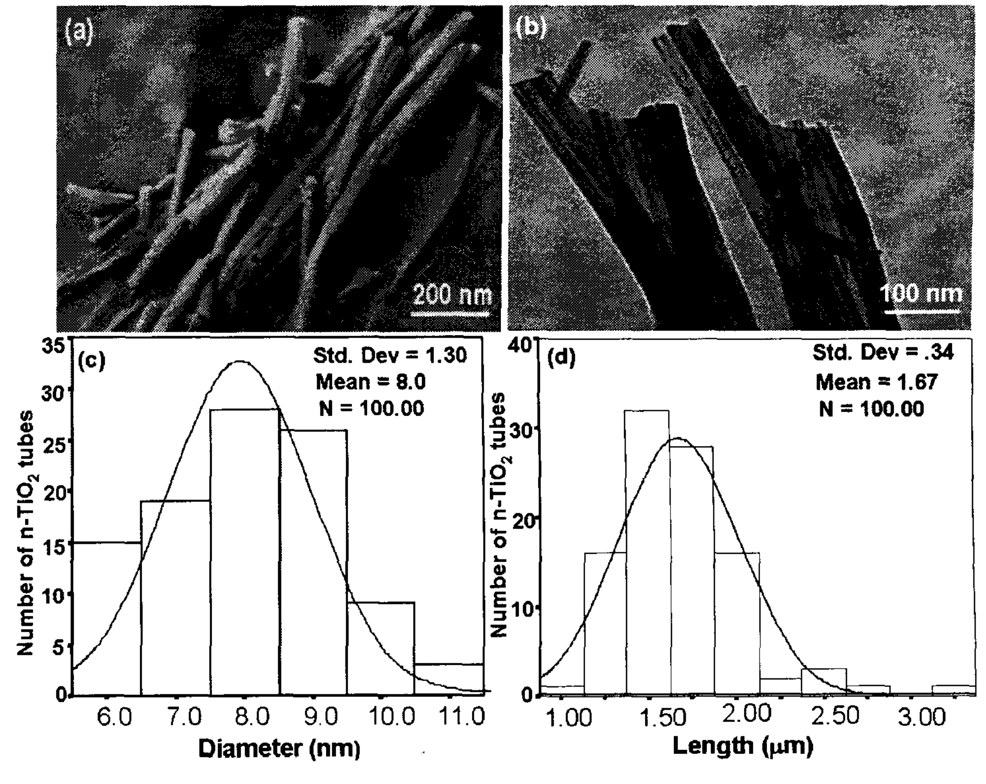

Figure 5.2. Electron microgrpahs of the functionalized n-TiO_2 tubes: (a) SEM (b) TEM; Size distribution of the n-TiO_2 tubes: (c) diameter and (d) length.

Figure 5.3 displays additional electron micrographs showing the dispersion of the n-TiO_2 tubes in the PMMA matrix (received after the K_{IC} test). The SEM of the fracture surface of the composites reinforced with 2 and 6 wt% functionalized n-TiO_2 tubes as shown in

Figure 5.3 a and b, reveals that the n-TiO_2 tubes when loaded at 2% disperse homogeneously in the composite with strong adhesion with the matrix (Figure 5.3 a). However, at 6wt% loading, the n-TiO_2 tubes agglomerate within the matrix (Figure 5.3 b). This behaviour can also be observed by the TEM images of the nanocomposites reinforced with 2 and 6wt% functionalized n-TiO_2 tubes as shown in Figure 5.3 c and d, respectively, which were taken from the ultra-microtomed surface of the composites.

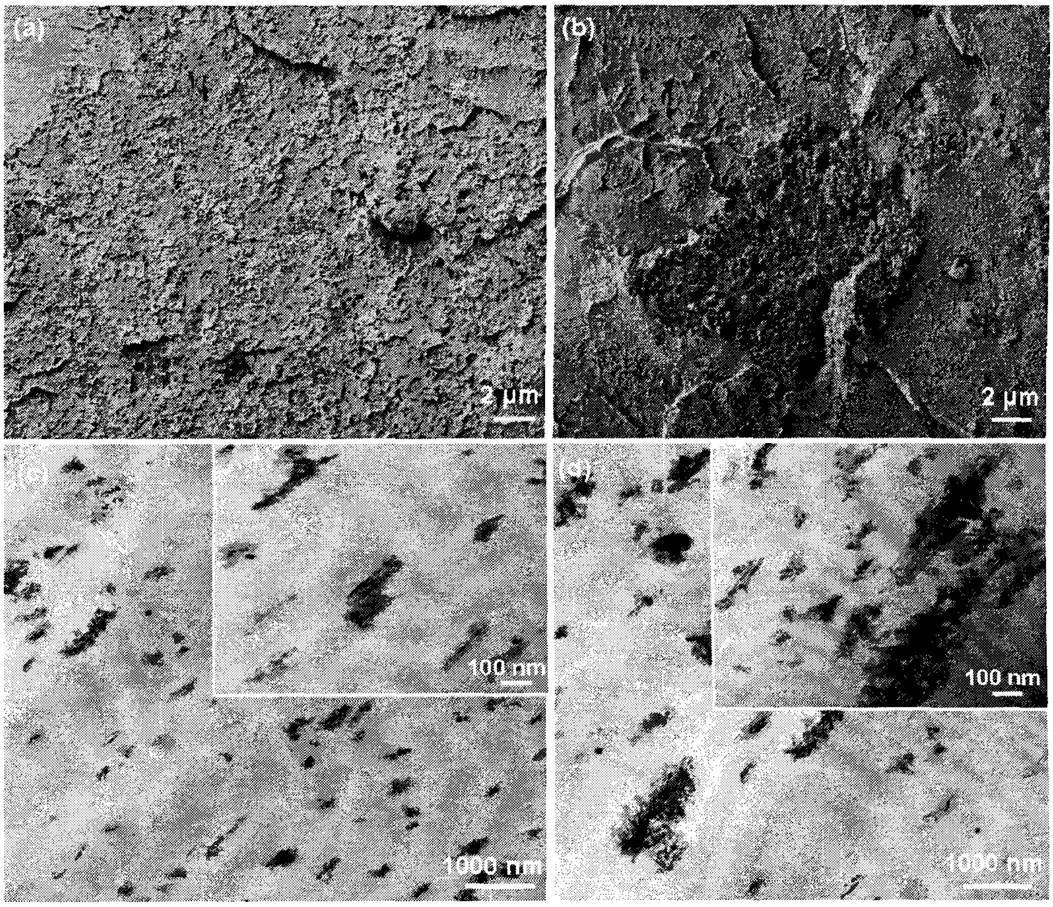

Figure 5.3. SEM of the fracture surfaces of PMMA matrix reinforced with: (a) 2 % functionalized n-TiO_2 tubes and (b) 6% functionalized n-TiO_2 tubes; TEM of the microtomed slice of the PMMA matrix reinforced with :(c) 2 % functionalized n-TiO_2 tubes and (d) 6% functionalized n-TiO_2 tubes. The insets are the ones with higher magnification.

5.3.3. TGA

The functionalization of the n-TiO_2 tubes was quantitatively evaluated by TGA as shown in Figure 5.4 a. The non-functionalized n-TiO_2 tube sample showed negligible weight loss, while the functionalized n-TiO_2 tubes exhibited 10 % weight loss in the temperature range of 355 to 455 °C, corresponding to removal of the bonded carboxylic groups from the titania surface.[193,194]

TGA also provides an effective way to test the thermal stability of the material by investigating the degradation (weight loss) of the material with temperature.[230,231] Figure 5.4 b shows the traces of weight loss and rate of weight loss (DTG) with temperature of the unfilled PMMA matrix as well as the PMMA reinforced with 2 wt% non-functionalized n-TiO_2 tubes and functionalized (10% functionalization) n-TiO_2 tubes. As shown in the figure, the nanocomposites exhibit higher thermal stability compared to the unfilled PMMA, which is revealed from the higher onset temperature of degradation of the resulting composites. The DTG traces of both the unfilled matrix and the nanocomposites show three peaks, amongst which the peak in the temperature range of 350-450 °C is attributed to the random scission of the long polymer chains entangled within the matrix.[193,194]

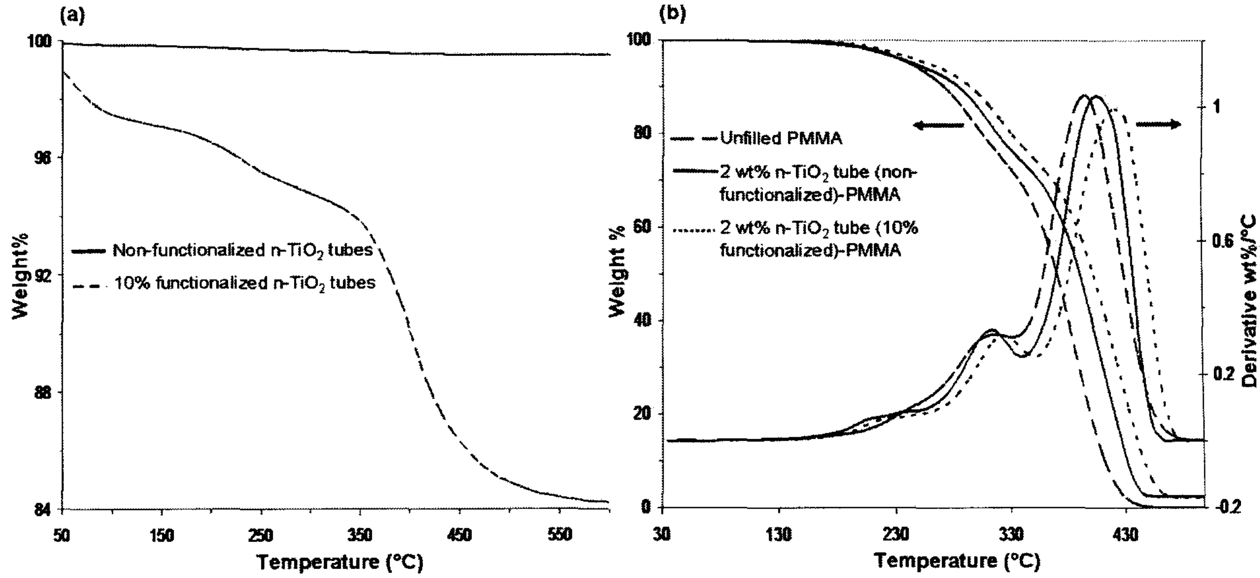

Figure 5.4. Thermogravimetric analysis: (a) Functionalized n-TiO_2 tubes and (b) Thermal degradation of unfilled PMMA and n-TiO_2 tube-PMMA composites.

The average temperature of this degradation increased by 12 and 24 °C for the composites reinforced with 2wt% non-functionalized and functionalized n-TiO_2 tubes, respectively, compared to the unfilled matrix. High aspect ratios (L/D = 209) and hollow tubular morphology allow the n-TiO_2 tubes to interact with the polymer chains through physical interlocking providing a barrier effect to the polymer molecules evaporated during the thermal degradation. In the case of functionalized n-TiO_2 tubes, this effect becomes more pronounced as the functionalized n-TiO_2 tube establishes strong adhesion with the polymer chains through chemical bonds. This additional bonding renders much stronger hindrance to the polymer during degradation compared to that provided by the non-functionalized n-TiO_2 tubes.[20,230,231] These TGA results reveal that functionalization provides stronger and enhanced interfacial adhesion between the n-TiO_2 tubes and matrix which in turn leads to effective reinforcement of the composites.

5.3.4. Dynamic Young's modulus

Non-destructive ultrasonic techniques as used to determine the dynamic elastic modulus are an effective method to analyze the discontinuity within a material.[21,152] Thus, it reflects the interfacial adhesion of the nanofillers with the matrix as well as the isotropy of the composites.[20-22] As explained in Chapter 2, the ultrasonic pulse technique involves the transmission of an ultrasonic wave within the test specimen, which propagates through the vibration of the particles within the matrix. The faster the wave propagates, the higher the value of dynamic elastic modulus of the composite. Strong interfacial bonding between the filler and matrix provides strong adhesion allowing the effective transfer of the interfacial shear strength from the fillers to the matrix and vice versa.[20] The values of dynamic Young's moduli of the unfilled PMMA as well as the PMMA reinforced with 2 wt% of non-functionalized and functionalized n-TiO_2 tubes are shown in Table 5.1. Nanocomposites reinforced with functionalized n-TiO_2 tubes exhibits the highest value of dynamic Young's modulus, which is significantly higher than that exhibited by the composites with non-functionalized n-TiO_2 tubes and unfilled PMMA at $P<0.05$.

Table 5.1. Dynamic Youngs moduli of the composites reinforced with non-functionalized and functionalized n-TiO_2 tubes

Wt % n-TiO_2 tubes	Dynamic Young's Modulus (GPa)	
	Non-functionalized	Functionalized
0	6.05 ± 0.07	6.05 ± 0.07
2	6.5 ± 0.2[a]	7.55 ± 0.08[b]

Mean ±2SE, P<0.05

Strong interfacial adhesion between the functionalized n-TiO_2 tubes and the PMMA matrix allows the ultrasonic wave to propagate more effectively and faster than that reinforced with non-functionalized n-TiO_2 tubes.

5.3.5. Fracture toughness

As described in Chapter 4, K_{IC} is a very important material property, which reflects the ability of the material to absorb fracture energy before breaking. Figure 5.5 shows the K_{IC} of the PMMA based composites reinforced with 2, 4 and 6 wt% functionalized n-TiO_2 tubes.

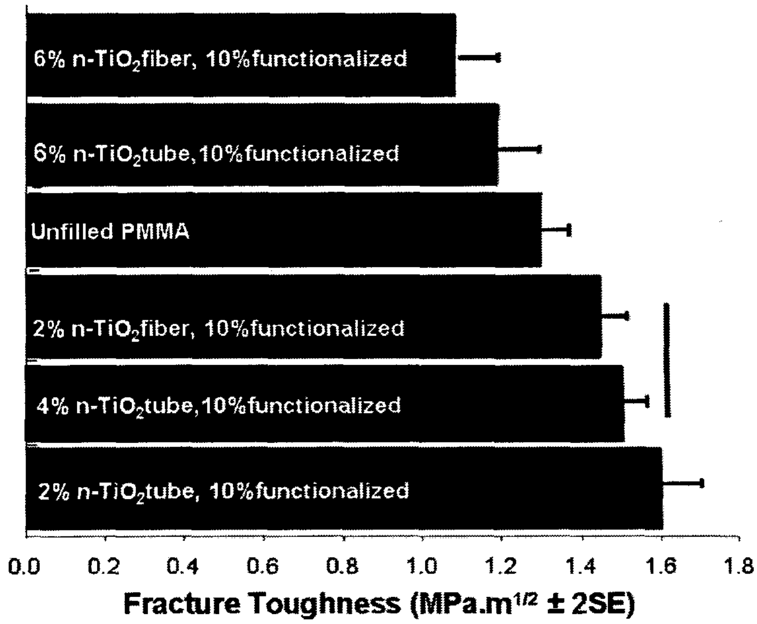

Figure 5. 5. Fracture toughness of composites reinforced with n-TiO_2 tubes

For comparison purpose, the K_{IC} values of the nanocomposites with functionalized n-TiO_2 fibers as well as the unfilled PMMA are presented in the graph. It is clear from this multiple comparative study that the nanocomposites with 2% functionalized n-TiO_2 tubes exhibit the highest K_{IC} value which is significantly higher than that exhibited by the nanocomposites with 2% n-TiO_2 fibers as well as the unfilled PMMA matrix at $P<0.05$. However, the K_{IC} values start decreasing when the nanocomposite is loaded with 4 and 6% functionalized n-TiO_2 tubes, although the composite with 4% n-TiO_2 tubes possesses substantially higher fracture toughness than the composites containing 2% n-TiO_2 fibers and the unfilled PMMA. The fracture toughness is quantified in terms of the energy absorbed per unit crack extension, and thus any process which absorbs energy at the crack tip can give rise to an increase in toughness.[45] For a reinforced composite, this process can be achieved by several options such as[232]: 1) the use of tough matrices including rubber toughened matrices, 2) the reduction of stress concentrating effect by using a coupling agent between the filler and matrix that acts as an interlayer, 3) the use of the fiber "pull out" phenomena where the fibrous/tubular fillers bridge the gap so that work must be done to pull out the fibers out of the matrix, and 4) the use of a weak interface between the filler and the matrix such that a crack blunting mechanism takes place. The weakly bonded fibers are not capable to transfer the interfacial shear stress within the composite, eventhough, they still take part in crack blunting and deviating mechanism to increase the toughness of the material.[232,233] In the case of n-TiO_2 tube-PMMA composites used in this work, toughness enhancement was achieved through the second and third mechanisms described above. Functionalization allows the Ti atom to form a reactive bridge with the PMMA matrix, which reduces the possibility of void formation in the filler/matrix interfacial area. This minimizes the sites for local stress concentration during tensile loading and therefore, takes part in increasing the K_{IC} of the composite.[204] On the other hand, as shown in the SEM of the fracture surface obtained from the K_{IC} test of the composites (Figure 5.6), there is a certain extent of nanotube "pull out" occuring within the fractured composites. This nanotube "pull out" effect may significantly increase the work of fracture due to interfacial friction between the nanotube and matrix resulting from the extra-ordinary high surface area of the nanotubes, and the strong interfacial shear strength between the functionalized n-TiO_2 tubes and the PMMA matrix.[234]

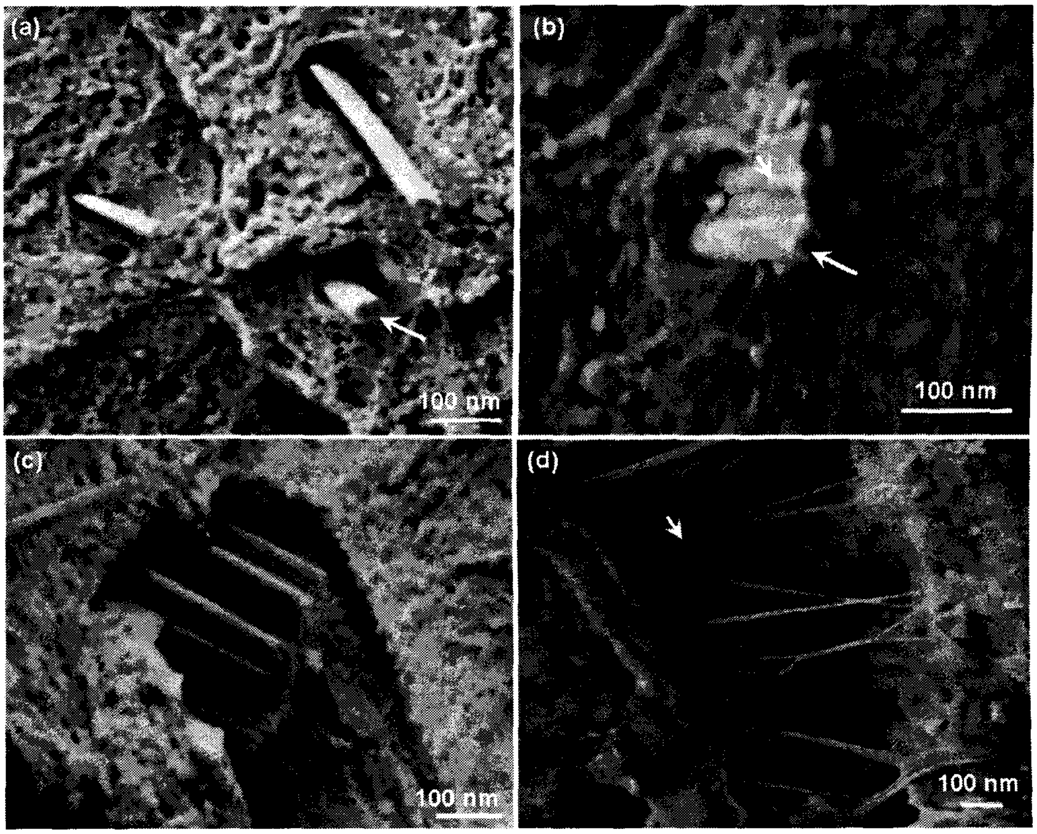

Figure 5.6. SEM of fracture surface showing the micro-mechanism of fracture toughness of PMMA nanocomposites reinforced with 2% non-functionalized n-TiO_2 tubes (a) 2% functionalized n-TiO_2 tubes (b) and 6% functionalized n-TiO_2 tubes (c); Crack bridgeing within the PMMA nanocomposite reinforced with 2% functionalized n-TiO_2 tubes (d). (long arrow indicates polymer inside the tube and short arrow indicates polymer outside the tube)

As studied by Fiedler B. *et al.*[235] the energy needed to pull out fibers of length, l and radius, r over a unit area of fracture plane can be expressed as,

$$G_{pullout} = \frac{V_f l^2 \tau_i}{3r} \tag{5.1}$$

where, V_f is volume fraction of fiber and τ_i is the interfacial shear strength. Functionalized n-TiO_2 tubes having high aspect ratio (l/2r = 209) establish strong covalent bonds with the matrix, which is believed to increase the interfacial shear strength between the n-TiO_2 tube and PMMA matrix. This thereby increases the required energy for pulling the n-TiO_2 tubes out of the fracture plane. Finally, these partially pulled out n-TiO_2 tubes may take part in bridging the crack during crack propagation, further increasing the K_{IC} of the composite.[234] This phenomena of increasing K_{IC} is pronounced in the case of nanocomposites reinforced with low percentage (2%) of n-TiO_2 tubes which display a uniform dispersion of the nanofillers (Figure 5.6 a and b). However, without having any chemical bond with the matrix, the non-functionalized n-TiO_2 tubes seem to have very poor adhesion with the matrix and protrude out of the fracture plane with a clean smooth surface as shown in Figure 5.6 a. The functionalized n-TiO_2 tubes exhibit very strong adhesion with the matrix and the pulled out tubes contain polymer on their surface as shown in Figure 5.6 b. Moreover, the partially pulled out functionalized n-TiO_2 tubes are shown to bridge the crack (Figure 5.6 d), which makes its role of enhancing the K_{IC} more pronounced. However, with higher loading of n-TiO_2 tubes (e.g. 6%), there is also clear evidence of agglomeration of the n-TiO_2 tubes (Figure 5.6 c) at the fracture plane which is associated with voids responsible for accelerating the crack propagation through the local stress concentrators.[6]

5.3.6. Flexural strength and modulus

The values of FS and FM of the PMMA composites are shown in Figure 5.7 using a multiple comparative study among the nanocomposites with functionalized n-TiO_2 tubes and fibers as well as the unfilled PMMA matrix at 95% level of confidence. As shown in this figure, the composite with 2% functionalized n-TiO_2 tubes exhibits the higher magnitude of FS and FM which is significantly higher than that exhibited by the composite with 2% n-TiO_2 fibers having the same extent of functionalization as well as the unfilled PMMA matrix at $P<0.05$.

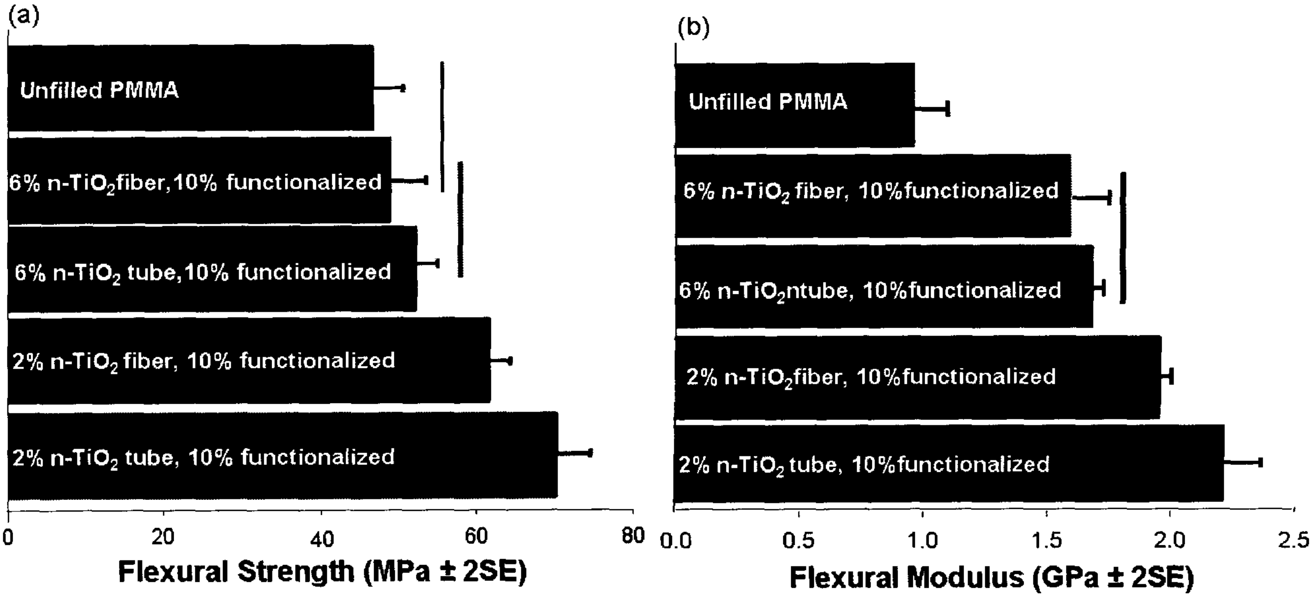

Figure 5.7. Flexural properties of PMMA composites reinforced with n-TiO_2 tubes: (a) Flexural strength and (b) Flexural modulus.

As mentioned in Chapter 4, the flexural properties of the reinforced composites are influenced mostly by the degree of interfacial adhesion and interaction between the filler materials and matrix, which determines the effectiveness of the transfer of interfacial shear stress from the filler to the matrix.[206,207] Having the same extent of functionalization, it is assumed that the n-TiO_2 tubes and n-TiO_2 fibers establish the same extent of chemical adhesion with the matrix. However, having a higher aspect ratio than the nanofibers, the n-TiO_2 tubes provide additional physical interlocks with the polymer chains. Moreover, the hollow and open-ended tubular structure (as confirmed by SEM and TEM images in Figure 5.2) may allow the monomer to enter into the tube due to capillary suction which may subsequently polymerize inside the tube.[236] This possible phenomena is evidenced by the presence of solid polymer inside the n-TiO_2 tube as shown by the SEM of the fracture surface of the nanocomposites (Figure 5.6 a and b). This polymer entrapment may facilitate additional mechanical interlock through the interior surface of the n-TiO_2 tubes. Therefore, the functionalized n-TiO_2 tubes are capable of establishing an enhanced network with the polymer chains which is also reflected from the higher thermal degradation temperature of the resulting composites (Figure 5.4 b). The load transfer efficiency within the composites increases with a higher degree of cross-linking and network formation. Hence, the nanocomposite containing the functionalized n-TiO_2 tubes exhibits a substantially higher FS value with a similar enhancement in FM, as also reflected from the typical load-deflection curves (Figure 5.8) developed during the flexural test.

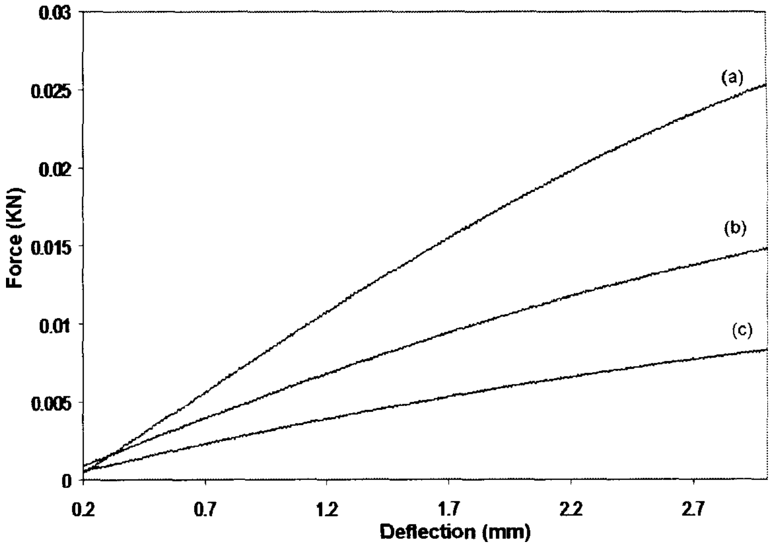

Figure 5.8. Force-deflection curves for the PMMA composites produced in flexural test: (a) PMMA composite reinforced with 2% functionalized n-TiO_2 tube, (b) PMMA composite reinforced with 2% functionalized n-TiO_2 fibers and (c) unfilled PMMA.

It is clear from the force-deflection curves that the nanocomposite with the n-TiO_2 tubes requires a higher magnitude of load for similar amounts of deflection as compared with the composite with n-TiO_2 fibers and unfilled PMMA, thus reflecting its superior FS. On the other hand, the higher initial slope of the linear portion of the load-deflection curves of the n-TiO_2 tube-reinforced composites accounts for its high FM value.

5.3.7. Rheology

Study of the rheology during curing time determines the flow properties of the setting polymer nanocomposites, which plays a significant role determining the time for insertion of the cement in the joint cavity and also the extent of penetration of the cement into the porous cancellous bone. As reported in the previous chapter, a rheology study was performed in terms of the change of complex viscosity with curing time. Figure 5.9 shows the complex viscosity of unfilled PMMA as well as PMMA reinforced with 2 and 6 wt% n-TiO_2 tubes, each functionalized and nonfunctionalized as a function of time, one minute after the start of mixing, at a temperature of 25 ± 1 °C. The rheological parameters (t_{ons} and t_{cure}) as defined in the previous chapter were obtained from the complex viscosity–time traces and are listed in Table 5.2.

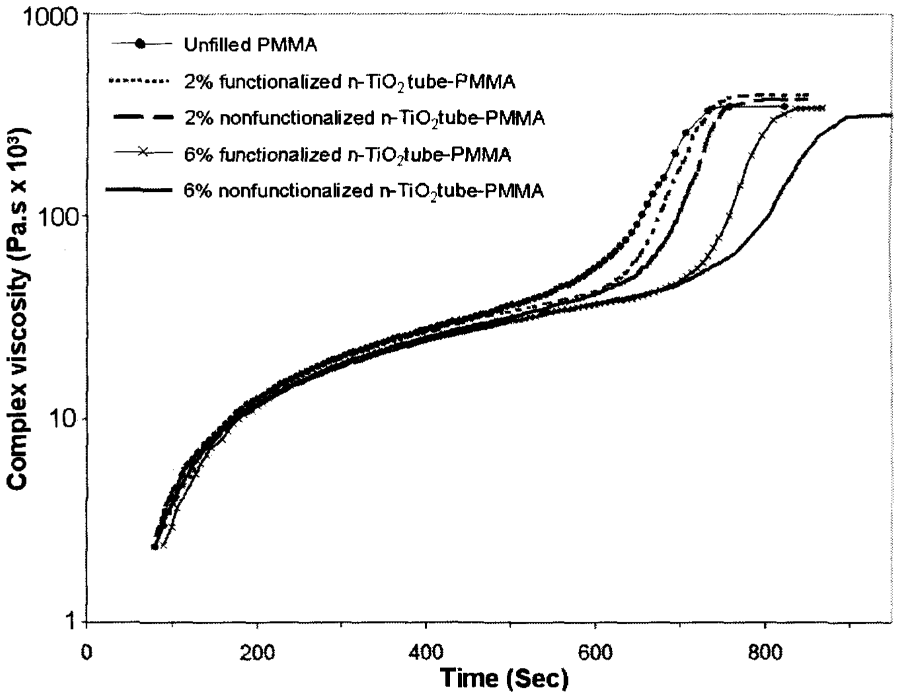

Figure 5.9. Viscosity during setting of PMMA and n-TiO$_2$ tube-PMMA at 25 °C.

The complex viscosity curves for the curing n-TiO$_2$ tube-PMMA composites exhibit a similar pattern compared to the curing n-TiO$_2$ fiber-PMMA composites with two distinct phases: 1) initial gradual increase in the viscosity followed by its final rapid increase, and 2) final plateau of the viscosity. Due to the decreased polymer to monomer ratio, the initial viscosity of the n-TiO$_2$ tube-PMMA composites is lower than that of the unfilled PMMA, which leads to the higher values of t_{ons} and t_{cure} of the composites as previously explained in Chapter 4. Moreover, as in the case of n-TiO$_2$ fiber-PMMA composites, the functionalized n-TiO$_2$ tubes provide higher extent of reactive sites (through its functionalized outer and inner surfaces) compared to the non-functionalized tubes which may increase the rate of the free radical polymerization reaction resulting in lower values of t_{ons} and t_{cure}.

Table 5.2. t_{ons} and t_{cure} of the unfilled PMMA and n-TiO_2 tube-PMMA at 25 °C.

Nanocomposite Composition	t_{ons} (min)	t_{cure} (min)
Unfilled PMMA	10.00 ± 0.02^{a}	12.00 ± 0.04^{a}
2% functionalized n-TiO_2 tube-PMMA	10.50 ± 0.02^{b}	12.25 ± 0.03^{b}
2% nonfunctionalized n-TiO_2 tube-PMMA	10.83 ± 0.04^{c}	12.50 ± 0.04^{c}
6% functionalized n-TiO_2 tube-PMMA	11.50 ± 0.04^{d}	13.58 ± 0.04^{d}
6% nonfunctionalized n-TiO_2 tube-PMMA	12.70 ± 0.03^{e}	14.53 ± 0.02^{e}

Mean ± 2SE, P<0.05

This phenomena leads to the presence of higher amounts of unreacted monomer in the composite reinforced with non-functionalized n-TiO_2 tubes than with functionalized n-TiO_2 tubes. This can be qualitatively characterized by FTIR analysis of the curing composites after 10 and 12 minutes from the start of mixing as shown in Figure 5.10.

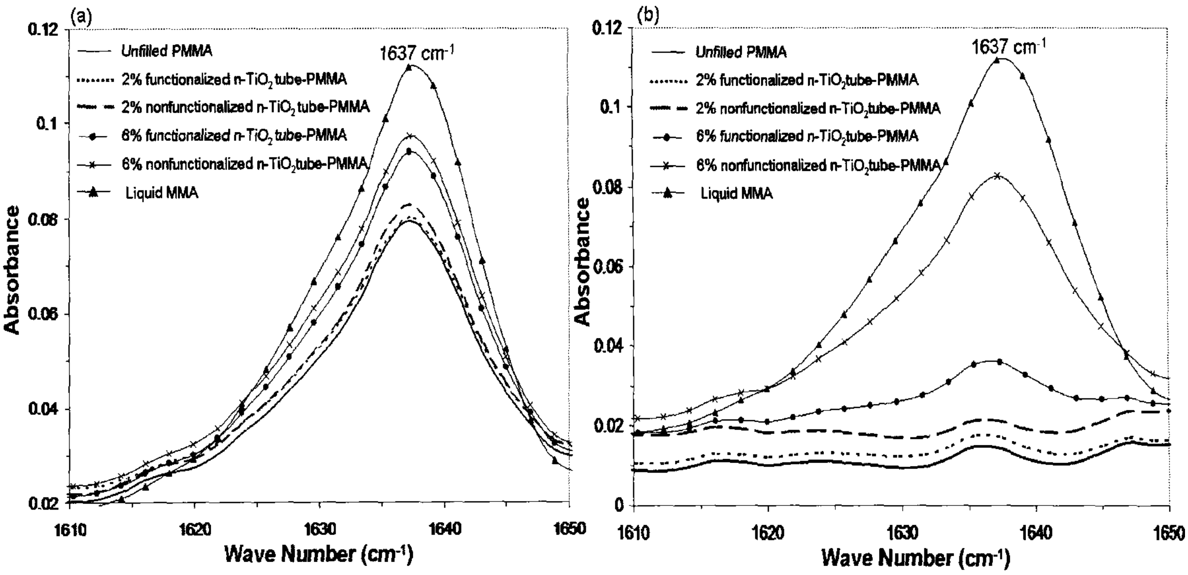

Figure 5.10. FTIR spectra of the curing n-TiO_2 tube-PMMA composites after 10 minutes (a) and 12 minutes (b) of the mixing.

In figure 5.10, the residual monomer on the cement surface is shown by the absorption peak at 1637 cm^{-1}, which confirms the presence of C=C bond of the unreacted MMA.[215]

As shown in this figure, the liquid MMA exhibits the highest peak at 1637 cm^{-1}attributed to the unsaturated vinyl bond of this monomer. After 10 minutes of the initial mixing, the unfilled PMMA matrix reaches the onset stage of viscosity increase, while the other composites still stay in the wetting phase (Figure 5.10 and Table 5.2). This is why the unfilled PMMA shows a comparatively lower absorption peak than the other composites at 1637 cm^{-1} after 10 minutes (Figure 5.10 a). On the other hand, unfilled PMMA reaches its curing stage after 12 minutes, while composites with 2% functionalized and non-functionalized n-TiO_2 tubes as well as the 6% functionalized n-TiO_2 tubes stay in the polymerization stage (Table 5.2). Hence, all these composites exhibit a lower absorption peak at 1637 cm^{-1} compared to that after 10 minutes. However, the composite with 6% non-functionalized n-TiO_2 tubes exhibits the existence of a substantial amount of the unsaturated C=C bond after 12 minutes, thus remaining in the wetting (Table 5.2).

However, the values of t_{ons} and t_{cure} exhibited by the curing n-TiO_2 tube-PMMA composites are much lower than those exhibited by the n-TiO_2fiber-PMMA composites with the same loading and the same extent of functionalization as shown in Table 4.4 and Table 5.2. Higher surface area and a hollow interior allow the nanotubes to establish enhanced interlocking with the matrix through its outer and inner surfaces both physically and chemically, which may contribute to the lower amount of unreacted monomer within the composites. The main limitation associated with this technique of measuring residual MMA is that it primarily measures the surface MMA content of the composite.

5.3.8. Radiopacity

As mentioned in Chapter 4, radiopacity is a very important property for a composite when applied as a bone cement, as this property allows the post operative assessment of the cement and cemented joint prosthesis. The radiopacity values in Al equivalent of 1mm specimen thickness for PMMA composite reinforced with 2 % n-TiO_2 tube is presented in Figure 5.11, along with the unfilled PMMA and 2% n-TiO_2 fiber-PMMA composite.

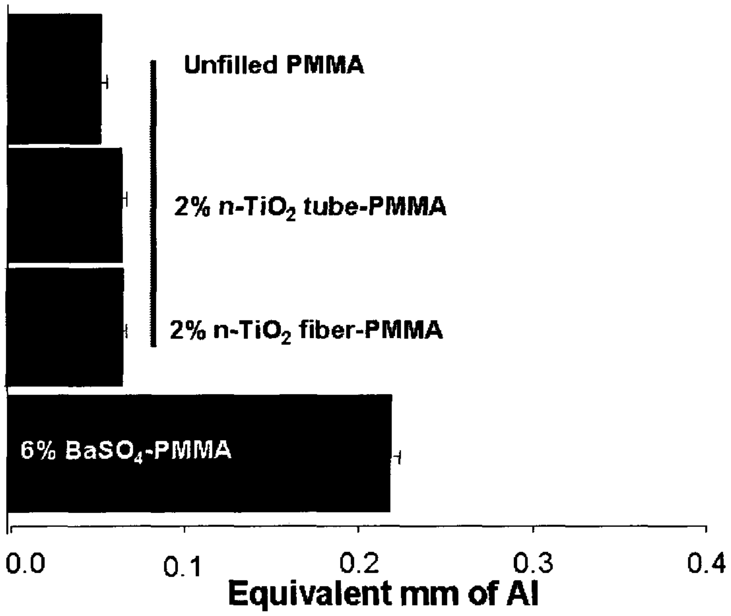

Figure 5.11. Radiopacity of different composites expressed in terms of equivalent Al thickness.

As shown in this figure, all the composites loaded with 2% n-TiO_2 exhibit a low level of radiopacity that is not significantly different from the unfilled PMMA at P=0.05. The reason for the poor radiopacity of the composite reinforced with 2% n-TiO_2 tubes is the same as that for the composite with 2% n-TiO_2 fibers, i.e. the low capacity of the titanium atom to attenuate X-ray photons of the standard medical X-ray equipment.

5.4. Conclusion

n-TiO_2 tubes have been successfully incorporated into a PMMA matrix as reinforcing agents to produce nanocomposites. Functionalized nanotubes established strong interfacial adhesion and extended interfacial interaction with the polymer matrix through both its exterior and interior surfaces as confirmed by the micrographic analysis of the fracture surfaces of the nanocomposites. The increased interfacial shear strength was also confirmed by thermogravimetric and dynamic Young's moduli analysis of the produced nanocomposites. The rare combination of extreme toughness with firm flexural strength was achieved due to the strong and enhanced interfacial adhesion between the nanotubes and the polymer. It was found that 2wt% n-TiO_2 tubes with an increased extent of functionalization (10wt %) provided the highest magnitude of fracture toughness and flexural strength amongst all tested materials. This provided a superior reinforcing effect compared to reinforcement with titania nanofibers. However, with the optimum incorporation (2wt %) of n-TiO_2 tubes, the nanocomposites did not exhibit sufficient radiopacity with the standard X-ray exposure available for medical treatment.

Chapter 6: Modification of nanostructured titania tube with strontium and nanocomposite preparation

This chapter describes one of the modification techniques of the nanostructured titania tubes (n-TiO_2 tube) for improving their capacity to attenuate X-ray photons and radiopacifying properties. The effect of these modified tubes on the mechanical and biological properties of the PMMA matrix is also described in this chapter. Part of this chapter was reproduced from an article submitted to Acta Biomateriallia with the title: "Synthesis and Characterization of PMMA Based Composites Reinforced with TiO_2-SrO Nanotubes" and another article under preparation to be submitted to Langmuir.

Strontium oxide (SrO), a well known and strong radiopacifier was incorporated into the n-TiO_2 tube in-situ during the synthesis of the tubes through the alkaline hydrothermal technique. The TEM and SEM micrographs revealed the incorporation of the SrO within the tubes, while energy dispersive spectroscopy (EDS) mapping and backscattered SEM confirmed the uniform distribution of SrO. The nanocomposite reinforced with 2 wt% SrO incorporated n-TiO_2 tubes (SrO-n-TiO_2 tube) exhibited sufficient radiopacity similar to the commercial bone cement. It also retained the fracture toughness as imparted by n-TiO_2 tubes at the same loading. Moreover, the resulting nanocomposites exhibited significant enhancement in cellular proliferation *in vitro* compared to the control (unfilled PMMA matrix) at $P<0.05$..

6.1. Introduction

It is clear from the various scientific and clinical studies that the radiopacifying agents ($BaSO_4$ or ZrO_2) used in the commercially available PMMA based bone cements impart a deleterious effect on its mechanical properties. These are caused by poor wetting and weak interfacial bonding between these inorganic fillers and the non-polar polymer matrix.[12,16,198,220,237] Therefore, there is a sustained interest in alternative radiopacifiers which can act also as reinforcement agents for bone cements. In an attempt to achieve this, we have introduced nano-sized titania fibers and tubes in an acrylic matrix as examined in the previous chapters. We have managed to utilize the advantage of the high aspect ratio of the one-dimensional nanomaterials to enhance the mechanical properties of the matrix. However, the optimum loading of the nanomaterials as determined from the mechanical properties of the resulting nanocomposites failed to render sufficient radiopacity to the matrix using standard medical X-rays. In this chapter we have introduced one approach to modify the nano-sized titania tubes to provide enhanced radiopacity at the optimum loading in the acrylic matrix. Strontium (Sr) is a highly radiopaque substance having an atomic number of 38 and K-edge energy of 16.10 KeV.[238] This is why Sr is assumed to exhibit similar radiopacity compared to Zr.[239] Sr is currently utilized in some commercially available dental cement brands as a radiopacifier.[240] Many researchers studied the incorporation of Sr in an acrylic bone cement matrix in an attempt to evaluate alternative radiopacifiers either combined with other materials or in the pure oxide form. One of the most recent investigations was done by L. Hernandez and *et al.*[210] who used strontium hydroxyapatite as filler particles in a PMMA based cement. In another attempt, G. Lewis *et al.*[239] reported the incorporation of strontium oxide (SrO) particles as an alternative radiopacifier in acrylic cement matrix. Besides providing radiopacity as high as that exhibited by a $BaSO_4$ containing cement, SrO showed the potential to act as a bacterial growth inhibitor. Moreover, the inclusion of

Sr is reported to increase the biocompatibility of the cement.[241] Because of its high reported radiopacity, antibacterial activity and biocompatibility, we have modified the n-TiO_2 tubes with SrO. This is the first approach to combine the effectiveness of SrO with enhanced radiopacity and biocompatibility and nano-structured materials to achieve advanced nanocomposites with enhanced mechanical properties. In order to introduce the SrO into the n-TiO_2 tube, we followed a one step in-situ decoration/incorporation procedure of strontium acetate into the titanate nanotube by treating it with commercial titania nanopowder through the alkaline hydrothermal technique. Being soluble in the aqueous alkali solution, strontium acetate generates Sr^{2+} in solution which is incorporated in between the layers or in the cavity of the growing titanate nanotube during synthesis. Finally the anatase titania nanotube incorporated with SrO was obtained after calcining the modified titanate in air. Hence, the objective of this study is to synthesize and characterize advanced n-TiO_2 tubes incorporated with SrO (SrO-n-TiO_2 tube). In addition, the effect of the inclusion of these advanced nanotubes on the radiopacity, mechanical properties and in vitro biocompatibility of the PMMA based nanocomposites is also studied in this work.

6.2. Materials and Methods

6.2.1. Materials

Titanium oxide nanopowder (<100 nm, 99.9% metal basis), strontium acetate powder (~3% H_2O) and reagent grade 37% hydrochloric acid were purchased from Sigma-Aldrich and used as received. Sodium hydroxide pellets (assay, Ca: 0.0002%, K: 0.007%, Na_2CO_3: 0.4%, Cl: <0.001%, Cu: <0.001% , Mg: <0.0002%) were purchased from J.T. Baker and used as received. All other materials used to functionalize the n-TiO_2-SrO and to prepare the nanocomposites were the same as used in Chapter 4 and 5. Moreover, the materials used for the in vitro biocompatibility study were the same as described in section 2.7 of Chapter 2.

6.2.2. Synthesis of SrO-n-TiO_2 tube

0.24 gram of strontium acetate powder was dissolved in 30 mL of 10M NaOH solution in a 125 mL teflon- nalgene flask and was subjected to constant stirring for 24 hours. 2 gram of titanium oxide nanopowder was then mixed into the solution of strontium acetate in 10M NaOH and the whole mixture was kept under constant stirring for another 24 hours. Finally the whole content was transferred to a 40 mL teflon flask enclosed in a 125 mL stainless steel autoclave (Parr 4748, Parr instrument, IL, USA). The reaction was carried out at 120 °C for 20 hours without stirring. The alkali-treated powders thus obtained were rinsed with distilled water followed by 0.1M HCl solution until its pH became ~7. Then the titania-based powder was subjected to vacuum drying at 80 °C overnight. Finally the dried powder was calcined at 400 °C for 2 hours at a heating rate of 10 °C/min in air.

6.2.3. Functionalization of SrO-n-TiO_2 tube

In order to functionalize the surface of the SrO -n-TiO_2 tube, 0.1 g of calcined powder was dispersed in 35 mL of 2-propanol with the aid of ultrasonic agitation, followed by reacting with 3 mL of MA at 80-85 °C for 24 hours with constant stirring. The reaction was carried out at pH of 5.5 (as measured by pH meter UWR SB301) adjusted by adding a few drops (5-12 drops) of potassium hydroxide solution (0.3 N) to the reaction mixture prior to the reaction. The treated powder was then filtered and washed with distilled water and 2-propanol to remove the unreacted MA. Finally the wet powder was dried at 80 °C under vacuum for 5 hours. 10 wt% functionalization on the modified nanotubes was achieved as studied by TGA analysis (not shown in this chapter)

6.2.4. Preparation of SrO-n-TiO_2 tube -PMMA composites

The nanocomposites were prepared following the standard technique recommended to prepare bone cements by mixing the powder part consisting of the prepolymerized PMMA beads and initiator with the liquid part consisting of MMA and activator. During preparation of the SrO-n-TiO_2 tube-PMMA composite, the functionalized SrO-n-TiO_2 tubes were dispersed in the liquid part of the cement by ultrasonic agitation for 15 minutes. The resulting materials were hand mixed into a dough state with the powder portion of the cement according to the technique described in previous chapters and a published work.[20] Nanocomposite specimens with 2 wt% loading of functionalized SrO-n-TiO_2 tube were prepared for determination of the mechanical and other properties. Moreover, control specimens were prepared using the PMMA nanocomposites reinforced with 2 wt% functionalized n-TiO_2 tubes.

6.2.5. Characterization of SrO-n-TiO_2 tube and the nanocomposites

The microstructure and morphology of the SrO-n-TiO_2 tubes were examined by transmission electron microscope (TEM, Philip CM10, AMT digital camera, Eindhoven, Netherlands) operated at an accelerating voltage of 100 kV. The morphology of the n-TiO_2-SrO was also investigated by using a scanning electron microscope (SEM, LEO 1540XB, Zeiss, Oberkochen, Germany) at an accelerating voltage of 1 kV. The distribution of the SrO in the SrO-n-TiO_2 tube was examined by the back-scattered electron signal produced from the SEM analysis of the sample. The distribution was also investigated by energy dispersive X-ray spectroscopy (EDS) using the elemental mapping of Sr, Ti and O atoms of the SrO-n-TiO_2 tube samples using the same SEM microscope operated at an accelerating voltage of 20 kV.

K_{IC} of the nanocomposite specimens loaded with 2 wt% of functionalized SrO-n-TiO_2 tube was determined using the notchless triangular prism (NTP) method as described in chapter 2. Triangular prism specimens (n=12) (6mm x 6mm x 12mm) were produced. Testing was conducted using a computer controlled Instron 3345 at a crosshead speed of 0.1 mm/min with the specimens in the wet condition.

The radiopacity of the nanocomposites based on 2 wt% loading of the functionalized SrO-n-TiO_2 tubes was evaluated and expressed in terms of equivalent aluminum (Al) thickness according to the method described in chapter 2 with the calibration curve and regression equation described in Chapter 4.

6.2.6. Determination of *in vitro* biocompatibility of the SrO-n-TiO_2 tube-PMMA composites

In vitro biocompatibility was evaluated for the nanocomposites reinforced with 2 wt% functionalized SrO-n-TiO_2 tubes as well as the control specimens (PMMA with 2 wt% n-TiO_2 tubes and unfilled PMMA) using disc specimens, 14.0 mm in diameter and 1.0 mm in thickness. The biocompatibility study was performed using primary rat calvarial osteoblasts (RCOs) according to the methods described in section 2.7 of Chapter 2. In order to avoid the effect of unreacted monomer, all the nanocomposite specimens were subjected to incubation at 60 °C for 72 hours prior to the cell culture. Moreover, specimens were plasma cleaned using argon gas and plated in 24 well tissue culture plastic before seeding the RCOs.

For live/dead analysis, RCOs were plated at a density of 10 000 cells per specimen and cultured for 24, 48 and 72 hours. Cells were stained with Invitrogen's live/dead kit to determine the viability/cytotoxicity of cells by differentiating between live and dead cells using a two colour fluorescence. Ten images per surface were captured with an Axiphot microscope (Zeiss, Oberkochen, Germany), a Fast1394 digital camera (QICAM, QImaging, Surray, BC, Canada) and Northern Eclipse software (EMPIX, EMPIX Imaging Inc., Cheektowaga, NY, USA). Only the images with live cells are presented in the cell proliferation study. All data for proliferation experiments were normalized to control surfaces at 24 hours. 3 independent experiments were analyzed with 3 repeats per experiment.

6.3. Results and Discussion

6.3.1. TEM and SEM

The microstructure of the synthesised material after calcination at 400 °C was investigated by TEM and is represented in Figure 6.1 b. The TEM image of the n-TiO_2 tubes is also represented in Figure 6.1 a for comparison purposes.

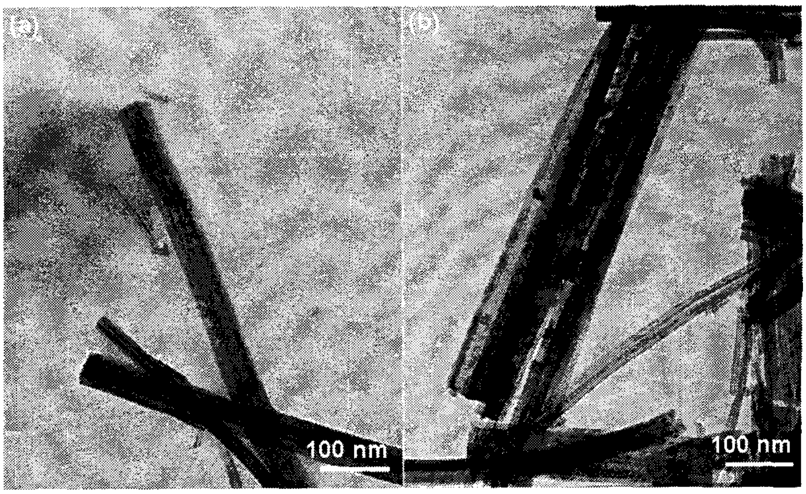

Figure 6.1. TEM: (a) n-TiO_2 tube and (b) SrO-n-TiO_2 tube

As shown in the figure, the SrO-n-TiO_2 tubes exhibit a multi-layered tubular morphology similar to the n-TiO_2 tube structure. The SEM image of the SrO-n-TiO_2 tube also reveals its tubular morphology with a smooth surface containing very little amount of SrO particles on its surface which indicates the possible entrapment of most of the SrO particles inside the tube in its cavity or in the interlayer spaces (Figure 6.2. a).

6.3.2. Backscattered SEM

The SEM image of the SrO-n-TiO_2 tube generated by backscattered electrons is shown in Figure 6.2 b, which shows an image contrast. Backscattered electrons are incident electrons reflected back from a target sample and imaged by SEM.[242] The contrast of the backscattered image results from the energy spectrum of the emitted electrons which are elastically scattered from the nucleus of different atoms the sample consists of.[243] Therefore, the image contrast reveals the distribution of atoms with different atomic number or the Z-contrast of the sample.

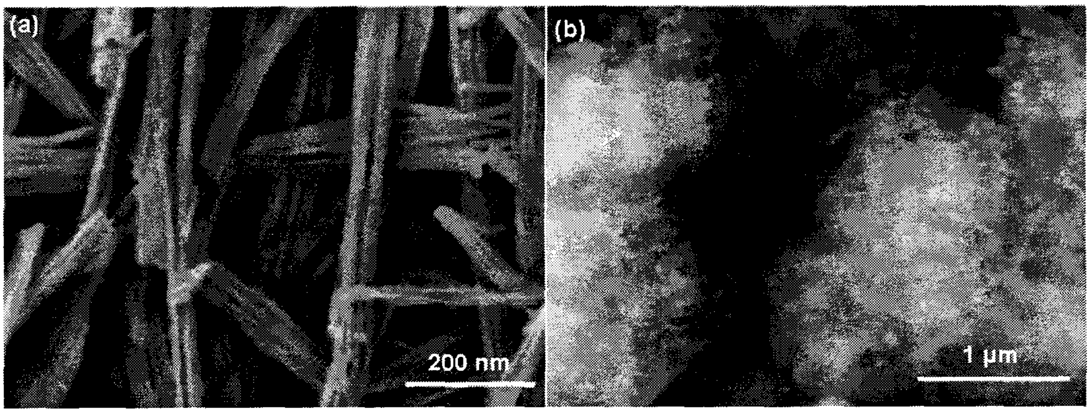

Figure 6.2. SEM image of SrO-n-TiO_2 tube (a) and backscattered SEM image of SrO-n-TiO_2 tube

Hence, in Figure 6.2.b, the homogeneous image contrast reflects the good distribution of the Sr atoms in the Ti matrix.

6.3.3. EDS

Figure 6.3 shows the EDS elemental analysis of the SrO-n-TiO_2 tube using titanium, strontium and oxygen mapping. In Figure 6.3 b-d, the elemental maps represent the distribution of atomic concentrations of Ti, Sr and O in the nanotubes and it reveals that the titanium and strontium elements are homogenously dispersed throughout the samples. EDS elemental analysis was also performed to investigate the atomic composition of the elements in the SrO-n-TiO_2 tube sample. The elemental analysis was performed by taking the spectrum on three different sites of the sample with the average values of the composition along with the standard deviations being provided in Table 6.1. The elemental analysis contains a certain amount (21.58 at.%) of C which comes from the carbon grid on the Al stub used for holding the samples during the EDS analysis. The atomic composition of Sr as revealed from the EDS analysis is 2.1% (excluding the C), which is less than the atomic composition of Sr (4.4%) in the precursor mixture.

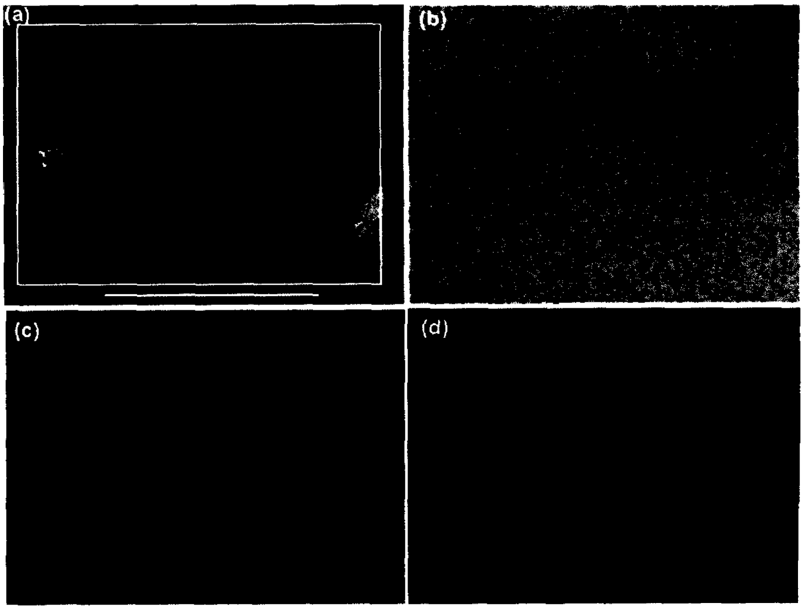

Figure 6.3. EDS elemental mapping: (a) Selected area on the sample (b) Ti mapping; (c) O mapping and (d) Sr mapping. Scale bar in 5 μm.

It is anticipated that some Sr cations are removed and some are replaced by hydrogen ions during the washing steps using water and HCl solution respectively. A small amount of Na atoms in the elemental analysis comes from the NaOH solution used as medium for the hydrothermal reaction.

Table 6.1. Atomic composition of different elements of SrO-n-TiO_2 tube as measured by EDS elemental analysis.

Elements	Composition (atomic%) ± SD
C	21.58 ± 4.49
O	59.92 ± 1.76
Na	0.44 ± 0.16
Ti	16.40 ± 2.47
Sr	1.65 ± 0.32

6.3.4. FTIR

The functionalization of the SrO-n-TiO_2 tube was confirmed by FTIR analysis of the sample which exhibited a similar absorption band as exhibited by the functionalized n-TiO_2 tubes and shown in Figure 6.4.

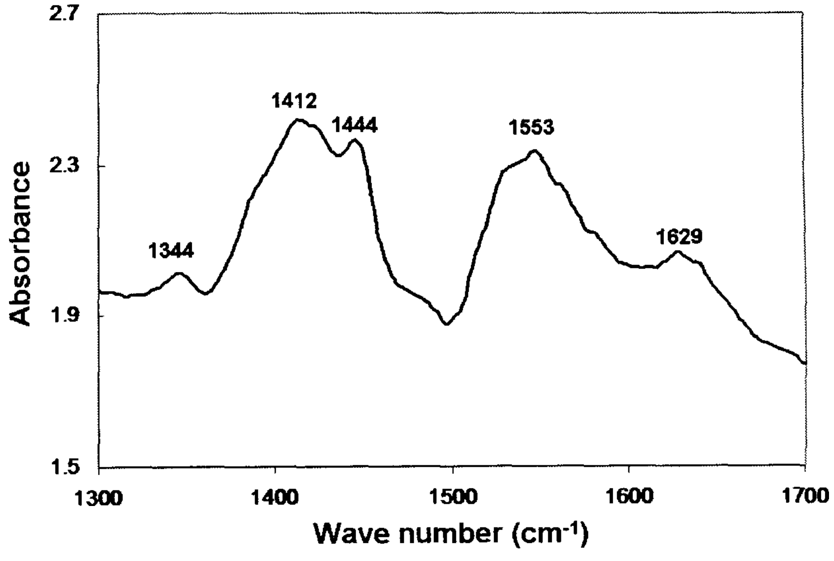

Figure 6.4. FTIR spectra of the functionalized SrO-n-TiO_2 tube.

It is anticipated that most of the SrO particles are incorporated within the bulk of the n-TiO_2 tube, not on the surface. Therefore, the functionalizing agent, MA is anticipated to interact with the titanium atom on the tubular surface. As shown in Figure 6.4, the two absorbance bands at 1553 and 1412 cm^{-1} are ascribed to asymmetric and symmetric mode of ν(O-C-O).[244] The highest wave number mode at 1553 cm^{-1} and the lowest wave number mode at 1412cm^{-1} are separated by 139 cm^{-1} and hence suggest the carboxylic group of MA is coordinated to the titania surface through bridging bindendate coordination mode.[245] The absorption band at 1629 cm^{-1} corresponds to the C=C bond of the MA coupled with the SrO-n-TiO_2 surface.[20]

6.3.5. Fracture toughness

The mechanical properties of the PMMA composites reinforced with 2 wt% of functionalized SrO-n-TiO_2 tube were investigated for K_{IC}. Figure 6.4 shows the comparative study of the K_{IC} values of the resulting nanocomposite as well as composites with 2 wt% functionalized n-TiO_2 tubes and fibers at the same level of functionalization.

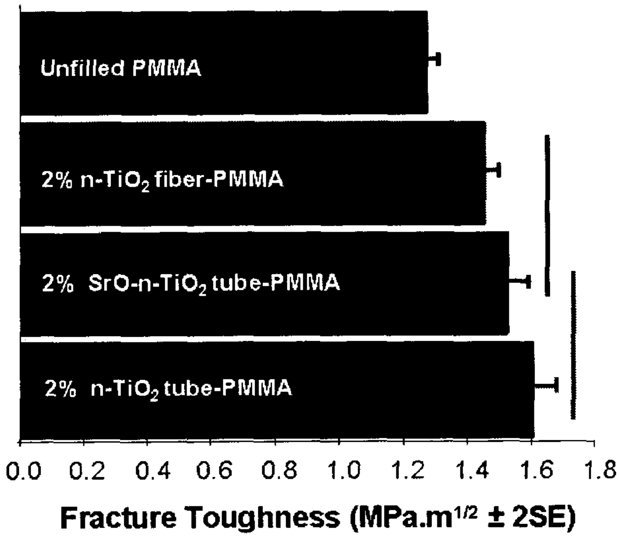

Figure 6.5. Fracture toughness of unfilled PMMA and different nanocomposites

As shown in this figure, the K_{IC} value of the composite reinforced with 2 wt% of functionalized SrO-n-TiO_2 tubes is not significantly different from those of composites reinforced with 2% n-TiO_2 fibers and tubes, $P>0.05$. However, it is significantly higher than the unfilled PMMA matrix, $P<0.05$. After modification with SrO, the n-TiO_2 tube preserved its tubular morphology which was confirmed by the TEM and SEM analysis. Therefore the SrO-modified titania nanotube renders a similar toughening effect to the nanocomposites as provided by the pure n-TiO_2 tubes.

6.3.6. Radiopacity

The radiopacity values in Al equivalent of 1mm specimen thickness for composites with 2 wt% SrO-n-TiO_2 tube and 2 wt% n-TiO_2 tube as well as unfilled PMMA and PMMA reinforced with 6% commercial $BaSO_4$ are presented in Figure 6.6. As shown in this figure, the Sr-incorporated n-TiO_2 tube provides significantly higher radiopacity (> 100%) to the PMMA matrix than that provided by n-TiO_2 alone at the same level of loading. The increased radiopacity results from the Sr atom incorporated in the nanotube.

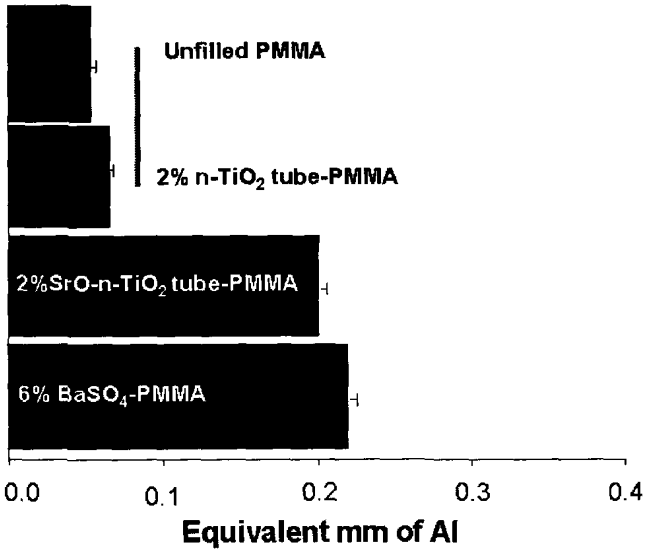

Figure 6.6. Radiopacity in equivalent Al thickness

It is calculated from the weight percentage elemental analysis that nanocomposites reinforced with 2 wt% of SrO-n-TiO_2 tube basically contains 0.73 wt% Ti and 0.40 wt% Sr, while the nanocomposite reinforced with 2 wt% n-TiO_2 tube contains about 1.1 wt% of Ti. Therefore, the enhanced radiopacity of the PMMA composites is due to the presence of Sr with Ti atom.

6.3.7. *In vitro* biocompatibility

Figure 6.7 represents the RCO cell adhesion and proliferation on the surface of the PMMA nanocomposite reinforced with 2 wt% SrO-n-TiO_2 tubes. It also shows the cell proliferation on the unfilled PMMA surface as well as on the composite reinforced with 2 wt% n-TiO_2 tube. RCOs attach and spread to different extents on different composite surfaces by 24 hours. The SrO-n-TiO_2 tube-PMMA composite surface exhibits the highest degree of cell spreading with a flattened morphology of RCOs attached on it (Figure 6.7 c), reflecting its excellent cell viability compared to the unfilled PMMA and composite reinforced with 2 wt% n-TiO_2 tubes. The RCOs reach confluency in 72 hours exhibiting a higher extent of cell growth on the n-TiO_2-SrO-PMMA surface than that which occurs on the unfilled PMMA and n-TiO_2 tube-PMMA composites.

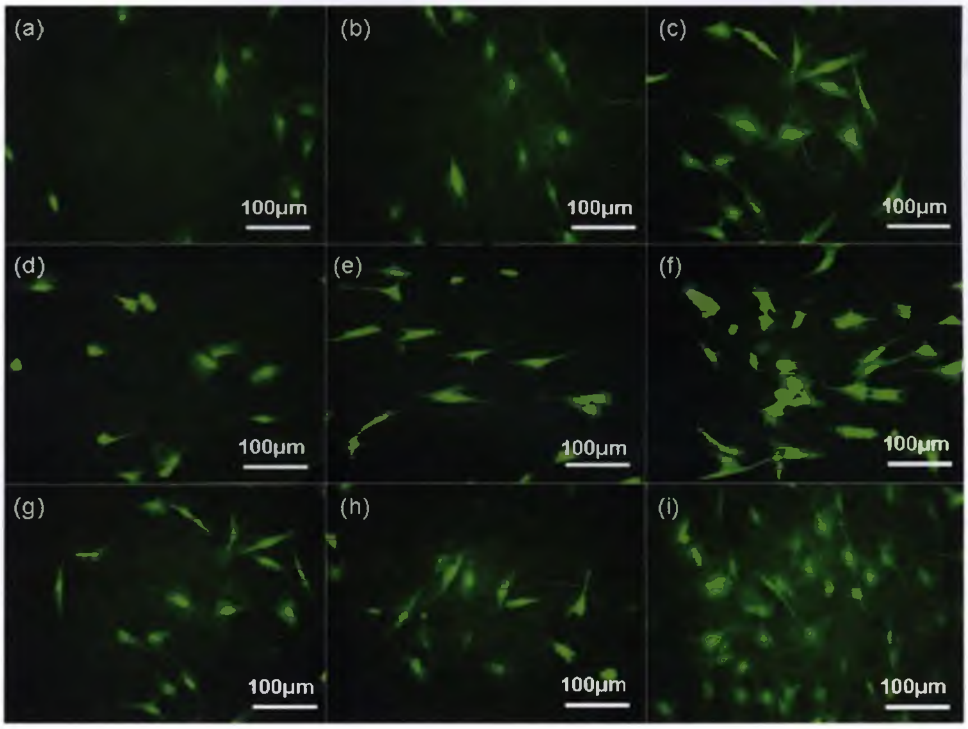

Figure 6.7. RCOs proliferation for 24 hours on surfaces of (a) unfilled PMMA matrix, (b) 2% n-TiO_2 tube-PMMA and (c) 2% SrO-n-TiO_2 tube-PMMA; RCOs proliferation for 48 hours on surfaces of (d) unfilled PMMA matrix, (e) 2% n-TiO_2 tube-PMMA and (f) 2% SrO-n-TiO_2 tube-PMMA; RCOs proliferation for 72 hours on surfaces of (g) unfilled PMMA matrix, (h) 2% n-TiO_2 tube-PMMA and (i) 2% SrO-n-TiO_2 tube-PMMA; Only live cells are shown.

Analysis of the live cell numbers reveals that although RCOs proliferate almost similarly on both the unfilled PMMA and n-TiO_2 tube-PMMA surface for up to three days, there is a 2.0 fold increase at 48 hours and 4.0 fold increase at 72 hours on the surface of n-TiO_2-SrO-PMMA composite (Figure 6.8 a). Moreover, analysis of the live/dead RCOs revealed that cell survival (viability) ranges from 92-98 % for the composite reinforced with 2 wt% n-TiO_2-SrO, while for the unfilled PMMA and 2 % n-TiO_2 tube-PMMA composite it ranges from about 85-94% and 88-96% respectively (Figure 6.8 b). Hence, all these results from the cell study indicate that SrO-n-TiO_2 tubes enhance the cytocompatibility of the PMMA matrix significantly compared to that containing the n-TiO_2 tube alone at $P<0.05$.

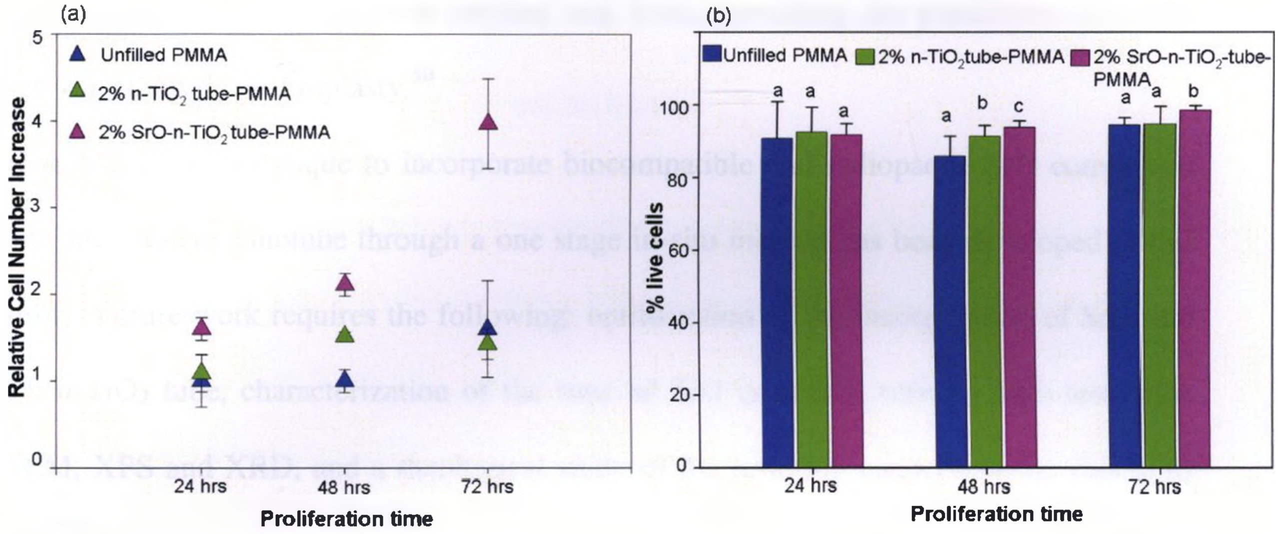

Figure 6.8. a) Proliferation and b) Live/dead analysis of RCOs seeded on unfilled PMMA and different nanocomposite surfaces.

Hence, there is clear evidence that SrO plays an important role in enhancing the cytocompatibility of the composites. Basically, Sr is a natural bone-seeking trace element that accumulates in the skeleton.[246] Because of its chemical similarity with calcium (both reside in the same group in the periodic table), Sr enhances the proliferation and growth of bone cells in vitro.[247] Moreover, Sr stimulates bone formation and inhibit bone resorption, thereby exhibits a potential therapeutic effects in osteopenic disorders.[247]

From the above discussion, it can be rationalized that functionalized n-TiO_2 tubes act as ideal reinforcing agents for acrylic matrix in order to produce a new generation of bone cements, when doped with SrO. The resulting nanocomposites retain the enhanced mechanical properties as exerted by the undoped counter-part, but exhibit substantially higher radiopacity and biocompatibility compared to that exhibited by the n-TiO_2 tube-PMMA composite. Moreover, the nanotubes are chemically bonded to the acrylic matrix with the SrO enclosed into its cavity or inter-layer space, which inhibits the chance of possible loosing of these components into the surrounding biological atmosphere during wear of the bone cement with implant and bone, providing the possibility of longer service life of the arthroplasty.[50]

Hence, a novel technique to incorporate biocompatible and radiopaque SrO component into the titanate nanotube through a one stage in-situ method has been developed in this study. Future work requires the following: optimization of the incorporation of SrO into the n-TiO_2 tube, characterization of the state of SrO in n-TiO_2 tube by high resolution TEM, XPS and XRD, and a rheological study of the resulting nanocomposite during its curing.

6.4. Conclusion

A novel nanostructured tubular TiO_2 modified with SrO was successfully synthesized and introduced into the PMMA matrix to enhance its mechanical, physical and biological properties. The augmented K_{IC} resulted from the high aspect ratio of the functionalized nanotube which establishes strong and extended interfacial bonding with the matrix, while the increase in radiopacity and osteoblast cell viabilty was attributed to the modification of the n-TiO_2 tubes with SrO. Therefor, this study demonstrated a novel pathway to develop an alternative radiopacifier for bone cements which also acts as a reinforcing agent.

Chapter 7: Reinforcement of a commercial bone cement using nanotitania

In the last four chapters we have examined the development of a novel technique to functionalize nanostructured titania fibers, spheres and tubes along with the reinforcing effect of these functionalized nanomaterials on a PMMA matrix. The resulting nanocomposites were studied focusing on their potential application as a new generation of bone cements having an optimum combination of toughness and strength, radiopacity and biocompatibility. In order to evaluate the commercial applicability of this reinforcement technique we have applied this methodology to a commercially available acrylic bone cement. The present chapter deals with the reinforcement of a clinically used commercial bone cement using the functionalized titania nanofibers and nanotubes. Part of this chapter has been reproduced from one article accepted for publication in the Journal of Biomaterials Application on October 2009 with the title: "Physical and Mechanical Properties of PMMA Bone Cement Reinforced With Nano-sized Titania Fibers", and another article with the title:"Reinforcement of Resin Cement With Titania Nanotube", which has been accepted for publication in Dental Materials on September, 2009.

One of the limitations of the commercial bone cement is its poor mechanical properties particularly FS and K_{IC} which result from the deleterious effects of the radiopacifier ($BaSO_4$ or ZrO_2). These lower properties facilitate the chance of implant loosening resulting from cement mantle failure. The present study was performed to enhance the mechanical properties of a commercially-available cement (CMW$^{®}$1) by introducing novel nanostructured titania fibers (n-TiO_2 fibers) and tubes (n-TiO_2 tube) into the cement matrix, with the fibers or tubes acting as a reinforcing phase.

The hydrophilic nature of the n-TiO_2 was modified by using the bi-functional monomer, methacrylic acid. The effect of n-TiO_2 on the cement was systematically studied by varying the content of the nanomaterials from 0 to 2 wt. %. The resulting reinforced cements were characterized by available ASTM and ISO standards for bone cement evaluation. Along with the mechanical properties K_{IC}, FS and FM of the reinforced cements, the following properties were investigated: complex viscosity-versus-time, maximum polymerization temperature (T_{max}), dough time (t_{dough}), setting time (t_{set}), radiopacity, and *in-vitro* biocompatibility. On the basis of the determined mechanical properties, the optimized composition was found at 1wt. % n-TiO_2 fibers and 1 wt. % n-TiO_2 tubes. In the case of nanofibers this optimized loading provided a significant increase in K_{IC} (63%), FS (20%) and FM (22%) of the cement, while in the case of nanotubes it provided a more significant increase in K_{IC} (73%), FS (42%) and FM (56%). In both cases, the handling properties and *in-vitro* biocompatibility of the reinforced cements compared to that exhibited by the control cement (CMW$^{®}$1) were retained. Moreover, compared to the control cement, there was no significant change in the radiopacity of any of the reinforced cements at P=0.05. Enhanced interaction and strong adhesion between the functionalized n-TiO_2 and acrylic matrix allows external mechanical stress to be more effectively transferred through the filler-matrix interface. This novel approach to reinforce polymer matrix with a small loading of n-TiO_2 in conjunction with existing fillers can be applied to any kind of acrylic or resin based composite including orthopaedic and dental cements without altering other important cement properties such as the rheology, radiopacity or biocompatibility.

7.1. Introduction

Self-curing acrylic cements have been widely used in orthopaedic surgery for the fixation of joint prostheses in cemented arthroplasties.[137,248] Cemented total joint arthroplasties are cost-effective interventions for reducing pain, improving function, and enhancing the quality of life in patients with arthritis of the hip and knee.[28,221] In this application, the main functions of the bone cement are to transfer body weight and service loads from the prosthesis to the bone and /or increase the load-carrying capacity of the prosthesis-bone cement-bone system.[2,12] Due to the excellent primary fixation of the implant and fast recovery times for the patient, cemented arthroplasties are drawing significant attention world-wide.[13] However, in-spite of having admirable records of performance, commercial bone cements suffer from poor mechanical performance which facilitates their failure due to bending induced breakage and fracture related cracking [99,249] A typical successful total hip replacement has a service life of 10-20 years with over 75% of failures due to aseptic loosening, attributed to the cement mantle failure.[102] According to a survey performed in 2003, bone cement failure is responsible for a significant portion of the estimated 36,000 revision hip arthroplasties in the United States.[99,250,251] Therefore, there is a considerable interest to improve the mechanical properties of acrylic cement.

One of the main efforts in the improvement of bone cements is to reinforce the existing cements by incorporating small amounts of various additive materials into the cement matrix.[12] For example, stainless steel fibers, glass fibers, long macroscopic carbon fibers, polyethylene fibers, metal wires and titanium fibers have been added to bone cement, in attempts to enhance the transfer of external load as well as to hinder the crack propagation through the cement.[252-258] Due to the large size of the fillers, poor filler-bone cement matrix bonding (and subsequent debonding), nonuniform filler material distribution, and function of the pores as stress concentration sites are among the reasons why these efforts have been less than ideally successful.[99,222]

Nanotechnology provides a new avenue to develop composites with a combination of superior mechanical and physical properties. One of the main features of nanoparticles is their high surface area to volume ratio. This allows them to provide substantially higher interfacial area for load transfer when incorporated into a composite matrix compared to their micro counterparts.[160,259] Very few studies have examined the enhancement of mechanical properties of bone cements using nanotechnology. Marrs *et al.*[99] reported the augmentation of acrylic bone cement by incorporating multi-walled carbon nanotubes (MWCNT) into a cement matrix. An optimum composition of 2 wt. % MWCNT was found, which enhanced the flexural strength and bending modulus by 12.8 and 3.7 % respectively compared to the cement without MWCNT. This small increase in mechanical properties might be due to the lack of bonding between the MWCNT and the acrylic matrix. Moreover, there is a sustained debate on the biocompatibility of carbon nanotubes, and the bone cement reinforced with MWCNT may have adverse effects on the living cells surrounding the prosthesis.[99,100] J-H. Wang *et al.*[101] investigated the reinforcement of acrylic bone cement by incorporating organically modified montmorillonite (MMT) nanoclay into a cement matrix. A 54% increase in impact strength was found compared to the control cements by intercalating the acrylic polymer chains using 9 wt. % MMT. However, with nanoclay loading as high as 9 wt.%, the intercalation of PMMA chain into the inter-lameller spaces of MMT may pose an adverse effect on the rheological properties of the resulting cements, which was not investigated. Hill *et al.*[102] Investigated the inclusion of calcium carbonate ($CaCO_3$) nanoparticles into a bone cement matrix (Colacryl B866) in an attempt to increase its mechanical properties. In order to enhance the dispersion of the nanoparticles, its surface was treated with sodium citrate. An optimum loading of 0.25 wt. % $CaCO_3$ nanoparticles was reported which exhibited an increase in bending strength and bending modulus by 6.5 and 7.4 %, respectively, compared to the control cement. This poor increase in bending properties is attributed to the lack of adhesion between the nanoparticles and the cement matrix. A. H. Gomoll *et al.*[103] reported the enhancement of mechanical strength of a commercial bone cement by incorporating nano-sized (100 nm) $BaSO_4$ particles. A 41% increase in tensile strain-to-failure and 70% increase in tensile work-of-fracture were reported for the cement containing 10 wt.% nanosized $BaSO_4$ particles, compared with the micron sized commercial $BaSO_4$ particles. However, without having any chemical bonding between the inter-bead PMMA matrix and the nano-$BaSO_4$ particles, the ultrafine nanoparticles may release from wear into the surrounding biological tissue, causing inflammation and implant loosening.

Thus, nanostructured fillers that are capable of establishing a chemical bond with the acrylic matrix of a commercial orthopaedic cement, by preventing phase separation, may help to enhance its mechanical properties without compromising radiopacity and rheological properties.[28,172] Moreover, chemical bonding between the acrylic matrix and the nanofillers is expected to reduce the production of abrasive nanofiller debris in tissue surrounding the prosthetic joints.[50] In the present work we used nano-sized titania fibers and tubes as the reinforcing agents in the matrix of the commercial bone cement, CMW®1. In order to compatibilize the inorganic n-TiO_2 with the organic polymer matrix, we have functionalized the n-TiO_2 using a bi-functional monomer, methacrylic acid, which is capable of binding the surface of n-TiO_2 through its carboxylic group while establishing a molecular bridge with the PMMA matrix by covalent bonding through its vinyl (C=C) bond.

Although titania is an established biocompatible material,[97] nanomaterials are well known to exhibit completely different characteristics at their nano-dimensions, often being more toxic. This is attributed to their larger surface area, enhanced chemical reactivity, and easier penetration into cells.[119] Hence, bone cement reinforced with n-TiO_2 needs to be evaluated in terms of osteoblast cell adhesion, proliferation and in general cytotoxicity.

The objectives of the present study are to investigate the influence of the inclusion of n-TiO_2 fibers and tubes on the following properties of the commercially-available PMMA bone cement, CMW®1: complex viscosity-versus-time, maximum polymerization temperature, dough time, setting time, radiopacity, fracture toughness, flexural strength and flexural modulus. This study also investigates the *in vitro* biocompatibility of the cement reinforced with n-TiO_2 fiber and tubes using primary osteoblasts obtained from rat calvarias.

7.2. Experimental details

7.2.1. Materials

The n-TiO_2 fibers were synthesized using a direct sol-gel method in supercritical carbon dioxide, while the n-TiO_2 tubes were synthesised using an alkaline hydrothermal technique.[223,128] The commercially-available cement used was CMW®1 (Depuy, Warsaw, IN, USA) (for its composition, see Appendix 4), with an average molecular weight of its prepolymerized PMMA mixed in the powder part as 535 kDa (as measured by GPC, see appendix 5). In order to functionalize the n-TiO_2, 2-propanol and MA (99.99%, Sigma-Aldrich) were used as received. Moreover, the materials for the *in vitro* biocompatibility study were the same as described in section 2.7 of Chapter 2.

7.2.2. Functionalization of n-TiO_2

The synthesized n-TiO_2 fibers were calcined at 600°C to impart crystallinity and thermodynamic stability.[171] Similarly, the synthesised hydrogen titanate nanotubes were calcined at 400°C in air in order to obtain anatase n-TiO_2 with tubular morphology.[227,228] In order to functionalize the surface of both the nanofibers and tubes, 0.1 g of calcined n-TiO_2 powder was dispersed in 35 mL of 2-propanol with the aid of ultrasonic agitation, followed by reacting with 3 mL of MA at 80-85 °C for 24 hours with constant stirring. The reaction was carried out at pH 5.5 (as measured by pH meter UWR SB301) adjusted by adding a few drops (10-12 drops) of potassium hydroxide solution (0.3 N) to the reaction mixture prior to the reaction.

7.2.3. Preparation of reinforced CMW1 composites

Bone cements are prepared clinically by a free radical bulk polymerization technique by mixing the liquid and powder components in ratios as specified by the manufacturer. During the preparation of n-TiO_2-CMW1 cement in this work, the functionalized TiO_2 was dispersed in the liquid monomer portion of the CMW®1 cement by ultrasonic agitation for 15 minutes. The CMW®1 powder portion was added to liquid monomer containing the dispersed n-TiO_2 at a ratio of 2.18 and hand mixed into a dough state and loaded into Teflon molds. The molds were kept for 24 h at room temperature for complete curing. Nanocomposite specimens with 0.5, 1.0, 1.5 and 2.0 wt% loading of functionalized n-TiO_2 were prepared. Moreover, control specimens were produced using the as received CMW® 1 cement.

7.2.4. Characterization of reinforced cements

The morphology of the functionalized n-TiO_2 fibers and tube as well as the $BaSO_4$ particles in the cement powder were investigated using a scanning electron microscope (SEM, LEO 1540XB, Zeiss, Oberkochen, Germany) at an accelerating voltage of 1 kV. The micrographs of fracture surfaces of the reinforced cements after the fracture toughness test were also examined using the same scanning electron microscope.

The evolution of the polymerization process was observed at a working temperature of 37 °C according to the technique described in Chapter 2. The maximum temperature and setting time were measured and calculated as described by ISO 5833 standards,[136] with the results being the average of at least three measurements.

The rheology of the cement was determined using a rheometer (AR 2000ex, TA instruments Ltd. Delaware, USA) in terms of the complex viscosity of the cement dough as a function of time elapsed from commencement of mixing the powder and liquid components. The tests were performed according to the method described in Chapter 2. All measurements (n=3) were made at 37 ± 1 °C in order to mimic the body temperature. The onset time of viscosity increase and the curing time of the cement were determined from the complex viscosity-versus-time results, with the values compared to the setting times as measured according to ISO 5833.

The radiopacity of the reinforced cements containing 0.5, 1.0, 1.5 and 2.0 wt% n-TiO_2 fiber and tube separately as well as the control cement in terms of equivalent Al thickness were determined according to the method described in Chapter 2. From the Al step-wedge radiograph, a calibration curve relating the logarithm of % RGB vs. the logarithm of Al thickness was constructed (Figure 7.1). The radiopacity of the specimens was

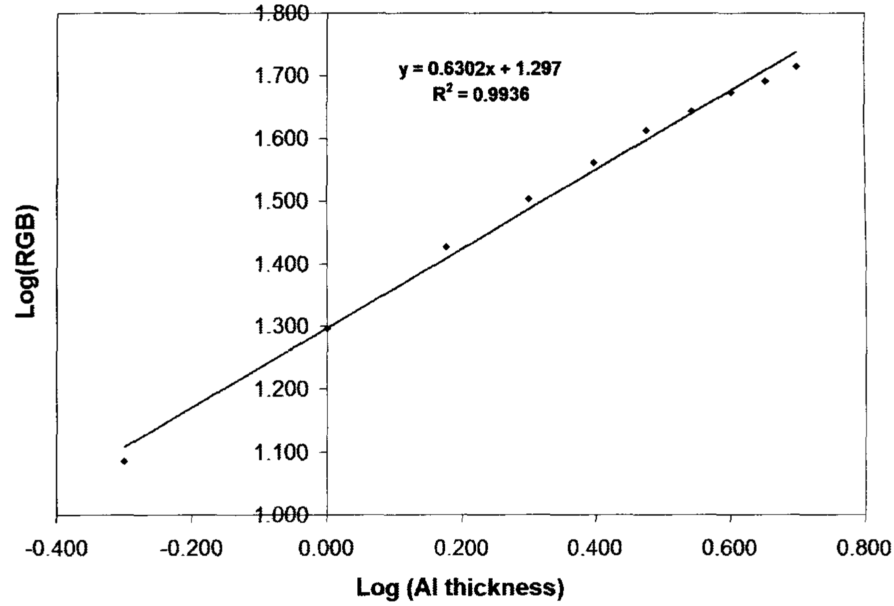

Figure 7.1. Calibration curve of % RGB versus Al thickness for measuring the radiopacity of n-TiO_2-CMW1 composites

calculated from the regression (R^2=0.9936) equation obtained from the calibration curve in terms of mm Al thickness as shown below:

$$\log(\mathrm{Al}) = \frac{\log(\%\mathrm{RGB}) - 1.297}{0.6302} \qquad (7.1)$$

To obtain the radiopacity in terms of Al equivalent of 1mm specimen thickness, each radiopacity value was divided by its specimen thickness.

K_{IC} of the reinforced cements was determined using the notchless triangular prism (NTP) specimens according to the method described in section 2.7 of Chapter 2.with the method developed by Ruse *et al.*[149] This is a simplified modification of the Chevron notched short rod (CNSR) method, which is a recommended method for evaluating the K_{IC} of bone cements according to ASTM B771-87.[148,260]

Both the FS and FM of the reinforced cements were determined by the four-point bending test in accordance with the ISO 5833[102,136] specifications. The testing procedure is described in section 2.7 of Chapter 2.

7.2.5. Determination of *in vitro* biocompatibility

In vitro biocompatibility was evaluated for the cement reinforced with 1wt% functionalized n-TiO_2 fibers and tube separately as well as the control cement using disc specimens, 14.0 mm in diameter and 1.0 mm in thickness. In order to avoid the effect of unreacted monomer, all the cement specimens were subjected to incubation at 60 °C for 72 hours prior to the cell culture. Moreover, specimens were plasma cleaned using argon gas and plated in 24 well tissue culture plastic before seeding the RCOs. Proliferation and live/dead analysis of RCOs were performed according to the method described in section 2.7.5 of Chapter 2 and section 6.2.6 of Chapter 6.

7.3. Results and Discussion

7.3.1. Reinforcement of CMW®1 with n-TiO_2 fibers

7.3.1.1. Morphological features and fracture surfaces

The morphology of the functionalized n-TiO_2 fibers as well as the $BaSO_4$ particles mixed in the CMW®1 powder as observed by SEM are shown in Figure 7.2.

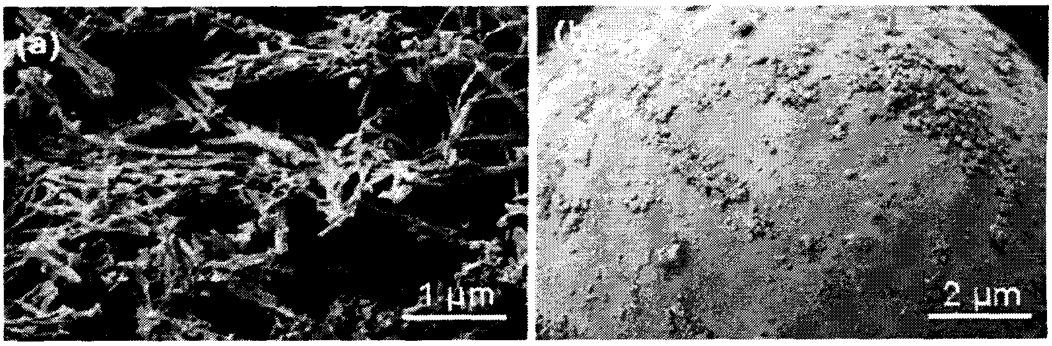

Figure 7.2. SEM: (a) Functionalized n-TiO_2 fibers; (b) $BaSO_4$ particles on PMMA beads of CMW®1

These micrographs show that n-TiO_2 following functionalization preserve their fibrous shape, while the $BaSO_4$ particles mixed by the manufacturer in the CMW®1 powder exhibit irregular shape morphology with a wide size range from 200 to 700 nm. The size and length distribution of the n-TiO_2 fibers were shown previously in Figure 3.4 of Chapter 3 which revealed an average diameter and length of 12 nm and 2 μm respectively.

The fracture surfaces of the cements obtained after the fracture toughness test were also examined under SEM with the micrographs are shown in Figure 7.3. The fracture surface of the CMW®1 cement (control) is shown in Figure 7.3 a, while Figure 7.3 b and c show the fracture surfaces of the CMW®1 cement matrix loaded with 1 and 2wt% functionalized n-TiO_2 fibers, respectively.

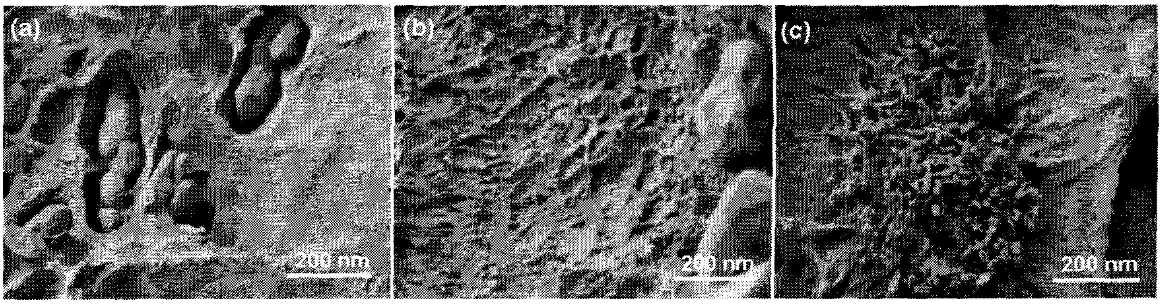

Figure 7.3. SEM: (a) Fracture surface of CMW®1; (b) Fracture surface of 1% functionalized n-TiO_2fibers-CMW1 and (c) Fracture surface of 2% functionalized n-TiO_2 fibers-CMW1.

As shown in Figure 7.3 a, some $BaSO_4$ particles are debonded from the matrix while some are loosely embedded in it surrounded by a number of pores. Figure 7.3 b shows that the n-TiO_2 fibers (1 wt.% loading) are surrounded by the $BaSO_4$ particles in the cement matrix, but unlike the $BaSO_4$ particles, the n-TiO_2 fibers are strongly embedded in the cement matrix. However, at 2wt% loading the n-TiO_2 fibers become agglomerated in the cement matrix (Figure 7.3 c). Functionalization provides organophilicity to the n-TiO_2 fibers, which resulted in strong adhesion of the nanofibers with the PMMA matrix. However, being incompatible with the acrylic matrix, $BaSO_4$ particles exhibited only a weak adhesion to the PMMA matrix.

7.3.1.2. Setting parameters of the cements

The setting parameters (t_{dough}, t_{set} and T_{max}) of CMW® 1 and CMW® 1 loaded with 0.5, 1.0, 1.5 and 2.0 wt.% n-TiO_2 fibers were determined from the time-temperature graphs of the curing cements (Figure 7.4), with the values listed in Table 7.1. As shown in the figure, T_{max} exhibited the highest value for the control cement, with this value decreasing with increasing incorporation of functionalized n-TiO_2 fibers. On the other hand, the value of t_{dough} and t_{set} for each of the reinforced cements increases with the wt. % of n-TiO_2 fibers. Setting parameters determine the handling/working characteristics of bone cements as well as the maximum temperature generated during the polymerization.

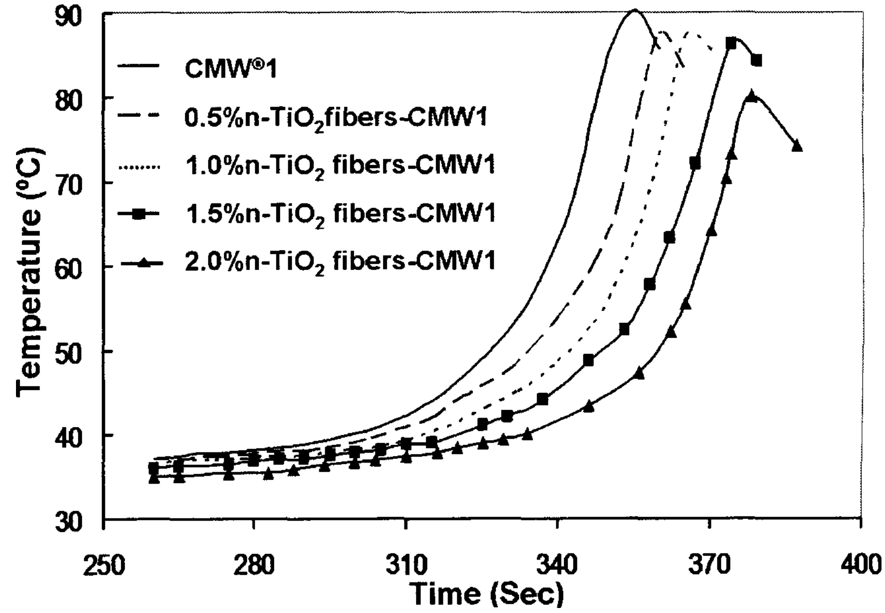

Figure 7.4. Variation of the temperature of the cements with the curing time

In order to simulate body conditions, the setting parameters were evaluated at 37 °C. As shown in Table 7.1, CMW®1 cement containing 6 wt.% $BaSO_4$ particles exhibits a peak temperature of 90.33 °C,[137] with this value decreasing with increased incorporation of n-TiO_2 fibers. In explanation, T_{max} results from the exothermic polymerization of the liquid monomer initiated by BPO. The observed decrease in the polymerization exotherm can be attributed to: 1) a decreased concentration of BPO in the modified cements,[137] and 2) a higher surface area from the nanofibers helping to dissipate the heat of polymerization. For similar reasons, the dough time and setting time increased when the amount of filler was increased.[33,212,261]

Table 7.1. Physical and mechanical properties of CMW® 1 and n-TiO_2 fibers-CMW1 composites

Cement property	Cement				
	Control	0.5 wt.% n-TiO_2 fiber-CMW1 composite	1.0 wt.% n-TiO_2fiber-CMW1 composite	1.5 wt.% n-TiO_2fiber-CMW1 composite	2 wt.% n-TiO_2fiber-CMW1 composite
t_{dough} (min)	2.10 (0.06)^a	2.15 (0.07)^a	2.20 (0.05)^a	2.28 (0.12)^b	2.33(0.08)^b
t_{set} (min)	5.77 (0.08)^c	5.85 (0.08)^c	5.91 (0.08)^{bc}	6.03 (0.07)^{ab}	6.10 (0.11)^a
T_{max} (°C)	90.33 (1.28)^b	87.67 (0.66)^b	87.27 (1.80)^b	86.30 (1.90)^b	80.73 (3.93)^a
t_{ons} (min)	5.71 (0.04)^c	5.81 (0.07)^{bc}	5.89 (0.03)^b	6.06 (0.06)^a	6.11 (0.05)^a
t_{cure} (min)	6.34 (0.02)^c	6.42 (0.04)^b	6.48 (0.06)^b	6.57 (0.03)^a	6.63 (0.05)^a
Radiopacity (mm Al)	0.35 (0.011)^a	0.36 (0.028)^a	0.37 (0.004)^a	0.37 (0.019)^a	0.35 (0.036)^a
K_{IC} (MPa.m$^{1/2}$)	0.80 (0.03)^d	0.98 (0.03)^c	1.32 (0.03)^a	1.21 (0.04)^b	1.10 (0.02)^b
FS (MPa)	63.76 (2.06)^a	68.08 (2.65)^b	79.53 (2.66)^d	72.10 (1.93)^c	70.13 (3.01)^{bc}
FM (GPa)	2.44 (0.06)^a	2.71 (0.12)^b	3.13 (0.04)^d	2.89 (0.07)^c	2.78 (0.08)^{bc}

Mean (2SE), $P<0.05$

However, with a small loading of n-TiO_2 fibers (up to 1 wt.%), this phenomenon did not play a significant role, reflecting the result that the polymerization exotherm and dough and setting time do not significantly change with the addition of 1 wt.% n-TiO_2 fibers when compared with CMW®1 at $P>0.05$.

and setting time do not significantly change with the addition of 1 wt.% n-TiO_2 fibers when compared with CMW®1 at P = 0.05.

7.3.1.3. Rheology of the cements during curing

Rheological properties of the curing cement were evaluated in terms of viscosity change with time during the setting period. Figure 7.5 shows the complex viscosity of the CMW®1 cement and CMW® 1 reinforced with 0.5, 1.0, 1.5 and 2.0 wt% functionalized n-TiO_2 fiber as a function of time, three minutes after the start of mixing at a temperature of 37 °C.

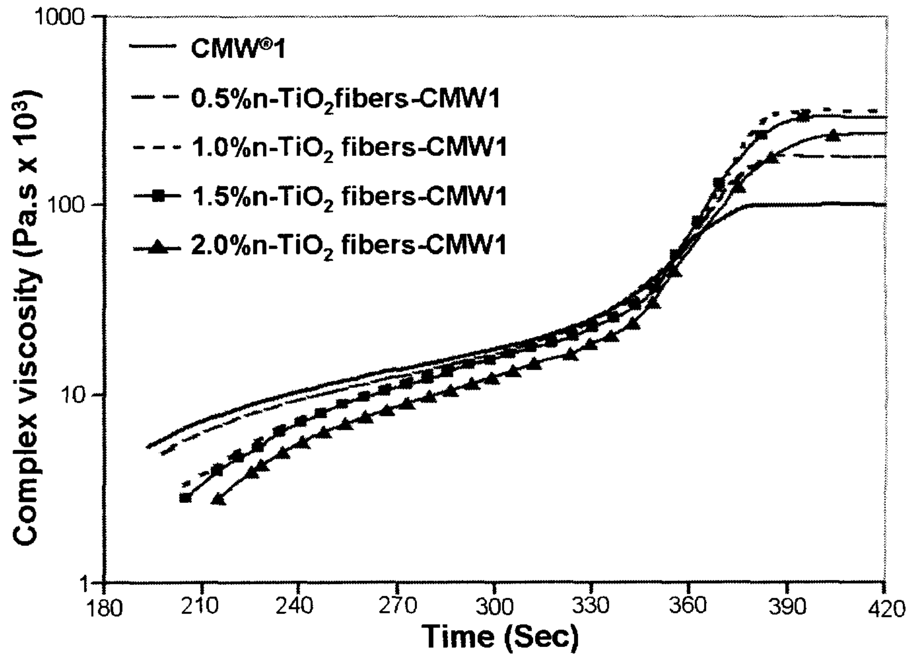

Figure 7.5. Viscosity during setting of CMW®1 and n-TiO_2 fibers-CMW1.

The rheological properties of bone cements during their curing phase are very important in determining their mixing/handling characteristics and viscoelastic properties. Furthermore, these properties have a significant influence on material porosity, ability to penetrate into bone, and the ultimate strength of the cement/prosthesis interface.[25] As shown in Figure 7.5, all the examined cements exhibit three distinct phases in the traces of complex viscosity versus time. There is an initial increase in viscosity which is followed by a plateau and then a final rapid increase in viscosity. The initial increase in viscosity is due to the swelling and dissolution of the PMMA beads in liquid monomer, while the final rapid increase in viscosity is due to polymer formation. [26,134] At the final stage of plateau, the cement viscosity is the highest and the cement is fully cured. It is clear from this figure that CMW®1 exhibits the highest initial viscosity, while the viscosity of the reinforced cements decreases with increasing incorporation of n-TiO_2. Moreover, in the case of CMW®1, the complex viscosity rises to the highest value faster than for any of the experimental reinforced cements.

There are two important setting parameters that can be obtained from the complex viscosity-time curves: 1) the onset time t_{ons}, is the time for the PMMA beads to dissolve and swell in monomer controlling the viscosity increase, and 2) the time when the cement mass reaches the plateau of the highest viscosity, is called the curing time, $t_{cure.}$[133,134] As studied by L. Hernandez *et al.*[25] there is a linear relationship between t_{ons} and $t_{set,}$ meaning the faster the increase of viscosity, the faster the setting of the cement. The values of t_{ons} and t_{cure} of the studied cements as determined from Figure 7.5 are summarized in Table 7.1. It is apparent that the magnitudes of both t_{ons} and t_{cure} for CMW®1 cement increase with an increasing amount of n-TiO_2 fibers. For example, with the incorporation of 1% n-TiO_2 fiber, the t_{ons} and t_{cure} of the cement increase about 3.1 and 2.2%, respectively, compared to CMW®1. CMW®1 is a known fast setting cement with low t_{ons} and $t_{set.}$[1]

When increasing the incorporation of n-TiO_2 fibers into the cement, the polymer to monomer ratio (P/M) in the cement mixture decreases, in part leading to the lower initial viscosity and longer setting times of the reinforced cements.[212] Hence, at 1wt% loading, the n-TiO_2 fibers does not influence the cements rheology; rather the P/M ratio plays a vital role to elongate the t_{ons} and t_{cure}. For potential clinical injectability of the cement, the P/M ratio can be easily adjusted for desired handling times.

7.3.1.4. Radiopacity of the cements

The radiopacity values in Al equivalent of 1mm specimen thickness for CMW®1, as well as CMW® 1 reinforced with 0.5, 1.0, 1.5 and 2 wt% functionalized n-TiO_2 fibers are presented in Table 7.1. With 6% $BaSO_4$ particles, CMW®1 exhibits a radiopacity of 0.35 mm Al, which when loaded with n-TiO_2 up to 2% does not decrease significantly, at P=0.05. Therefore, the incorporation of n-TiO_2 fibers up to the level of loading studied experimentally does not significantly alter the radiopacity of the reinforced cement compared to the control.

7.3.1.5. Fracture toughness

Table 7.1 compares the K_{IC} values of both unreinforced CMW®1 and reinforced with 0.5, 1.0, 1.5 and 2wt% functionalized n-TiO_2 fibers.. It can be seen that the cement reinforced with 1wt% functionalized n-TiO_2 fibers exhibited significantly higher K_{IC} values amongst all other experimental composites, being 63% higher than the control cement CMW®1 at $P<0.05$. As shown in the Table, the CMW®1 bone cement exhibited a significantly lower value of K_{IC} compared to the cement reinforced with n-TiO_2. However, the K_{IC} started to decrease with an increased loading of n-TiO_2 fibers (above 1wt. %). K_{IC} is defined as the energy absorbed by the material prior to crack propagation.[2] It is a measure of the energy required to initiate and propagate a crack in a material, which may lead to catastrophic failure. Hence, K_{IC} is a very important material property for bone cements which is also affected by the morphology and dispersion of the fillers as well as the filler-matrix interactions.[2,198] Being incompatible with the organophilic PMMA matrix, the clumps of $BaSO_4$ particles are debonded from the matrix during tensile loading resulting in the generation of pores within the CMW®1 cement. These pores act as stress concentrators and sites for initiating crack propagation during tensile loading on the cement.[2,28,172] This is also reflected by the SEM image of the fracture surface of the control cement as shown in Figure 7.3 a, where the $BaSO_4$ particles are shown to be protruding above the fracture plane.[2,198,262] No polymer is observed to be attached to the particles, providing no adhesion of the particles to the matrix. CMW®1 reinforced with 1wt% functionalized n-TiO_2 fibers exhibited the highest value for K_{IC}, attributed to the excellent dispersion of the nanofibers in the polymer matrix as well as the stronger interfacial bonding between the nanofibers and PMMA matrix, as reflected by Figure 7.3 b. As the advancing crack plane contacts the filler material, further propagation of the crack front demands additional energy be provided to separate the filler-matrix interface in this case, which results in the increased values of fracture toughness.[200] However, K_{IC} values started to decrease with an increased loading of n-TiO_2 fibers (over 1wt. %) attributed to the agglomeration of the n-TiO_2 in the cement matrix (Figure 7.3 c).

7.3.1.6. Flexural strength and modulus

Table 7.1 compares the FS of both unreinforced CMW®1 and that reinforced with 0.5, 1.0, 1.5 and 2.0 wt.% functionalized n-TiO_2 fibers. It is clear from this Table that 1% functionalization achieves the highest value of FS, which is approximately 24% higher than for the control cement ($P<0.05$). The values of FS, similar to K_{IC}, start decreasing with increased loading of n-TiO_2 fiber over 1 wt.%. Table 7.1 also provides a comparison of the FM of the cement and reinforced cements, which exhibits similar behaviour as in the case of FS. The FS and FM of bone cement reflect its resistance to flexural loading, which is a combination of tension and compression forces. The flexural properties (FS and FM) of reinforced composites are influenced mostly by the degree of interfacial adhesion and interaction between the filler materials and matrix, which determines the effectiveness of the transfer of interfacial shear stress from the filler to the matrix.[12] The high observed value of FS of the CMW1 reinforced with 1 wt.% n-TiO_2 fibers is attributed to the strong interfacial bonding of the functionalized n-TiO_2 fibers with the acrylic matrix, which facilitates the transfer of interfacial shear stress from the filler to the matrix.[206] The determined increase in FS is substantially higher than those obtained by incorporating other nanofillers in previous works.[99,102] The FS, similar to fracture toughness, starts decreasing with increased loading of n-TiO_2 over 1%, which is also attributed to the observed agglomeration of nanofibers in the cement matrix. Table 7.1 also provides a comparison of the FM of the cement and reinforced cements, which exhibits similar behaviour as in the case of FS.

7.3.1.7. In vitro biocompatibility of the reinforced cements

Cell morphology of RCOs as revealed from the florescence microscopic images (Figure 7.6), is similar for both CMW®1 and 1% n-TiO_2 fiber-CMW1 surfaces. RCOs attached and spread on both cement surfaces by 24 hours (Figure 7.6 a, b) and reached confluency near 72 hours (Figure 7.6 e, f). No differences in cell morphology were observed between CMW®1 and 1% n-TiO_2 fiber-CMW1 at any time. Analysis of cell numbers revealed a 3.5 fold increase at 48 hrs, and a 6.5 fold increase at 72 hrs on both the cement surfaces (Figure 7.7 a).

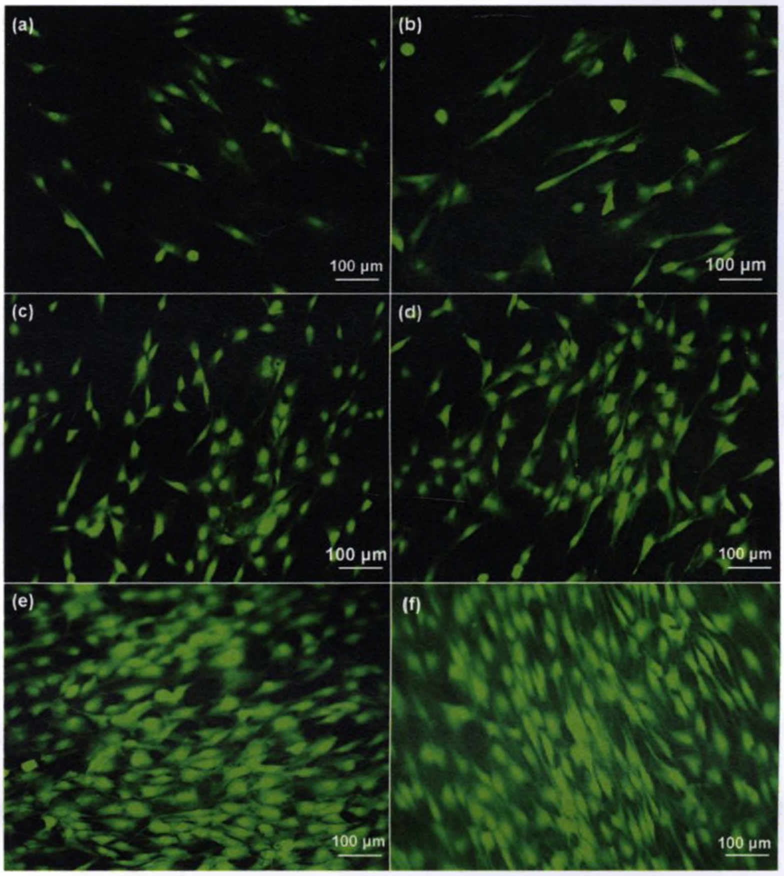

Figure 7.6. RCOs proliferation on cement surfaces in 24 hours: (a) CMW®1, (b)1% n-TiO_2 fiber-CMW1; in 48 hours: (c) CMW®1, (d) 1% n-TiO_2 fiber-CMW1; and in 72 hours: (e) CMW®1, (f) 1% n-TiO_2 fiber-CMW1. Cells were fixed with 4% PFA and stained with invitrogen's live/dead kit.

Analysis of live/dead cells revealed cell viability ranging from 97 - 99% with no significant difference (P=0.05), suggesting that both CMW®1 and 1% n-TiO_2 fiber-CMW1 are extremely biocompatible *in vitro* as shown in Figure 7.7 b. Therefore, it is obvious that CMW1 retains its excellent biocompatibility even after being reinforced with n-TiO_2 fibers.

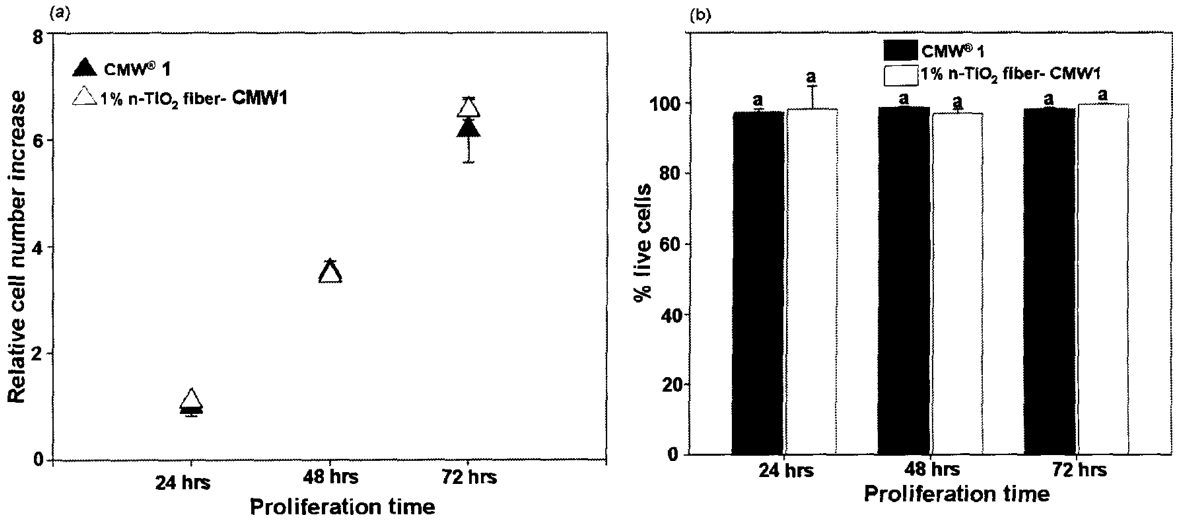

Figure 7.7. a) Proliferation and b) Live/dead analysis of RCOs seeded on CMW®1 and 1% n-TiO$_2$ fiber-CMW1.

From the above results, it can be rationalized that functionalized n-TiO$_2$ fiber acts as a reinforcing agent for the CMW® 1 bone cement by enhancing its mechanical and physical properties. The radiopacity was unaltered while the handling properties were only slightly affected according to the rheology study, but not significantly affected according to ISO 5833. Moreover, incorporation of the functionalized n-TiO$_2$ fibers retained the cyto-compatibility of the cement as confirmed from the *in-vitro* biocompatibility test.

7.3.2. Reinforcement of CMW®1 with n-TiO$_2$ tube

7.3.2.1. Morphological features and fracture surfaces

The morphology and microstructure of the calcined n-TiO$_2$ tubes after functionalization were shown by SEM and TEM in Figure 5.2 in chapter 5, reflecting its hollow tubular shape. The size and length distribution as shown in the same figure, revealed a mean value of the diameter and length of the n-TiO$_2$ tubes as 8 nm and 1.67 μm respectively. The micrographs of the fracture surfaces of the cements obtained after the K_{IC} test were examined by SEM and are shown in Figure 7.8.

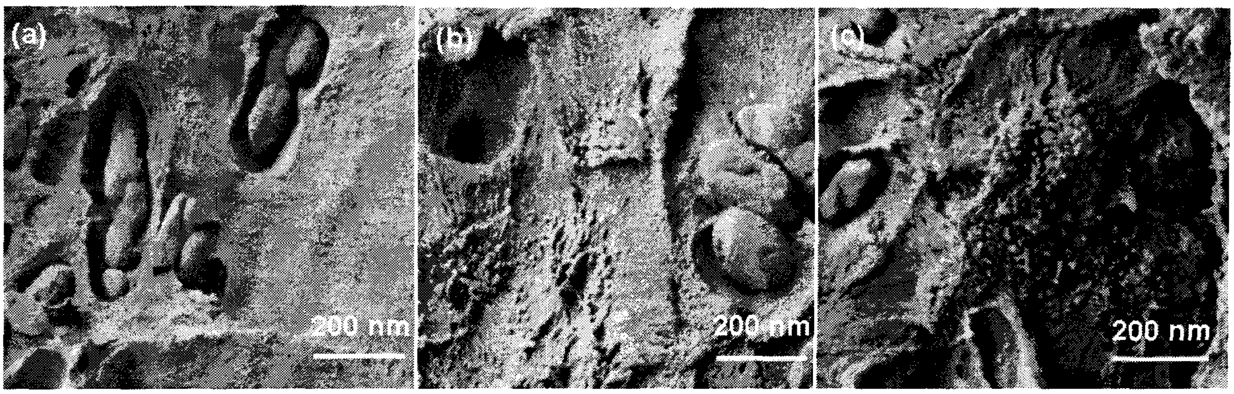

Figure 7.8. SEM: (a) Fracture surface of CMW®1; (b) Fracture surface of 1% functionalized n-TiO_2 tubes-CMW1 and (c) Fracture surface of 2% functionalized n-TiO_2 tubes-CMW1.

The fracture surface of the CMW®1 cement (control) is shown in Figure 7.8 a, while Figure 7.8 b and c show the fracture surface of CMW®1 cement matrix loaded with 1 and 2wt% functionalized n-TiO_2 tubes, respectively. As shown in Figure 7.8 a, the $BaSO_4$ particles are loosely embedded in the CMW®1 cement matrix with many of them removed from the matrix due to the poor adhesion. Figure 7.8 b shows that the n-TiO_2 tubes are strongly delaminated in the matrix while surrounded by the $BaSO_4$ particles. However, at 2wt% loading the n-TiO_2 tubes become agglomerated in the cement matrix (Figure 7.8 c). The functionalized n-TiO_2 tubes establish strong adhesion to the cement matrix resulting from the covalent chemical bonding between the nanotubes and the acrylic matrix.

7.3.2.2. Setting parameters of the reinforced cements

The setting parameters, (t_{dough}, t_{set}, and T_{max}), of CMW® 1 and CMW1 loaded with 0.5, 1.0, 1.5 and 2.0 wt.% n-TiO_2 tubes were determined from the time-temperature graphs of the curing cements with the values listed in Table 7.2. As shown in this table, the T_{max} exhibited the highest value for the control, i.e. 90.33 °C, with this value decreasing with increasing % incorporation of the functionalized n-TiO_2 tubes.

Table 7.2. Physical and mechanical properties of CMW$^{®}$ 1 and n-TiO_2 tubes-CMW1 composites.

Cement property	Cement				
	Control	0.5 wt.% n -TiO_2 tube-CMW1 composite	1.0 wt.% n -TiO_2 tube-CMW1 composite	1.5 wt.% n -TiO_2 tube-CMW1 composite	2 wt.% n -TiO_2 tube-CMW1 composite
t_{dough} (min)	2.10 (0.06)^a	2.14 (0.07)^a	2.21 (0.14)^a	2.26 (0.16)^a	2.33 (0.03)^a
t_{set} (min)	5.77 (0.02)^a	5.81 (0.05)^a	5.88 (0.04)^a	5.95 (0.05)^b	6.05 (0.04)^c
T_{max} (°C)	90.33 (1.28)^a	88.22 (0.66)^a	87.29 (1.80)^{ab}	86.13 (1.90)^b	79.10 (3.93)^c
t_{ons} (min)	5.71 (0.04)^a	5.75 (0.05)^a	5.78 (0.05)^a	5.81 (0.05)^a	5.85 (0.08)^a
t_{cure} (min)	6.34 (0.02)^d	6.36 (0.02)^{cd}	6.40 (0.04)^c	6.47 (0.04)^a	6.55 (0.05)^a
Radiopacity (mm Al)	0.32 (0.016)^a	0.32 (0.006)^a	0.31 (0.004)^a	0.30 (0.02)^a	0.30 (0.006)^a
K_{IC} (MPa.m$^{1/2}$)	0.80 (0.03)^d	1.11 (0.06)^c	1.42 (0.09)^a	1.34 (0.11)^{ab}	1.28 (0.14)^b
FS (MPa)	63.76 (2.06)^a	75.31 (1.94)^b	90.73 (2.88)^c	75.95 (1.93)^b	75.92 (1.56)^b
FM (GPa)	2.44 (0.06)^a	3.27 (0.07)^b	3.81 (0.09)^c	3.46 (0.03)^d	3.33 (0.07)^b

Mean (2SE), $P<0.05$

Conversely, the value of t_{dough} and t_{set} for each of the reinforced cements increased with increasing wt.% of the n-TiO_2 tubes. The observed decrease in the polymerization exotherm is attributed to the additional surface area provided by the n-TiO_2 tubes (both internal and external) dissipating the heat of polymerization.[224] Similarly, an increased amount of n-TiO_2 tubes contributes to the presence of residual monomer which may diffuse slowly out of the tubes causing the observed longer working and setting times for the reinforced cements.[33,261] However, like n-TiO_2 fiber, with a small loading of n-TiO_2 tubes (up to 1 wt.%), this phenomenon did not play a significant role, reflecting the result that the polymerization exotherm and dough and setting time do not significantly change with the addition of 1 wt.% n-TiO_2 tubes in comparison to CMW$^{®}$1 at $P>0.05$ (Table 7.2).

7.3.2.3. Rheology of the reinforced cement during curing

Rheological properties of the curing cement were evaluated in terms of the viscosity change with time during the setting period. Figure 7.9 shows the complex viscosity of the

CMW®1 cement and CMW 1 reinforced with 0.5, 1.0, 1.5 and 2.0 wt.% functionalized n-TiO_2 tubes as a function of time, at a temperature of 37 °C.

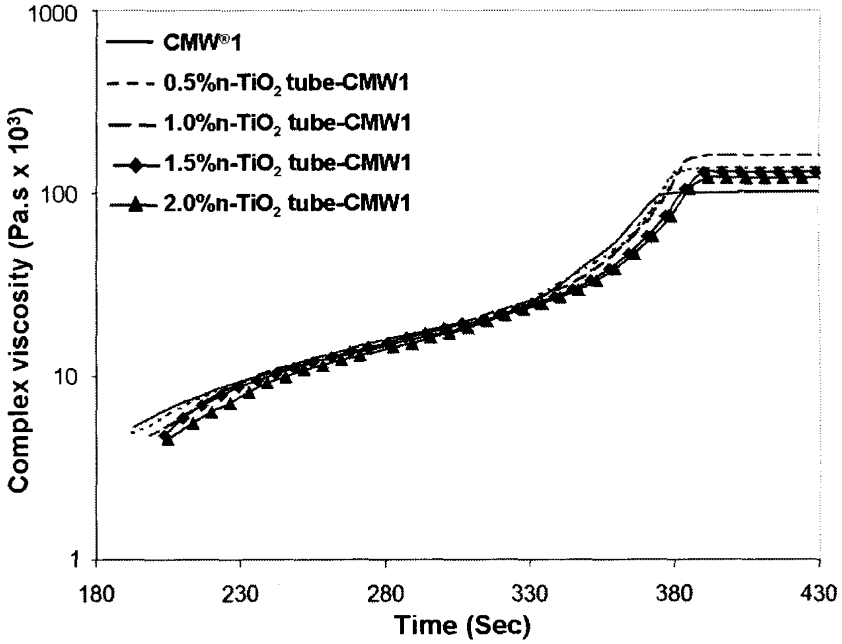

Figure 7.9. Viscosity during setting of CMW®1 and n-TiO_2 tubes-CMW1.

It is clear from this Figure that CMW®1 exhibits a higher initial viscosity than that of the reinforced cements with increasing incorporation of n-TiO_2 tubes. Moreover, in the case of CMW®1, the complex viscosity rises to the highest value earlier than for any of the experimental reinforced cements. However, the behaviour of the complex viscosity with respect to time in terms of t_{ons} and t_{cure} does not exhibit any statistically significant difference between the control and the reinforced cement with up to 1 wt.% of n-TiO_2 tubes, P=0.05, as displayed in Table 7.2. In the traces of complex viscosity versus time, all the examined cements exhibit an increase in viscosity from the slow initial start up phase to the rapid final plateau reflecting the transition from viscous to elastic (cured) phase. The initial increase in viscosity is due to the swelling and dissolution of the

PMMA beads in liquid monomer, while the final rapid increase in viscosity is due to the free radical polymerization of monomer.[26,134] There are two important setting parameters that can be obtained from the complex viscosity-time curves: 1) t_{ons}, is the time for the prepolymerized PMMA beads to control the viscosity increase through swelling and dissolution in monomer, and 2) t_{cure}, which is the time for the cement to reach the plateau of the highest viscosity.[133,134] The values of t_{ons} and t_{cure} of the studied cements, as determined from Figure 6.8, are summarized in Table 7.2. The magnitudes of both t_{ons} and t_{cure} for the modified cements increase with an increasing amount of n-TiO_2 tubes. For example, with the incorporation of 1% n-TiO_2 tubes, the value of t_{ons} and t_{cure} of the cement increases by about 1.22 and 0.95%, respectively, compared to CMW®1. When increasing the percentage n-TiO_2 tube in the cement, the proportionate reduction of PMMA beads leads to a decrease in the polymer/monomer ratio (P/M) in the cement mixture, in part leading to the observed lower initial viscosity and longer setting times of the reinforced cements. Hence, at all loadings, the n-TiO_2 tubes do not significantly influence the cements rheology; rather the P/M ratio plays a vital role to elongate the t_{ons} and t_{cure}. However, with a small loading of n-TiO_2 tubes (up to 1 wt.%), this phenomenon did not play a significant role, reflecting the result that the t_{ons} and t_{cure} do not significantly change with the addition of 1 wt.% n-TiO_2 tubes when compared with CMW®1 at $P>0.05$ (Table 7.2).

7.3.2.4. Radiopacity of the reinforced cements

The radiopacity values in Al equivalent of 1mm specimen thickness for CMW®1, as well as CMW 1 reinforced with 0.5, 1.0, 1.5 and 2 wt% functionalized n-TiO_2 tubes are presented in Table 7.2. With 6% $BaSO_4$ particles, CMW®1 exhibits a radiopacity of 0.33

mm Al, which when loaded with n-TiO_2 tubes up to 2%, does not decrease significantly, at $P>0.05$.

7.3.2.5. Fracture toughness of the reinforced cements

Table 7.2 displays the K_{IC} values of the CMW®1 reinforced with functionalized n-TiO_2 tubes at 0.5, 1.0, 1.5 and 2% loading, as well as the control cement. It can be seen that the cement reinforced with 1wt.% functionalized n-TiO_2 tubes exhibits significantly higher K_{IC} values amongst all other experimental composites, being 73% higher than the control cement CMW®1 at $P<0.05$. However, there is a decreasing trend of K_{IC} values at loading over 1% n-TiO_2 tube. As mentioned earlier, K_{IC} is a measure of the fracture tolerance capability of the bone cement, which is mostly affected by the adhesion of the fillers with the cement matrix. It was shown in Figure 7.8 a that the $BaSO_4$ particles are protruding above the fracture plane of the CMW®1 cement, due to the weak adhesion of the particles to the matrix. This poor adhesion accelerates debonding of the particles during tensile loading, resulting in the generation of microvoids within the matrix. These microvoids coalescence with the crack and accelerate its propagation through the matrix.[16,198,200] Functionalized n-TiO_2 tubes establish strong adhesion as well as enhanced interfacial interaction with the matrix, which can be noticed from the coherent continuous interface between the n-TiO_2 tubes and the cement matrix (Figure 7.8 b). This strong adhesion may help the modified cements in resisting and deflection of crack propagation generated from the voids caused by debonding of the $BaSO_4$ particles, which is also evidenced by the rough fracture surfaces. This observation is in aggrement with the literature.[200,262] However, at 2 wt% loading the n-TiO_2 tubes tend to agglomerate within the matrix and exhibit poor interaction resulting in lower mechanical properties compared to the composite reinforced with 1wt.% n-TiO_2 tube (Figure 7.8 c).

7.3.2.6. **Flexural strength and modulus of the reinforced cements**

Table 7.2 compares the FS of CMW®1 and CMW 1 reinforced with 0.5, 1.0, 1.5 and 2.0 wt% functionalized n-TiO_2 tubes. It is clear from the tabulated data that the cement reinforced with 1% n-TiO_2 tubes achieves the highest value of FS and FM which are approximately 42% and 56% higher than the control cement respectively ($P<0.05$). However, the FS, similar to K_{IC}, starts decreasing with increased loading of n-TiO_2 tubes over 1%. Table 7.2 also provides a comparison of the FM values of the CMW®1 and reinforced cements, which exhibit similar behaviour as in the case of FS. The results obtained for the FS and FM of the control and reinforced cements as given in Table 7.2 can also be explained by considering the degree of interfacial adhesion between the fillers and matrix. The extended and strong interfacial adhesion between the functionalized n-TiO_2 tube and acrylic matrix facilitate the effective transfer of the interfacial shear strength through the interface, which leads to the increased FM value of the reinforced cement.[206,207] A higher strength was obtained for the n-TiO_2 tube reinforced composite compared to that provided by the n-TiO_2 fiber at same level of loading. Hence, the hollow structure of the nanotube is believed to provide additional interlocking with the matrix through both the interior and exterior surfaces of the tubes. This is why the cement reinforced with 1 wt.% functionalized n-TiO_2 tube results in a marked increase in FS, which is accompanied by an increase in the FM. The determined increase in flexural properties is substantially higher than those obtained by incorporating different nanofillers in other works, as poorly bonded fillers cannot contribute effectively to an increase in FS.[99,102] The value of FS and FM in this work, similar to K_{IC}, starts decreasing with increased loading of n-TiO_2 tube over 1 wt%, which is also attributed to the observed agglomeration of nanotubes in the cement matrix.

7.3.2.7. *In vitro* biocompatibility of the reinforced cements

Figure 7.10 shows the adhesion and proliferation of RCOs on the control and reinforced cement surfaces over three days. The cell morphology of RCOs as revealed from this figure, is similar for both the CMW®1 and 1% n-TiO_2 tube-CMW1 surfaces. RCOs attached and spread on both cement surfaces by 24 hours (Figure 7.10 a, b) and reached confluency near 72 hours (Figure 7.10 e, f).

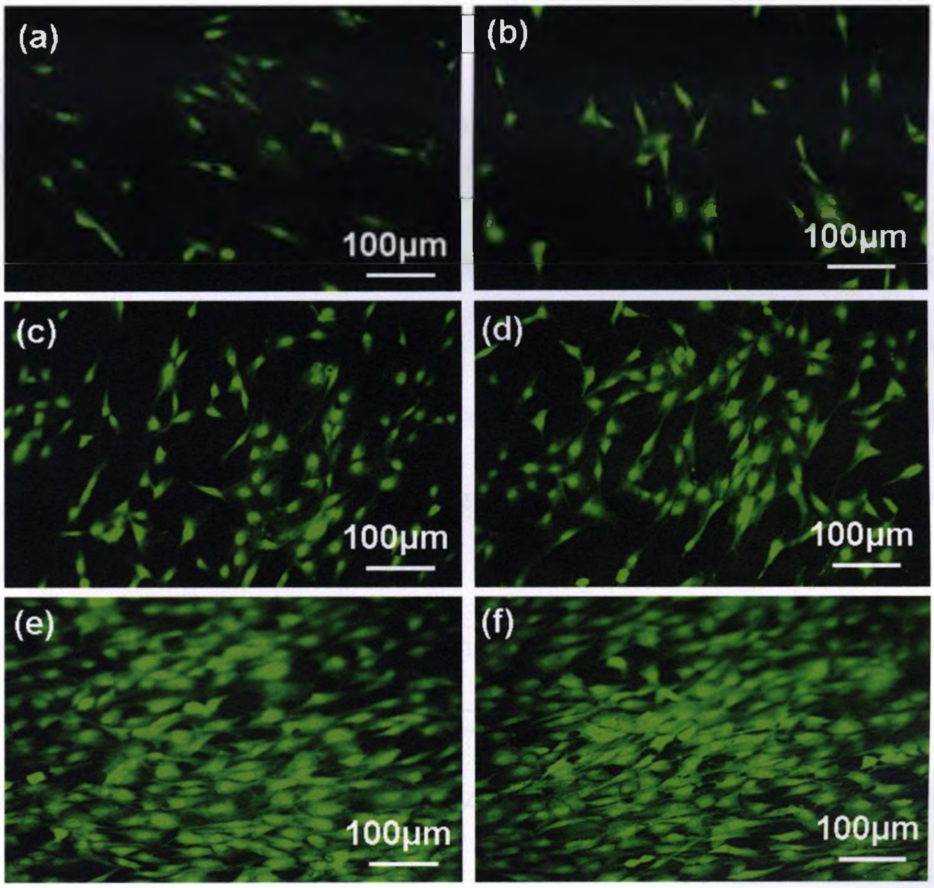

Figure 7.10. RCOs proliferation on cement surfaces in 24 hours: (a) CMW®1, (b)1% n-TiO_2 tube- CMW1; in 48 hours: (c) CMW®1, (d) 1% n-TiO_2 tube-CMW1; and in 72 hours: (e) CMW®1, (f) 1% n-TiO_2 tube-CMW1. Cells were fixed with 4% PFA and stained with invitrogen's live/dead kit.

No differences in cell morphology were observed between CMW®1 and 1% n-TiO_2 tube-CMW1 at any time.

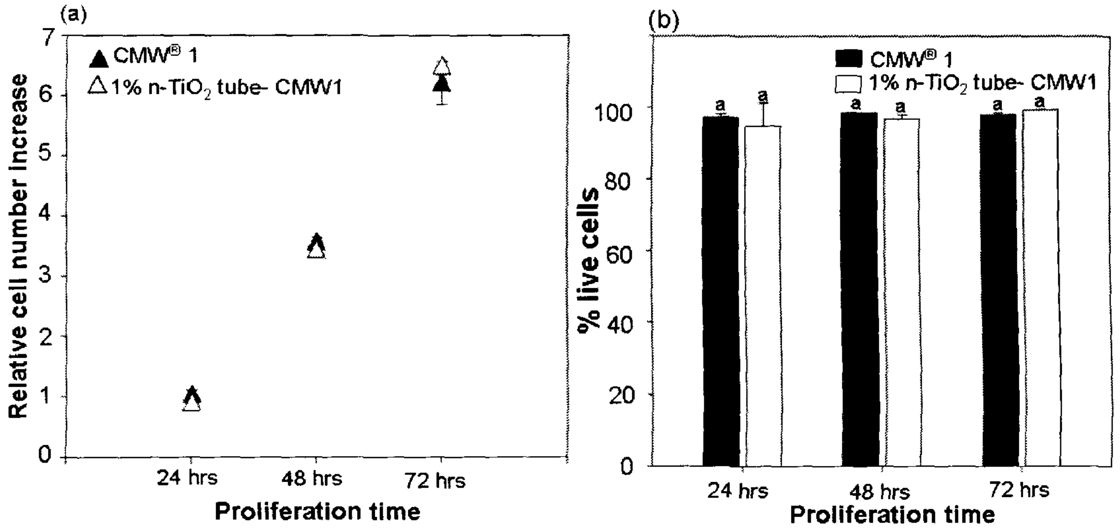

Figure 7.11. a) Proliferation and b) Live/dead analysis of RCOs seeded on CMW®1 and 1% n-TiO_2 tube-CMW1.

Analysis of cell numbers revealed a 3.5 fold increase at 48 hrs, and a 6.5 fold increase at 72 hrs on both the cement surfaces (Figure 7.11 a). Analysis of live/dead cells revealed that the cell viability ranged from 95 - 98% with no significant difference (P=0.05) suggesting that both CMW®1 and 1% n-TiO_2 tube-CMW1 are extremely biocompatible *in vitro* as shown in Figure 7.11 b. Therefore, from the cell-reinforced cement interaction as revealed from this study, it is obvious that the reinforced cement retains its cyto-compatibility after being reinforced with n-TiO_2 tubes.

From the above discussion, it can be rationalized that the functionalized n-TiO_2 tubes act as an effective reinforcement of the commercial bone cement by significant enhancement of its mechanical properties. The reinforcement did not alter other important physical properties of the cement such as radiopacity, setting and rheological characteristics.

Moreover, incorporation of the functionalized n-TiO_2 tubes retained the cyto-compatibility of the cement as confirmed from the *in-vitro* biocompatibility test.

7.4. Conclusion

Nano-sized titania fibers (n-TiO_2 fibers) and tubes (n-TiO_2 tubes) were successfully incorporated into CMW$^{®}$1 bone cement matrix as reinforcing fillers to produce nanocomposite bone cement. Enhanced mechanical properties of these nanocomposites were achieved due to the chemical interaction between these nanomaterials and the PMMA matrix. Amongst all tested nanocomposites, 1wt% n-TiO_2 tube provided the highest magnitude of flexural strength and fracture toughness with substantially higher values than those provided by the optimized 1wt% n-TiO_2 fibers. High aspect ratios (L/D: 209:1) and the hollow cylindrical shape of the functionalized n-TiO_2 tube establish extended and strong interfacial adhesion compared to that exhibited by the rigid n-TiO_2 fibers. Moreover, the optimized loading of the nanomaterials did not alter the handling properties, radiopacity and bio-compatibility of the commercial CMW$^{®}$1 cement. Nevertheless, being chemically bonded with the PMMA matrix of the cement,[20] the nanomaterials are less likely to become loose during wear, providing the possibility for longer service life.[50] This study demonstrated a novel technique to reinforce a wide variety of dental and orthopaedic cement without altering other expected properties such as radiopacity, rheology and biocompatibility.

Chapter 8: Summary and Conclusions

8.1. Outline

The successful reinforcement of poly(methyl methacrylate) matrix by nanostructured titania fiber and tubes shows that the incorporation of one-dimensional nanomaterials is a promising technique for augmenting the mechanical properties of acrylic based bone cements. The novel functionalizing technique presented in this thesis can be applied to a wide variety of ceramic oxide nanomaterials in order to establish chemical adhesion between the nanofillers and organic polymer matrix. The major outcomes from these studies include: (1) functionalized nanomaterials up to a certain limit of loading exhibit homogenous dispersion in the polymeric continuous phase; (2) one dimensional nanomaterials provide enhanced interaction with the polymer matrix because of their higher aspect ratio than that of the particulate materials; (3) reinforcement using nanomaterials is a promising technique only when there is a homogenous distribution of the nanomaterials to provide strong adhesion with the continuous phase; and (4) there is certain a critical loading of nanomaterials in the matrix which can provide effective reinforcement while keeping the rheology of the polymer unaffected.

The mechanical behaviour of any kind of composite reflects the interaction between the various phases. If there is no binding between the two phases either chemical or physical, the material's response to strain will be the same as the matrix which contains holes of a shape identical to that of the filler. On the other hand, if there is adhesion between the two phases, even at low strains, stress transfer can take place across the interface, thus allowing the filler to share the stress and by doing so, provide a reinforcing effect. In this study, the obtained reinforcing effect of the nanomaterials is attributed mainly to the strong interfacial chemical adhesion between the nanomaterials and the PMMA matrix. Titania nanotubes were found to be superior to titania nanofibers for the reinforcement of the acrylic matrix which is due to the higher aspect ratio of the nanotubes as well as the capability of the hollow nanotubes to bind to the matrix through their interior and exterior surfaces. However, both of these nanomaterials did not provide sufficient radiopacity to the PMMA matrix at the optimum level of loading which seems to be a major limitation for the potential application of the nanocomposites as bone cements.

In an attempt to address this limitation, this study focused on two different approaches: (1) treatment or modification of the titania nanomaterials to increase its radiopacity and; (2) incorporation of the nanostructured material into the commercial acrylic bone cement as reinforcing fillers while keeping the radiopacity of the cement intact.

The modification of the titania nanotubes was performed through a novel one stage hydrothermal technique by in-situ incorporation of strontium atoms into the layers of the titanate nanotube. The nanostructured titania tube modified with strontium atoms was shown to reasonably increase the radiopacity of the PMMA matrix. In addition, the presence of strontium favourably increased the biocompatibility of the nanocomposite to osteoblast cells. Strontium is chemically similar to calcium, which is one of the elements of bone mineral. The in situ modification technique presented in this study shows a promising way to incorporate different inorganic materials into tube layers for a wide variety of applications.

Moreover, the reinforcement of commercial bone cement by the functionalized nanofibers and nanotubes provides a promising alternative for augmenting the existing clinically used cements. As studied in this work, the loading of the functionalized nanomaterials was sufficiently small to alter the important cement properties of the commercial materials such as setting, flow, polymerization heat, biocompatibility and radiopacity. However, the mechanical properties were significantly increased because of the homogeneous dispersion of the nanomaterials with strong chemical adhesion with the matrix. This novel technique also demonstrates its potential in dental applications. In restorative dentistry, it is very common to use flowable resin composites in conjunction with a high stiffness restorative composite as an intermediate layer to relieve the contraction stress from the in-situ polymerization of the high modulus restorative. Typical characteristics of the flowable composites are low filler content which allows easy and convenient handling and insertion. Because of the low filler content, many commercial flowable composites are sufficiently weak to withstand significant occlusal force. The novel technique of incorporating nanomaterials in the commercial cement studied in this work can also be applied to enhance the mechanical properties of flowable composites which would act as reinforcing agents without altering flow properties.

8.2. Limitations of the work

There are some limitations of this study, which include the non-clinically relevant manner in which the cement powder and liquid monomer were mixed without following the vacuum mixing method. Moreover, omission of determining the fatigue life, fatigue crack propagation resistance and long term wear of the nanocomposites limits its immediate applicability and necessitates future work. However, the improvement in fracture toughness indicates a possible improvement in the fatigue life.[85,263] Similarly, being chemically bonded with the PMMA matrix of the cement,[20] the titania nanomaterials are less likely to become loose during wear, providing the possibility for longer service life.[50]

8.3. Future work recommendation

Recommendations for future work include:

1. Fatigue properties of the nanocomposites needs to be studied under sinusoidal cyclic loading to determine their life in the human body. One testing protocol reported in the literature is to use a four-point bending arrangement recommended by ISO5833 (ISO 2002)., The fatigue test will be carried out at frequencies ranging between 2-5Hz at stess levels 4-40N for five to ten million cycles in a buffered saline solution at 37 °C until failure occurs.
2. The amount of residual monomer of the reinforced composites as well as the leaching of unreacted monomer and activator enclosed in the bulk composites with time needs be studied by NMR and IR analysis as residual monomer content is a very important toxilogical issue for bone cement application.
3. The hydrothermal reaction to modify the titania nanotube with strontium atom need to be optimized in terms of concentration of strontium atom in the nanotubes. Moreover, the modified nanotubes need to be studied by HRTEM, XPS and XRD to evaluate the chemical and physical state of strontium oxide in the nano-tubular titania and how this can be controlled by the synthesis conditions.
4. In-vivo biocompatibility of the reinforced cements needs to be studied by implanting the cement in rat tibia for an extensive period of time.
5. The hydrothermal technique can be used to incorporate ferromagnetic materials such as cobalt and nickel oxide into the titania nanotube. These magnetically modified nanotubes

can be used to develop anisotropic nanocomposites by incorporating the modified nanotube in the polymer matrix in the presence of a strong magnetic field.

Bibliography

1. Kuhn K-D. Bone cements. New York: Springer; 2000. 246-247 p.
2. Lewis G. Properties of acrylic bone cement: state of the art review. Journal of Biomedical Materials Research (Applied Biomaterials) 1997;38:155-182.
3. Kotha SP, Li C, McGinn P, Schmid SR, Mason JJ. Improved mechanical properties of acrylic bone cement with short titanium fiber reinforcement. J Mater Sci Mater Med 2006;17:1403-1409.
4. Puska MA, Kokkari AK, Närhi TO, Vallittu PK. Mechanical properties of oligomer-modified acrylic bone cement. Biomaterials 2003;24:417-425.
5. Abboud M, Vol S, Duguet E, Fontanille M. PMMA-based composite materials with reactive ceramic fillers Part III: Radiopacifying particle-reinforced bone cements. Journal of Materials Science: Materials in Medicine 2000;11:295-300.
6. Dunne N. Mechanical properties of bone cements. In: Sanjukta D, editor. Orthopaedic bone cements. Boca Raton: CRC; 2008. p 240-255.
7. Lu J. Orthopedic Bone Cements. In: Poitout DG, editor. Biomechanics and Biomaterials in Orthopedics: Springer; 2004. p 86.
8. Haboush E. A new operation for arthroplasty of the hip based on biomechanics, photoelasticity, fast-setting dental acrylic, and other considerations. Bull Hosp Joint Dis 1953;14:242.
9. Charnley J. The bonding of prostheses to bone by cement. The Journal of Bone & Joints Surgery 1964;46:518-529.
10. Webb JC, Spencer RF. The role of Polymethylmethacrylate bone cement in modern orthopaedic surgery. The Journal of Bone & Joints Surgery 2007;89-B:851-857.
11. Kowalski R, Schmaehling R. Commecial aspects and delivery systems of bone cements. In: Sanjukta D, editor. Orthopaedic bone cements. Boca Raton: CRC; 2008. p 113-115.
12. Deb S. A Review of Improvements in Acrylic Bone Cements. Journal of Biomaterials Applications 1999;14:16-46.
13. Lasa V. Poly(methylmethacrylate) bone cement: chemical composition and chemistry. In: Sanjukta D, editor. Orthopaedic bone cements. Boca Raton: CRC; 2008. p 183-200.
14. Bergmann G, Graichen F, Rohlmann A. Hip joint loading during walking and running, measured in two patients. Journal of Biomechanics 1993;26:969-90.
15. Berme N, Paul J. Load actions transmitted by implants. Journal of Biomedical Engineering 1979;1:268-72.
16. Lewis G. Properties of acrylic bone cement: State of the art review. Journal of Biomedical Materials Research Part B: Applied Biomaterials 1997;38:155-182.
17. Bierogel C. Mechanical properties of polymers. In: Grellmann W, Seidler S, editors. Polymer testing. Munich: Hanser; 2007. p 138-144.
18. Craig RG, Ward ML. Restorative dental materials / edited [and selected] by Robert G. Craig, Marcus L. Ward. St. Louis, Mo: Mosby; 1997. 68-70 p.
19. Riley W, Sturges L, Morris D. Mechanics of Materials. New Jersy: John Wiley and Sons Inc.; 2007. 352-354 p.

20. Khaled SM, Sui R, Charpentier PA, Rizkalla AS. Synthesis of TiO_2-PMMA nanocomposite: using methacrylic acid as a coupling agent. Langmuir 2007;23:3988-3995.
21. Jones DW, Rizkalla AS. Characterization of experimental composite biomaterials. Journal of Biomedical Materials Research Part B: Applied Biomaterials 1996;33:89-100.
22. Rizkalla AS, Jones DW. Indentation fracture toughness and dynamic elastic moduli for commercial feldspathic dental porcelain materials. Dental Materials 2004;20:198-204.
23. Menard KP. Dynamic mechanical analysis: a practical introduction. Boca Raton: CRC; 1999. 4-7 p.
24. Boresi AP, J.Schmidt R. Advanced mechanics of materials. New York: John Wiley & Sons Inc.; 2003. 12-13 p.
25. Hernandez L, Gurruchaga M, Goni I. Influence of powder particle size distribution on complex viscosity and other properties of acrylic bone cement for vertebroplasty and kyphoplasty. J Biomed Mater Res Part B: Appl Biomaterials 2006;77B:98-103.
26. Farrar DF, Rose J. Rheological properties of PMMA bone cements during curing. Biomaterials 2001;22:3005-3013.
27. Amirouche A, Mouzali M, Watts DC. Radiopacity evaluation of Bis-GMA/TEGDMA/opaque mineral filler dental composites. Journal of Applied Polymer Science 2007;104:1632-1639.
28. Deb S, Abdulghani S, Behiri JC. Radiopacity in bone cements using an organo-bismuth compound. Biomaterials 2002;23:3387-3393.
29. Persson C, Guandalini L, Baruffaldi F, Pierotti L, Baleani M. Radiopacity of Tantalum-loaded acrylic bone cement. Journal of Engineering in Medicine 2006;220:787-791.
30. Lewis G, J. CS, Hooy-Corstjens V, Bhattaram A, Koole LH. Influence of the radiopacifier in an acrylic bone cement on its mechanical, thermal, and physical properties: Barium sulfate-containing cement versus iodine-containing cement. Journal of Biomedical Materials Research Part B: Applied Biomaterials 2005;73B:77-87.
31. Benthien J, Russlies M, Behrens P. Investigating the effects of bone cement, cyanoacrylate glue and marine mussel adhesive protein from Mytilus edulis on human osteoblasts and fibroblasts in vitro. Ann. Anat. 2004;186:561-566.
32. Lu J. Orthopedic bone cements. In: Poitout DG, editor. Biomechanics and Biomaterials in Orthopedics. New York: Springer; 2004. p 89-92.
33. Haas S, Brauer G, Dickson G. A characterization of polymethylmethacrylate bone cement. Journal of Bone joint Surgery 1975;57:380-391.
34. Schoenfeld C, Conard G, Lautenschlager EP. Monomer release from methacrylate bone cements during simulated in vivo polymerization. Journal of Biomedical Materials Research 1979;13(1):135-147.
35. Gentil B, paugam C, Wolf C, Lienhart A, Augereau B. Methacrylate plasma levels during total hip arthroplasty. Clin Orthop 1993;287:112-116.

36. Hofmann A, Wyatt R, Gilbertson A, Dekosss L, Miller J. The effect of air embolization from the femoral canal on hemodynamic parameters during hip arthroplasty. Clin Orthop 1987;218:290-296.
37. Crout D, Corkill J, James M, Ling R. Methylmethacrylate metabolism in man. The hydrolysis of methylmethacrylate to methacrylic acid during total hip replacement. Clin Orthop 1979;141:90-95.
38. Lundskog J. Heat and bone tissue. An experimental investigation of the thermal properties of bone and threshold levels for thermal injury. Scand J Plast Reconstr Surg 1972;9:1-80.
39. Lee AJ, Wrignton JD. Some properties of polymethyl methacrylate with reference to its use in orthopaedic surgery. Clin Orthop 1973;95:281-287.
40. Rhinelander FW, Nelson CL, Steward RD, Steward CL. Experimental reaming of the proximal femur and acrylic cement implantation: vascular and histologic effects. Clin Orthop 1979;141:74-89.
41. Lidgren L. The bone and joint decade 2000-2010. Bulletin of the World Health Organization 2003;81(9):629.
42. Merrill C, A E. Hospital stay involving musculoskeletal procedures, 1997-2005: Agency for Healthcare Research and Quality; 2007. Report nr 34.
43. Rand JA. Cement or cementless fixation in total knee arthroplasty? Clin Orthop Relat Res 1991;273:52-62.
44. Oishi CS, Walker RH, Colwell CW. The femoral component in total hip arthroplasty. Journal of Bone joint Surgery 1994;77B:1130-1136.
45. Lennon AB. Fracture toughness and fatigue characteristics of bone cements. In: Sanjukta D, editor. Orthopaedic bone cements. Boca Raton: CRC; 2008. p 265-275.
46. Rudigier J, Kirscnner P, Richter I, Schweikert C. Influence of different X-ray contrast materials on structure and strength of bone cements. In: Hastings G, William D, editors. Mechanical properties of biomaterials. New York: Wiley & Sons; 1980. p 289.
47. Vazquez B, Deb S, Bonfield W. Optimization of benzoyl peroxide concentration in an experimental bone cement based on poly(methyl methacrylate). Journal of Materials Science: Materials in Medicine 1997;8:455-460.
48. Holm N. The modulus of elasticity and flexural strength of some acrylic bone cements. Acta Orthop Scand 1977;48:436-440.
49. Sabokbar A, Fujikawa Y, Murray DW, Nicholas A. Radio-opaque agents in bone cement increase bone resorption. Journal of Bone joint Surgery 1997;79-B:129-134.
50. San Roman J, Vazquez Lasa B, Aguilar MR, Boesel LF. Modifications of bone cements. In: Sanjukta D, editor. Orthropaedic bone cements. Boca Raton: CRC; 2008. p 332-349.
51. Adams D. The granulomatous inflammatory response: a review. Americal Journal of Pathology 1976;84:164-191.
52. Sabokbar A, Anthanasou N, Murray D. Osteolysis induced by radiopaque agents. In: Walenkamp G, editor. Bone cements and cementing techniques. New York: Springer; 2001. p 149-162.

53. Lazarus M, Cuckler J, schumacher H, Ducheyne P, Baker D. Comparison of the inflammatory response to particulate polymethylmethacrylate debris with and without barium sulfate. Journal of Orthopaedic Research 1994;12:532-541.
54. Issac G, Atkinson J, Dowson D. The causes of femoral head roughening in explanted Charnley hip prosthesis. Engineering Medicine 1987;16(3):167-173.
55. Espehaug B, Furnes O, Havelin LI, Vollset SE. The type of cement and failure of total hip replacements. The Journal of Bone & Joints Surgery 2002;84-B:832-838.
56. Kjellson F, Wang JS, Almen T, Mattsson A, Klaveness J, Tanner KE, Lidgren L. Tensile properties of a bone cement containing non-ionic contrast media. Journal of Materials Science: Materials in Medicine 2001;12:889-894.
57. Hernandez L, Fernandez M, Colli F, Gurruchaga M, Goni I. Preparation of acrylic bone cements for vertebroplasty with bismuth salicylate as radiopaque agent. Biomaterials 2006;27:100-107.
58. Davy K, Anseau M, Odlyha M, Foster C. X-ray opaque methacrylate polymers for biomedical applications. Polymer Int. 1997;43:143-154.
59. Van Hooy-Corstjens C, Govaert L, Spoelstra A, Bulstra S, Wetzels M, Koole L. Mechanical behaviour of a new acrylic radiopaque iodine-containing bone cement. Biomaterials 2004;25:2657-2667.
60. Van Hooy-Corstjens C, Bulstra S, Knetsch L, Geusens P, Kuijer R, Koole L. Biocompatibility of a new radiopaque iodine-containing acrylic bone cement. Journal of Biomedical Materials Research Part B: Applied Biomaterials 2007;80B:339-344.
61. Vazquez B, Ginebra M, Gil F, Planell J, Lopez-Bravo A, San Roman J. Radiopaque acrylic cements prepared with a new acrylic derivative of iodoquinoline. Biomaterials 1999;20:2047-2053.
62. Ginebra M, Aparicio C, Albuixech E, Fernandez-Barragan E, Gil F, Planell J, Morejon L, Vazquez B, San Roman J. Improvement of the mechanical properties of acrylic bone cements by substitution of the radio-opaque agent. Journal of Materials Science: Materials in Medicine 1999;10:733-737.
63. Ginebra M, Albuixech L, Fernandez-Barragan E, Aparicio C, Gil F, San Roman J, Vazquez B, Planell J. Mechanical performance of acrylic bone cements containing different radiopacifying agents. Biomaterials 2002;23:1873-1882.
64. San Roman J, Vazquez Lasa B, Aguilar MR, Boesel LF. Modifications of bone cements. In: Sanjukta D, editor. Orthropaedic bone cements. Boca Raton: CRC; 2007. p 332-349.
65. Artola A, Goni I, Gil J, Ginebra P, Manero J, Gurruchaga M. A radiopque polymeric matrix for acrylic bone cements. Journal of Biomedical Materials Research Part B: Applied Biomaterials 2003;64B:44-55.
66. Artola A, Gurruchaga M, Vazquez Lasa B, San Roman J, Goni I. Elimination of barium sulphate from acrylic bone cements. Use of two iodine-containing monomers. Biomaterials 2003;24:4071-4080.
67. Behiri JC, Braden M, Khorosani D, Wiwattanadate D, Bonfield W. Advanced bone cement for long term orthopaedic implantation. Bioceramics 1991;4:301-307.
68. Abboud M, Casaubieilh L, Morvan F, Fontanille M, Duguet E. PMMA-based composite materials with reactive ceramic fillers: IV. Radiopacifying particles

embedded in PMMA beads for acrylic bone cements. Journal of Biomedical Materials Research Part B: Applied Biomaterials 2000;53:728-736.

69. Abboud M, Turner M, Duguet E, Fontanille M. PMMA-based composite materials with reactive ceramic fillers. Part1.—Chemical modification and characterisation of ceramicparticles. Journal of Materials Chemistry 1997;7(8):1527-1532.
70. Duguet E, Abboud M, Morvan F, Maheu P, Fontanille M. PMMA encapsulation of alumina particles through aqueous suspension polymerisation processes. Macromol. Symp. 2000;151:365-370.
71. Pourdehyimi B, Wagner HD. Elastic and ultimate properties of acrylic bone cement reinforced with ultra high molecular weight polyethylene fibers. Journal of Biomedical Materials Research 1989;23:63-80.
72. Yang JM, Huang PY, Yang MC. The effect of ultra high molecular weight polyehtylene fiber on the mechanical properties of acrylic bone cements. Journal of Applied Polymer Science 1997;4:41-46.
73. Hild DN, Schwartz P. Plasma treated ultra high strength polyethylene fibers, Part II. Increase adhesion to Poly(methylmethacrylate). Journal of Adhesion Science Technology 1992;6:897-917.
74. Yang JM, Huang PY, Yang MC. The graftingof methyl methacrylate onto high molecular weight polyethylene fiber by plasma and UV treatment. Journal of Applied Polymer Science 1997;65:365-371.
75. Yang JM, Huang PY, Yang MC, Sing KL. Effect of MMA-g-UHMWPE grafted fiber on mechanical properties of acrylic bone cement. Journal of Biomedical Materials Research (Applied Biomaterials) 1997;38:361-369.
76. Saha S, Pal S. Mechanical properties of bone cement: A review. Journal of Biomedical Materials Research 1984;18:435-462.
77. Saha S, Pal S. Mechanical characterisation of commercially made carbon-fiber reinforced polymethylmethacrylate. Ibid 1986;20:817-826.
78. Wright TM, Connely GM, Rimnac CM, Hertzberg RW, Burstein AM. Carbon fiber reinforcement of polymeric materials for total hip arthroplasty. In: Ducheyene P, Vander Perre G, Aubert AE, editors. Amsterdem: Elsevier science publication; 1984. p 67-72.
79. Pourdehyimi B, Robinson HH, Schwartz P, Wagner HD. Fracture toughness of kevlar 29/polymethyl methacrylate composite materials for surgical implantation. Ann. Biomed. Eng. 1986;14:277-294.
80. Pourdehyimi B, Wagner HD, Schwartz P. A comparison of mechanical properties of discontinuous Kevlar 29 fiber reinforced bone and dental cements. Journal of Biomedical Materials Research 1986;21:4468-4474.
81. Wright TM, Trent PS. Mechanical properties of aramid fiber reinforced acrylic bone cement. journal of materials science Letter 1979;14:503-505.
82. Taitsman JP, Saha S. Tensile strength of wire reinforced bone cement and twisted stainless steel wire. Journal of Bone and Joint Surgery 1977;59A:419-425.
83. Kotha SP, Li C, Schmid SR, Mason JJ. Fracture toughness of steel-fiber-reinforced bone cement. Journal of Biomedical Materials Research Part A 2004;70A:514-521.

84. Kotha SP, Lieberman M, Vickers A, Schmid SR, Mason JJ. Adhesion enhancement of steel fibers to acrylic bone cement through a silane coupling agent. Journal of Biomedical Materials Research Part A 2006;76:111-119.
85. Kotha SP, Chaodi L, Schmid S, Mason J. Reinforcement of bone cement using zirconia fibers with and without acrylic coating. Journal of Biomedical Materials Research 2008;88A:898-906.
86. Gilbert JA, Ney DS, Lautenschlager EP. Self reinforced composite poly(methyl methacrylate): static and fatigue properties. Biomaterials 1995;16:1043-1055.
87. Buckley CA, Gilbert JL, Lautenschlager EP. Thermomechanical processing of PMMA into high strength fibers. Journal of Applied Polymer Science 1992;44:1321-1330.
88. William JL, Johnson WJH. Elastic constants of composites formed from PMMA bone cements and anisotropic bovine tibial cancellous bone. Journal of Biomechanics 1989;22:673-682.
89. Dai K, Liu Y, Park JB, C. C, Nishiyama K. Bone particle impregnated bone cement: an in vivo weight bearing study. Journal of Biomedical Materials Research 1991;25:141-156.
90. Castaldini A, Cavalini A. Biological and biomedical performance of biomaterials. In: Christel P, Meunier A, Lee AJC, editors. Amsterdam: Elsevier Science Publishers; 1986. p 525-530.
91. Perek J, Pilliar RM. Fracture toughness of composite acrylic bone cements. Journal of Materials Science Materials in Medicine 1992;3:333-344.
92. Murukami A, Behiri JC, Bonfield W. HAP fiber reinforced bone cements. Phase Interaction in Composite Materials 1992;5:460-466.
93. Koo JH. Polymer Nanocomposites: processing, characterization, and application. New York: McGraw Hill; 2006. 1-5 p.
94. Luo JJ, Daniel IM. Characterization and modeling of mechanical behavior of Polymer/Clay nanocomposites. Composite Science Technology 2003;63:1607-1616.
95. Hussain F, Hojjati M. Review article: Polymer-matrix nanocomposites, processing, manufacturing, and application: An overview. Journal of Composite Materials 2006;40:1511-1560.
96. Thostenson E, Li C, Chou T. Review Nanocomposites in Context. Journal of Composites Science & Technology 2005;65:491-516.
97. Goto K, Tamura J, Shinzato S, Fujibayashi S, Hashimoto M, Kawashita M, Kokubo T, Nakamura T. Bioactive bone cements containing nano-sized titania particles for use as bone substitutes. Biomaterials 2005;26:6496-6505.
98. Uchida M, Kim H-M, Kokubo T, Nakamura T. Apatite-forming ability of titania gels with different structures. In: Ohgushi H, Hastings G, Yoshikawa T, editors. Bioceramics. Singapore: World Scientific Publishing; 1999. p 149-152.
99. Marrs B, Andrews R, Rantell T, Pienkowski D. Augmentation of acrylic bone cement with multiwall carbon nanotubes. J Biomed Mater Res 2006;77A:269-276.
100. Service F. Nanotechnology grows up. Science 2004;304:1732-1734.

101. Wang J-H, Young T-H, Lin D-J, Sun M-K, Huag H-S, Cheng L-P. Preparation of Clay/PMMA nanocomposites with intercalated or exfoliated structure for bone cement synthesis. Macromolecular Materials and Engineering 2006;291:661-669.
102. Hill J, Orr J, Dunne N. In vitro study investigating the mechanical properties of acrylic bone cement containing calcium carbonate nanoparticles. Journal of Materials Science: Materials in Medicine 2008;19:3327-3333.
103. Gomoll AH, Fitz W, Scott RD, Thornhill TS, Bellare A. Nanoparticulate fillers improve the mechanical strength of bone cement. Acta Orthopaedica 2008;79:421-427.
104. Ricker A, Liu-Snyder P, Webster TJ. The influence of nano MgO and BaSO4 particle size additives on properties of PMMA bone cement. International Journal of Nanomedicine 2008;3:125-130.
105. Barralet J, Lilley K, Grover L. Cements from nanocrystalline hydroxyapatite. Journal of Materials Science Materials in Medicine 2004;15:407-411.
106. Lilley K, Gbureck U, Knowles J. Alkali ion substituted calcium phosphate cement formation from mechanically activated reactants. Journal of Materials Science Materials in Medicine 2005;16:455-461.
107. Liu H, Slamovich E, Webster T. Increased osteoblast functions on poly-lactic-co-glycolic acid with highly dispersed nanophase titania. Journal of Biomedical Nanotechnology 2005;1:83-89.
108. Schulte K, Nolte MCM. Carbon nanotube and carbon nanofiber-reinforced polymer composites. In: MIchler GH, Balta-Calleja FJ, editors. Mechanical properties of polymers based on nanostructure and morphology. Boca Raton: CRC; 2005. p 603-622.
109. Williams DF. The role of titanium in current medical devices. In: Brunette DM, Tengvall P, Textor M, Thomsen P, editors. Titanium in medicine. New York: Springer; 2001. p 14-18.
110. Toth C, Szabo G, Kovacs L, Vargha K, Barabas J, Nemeth Z. Titanium implants with oxidized surfaces:the background and long-term results. Smart Material Structure 2002;11:813-818.
111. Wintermantel E, Eckert K-L, Huang N-P, Textor M, Brunette DM. Titanium ceramics for cell-carriers and for medical applications. In: Brunette DM, Tengvall P, Textor M, Thomsen P, editors. Titanium in medicine. New York: Springer; 2001. p 649-667.
112. Wintermantel E, Cima L, Schloo B, Langer R. Angiopolarity of cell-carriers: directional angiogenesis in resorbable liver cell transplantation devices. In: Steiner R, Weisz P, Langer R, editors. Angiogenesis: key principles science - technology - medicine. Birhaeuser: Basel; 1992. p 331-334.
113. Gurr J-R, Wang S, Chen C-H, Jan K-Y. Ultrafine titanium dioxide particles in the absence of photoactivation can induce oxidative damage to human bronchial epithelial cells. Toxicology 2005;213:66-73.
114. Bernard BK, Osheroff MR, Hofmann A, Mennear JH. Toxicology and carcinogenesis studies of dietary titanium dioxide-coated mica in male and female Fischer 344 rats. Journal of Toxicology and Environmental Health 1990;29:417-429.

115. Hart GA, Hesterberg TW. In vitro toxicity of respirable-size particles of diatomaceous earth and crystalline silica compared with asbestos and titanium dioxide. Journal of Occupational and Environmental Medicine 1998;40:29-42.
116. Nordman H, Berlin M. Titanium. In: Friberg L, Nordberg GF, Vouk VB, editors. Handbook on the toxicology of metals. Amsterdam: Elsvier; 1986. p 595-609.
117. Lomer MC, Thompson RP, Powel JJ. Fine and ultrafine particles of the diet: influence on the mucosal immune response and association with Crohn's disease. Proceedings of the Nutrition Society 2002;61:123-130.
118. Gelis S, Girard A, Mavon M, Delverdier N, Paillous V. Assessment of the skin photoprotective capacities of an organo-mineral broad-spectrum sunblock on two ex vivo skin models. Photodermatology, photoimmunology and photomedicine 2003;19:242-253.
119. Lam CW, James JT, McCluskey R, Hunter RL. Pulmonary toxicity of single-wall carbon nanotubes in mice 7 and 90 days after intratracheal instillation. Toxicology Science 2004;77:126-134.
120. Peral J, Munoz J, DOmenech X. Photosensitized CN-oxidation over TiO_2. Journal of Photochemistry and Photobiology A 1990;55:251-257.
121. Ohtani B, Ogawa Y, Nishimoto S. Photocatalytic activity of amorphous-anatase mixture of titanium (IV) oxide particles suspended in aqueous solution. Journal of physical chemistry B 1997;101:3746-3752.
122. Serpone N, pelizzetti E. Photocatalysis: fundamental and applicatiosn. New York: Wiley interscience; 1989.
123. Rehn B, Seiler F, Rehn S, Bruch J, Maier M. Investigations on the inflammatory and genotoxic lung effects of two types of titanium dioxide: untreated and surface treated. Toxicology and Applied Pharmacology 2003;189:84-95.
124. Dunford R, Salinaro A, Cai L, Serpone N, Horikoshi S, Hidaka H, Knowland J. Chemical oxidation and DNA damage catalysed by inorganic sunscreen ingredients. FEBS Letters 1997;418:87-90.
125. Peters K, Unger RE, Kirkpatrick CJ, Gatti AM, Monari E. Effects of nano-scaled particles on endothelial cell function in vitro: studies on viability, proliferation and inflammation. Journal of Materials Science Materials in Medicine 2004;15:321-325.
126. Yamamoto A, Honma R, Sumita M, Hanawa T. Cytotoxicity evaluation of ceramic particles of different sizes and shapes. Journal of Biomedical Materials Research 2004;68A:244-256.
127. Zhang Q, Kusaka Y, Sato K, Nakakuki K, Kohyama N, Donaldson K. Differences in the extent of inflammation caused by intratracheal exposure to three ultrafine metals: role of free radicals. Journal of Toxicology and Environmental Health 1998;53:423-438.
128. Sui R, Rizkalla AS, Charpentier PA. Formation of titania nanofibers: a direct sol-gel route in supercritical CO_2. Langmuir 2005;21:6150-6153.
129. Kasuga T, Hiramatsu M, Hoson A, Sekino T, Niihara K. Formation of titanium oxide nanotube. Langmuir 1998;14:3160-3163.
130. Shenoy AV. Rhology of Filled Polymer System. Boston: Kluwer academic publishers; 1999. 112-131 p.

131. Shenoy AV. Rheology of filled polymer systems. Boston: Kluwer academic publishers; 1999. 54-87 p.
132. Pal R. Rheology of particulate dispersions and composites. Boca Raton: CRC press; 2007. 306-309 p.
133. Lewis G, Carroll M. Rheological properties of acrylic bone cement during curing and the role of the size of the powder particles. Journal of Biomedical Materials Research Part B: Applied Biomaterials 2002;63:191-199.
134. Nicholas MKD, Waters MGJ, Holford KM, Adusei G. Analysis of rheological properties of bone cements. Journal of Materials Science: Materials in Medicine 2007;18:1407-1412.
135. ASTM. ASTM standard F451-99a: Standard specification for acrylic bone cement. West Conshohocken, PA, United States: American Society for Testing Materials.
136. ISO. ISO 5833 Implants for surgery-Acrylic resin cements. International Testing Organization. Switzerland; 2002.
137. Pascual B, Vtiquez B, Gurruchaga M, Goti I, Ginebra MP, Gil FJ, Planell JA, Levenfeld B, San Roman J. New aspects of the effect of size and size distribution on the setting parameters and mechanical properties of acrylic bone cements. Biomaterials 1996;17:509-516.
138. Yu S-B, Watson AD. Metal-based X-ray contrast media. Chem. Rev. 1999;99:2353-2377.
139. Watts; DC, Mccabe JF. Aluminium radiopacity standards for dentistry: an international survey. Journal of Dentistry 1999;27:73-78.
140. Toyooka H, Taira M, Wakasa K, Yamaki M, Fujita M, Wada T. Radiopacity of 12 visible-light-cured dental composite resins. Journal of Oral Rehabilitation 1993;20:615-622.
141. Morrow HW, Kokernak RP. Statics and strength of materials. New Jersey: Pearson Prentice Hall; 2007. 469-476 p.
142. Morrow HW, Kokernak RP. Statics and strength of materials. New Jersey: Pearson Prentice Hall; 2007. 286-287 p.
143. ASTM. Specification D790-95a. Standard test method for flexural properties of unreinforced and reinforced platics and electrical insulating materials. 1996 Annual Book of ASTM Standards. Philadelphia, PA: Americal Society for Testing and Materials; 1996. p 155-165.
144. Richerson DW. Modern ceramic engineering. Properties, processing and use in design. New York: Marcel Dekker Inc.; 1982. 86-88 p.
145. Ugural AC. Mechanics of Materials. New Jersey: John Wiley & Sons, Inc.; 2008. 472-476 p.
146. Richerson DW. Modern ceramic engineering. Properties, processing and use in design. New York: Marcel Dekker Inc.; 1982. 91-92 p.
147. Barker LM. A somplified method for measuring plane strain fracture toughness. Engineering Fracture Mechanics 1977;9:361-369.
148. ASTM. Specification B771-87(1997). Standard test method for short rod fracture toughness of cemented carbides. 2000 Annual Book of ASTM Standards. West Conshohocken, Pennsylvania: American Society for Testing and Materials; 2000.

149. Ruse ND, Troczynski T, MacEntee MI, Feduik D. Novel fracture toughness test using a notchless triangular prism (NTP) specimen. Journal of Biomedical Materials Research 1996;31:457-463.
150. Bubsey RT, Munz D, Pierce WS, Shannon JL. Compliance calibration of the short rod chevron notch specimen for fracture toughness testing of brittle materials. International journal of Fracture 1982;18:125-133.
151. Busse G. Non-destructive polymer testing. In: Grellmann W, Seidler S, editors. Polymer Testing. Munich: Hanser; 2007. p 454-455.
152. Babikov OI. Untrasonics and its industrial application. New York: Consultant Bureau Inc.; 1960. 21-23 p.
153. Bellows CG, Aubin JE. Determination of numbers of osteoprogenitors present in isolated fetal rat calvaria cells in vitro. Developmental Biology 1989;133:8-13.
154. Yoshida K, Taira Y, Atsuta M. Properties of opaque resin composite containing coated and silanized titanium dioxide. J Dent Res 2001;80:864-868.
155. Wypych F, Satyanarayana KG. Functionalization of single layers and nanofibers: a new strategy to produce polymer nanocomposites with optimized properties. J Colloid Interface Sci 2005;285:532-543.
156. Ramires PA, Giuffrida A, Milella E. Three-dimensional reconstruction of confocal laser microscopy images to study the behaviour of osteoblastic cells grown on biomaterials. Biomaterials 2002;23:397-406.
157. Lu M-D, Yang S-M. Syntheses of polythiophene and titania nanotube composites. Synthetic Metals 2005;154:73-76.
158. Teo BK, Li CP, Sun XH, Wong NB, Lee ST. Silicon-silica nanowires, nanotubes, and biaxial nanowires: inside, outside, and side-by-side growth of silicon versus silica on zeolite. Inorg. Chem. 2003;42:6723-6728.
159. Wang Q, Xia H, Zhang C. Preparation of polymer/inorganic nanoparticles composites through ultrasonic irradiation. J Appl Poym Sci 2001;80(9):1478-1488.
160. Jordan J, Jacob KI, Tannenbaum R, Sharaf MA, Jasiuk I. Experimental trends in polymer nanocomposites-a review. Mater Sci Eng, A 2005;A393(1-2):1-11.
161. Goto K, Hashimoto M, Fujibayashi S, Kokubo T, Nakamura T. New bioactive bone cement containing nano-sized titania particles. Key Engineering Materials 2005;284-286:97-100.
162. Matsumura H, Nakabayashi N. Adhesive 4-META/MMA-TBB opaque resin with poly(methyl methacrylate)-coated titanium dioxide. J Dent Res 1988;67(1):29-32.
163. Nakamoto K. Infrared and raman spectra of inorganic and coordination compounds. New York: A Wiley-Interscience Publication; 1997. 59-62 p.
164. Gratzel M. Solar energy conversion by dye-sensitized photovoltaic cells. Inorg Chem 2005;44(20):6841-6851.
165. Rotzinger FP, Kesselman-Truttmann JM, Hug SJ, Shklover V, Gratzel M. Structure and vibrational spectrum of formate and acetate adsorbed from Aqueous solution onto the TiO_2 rutile (110) surface. J. Phys. Chem. B 2004;108(16):5004-5017.
166. Foster AS, Nieminen RM. Adsorption of acetic and trifluoroacetic acid on the TiO_2(110) surface. Journal of Chemical physics 2004;121(18):9039.

167. Alfrey T, Price CC. Relative reactivities in vinyl copolymerization. Journal of Polymer Science 1947;2:101-106.
168. Odian G. Principles of polymerization. New Jersey: John Wiley & Sons Inc.; 2004. 500-503 p.
169. Rufino ES, Monteiro EEC. Infrared study on methyl methacrylate–methacrylic acid copolymers and their sodium salts. Polymer 2003;44:7189-7198.
170. Yu DG, An JH, Bae JY, Ahn SD, Kang SY, Suh KS. Preparation of Titanium Dioxide/Poly(methyl methacrylate-co-n-butyl acrylate-co-methacrylic acid) Hybrid Composite Particles Via Emulsion Polymerization. Journal of Applied Polymer Science 2005;97:72-79.
171. Zhang H, Banfield JF. Thermodynamic Analysis of Phase Stability of Nanocrystalline Titania. J Mater Chem 1998;8(9):2073-2076.
172. Abboud M, Casaubieilh L, Morvan F, Fontanille M, Duguet E. PMMA-based composite materials with reactive ceramic fillers: IV. Radiopacifying particles embedded in PMMA beads for acrylic bone cements. Journal of Biomedical Research 2000;53(6):728-736.
173. Sui R, Rizkalla AS, Charpentier PA. FTIR study on the formation of TiO_2 nanostructures in supercritical CO_2. J. Phys. Chem. B 2006;110(33):16212-16218.
174. Finnie KS, Bartlett JR, Woolfrey JL. Vibrational spectroscopic study of the coordination of (2,2'-Bipyridyl-4,4'-dicarboxylic acid)ruthenium(II) complexes to the surface of nanocrystalline titania. Langmuir 1998;14(10):2744-2749.
175. Henrich VE, P.A.Cox. Adsorption on d^0 transition-metal oxides. The Surface Science of Metal Oxides. Cambridge: Cambridge University Press; 1994. p 318-319.
176. Schulte K, H. F, Sandler JKW. Carbon nanotube-reinforced polymers: a state of the art review. In: Friedrich K, Fakirov S, Zhang Z, editors. Polymer Composites From Nano- to Macro-Scale. New York: Springer; 2005. p 11-16.
177. Tang W, Santare MH, Advani SG. Melt processing and mechanical property characterization of multi-walled carbon nanotube/high density polyethylene (MWNT/HDPE) composite films. Carbon 2003;41:2779-2785.
178. Hussain F, Hojjati M, Okamoto M, Gorga RE. Review article: Polymer-matrix nanocomposites, processing, manufacturing, and application: An overview. Journal of Composite Materials 2006;40(17):1511-1517.
179. Fried JR. Polymer science and technology. Upper Saddle River, NJ: Prentice Hall Professional Technical Reference; 2003. 154-170 p.
180. Jaupert F, Wetzel B. Reinforcement of Thermosetting polymers by the Incorporation of Micro-and Nanoparticles. In: Friedrich K, Fakirov S, Zhang Z, editors. Polymer Composites From Nano-to Macro-Scale. New York: Springer; 2005. p 57.
181. Ash BJ, Siegel RW, Schadler LS. Glass-transition temperature behavior of Alumina/PMMA nanocomposites. Journal of Polymer Sceince:Part B: Polymer physics 2004;42:4371-4383.
182. Mesquita RV, Axmann D, Geis-Gerstorfer Jr. Dynamic visco-elastic properties of dental composite resins. Dental Materials 2006;22:258-267.

183. Antonucci V, Hsiao K-T, Advani SG. Review of polymer composites with carbon nanotubes. In: Shonaike GO, Advani SG, editors. Advanced Polymeric Materials Structure Property Relationships. Boca Raton: CRC Press; 2003. p 421-425.
184. Qian D, Dickey EC, Andrews R, Rantell T. Load transfer and deformation mechanisms in carbon nanotube-polystyrene composites. Applied Physics Letters 2000;76(20):2868-2874.
185. Shinzato S, Nakamura T, Kokubo T, Kitamura Y. Bioactive bone cement: Effect of filler size on mechanical properties and osteoconductivity. Journal of Biomedical Materials Research 2001;56(3):452-458.
186. Nzihour A, Attias L, Sharrock P, Ricard A. A rheological, thermal and mechanical study of bone cement - from a suspension to a solid biomaterial. Powder Technology 1998;99:60-69.
187. Kommireddy DS, Patel AA, Shutava TG, Mills DK, Lvov YM. Layer-by-layer assembly of TiO_2 nanoparticles for stable hydrophilic biocompatible coatings. Journal of Nanoscience and Nanotechnology 2005;5(7):1081-1087.
188. Textor M, Sitting C, Frauchiger V, Tosatti S, Brunette DM. Properties and biological significance of natural oxide films on titanium and its alloys. In: Brunette DM, Tengvall P, Textor M, Thomsen P, editors. Titanium in medicine. Material Science, surface Science, engineering, biological response and medical applications. New York: Springer; 2001. p 204-205.
189. Parfitt GD. The surface of titanium oxide. Progress in Surface and Membrane Science. New York: Academic Press; 1976. p 181-226.
190. Boehm HP. Acidic and basic properties of hydroxylated metal oxide surfaces. Discuss Faraday Soc. 1971;52:264-277.
191. Parks GA. The isoelectric point of solid oxides, solid hydroxides and aqueous hydroxo compolex systems. Chem. Rev. 1965;65:177-198.
192. Gold JM, Schmidt M, Steinemann SG. XPS study of amino-acid adsorption to titanium surfaces. Helv. Phys. Acta. 1989;62(2-3):246-249.
193. Zhao Q, Samulski ET. A comparative study of poly(methyl methacrylate) and polystyrene/clay nanocomposites prepared in supercritical carbon dioxide. Polymer Testing 2006;47(2):663-671.
194. Kashiwagi T, Inaba A, Brown JE, Hatada K, Kitayama T, Masuda E. Effects of weak linkages on the thermal and oxidative degradation of poly(methyl methacrylates). Macromolecules 1986;19(8):2160-2168.
195. Hirata Y, Kamikakimoto J, NIshimoto A, Ishihara Y. Interaction between α-Alumina surface and polyacrylic acid. Journal of Ceramic Society of Japan 1992;100(1):7-12.
196. Babikov OI. Ultrasonics and its industrial applications. New York: Consultant Bureau Inc.; 1969. 14-15 p.
197. Anderson T. Fracture mechanics: fundamentals and applications. Boston: CRC Press; 1995. 120-135 p.
198. Lewis G. Alternative acrylic bone cement formulations for cemented arthroplasties: Present status, key issues, and future prospects. Journal of Biomedical Materials Research Part B: Applied Biomaterials 2008;84 B(2):301-319.

199. Kurtz SM, Villarraga ML, Zhao K, Edidin AA. Static and fatigue mechanical behavior of bone cement with elevated barium sulfate content for treatment of vertebral compression fractures. Biomaterials 2005;26:3699-3712.
200. Michler GH. Micromechanical mechanisms of toughness enhancement in nanostructured amorphous and semicrystalline polymers. In: Michler GH, Calleja FJ, editors. Mechanical properties of polymers based on nanostructure and morphology. Boca Raton: Taylor & Francis; 2005. p 391-395.
201. Topoleski LD, Ducheyene P, Cuckler JM. Flow intrusion characteristics and fracture properties of titanium-fibre-reinforced bone cement. Biomaterials 1998;19:1569-1577.
202. Nelson PK, Victor C, Kamada T. Fracture toughness of microfiber reinforced cement composites. Journal of Materials in Civil Engineering 2002;14(5):384-391.
203. Cogswell FN. Continuous fiber reinforced thermoplastic. In: Clegg DW, Collyer AA, editors. Mechanical properties of reinforced thermoplastic. London: Elsevier Applied Science Publishers; 1986. p 100-102.
204. Burton RH, Folkes MJ. Fiber-matrix interacitons in reinforced thermoplastics. In: Clegg DW, Collyer AA, editors. Mechanical properties of reinforced thermoplastics. NewYork: Elsevier Applied Science Publishers; 1986. p 269-270.
205. Rayson HW, McGrath GC. Fibres, whiskers and flakes for composite application. In: Clegg DW, Collyer AA, editors. Mechanical properties of reinforced thermoplastics. NewYork: Elsevier Applied Science Publishers; 1986. p 50-52.
206. Segerström S, Ruyter IE. Effect of thermal cycling on flexural properties of carbon–graphite fiber-reinforced polymers. Dental Materials 2009;25:845-851.
207. Vallo CI, Abraham GA, Cuadrado TR, San Román J. Influence of cross-linked PMMA beads on the mechanical behavior of self-curing acrylic cements. Journal of Biomedical Materials Research Part B: Applied Biomaterials 2004;70B(2):407-416.
208. Mallick RP. Fiber reinforced composites. Materials, Manufacturing and design. NewYork: CRC; 1998. 69-71 p.
209. Hernandez L, Gurruchaga M, Goni I. Influence of Powder Particle Size Distribution on Complex Viscosity and Other Properties of Acrylic Bone Cement for Vertebroplasty and Kyphoplasty. J Biomed Mater Res Part B: Appl Biomaterials 2006;77B:98-103.
210. Hernandez L, Gurruchaga M, Goni I. Injectable acrylic bone cements for vertebroplasty based on a radiopaque hydroxyapatite. Formulation and rheological behaviour. Journal of Materials Science: Materials in Medicine 2009;20:89-97.
211. Musanje L, Ferracane JL. Effects of resin formulation and nanofiller surface treatment on the properties of experimental hybrid resin composite. Biomaterials 2004;25:4065-4071.
212. Puska MA, Lassila LV, Aho AJ, Yli-Urpo A, Vallittu PK, Kangasniemi I. Exothermal characteristics and release of residual monomers from fiber-reinforced oligomer-modified acrylic bone cement. J Biomater Appl 2005;20:51-64.

213. Dyer SR, Lassila VJ, Jokinen M, Vallittu PK. Effect of fiber position and orientation on fracture load of fiber-reinforced composite. Dental Materials 2004;20:947-955.
214. Behr M, Rosentritt M, Lang R, Handel G. Flexural properties of fiber reinforced composite using a vacuum/pressure or a manual adaptation manufacturing process. Journal of Dentistry 2000;28:509-514.
215. Rehman I, Harper EJ, Bonfield W. In situ analysis of the degree of polymerization of bone cement by using FT-Raman spectroscopy. Biomaterials 1996;17:1615-1619.
216. Wade LG. Organic chemistry. New Jersey: Pearson Prentice Hall; 2006. 531 p.
217. Williams JA, Billington RW. A new technique for measuring the radiopacity of natural tooth substance and restrorative materials. Journal of Oral Rehabilitation 1987;14:267-269.
218. Kjellson F, Alme´n T, Tanner KE, McCarthy ID, Lidgren L. Bone Cement X-ray Contrast Media: A Clinically Relevant Method of Measuring their Efficacy. Journal of Biomedical Materials Research Part B: Applied Biomaterials 2004;70 B:354-361.
219. Weast EC. CRC Handbook of Chemistry and Physics. Boca Raton, FL: CRC press; 1986. F-170 p.
220. Shenoy AV. Rheology of filled polymer systems. Boston: Kluwer Academic Publishers; 1999. 11-18 p.
221. Lewis G. Fatigue testing and performance of acrylic bone-cement materials: State-of-the-art review. Journal of Biomedical Materials Research Part B: Applied Biomaterials 2003;66 B(1):457-486.
222. Topoleski L, Ducheyne P, Cuckler J. The fracture toughness of titanium-fiber-reinforced bone cement. J Biomed Mater Res 1992;26:1599-1617.
223. Kasuga T, Hiramatsu M, Hoson A, Sekino T, Niihara K. Titania nanotubes prepared by chemical processing. Advanced Materials 1999;11(15):1307-1311.
224. Bavykin DV, Friedrich JM, Walsh FC. Protonated titanates and TiO_2 nanostructured materials: synthesis, properties, and applications. Advanced Materials 2006;18(21):2807-2824.
225. Chen Q, Du GH, Zhang S, Peng LM. The structure of trititanate nanotubes. Acta Crystallographica, Section B: Structural Science 2002;58(4):587-593.
226. Zhang M, Jin Z, Zhang J, Guo X, Yang J, Li W, Wang X, Zhang Z. Effect of annealing temperature on morphology, structure and photocatalytic behavior of nanotubed $H_2Ti_2O_4(OH)_2$. Journal of Molecular Catalysis A:Chemical 2004;217:203-210.
227. Kim G-S, Ansari SG, Seo H-K, Kim Y-S, Shin H-S. Effect of annealing temperature on structural and bonded states of titanate nanotube films. Journal of Applied Physics 2007;101:024314-024320.
228. Weng L-Q, Song S-H, Hodgson S, Baker A, Yu JC. Synthesis and characterisation of nanotubular titanates and titania. Journal of the European Ceramic Society 2006;26:1405-1409.
229. Zhang L, Lin H, Wang N, Lin C, Li J. The evolution of morphology and crystal form of titanate nanotubes under calcination and its mechanism. Journal of Alloys and Compounds 2007;431(1-2):230-235.

230. Zheng K, Chen L, Li Y, Cui P. Preparation and thermal properties of silica-graft acrylonitrile-butadiene-styrene nanocomposites. Polymer Engineering Science 2004;44:1077-1082.
231. Huang X, Brittain WJ. Synthesis and Characterization of PMMA nanocomposites by suspension and emulsion polymerization. Macromolecules 2001;34:3255.
232. Rayson HW, McGrath GC. Fibres, whiskers and flakes for comoposite applications. In: Clegg DW, Collyer AA, editors. Mechanical properties of reinforced thermoplastics. NewYork: Elsevier Applied Science Publishers; 1986. p 55-56.
233. Wichmann HG, Schulte K, Wagner HD. On nanocomposite toughness. Composites Science and Technology 2008;68:329-331.
234. Gojny FH, Wichmann MHG, Kopke U, Fiedler B, Schulte K. Carbon nanotube-reinforced epoxy-composites: enhancedstiffness and fracture toughness at low nanotube content. Composites Science and Technology 2004;64:2363-2371.
235. Fiedler B, Gojny FH, Wichmann HG, Nolte CM, Schulte K. Fundamental aspects of nano-reinforced composites. Composites Science and Technology 2006;66:3115-3125.
236. Ma R, Sasaki T, Bando Y. Layer-by-layer assembled multilayer films of titanate nanotubes, Ag- or Au-Loaded nanotubes, and nanotubes/nanosheets with polycations. The Journal of the American Chemical Society 2004;126:10382-10388.
237. Lewis G, Bhattaram A. Influence of a pre-blended antibiotic (Gentamicin Sulfate powder) on various mechanical, thermal, and physical properties of three acrylic bone cements. J Biomater Appl 2006;20:377-408.
238. Bearden JA, Burr AF. Reevaluation of X-ray atomic energy levels. Reviews of Modern Physics 1967;39:125-142.
239. Lewis G, Xu J, Madigan S, Towler MR. Influence of strontia on various properties of Surgical Simplex P acrylic bone cement and experimental variants. Acta Biomaterialia 2007;3:970-979.
240. Stamboulis A, Law RV, Hill R. Characterisation of commercial ionomer glasses using magic angle nuclear magnetic resonance (MAS NMR). Biomaterials 2005;25:3907-3913.
241. Guida A, Towler MR, Wall JG, Hill RG, Eramo S. Preliminary work on the antibacterial effect of strontium in glass ionomer cements. Journal of Materials Science Letter 2003;22:1401-1403.
242. Schaffer GB, Huo SH, Drennan J, Auchterlonie GJ. The effect of trace elements on the sintering of an Al–Zn–Mg–Cu alloy. Actra Materialia 2001;49:2671-2678.
243. Lloyd GE. Atomic number and crystallographic contrast images with the SEM: a review of backscattered electron techniques. Mineralogical Magazine 1987;51:3-19.
244. Luo Y-B, Wang X-L, Xu D-Y, Wang Y-Z. Preparation and characterization of poly(lactic acid)-grafted TiO_2 nanoparticles with improved dispersions. Applied Surface Science 2009;255:6795-6801.
245. Uetsuka H, Henderson MA, Sasahara A, Onishi H. Formate adsorption on the (111) surface of rutile TiO_2. Journal of Physical Chemistry B 2004;108:13706-13710.

246. Johnson AR, Armstrong WD, Singer L. The incorporation and removal of large amounts of strontium by physiologic mechanisms in mineralized tissues. Calcified Tissue Research 1968;2:242-252.
247. Marie PJ, Ammann P, Boivin G, Rey C. Mechanisms of action and therapeutic potential of strontium in bone. Calcified Tissue International 2001;69:121-129.
248. Haboush E. A new operation for arthroplasty of the hip based on biomechanics photoelasticity, fast-setting dental acrylic and other considerations. Bull Hosp Joint Dis Orthop Inst 1953;14:242-250.
249. Schurman D, Bloch D, Segal M, Tanner C. Conventional cemented total hip arthroplasty. Clin Orthop Relat Res 1989;240:173-179.
250. Praemer A, Furner S, Rice D. Musculoskeletal conditions in the United States. Rosemont: American Academy of Orthopaedic Surgeons; 1999. 130-140 p.
251. Burns AWR, Bourne RB. Economics of revision total hip arthroplasty. Current Orthopaedics 2006;20:203-207.
252. Kotha S, Li C, Schmid S, Mason J. Fracture toughness of steel-fiber-reinforced bone cement. J Biomed Mater Res A 2004;70:514-521.
253. Bowman A, Manley T. The elimination of breakages in upper dentures by reinforcement with carbon fibre. Br Dent J 1984;156:87-89.
254. Stipho H. Effect of glass fiber reinforcement on some mechanical properties of autopolymerizing polymethyl methacrylate. J Prosthet Dent 1998;79:580-584.
255. Vallittu P. Dimensional accuracy and stability of polymethyl methacrylate reinforced with metal wire or with continuous glass fiber. J Prosthet Dent 1996;75:617-621.
256. Manley T, Bowman A, Cook M. Denture bases reinforced with carbon fibres. Br Dent J 1979;146:25-30.
257. Saha S, Pal S. Mechanical characterization of commercially made carbon-fiber-reinforced polymethylmethacrylate. J Biomed Mater Res 1986;20:817-826.
258. Pourdeyhimi B, Wagner H. Elastic and ultimate properties of acrylic bone cement reinforced with ultrahigh molecular weight polyethylene fibers. J Biomed Mater Res 1989;23:63-80.
259. Njuguna J, Pielichowski K. Polymer nanocomposites for aerospace applications: characterization. Advanced Engineering Materials 2004;6:204-210.
260. Lewis G. Effect of lithotriptor treatment on the fracture toughness of acrylic bone cement. Biomaterials 1991;13(4):225-230.
261. Meyer PR, Lautenschlager EP, Moore BK. On the setting properties of acrylic bone cement. The Journal of Bone & Joints Surgery 1973;55:149-156.
262. Kurtz SM, Villarraga ML, Zhao K, Edidin AA. Static and fatigue mechanical behavior of bone cement with elevated barium sulfate content for treatment of vertebral compression fractures. Biomaterials 2005;26:3699-3712.
263. Topoleski LD, Ducheyene P, Cuckler JM. A fractographic analysis of *in vivo* poly(methyl methacrylate) bone cement failure mechanisms. J Biomed Mater Res 1990;24:135-154.

Appendices

Appendix 1. American Chemical Society's Policy on Theses and Dissertations

If your university requires a signed copy of this letter see contact information below:

Thank you for your request for permission to include your paper(s) or portions of text from your paper(s) in your thesis. Permission is now automatically granted; please pay special attention to the implications paragraph below. The Copyright Subcommittee of the Joint Board/Council Committees on Publications approved the following:

Copyright permission for published and submitted material from theses and dissertations

ACS extends blanket permission to students to include in their theses and dissertations their own articles, or portions thereof, that have been published in ACS journals or submitted to ACS journals for publication, provided that the ACS copyright credit line is noted on the appropriate page(s).

Publishing implications of electronic publication of theses and dissertation material:

Students and their mentors should be aware that posting of theses and dissertation material on the Web prior to submission of material from that thesis or dissertation to an ACS journal may affect publication in that journal. Whether Web posting is considered prior publication may be evaluated on a case-by-case basis by the journal's editor. If an ACS journal editor considers Web posting to be "prior publication", the paper will not be accepted for publication in that journal. If you intend to submit your unpublished paper to ACS for publication, check with the appropriate editor prior to posting your manuscript electronically.

If your paper has not yet been published by ACS, we have no objection to your including the text or portions of the text in your thesis/dissertation in print and microfilm formats; please note, however, that electronic distribution or Web posting of the unpublished paper as part of your thesis in electronic formats might jeopardize publication of your paper by ACS. Please print the following credit line on the first page of your article: "Reproduced (or 'Reproduced in part') with permission from [JOURNAL NAME], in press (or 'submitted for publication'). Unpublished work copyright [CURRENT YEAR] American Chemical Society." Include appropriate information.

If your paper has already been published by ACS and you want to include the text or portions of the text in your thesis/dissertation in print or microfilm formats, please print the ACS copyright credit line on the first page of your article: "Reproduced (or 'Reproduced in part') with permission from [FULL REFERENCE CITATION.] Copyright [YEAR] American Chemical Society." Include appropriate information.

Submission to a Dissertation Distributor: If you plan to submit your thesis to UMI or to another dissertation distributor, you should not include the unpublished ACS paper in your thesis if the thesis will be disseminated electronically, until ACS has published your paper. After publication of the paper by ACS, you may release the entire thesis (not the individual ACS article by itself) for electronic dissemination through the distributor; ACS's copyright credit line should be printed on the first page of the ACS paper.

Use on an Intranet: The inclusion of your ACS unpublished or published manuscript is permitted in your thesis in print and microfilm formats. If ACS has published your paper you may include the manuscript in your thesis on an intranet that is not publicly available. Your ACS article cannot be posted electronically on a publicly available medium (i.e. one that is not password protected), such as but not limited to, electronic archives, Internet, library server, etc. The only material from your paper that can be posted on a public electronic medium is the article abstract, figures, and tables, and you may link to the article's DOI or post the article's author-directed URL link provided by ACS. This paragraph does not pertain to the dissertation distributor paragraph above.

Questions? Call +1 202/872-4368/4367. Send e-mail to copyright@acs.org_or fax to +1 202-776-8112. 10/10/03, 01/15/04, 06/07/06

Appendix 2. Molecular weight distribution of PMMA powder obtained from Ivoclar Vivadent

Auto-Scaled Chromatogram

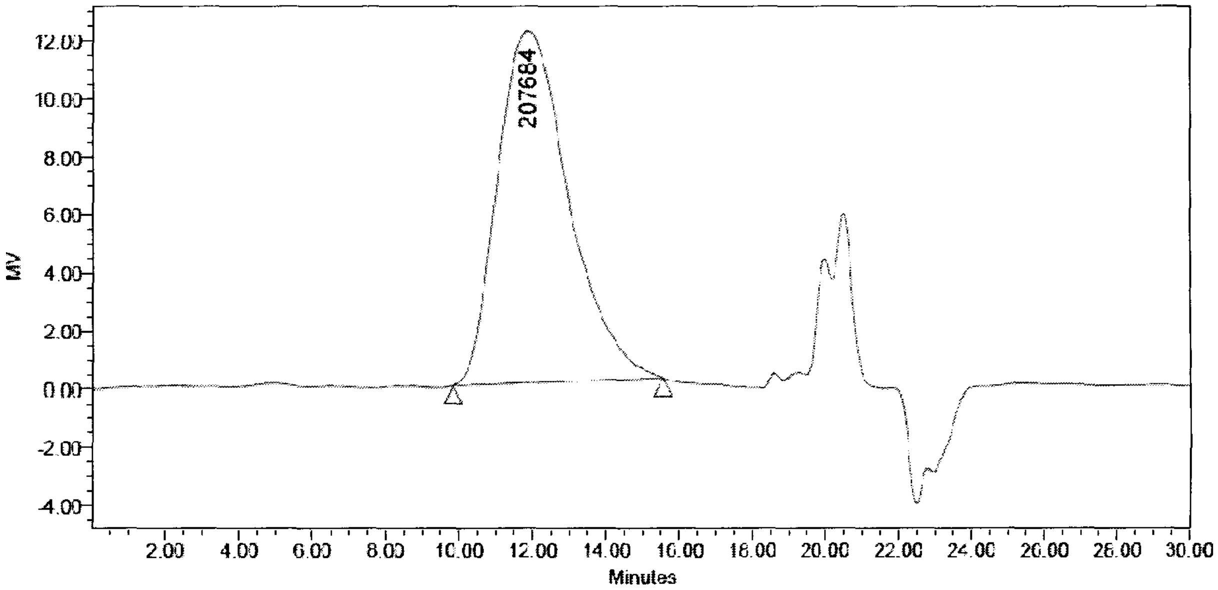

GPC Results

	Dist Name	Mn	Mw	MP	Mz	Mz+1	Mv	Polydispersity	MW Marker 1	MW Marker 2
1		126858	218124	207684	333174	457787		1.719437	100000	350000

Appendix 3. X-ray diffraction of commercial titania nanopowder obtained from Sigram-Aldrich

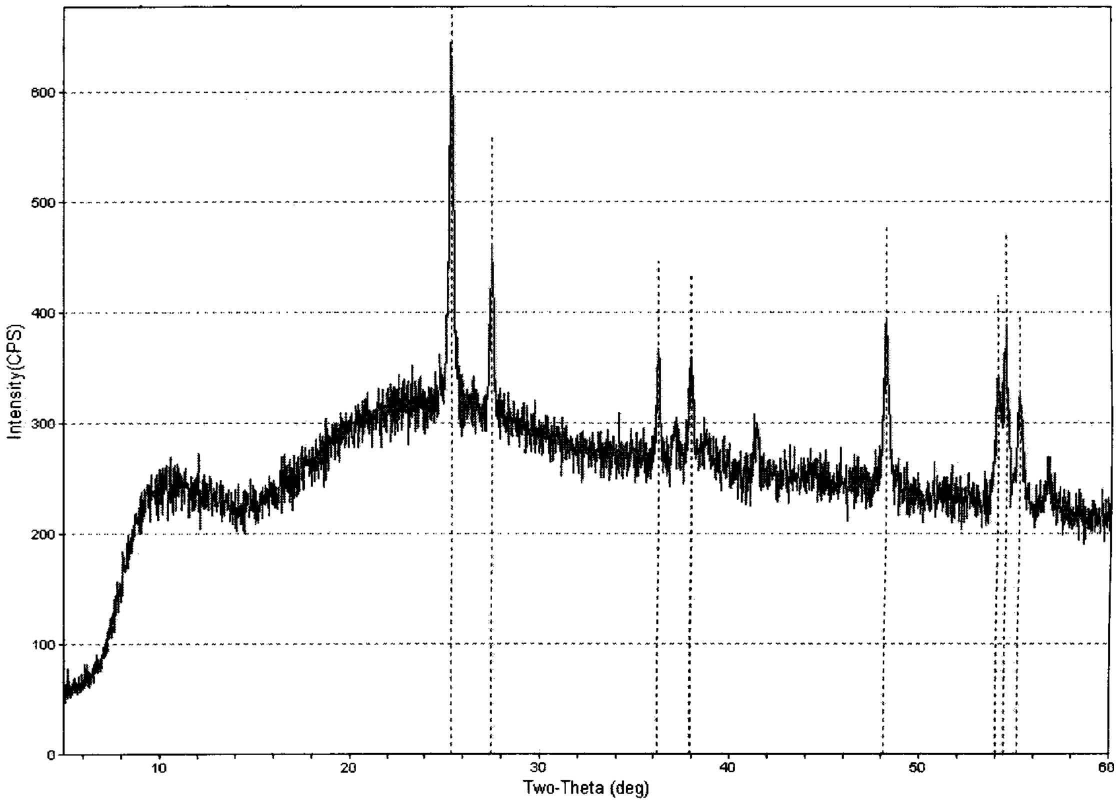

Appendix 4. Composition of the CMW®1 cement as supplied by the manufacturer

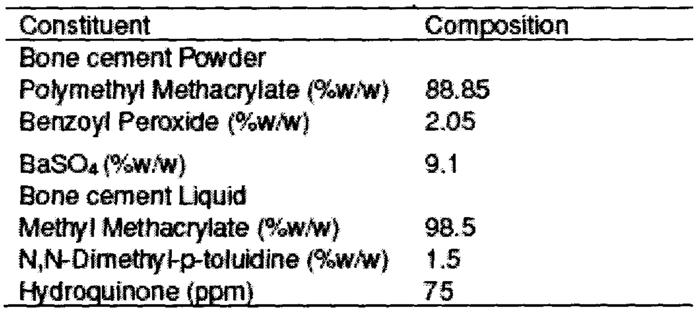

Constituent	Composition
Bone cement Powder	
Polymethyl Methacrylate (%w/w)	88.85
Benzoyl Peroxide (%w/w)	2.05
$BaSO_4$ (%w/w)	9.1
Bone cement Liquid	
Methyl Methacrylate (%w/w)	98.5
N,N-Dimethyl-p-toluidine (%w/w)	1.5
Hydroquinone (ppm)	75

Appendix 5. Average molecular weight distribution of the prepolymerized PMMA of the powder part of CMW®1

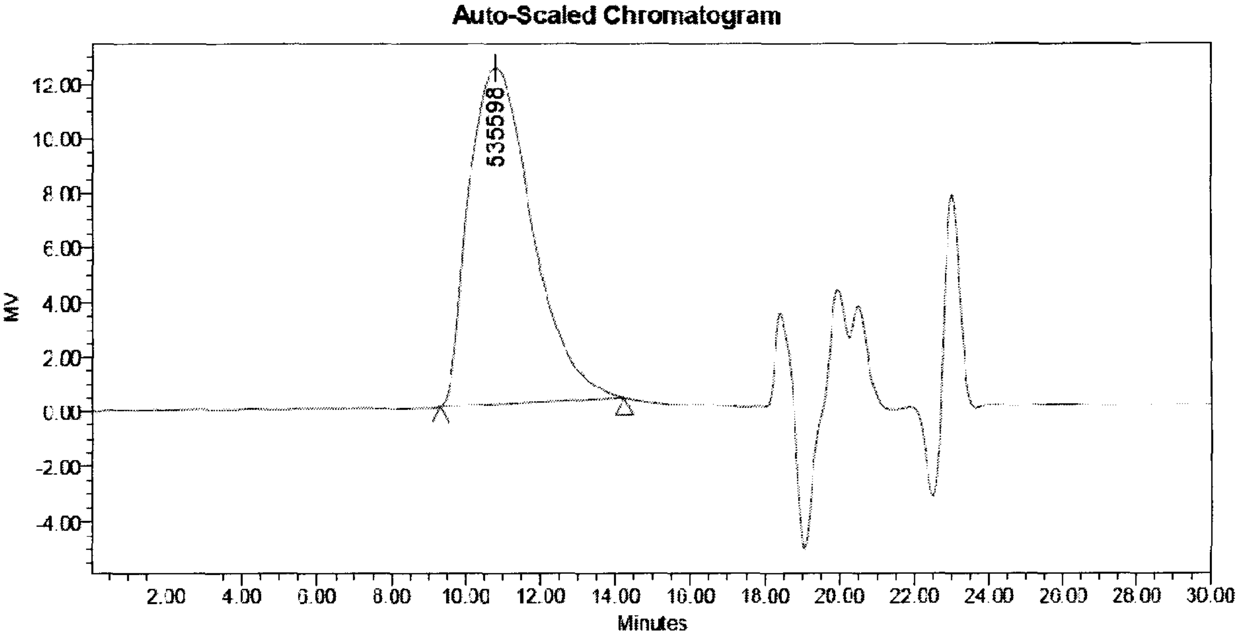

GPC Results

Dist Name	Mn	Mw	MP	Mz	Mz+1	Mv	Polydispersity	MW Marker 1	MW Marker 2
1	320958	541071	535598	734708	1006948		1.685800	100000	350000